Carnegie Mellon University

Department of Physics

The Scalar Glueball and $K\pi$ Scattering from Lattice QCD

Ruairí Brett

Adviser:
Prof. Colin Morningstar

Submitted in partial fulfillment of the
requirements for the degree of
Doctor of Philosophy
at
Carnegie Mellon University
Department of Physics
Pittsburgh, Pennsylvania

July 2019

Abstract

The scalar glueball and $K\pi$ scattering are studied using Markov-chain-based Monte Carlo computations with quantum chromodynamics (QCD) formulated on a space-time lattice. Lattice QCD offers an *ab initio*, systematically improvable framework in which to probe the low-lying, non-perturbative spectrum of QCD using numerical calculations. Here the finite-volume spectrum of the notoriously challenging scalar sector of QCD is studied on an anisotropic $24^3 \times 128$ lattice with spacing $a_s \sim 0.12$ fm and $m_\pi \sim 390$ MeV. Mixing effects between quark-antiquark, meson-meson, and glueball states are included for the first time. With the inclusion of a scalar glueball interpolating operator, no additional finite-volume states are observed below ~ 2 GeV. Furthermore, only two states in this region are observed to be created predominantly by quark-antiquark interpolating operators which can be associated with the σ and $f_0(980)$ resonances. The extraction of infinite-volume scattering amplitudes from finite-volume two-particle energies is then addressed. Following an earlier calculation, a simultaneous extraction of elastic s- and p-wave $K\pi$ scattering amplitudes is presented, using an isotropic ensemble of $48^3 \times 128$ gauge field configurations with spacing $a \sim 0.064$ fm generated by the CLS effort. Breit-Wigner resonance parameters for the vector $K^*(892)$ meson along with the s-wave $K\pi$ scattering length are determined for $(m_\pi, m_K) = (280, 460)$ MeV.

Acknowledgements

The work in this thesis could not have been completed without the help and support of a number of people. First, my adviser Colin Morningstar, for his patience, guidance, and encouragement throughout my PhD. I am also grateful for my scientific collaborators, John Bulava, Jacob Fallica, Andrew Hanlon, Ben Hörz, and Danny Darvish, for endless discussions, debates, and advice, both professional and personal. Additionally, I am indebted to my fellow graduate students and friends at CMU, in Pittsburgh, and further afield, for their support and friendship. Finally, I would like to thank my family, for their endless encouragement and support throughout my time at CMU. This work was supported by the U.S. National Science Foundation under award PHY-1613449, and the John Peoples Jr. Research Fellowship at CMU. Computing resources were provided by the Extreme Science and Engineering Discovery Environment (XSEDE) under grant number TG-MCA07S017.

Ah, there's nothing more exciting than science.
You get all the fun of sitting still, being quiet,
writing down numbers, paying attention...
Science has it all.
– Principal Seymour Skinner

Contents

1 Introduction **1**

2 Lattice QCD **6**

2.1 QCD Lagrangian . . . 7

2.1.1 Imaginary Time . . . 8

2.2 Discretising Spacetime . . . 10

2.2.1 Naïve Discretisation of Fermions . . . 11

2.2.2 Fermion Doubling . . . 13

2.2.3 Gauge Action . . . 15

2.3 Action Improvement and Scale Setting . . . 16

2.3.1 Anisotropic HadSpec Ensembles . . . 17

2.3.2 Isotropic CLS Ensembles . . . 19

2.3.3 Tuning the Action and Scale Setting . . . 21

2.4 Euclidean Two-Point Functions . . . 23

2.4.1 Hermiticity . . . 24

2.5 Monte Carlo Integration . . . 26

2.5.1 Hybrid Monte Carlo . . . 29

2.5.2 Rational Hybrid Monte Carlo . . . 30

3 Constructing Hadron Operators **31**

3.1 Basic Building Blocks . . . 31

3.1.1 Gauge Link Smearing . . . 32

3.1.2 Quark Field Smearing . . . 33

3.1.3 Covariant Displacements . . . 36

3.2 Single-Hadron Operators . . . 36

3.2.1 Flavour Structure: Isospin, and G-Parity . . . 36

3.2.2 Elemental Baryons . . . 38

3.2.3 Elemental Mesons . . . 40

3.3 Symmetry Channels . . . 42

3.4 Rotational Symmetry on the Lattice . . . 43

3.4.1 The Octahedral Group and Point Group . . . 44

3.4.2 Moving Frames . . . 46
3.4.3 Projection onto Symmetry Groups . . . 46
3.5 Multi-Hadron Operators . . . 48
3.6 Exotic Operators . . . 50
3.6.1 Tetraquarks . . . 50
3.6.2 Glueballs . . . 51

4 Stochastic Estimation of Correlation Functions 53
4.1 Quark Lines . . . 53
4.1.1 The LapH Subspace . . . 56
4.2 Stochastic Matrix Inversion . . . 57
4.2.1 Dilution Schemes . . . 58
4.3 Stochastic Estimates of Quark Lines . . . 59
4.4 Correlation Function Factorisation . . . 60
4.4.1 Baryon-to-Baryon Correlations . . . 60
4.4.2 Meson-to-Meson Correlations . . . 62
4.4.3 More Complicated Correlation Functions . . . 63

5 Extracting the Finite-Volume Spectrum 65
5.1 Correlator Matrix Analysis . . . 65
5.1.1 The Generalised Eigenvalue Problem . . . 66
5.1.2 The Single Pivot . . . 68
5.2 Temporal Wrap-Around Effects . . . 69
5.3 Fitting Diagonal Correlators . . . 71

6 Scattering Observables from the Lattice 74
6.1 Quantisation Condition . . . 74
6.1.1 Quantum Mechanics in One Dimension . . . 75
6.1.2 Lüscher Quantisation Condition - Overview . . . 77
6.1.3 Lüscher Quantisation Condition - Derivation . . . 78
6.2 Box Matrix and Block Diagonalisation . . . 83
6.2.1 The K-Matrix and Box Matrix . . . 83
6.2.2 Block Diagonalisation . . . 85
6.3 Fitting the K-Matrix . . . 87
6.3.1 Determinant Residual Method and the Ω Function . . . 88

7 The Scalar Glueball 89
7.1 Analysis Details . . . 89
7.1.1 Ensemble Info . . . 90
7.1.2 Correlator Matrix Construction . . . 90

7.1.3 Correlator Matrix Analysis . . . 91
7.2 Results . . . 93

8 $K\pi$ Scattering **104**
8.1 Analysis Details . . . 104
8.1.1 Ensemble Info . . . 104
8.1.2 Spectrum Determination . . . 105
8.1.3 K-Matrix Fits . . . 106
8.2 Results . . . 107

9 Conclusions **113**

Appendix A Extracting Observables from Monte Carlo Data **115**
A.1 Resampling Techniques . . . 116
A.2 Correlated χ^2 Fitting . . . 117

Appendix B Correlator Matrices **118**

Appendix C $t_{\min}$-Plots **131**
C.1 $K\pi$ Scattering . . . 132

Appendix D Computational Details and Approximations **147**
D.1 Computational Details . . . 147
D.2 Approximations . . . 148

List of Figures

1.1 Running of the QCD coupling α_S as a function of energy scale Q. 2

2.1 Graphical representation of the gauge link variables 12

3.1 Effective masses for nucleon operators having different covariant displacements with and without smearing. 35
3.2 The displaced baryon operators we use. 40
3.3 The displaced meson operators we use. 42
3.4 The rotation axes corresponding to the group elements C_{nj} of O. 45
3.5 The tetraquark operator displacements we plan to use. 51
3.6 Comparison of the effective masses for three different scalar glueball operators . . . 52

4.1 The three types of quark lines we must consider in the evaluation of hadronic temporal correlation functions. 55
4.2 A diagrammatic depiction of a baryon-to-baryon correlation function. 62
4.3 A diagrammatic depiction of a meson-to-meson correlation function. 63
4.4 A diagrammatic depiction of the temporal correlation between a two-meson source and a single-meson sink. 64

5.1 Effective energies from a toy model demonstrating the effectiveness of solving the generalised eigenvalue problem. 68
5.2 Comparison of different fit ansätze used to account for effects from the finite temporal extent. 73

6.1 Typical interacting and non-interacting energy levels as a function of volume for a weak interaction. 76
6.2 Diagrammatic expansion of the finite-volume correlator in terms of Bethe-Salpeter kernels. 79
6.3 The finite-volume loop momentum sum expressed as the infinite-volume loop momentum integral plus a finite-volume correction. 81
6.4 Diagrammatic representation of the subtracted correlator. 82

7.1 Flavoured staircase plot for the A_{1g}^{+} channel using only $\overline{q}q$-type operators 94

7.2 Effective masses in the A_{1g}^{+} channel without the glueball operator. 96
7.3 Overlaps $|Z^{(n)}|^2$ for the A_{1g}^{+} channel excluding the glueball operator. 97
7.4 Effective masses in the A_{1g}^{+} channel including the glueball operator. 98
7.5 Overlaps $|Z^{(n)}|^2$ for the A_{1g}^{+} channel including the glueball operator. 99
7.6 Flavoured staircase plot for the A_{1g}^{+} channel without the glueball operator 100
7.7 Flavoured staircase plot for the A_{1g}^{+} channel including the glueball operator 101

8.1 Finite-volume energies in each of the irreps used for $K\pi$ scattering. 110
8.2 p-wave box matrix elements as a function of E_{cm}/m_π. 111
8.3 p-wave scattering phase shift as a function of E_{cm}/m_π. 112

B.1 Layout of correlator matrix plots. 118
B.2 Real part of the correlation matrix used in the scalar glueball study. 124
B.3 Imaginary part of the correlation matrix used in the scalar glueball study. 130

C.1 t_{min}-plots for the $P^2 = 0$, A_{1g} irrep on the N200 ensemble. 132
C.2 t_{min}-plots for the $P^2 = 0$, T_{1u} irrep on the N200 ensemble. 133
C.3 t_{min}-plots for the $P^2 = 1$, A_1 irrep on the N200 ensemble. 135
C.4 t_{min}-plots for the $P^2 = 1$, E irrep on the N200 ensemble. 136
C.5 t_{min}-plots for the $P^2 = 2$, A_1 irrep on the N200 ensemble. 138
C.6 t_{min}-plots for the $P^2 = 2$, B_1 irrep on the N200 ensemble. 139
C.7 t_{min}-plots for the $P^2 = 2$, B_2 irrep on the N200 ensemble. 140
C.8 t_{min}-plots for the $P^2 = 3$, A_1 irrep on the N200 ensemble. 142
C.9 t_{min}-plots for the $P^2 = 3$, E irrep on the N200 ensemble. 143
C.10 t_{min}-plots for the $P^2 = 4$, A_1 irrep on the N200 ensemble. 145
C.11 t_{min}-plots for the $P^2 = 4$, E irrep on the N200 ensemble. 146

List of Tables

3.1 Flavour combinations of three quarks with definite isospin, isospin projection, and strangeness. 39
3.2 Flavour structure of the elemental hadron operators we use. 41
3.3 The number of times that the irrep Γ of O occurs in the reducible subduction of the J irrep of $SO(3)/SU(2)$ 46
3.4 The subductions of the single- and double-valued irreps of O_h^D onto the irreps of the little groups C_{4v}, C_{3v}, and C_{2v}. 47

6.1 Relationship between box matrix irrep and full symmetry irrep. 86

7.1 Details of the anisotropic ensemble used in the scalar glueball study. 90
7.2 The operator basis we use in the glueball study. 93
7.3 Fit results in the A_{1g}^+ channel excluding the glueball operator. 95
7.4 Fit results in the A_{1g}^+ channel including the glueball operator. 102

8.1 Details of the isotropic ensemble used in the $K\pi$ scattering study. 105
8.2 Irreps of the appropriate little group for various total momenta used for $K\pi$ scattering. 105
8.3 Single- and two-hadron operators used in the $K\pi$ scattering analysis. 106
8.4 Finite-volume two-hadron energies in the center-of-mass frame with corresponding box matrix elements. 109
8.5 $\widetilde{K}$-matrix fit results for s- and p-wave elastic $K\pi$ scattering. 110

Chapter 1

Introduction

With the invention of bubble chambers and spark chambers in the 1950's and 1960's, experimental particle physics saw the discovery of an abundance of new particles, which were called hadrons. Such a large number of particles suggested some unknown substructure. These new states were classified first by charge and isospin, then by strangeness, until in 1964 Gell-Mann [1] and Zweig [2,3] independently proposed that hadrons were comprised of fractionally-charged particles called quarks (although Zweig called them aces). In this quark model, the lightest hadrons could be classified according to an $SU(3)$ symmetry involving a property of quarks known as "flavor". The flagship result from this quark model was the successful prediction of the Ω^- (sss) baryon, discovered in 1964 [4]. This and states like the Δ^{++} (uuu) led to the introduction of an additional $SU_c(3)$ "colour" symmetry for the quarks, which in 1973, was proposed as the gauge symmetry underpinning the strong interaction, and the resulting theory was known as Quantum Chromodynamics (QCD) [5]. QCD describes the strong interactions between the quarks and gluons, the fundamental particles that make up all hadronic matter, in an $SU_c(3)$ Yang-Mills theory with 6 flavours of colour-charged fermions (the quarks).

Today, QCD is well established as the gauge theory of the strong interaction; asymptotic freedom [6, 7] allows for perturbative expansions in the gauge coupling at high energies[1] ($q^2 \approx m_Z^2$) which reproduce various experimental results with great accuracy; and at low energies ($q^2 \approx m_\pi^2$), chiral effective theories based on the symmetries of QCD are successful at reproducing a range of experimental results. However, it is in the intermediate energy regime ($q^2 \approx 1$ GeV^2) that difficulties arise. Here the QCD coupling is too large for a perturbative expansion (see fig. 1.1), while the energy is large enough for many excited hadron states to form. Hence a non-perturbative approach in this regime is required. Lattice QCD provides the only non-perturbative, first-principles, systematically improvable approach to calculations at this energy scale, wherein the dynamics of QCD are simulated numerically on a discrete Euclidean space-time lattice.

Despite numerous advances in the experimental, phenomenological, and theoretical approaches

[1] Note that for certain processes involving hadrons, e.g. deep inelastic scattering, factorisation theorems exist for factoring cross sections into subsets which are independently perturbatively and non-perturbatively calculable [8].

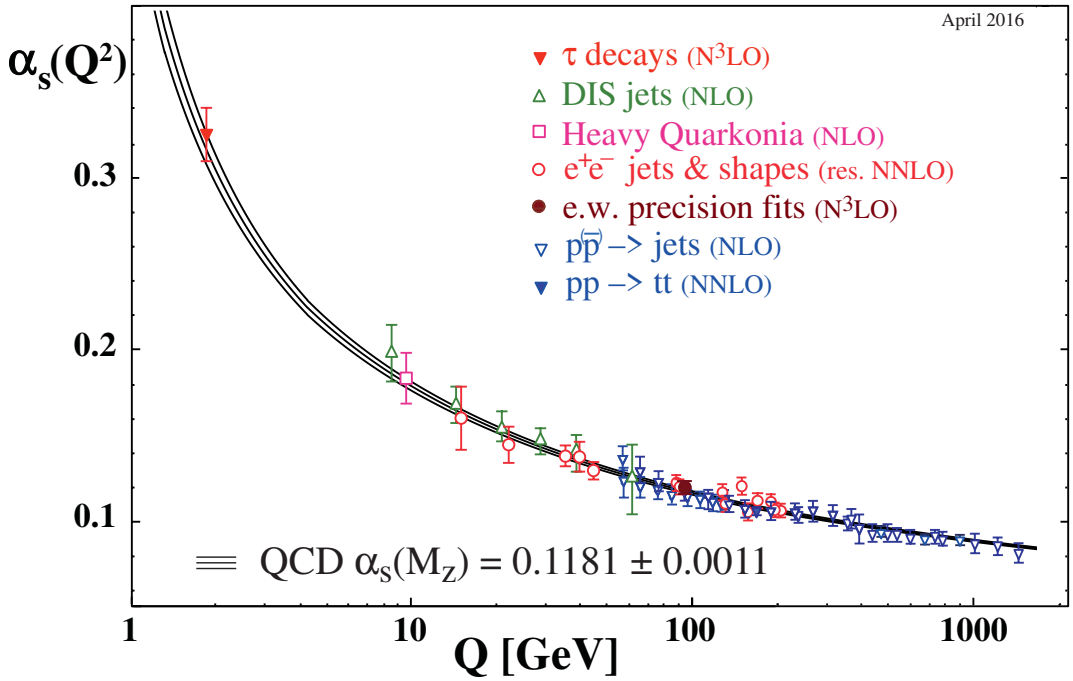

Figure 1.1: Running of the QCD coupling α_S as a function of the energy scale Q. The respective degree of QCD perturbation theory used in the extraction is indicated in the brackets. Figure from Ref. [9].

to studying hadronic physics, the rich spectrum of QCD remains poorly understood. For example, the first excited state of the nucleon, the Roper resonance, is difficult to study in lattice QCD with three-quark operators only, and it lies below the lightest negative parity nucleon, in direct contradiction to most quark models [10]. The light scalar mesons (mesons with $J^{PC} = 0^{++}$ containing only u, d, and s valence quarks) are notoriously challenging in lattice QCD due to disconnected quark diagrams and signal-to-noise problems, and their mass orderings are, in a simple $q\overline{q}$ quark model, inverted as compared to the experimental observations [11]. Similarly, throughout the low-lying spectrum of QCD there are numerous open questions as to the nature of, or even existence of, non-conventional hadronic states such as glueballs (purely gluonic states), tetraquarks ($qq\overline{q}\overline{q}$), hybrid mesons (mesons with exotic/non-$q\overline{q}$ quantum numbers), etc.

Lattice QCD is currently the best method to tackle many of these problems in hadron spectroscopy. Considerable progress has been made in recent years in extracting the excited state spectrum of QCD due to both the increased amount of computational resources and a multitude of new numerical techniques, some of which we describe and employ here. Our approach focuses on extracting the stationary states of QCD in a finite-volume from matrices of two-point temporal

correlation functions using correlation matrix methods [12–14]. Central to our approach is the use of the stochastic LapH method [15] for estimating the computationally daunting quark lines/Wick contractions that arise in hadronic correlation functions. With these tools, we are able to study the finite-volume eigenstates of QCD using large and carefully designed interpolating operator bases. With the stochastic LapH method, the inclusion of multi-particle interpolating operators in our calculation is practical. By identifying the $q\bar{q}$ dominated stationary states in a given symmetry sector, we can compare to the experimental resonances expected in that sector, in order to shed some light on the gaps in our current understanding of the QCD spectrum.

As lattice calculations are necessarily restricted to a finite volume, it is important to connect to the infinite-volume physics of the real world. This is possible through a formalism first discussed by Lüscher [16], and then expanded upon by numerous others, for relating finite-volume stationary state energies to the infinite-volume scattering matrix. The finite volume is exploited using the Lüscher quantisation condition to sidestep the no-go theorem of Maiani and Testa [17] which prevents the direct extraction of Minkowski space-time scattering information from Euclidean correlation functions. This approach has proved to be very successful for elastic meson-meson scattering (see Refs. [18–20] for some results from our collaboration), and has recently also been applied to elastic meson-baryon scattering [21].

The usefulness of lattice QCD extends far beyond hadron spectroscopy, and it is in fact one of the most powerful non-perturbative probes of strongly-interacting gauge theories in physics today. Cutting edge lattice calculations are used today, for example, in precision determinations of fundamental parameters of the Standard Model, such as the strong coupling constant, and in predicting hadronic contributions to the anomalous magnetic moment of the muon, $g_\mu - 2$. In a series of whitepapers released this year [22–28] the USQCD collaboration summarises the current status and outlines some of the upcoming opportunities for lattice calculations in several physics areas, including hadron spectroscopy, quark and lepton flavour physics, searches for physics beyond the Standard Model (BSM), and more.

In this thesis we will first outline the basics of the lattice discretisation of QCD in chapter 2, discussing the difficulties in formulating the theory in a discrete space-time, along with some details on how Monte Carlo techniques are used to generate configurations of gauge field ensembles in evaluating correlation functions using the path integral formulation of quantum field theory (QFT). After this groundwork has been set, we then describe in chapter 3 our method of constructing large sets of hadronic interpolating operators with the appropriate transformation properties to extract as much of the low-lying spectrum as possible. Chapter 4 then contains the details of how we estimate correlation functions of such operators using the stochastic LapH method [15], followed by the application of correlation-matrix techniques to extract the finite-volume spectrum in chapter 5. We present the Lüscher quantisation condition for relating finite-volume energies to the infinite-volume scattering matrix in chapter 6, along with our implementation of the formalism and the introduction of the quantity we call the *box matrix* [29]. Finally, in chapters 7 and 8 we present the main results of this work, a first study of the scalar glueball in which the contributions

from $q\overline{q}$ and meson-meson states are included in full QCD, and a study of elastic $K\pi$ scattering where we extract the s- and p-wave scattering amplitudes to study both the well-established vector $K^*(892)$ meson, and probe the contentious scalar $K_0^*(700)$ resonance[2].

The Scalar Glueball

The three-gluon and four-gluon coupling terms in the QCD Lagrangian suggest the existence of composite states consisting solely of gluons, called glueballs. Such states are of great interest especially as they are distinct from the prototypical $\overline{q}q$ and qqq hadronic states predicted by constituent quark models. Even in an era where searches for beyond the standard model (BSM) physics draw more and more attention, incontrovertible experimental evidence for their existence remains elusive. Experimentally there are several candidates for the lightest scalar glueball, the $f_0(1370)$, $f_0(1500)$, and $f_0(1710)$ states. However, none have yet been unambiguously identified as a glueball state [30]. To identify which of the three is most likely a glueball or gluon-dominated state, model independent, first principles lattice calculations are required (see, e.g. Ref. [31]).

The glueball spectrum in pure Yang-Mills gauge theory has been extensively mapped out [32–34]. The lowest-lying scalar and tensor glueballs have previously been studied in quenched QCD, but the quenched approximation[3] makes such studies unreliable. For the scalar glueball, quenched calculations yield a glueball mass in the range $1.5 - 1.7$ GeV, potentially suggesting the exclusion of the $f_0(1370)$ as a glueball candidate. Again, the quenched approximation makes such conclusions unreliable.

More recent studies have included the effects of sea quarks on glueballs [35–40], giving largely compatible results with each other, and with quenched calculations in the scalar, and tensor sectors, though the presence of the $U_A(1)$ anomaly in the pseudoscalar sector complicates matters, meaning that contributions from the η' meson must be understood further. The most important takeaway from these studies is that the mixing between glueball and conventional meson states has been neglected thus far. The full inclusion of meson and meson-meson states is crucial for any definitive conclusions about the nature, or even existence of such glueball states. This is highlighted for instance in the recent calculation in Ref. [40] where, for the scalar glueball, the authors find the ground state energy extracted from gluonic correlation functions to be $\sim 1.4 - 1.5$ GeV, close to the ground state of correlation functions involving quark bilinears (i.e. $\overline{q}q$ operators). This indicates, at least at the quite heavy pion masses used in Ref. [40], that the mixing between flavour singlet meson (and meson-meson) states and glueball states is critical to studies of glueball states.

Furthermore, while quenched calculations exhibit stable glueball states, in QCD the hypothetical states will most likely manifest as unstable resonances, as their expected masses lie well above

[2]Sometimes known as the κ resonance.

[3]In early lattice calculations, the computationally expensive effects of dynamical sea quarks were neglected by setting the fermion determinant to unity, i.e. setting $\det D = 1$ in eq. (2.91). Nowadays quenched calculations are largely unnecessary, though a wealth of computational hurdles remain in unquenched glueball calculations. These are discussed further in chapter 7.

various two-hadron thresholds. This necessitates the calculation of infinite-volume scattering amplitudes for these states. Hence, while we lack the required precision for rigorous determinations of the scattering matrix using the methods of chapter 6, we present in chapter 7 the next step towards such a calculation, the inclusion of fully dynamical $\overline{q}q$ and two-meson states in the low-lying scalar glueball sector of QCD.

Elastic $K\pi$ Scattering

As will be detailed in chapter 6, the restriction to finite, Euclidean spacetime in lattice QCD prevents the direct extraction of real-time hadronic scattering amplitudes [17]. Instead, this difficulty can be circumvented using an approach first developed by Lüscher [13], in which such amplitudes can be inferred from the deviations of finite-volume interacting two-particle energies from their non-interacting values. The development of this program for extracting scattering data from finite-volume energies, and a brief derivation of the all-important *quantisation condition* for relating the two are outlined in chapter 6. Our approach, as described in sections 6.2 and 6.3 has previously been applied successfully to a number of scattering processes [18, 20, 21], including a recent study of elastic $K\pi$ scattering on an anisotropic lattice, similar to the one used in chapter 7 but at a lighter pion mass in Ref. [19].

Elastic $I = \frac{1}{2}$ $K\pi$ scattering has been well studied on the lattice to date [19, 41–45], with the majority of those studies focused on extracting resonance parameters from the p-wave scattering amplitude for the vector $K^*(892)$ resonance. In fig. 6 of Ref. [19], the $K^*(892)$ resonance parameters are compared from a subset of these studies, showing a general agreement across differing pion masses. In Ref. [45] s- and p-wave amplitudes are extracted on a set of ensembles with pion masses ranging from ~ 240 MeV to ~ 400 MeV, showing the movement of the K^* pole mass from a bound state at the heaviest pion mass, to a genuine resonance as the pion mass is lowered.

The analysis presented here is an early part in a larger effort to map out the s- and p-wave amplitudes using a set of the CLS ensembles described shortly, following the non-traditional quark mass trajectory described in section 2.3.3. Our aim is to study the behaviour of these amplitudes along the $\mathrm{Tr}\, M_q = \text{const.}$ quark mass trajectory, both to examine the quark mass dependence of these amplitudes, and to provide high precision s-wave scattering data for the amplitude analysis community to study properties of the poorly understood scalar $K_0^*(700)$ resonance.

Chapter 2

Lattice QCD

Lattice QCD [46] is a non-perturbative approach to calculations where QCD is regulated in such a way as to facilitate numerical evaluation. By restricting spatial and temporal coordinates to discrete values ($x_\mu = na_\mu,\ n = 0, 1, \ldots,$ where a_μ is the lattice spacing in the μ direction.), an ultraviolet cutoff ($\Lambda \sim \frac{1}{a}$) is naturally introduced, regularising the theory. Typically, an isotropic lattice is used in which the $a_\mu = a$ in each direction are all taken to be the same. Another common situation is an anisotropic lattice in which the three spatial directions are taken to have the grid size with the temporal spacing being smaller. The discretisation is performed in such a way as to recover the continuum QCD action in the continuum limit, $a \to 0$. Discretising spacetime in this manner results in an action that is no longer invariant under the full Poincaré group of rotations, translations, and boosts, but one that is invariant under a subgroup corresponding to allowed rotations, translations, and boosts on a hyper-cubic lattice.

This chapter will outline the basics of lattice QCD and set up the groundwork that allows us to calculate observables within the theory (see for example, Refs. [47, 48]). Constructing continuum QCD is briefly reviewed, with a discussion on how to represent the theory in imaginary time. Then in section 2.2, the issue of discretisation is discussed. S_{QCD} may be represented as the continuum limit of a large class of discrete lattice actions, which will differ at most by irrelevant operators that vanish in the continuum limit. A key issue that must be addressed by our choice of lattice action is that of fermion doubling, a phenomenon in which additional (degenerate) fermionic modes appear that do not exist in the continuum. Our choice of fermion action that alleviates this issue will lead to chiral symmetry breaking, an unavoidable consequence of the Nielson-Ninomiya theorem [49].

We follow this in section 2.3 with a discussion detailing how a given discretisation of S_{QCD} can be systematically improved to address the leading order errors due to discretisation. There we also outline various properties of the two classes of gauge ensembles that are used in this work, namely the anisotropic HadSpec ensemble used in the scalar glueball study in chapter 7, and the CLS ensembles used in the $K\pi$ scattering analysis in chapter 8.

Then, in section 2.4 we outline our primary aim of calculating hadronic two-point correlation functions in order to extract the stationary state spectrum of QCD in finite-volume. Finally, we

close out the chapter in section 2.5 with a brief outline of the Monte Carlo integration techniques used to generate field ensembles for the gauge fields, including effects from dynamical quarks.

2.1 QCD Lagrangian

To build a field theory that describes the strong interaction between quarks and gluons we take the colour charge of the strong interaction and form a non-abelian gauge theory with $SU_c(3)$ as the gauge symmetry group [46]. Our total QCD Lagrangian density is

$$\mathcal{L}[\psi, \overline{\psi}, G] = \sum_{f=1}^{N_f} \overline{\psi}^{(f)}_{a\alpha}(i\gamma^{\mu}_{\alpha\beta}\mathcal{D}_{\mu ab} - m^{(f)}\delta_{\alpha\beta}\delta_{ab})\psi^{(f)}_{b\beta} - \frac{1}{4}G^a_{\mu\nu}G^{\mu\nu}_a, \tag{2.1}$$

where γ^{μ} are the Dirac gamma matrices which satisfy

$$\{\gamma_{\mu}, \gamma_{\nu}\} = 2g_{\mu\nu}, \quad \gamma^{\dagger}_{\mu} = \gamma_0\gamma_{\mu}\gamma_0, \quad \gamma^5 \equiv i\gamma^0\gamma^1\gamma^2\gamma^3. \tag{2.2}$$

The fermionic quarks are represented by massive Dirac spinors

$$\psi^{(f)}_{a\alpha}(x), \qquad \overline{\psi}^{(f)}_{a\alpha}(x), \tag{2.3}$$

with colour indices $a = 1, 2, 3$, Dirac indices $\alpha = 1, 2, 3, 4$ and quark flavour indices $f = 1, 2, \ldots, N_f$. These fields transform under the fundamental ($\mathbf{3}$) and anti-fundamental ($\overline{\mathbf{3}}$) representations of $SU_c(3)$. Though we could imagine the theory with any number of flavours, in nature $N_f = 6$. In our simulations, we deal only with $N_f = 2 + 1$, that is, two degenerate light quarks and a strange quark. In treating the up and down quarks as degenerate ($m_u = m_d$), the reduced isospin symmetry $SU_I(2)$ is exact[1].

The gauge-covariant derivative $\mathcal{D}_{\mu}$ has been defined as

$$\mathcal{D}_{\mu} = \partial_{\mu} + ig\mathcal{A}_{\mu}, \tag{2.4}$$

where g will denote the coupling strength of the gauge fields, $\mathcal{A}_{\mu}$, to the quarks, generally taken to be $\neq 0$. The gluon fields describe a vector boson that transforms under the adjoint ($\mathbf{8}$) representation of $SU_c(3)$

$$\mathcal{A}_{\mu}(x) = \mathcal{A}^a_{\mu}(x)\frac{\lambda_a}{2}, \tag{2.5}$$

where $\lambda_a, a = 1, 2, \ldots, 8$ are the Gell-Mann matrices which generate the Lie group $SU_c(3)$. The Gell-Mann matrices are given by

$$\begin{aligned} \lambda_1 &= \begin{pmatrix} 0 & 1 & 0 \\ 1 & 0 & 0 \\ 0 & 0 & 0 \end{pmatrix}, \quad \lambda_2 = \begin{pmatrix} 0 & -i & 0 \\ i & 0 & 0 \\ 0 & 0 & 0 \end{pmatrix}, \quad \lambda_3 = \begin{pmatrix} 1 & 0 & 0 \\ 0 & -1 & 0 \\ 0 & 0 & 0 \end{pmatrix}, \quad \lambda_4 = \begin{pmatrix} 0 & 0 & 1 \\ 0 & 0 & 0 \\ 1 & 0 & 0 \end{pmatrix}, \\ \lambda_5 &= \begin{pmatrix} 0 & 0 & -i \\ 0 & 0 & 0 \\ i & 0 & 0 \end{pmatrix}, \quad \lambda_6 = \begin{pmatrix} 0 & 0 & 0 \\ 0 & 0 & 1 \\ 0 & 1 & 0 \end{pmatrix}, \quad \lambda_7 = \begin{pmatrix} 0 & 0 & 0 \\ 0 & 0 & -i \\ 0 & i & 0 \end{pmatrix}, \quad \lambda_8 = \frac{1}{\sqrt{3}}\begin{pmatrix} 1 & 0 & 0 \\ 0 & 1 & 0 \\ 0 & 0 & -2 \end{pmatrix}. \end{aligned} \tag{2.6}$$

[1] In nature $m_u \sim m_d$ are on the order of a few MeV while $m_s \approx 95$ MeV.

These span all traceless Hermitian matrices and obey the relations

$$[\lambda_a, \lambda_b] = 2i \sum_{c=1}^{8} f_{abc}\lambda_c, \qquad \mathrm{Tr}(\lambda_a\lambda_b) = 2\delta_{ab}, \tag{2.7}$$

where the structure constants f_{abc} are fully antisymmetric. The gluon field strength tensor, $G_{\mu\nu}$, is defined in terms of these gluon fields as

$$\begin{aligned} G_{\mu\nu}(x) &= \frac{1}{2}G^a_{\mu\nu}\lambda_a \\ &\equiv -\frac{i}{g}[\mathcal{D}_\mu, \mathcal{D}_\nu] \\ &= \partial_\mu\mathcal{A}_\nu - \partial_\nu\mathcal{A}_\mu + ig[\mathcal{A}_\mu, \mathcal{A}_\nu] \\ &= \frac{1}{2}\lambda_a(\partial_\mu\mathcal{A}^a_\nu - \partial_\nu\mathcal{A}^a_\mu - gf^{abc}\mathcal{A}^b_\mu\mathcal{A}^c_\nu). \end{aligned} \tag{2.8}$$

An important property of the Lagrangian in eq. (2.1) is its invariance under a local $SU(3)$ gauge transformation, under which the quark and gluon fields transform according to

$$\psi(x) \to \psi'(x) = \Omega(x)\psi(x), \tag{2.9a}$$

$$\overline{\psi}(x) \to \overline{\psi}'(x) = \overline{\psi}(x)\Omega^\dagger(x), \tag{2.9b}$$

$$\mathcal{A}_\mu(x) \to \mathcal{A}'_\mu(x) = \Omega(x)\mathcal{A}_\mu(x)\Omega^\dagger(x) + i\left(\partial_\mu\Omega(x)\right)\Omega^\dagger(x), \tag{2.9c}$$

where $\Omega(x) \in SU_c(3)$. A CP violating term $\theta\frac{1}{32\pi^2}G^a_{\mu\nu}G^a_{\rho\sigma}\varepsilon^{\mu\nu\rho\sigma}$ should also be included in our Lagrangian, though as experimental evidence suggests that θ is negligible [50], we will not include it here.

2.1.1 Imaginary Time

Observables in lattice QCD are obtained by evaluating correlation functions of relevant quantum mechanical operators in the theory via Feynman path integrals. However, the oscillating path integral weight e^{iS_M}, where S_M is the action defined in Minkowski spacetime, is complex, and thus unsuitable for importance sampling in our Monte Carlo calculations. Rotating to imaginary time, $t \to -i\tau$, yields a positive weighting factor e^{-S}, where S is the action defined in Euclidean spacetime, that is suitable for our numerical calculations. The Euclidean theory is defined such that the action is invariant under all symmetries of Euclidean spacetime and all Green's functions of the theory are identical to the Green's functions of the Minkowski theory, analytically continued to imaginary time, $t \to -i\tau$.

We define the following relationships between coordinates and derivatives in Minkowski and Euclidean spacetime, where a subscript or superscript M denotes Minkowski spacetime:

$$x^4 = x_4 = ix^0_M = ix^M_0, \quad x^j = x_j = x^j_M = -x^M_j, \tag{2.10a}$$

$$\partial^4 = \partial_4 = -i\partial^0_M = -i\partial^M_0, \quad \partial^j = \partial_j = -\partial^j_M = \partial^M_j. \tag{2.10b}$$

From the definition of the covariant derivative, the Euclidean gluon fields are defined by

$$\mathcal{A}^4 = \mathcal{A}_4 = -i\mathcal{A}^0_M = -i\mathcal{A}^M_0, \quad \mathcal{A}^j = \mathcal{A}_j = -\mathcal{A}^j_M = \mathcal{A}^M_j, \tag{2.11}$$

from which we obtain the Euclidean gluon field strength tensors

$$G^M_{0k} = -G^{0k}_M = iG_{4k} = iG^{4k}, \quad G^M_{ij} = G^{ij}_M = G_{ij} = G^{ij}. \tag{2.12}$$

Finally, we define the Euclidean γ matrices,

$$\{\gamma_\mu, \gamma_\nu\} = 2\delta_{\mu\nu}, \quad \gamma^\dagger_\mu = \gamma_\mu, \quad \gamma_5 = \gamma_4\gamma_1\gamma_2\gamma_3, \tag{2.13}$$

with the following relationship to the Minkowski γ_M matrices,

$$\begin{aligned} \gamma^4 &= \gamma_4 = \gamma^0_M = \gamma^M_0, \\ \gamma_k &= \gamma^k = -i\gamma^k_M = i\gamma^M_k, \\ \gamma_5 &= \gamma^5 = \gamma^5_M. \end{aligned} \tag{2.14}$$

Unless stated otherwise, we use the Dirac-Pauli representation given by

$$\gamma_k = \begin{pmatrix} 0 & -i\sigma_k \\ i\sigma_k & 0 \end{pmatrix}, \qquad \gamma_4 = \begin{pmatrix} \mathbb{1} & 0 \\ 0 & -\mathbb{1} \end{pmatrix}, \qquad \gamma_5 = \begin{pmatrix} 0 & \mathbb{1} \\ \mathbb{1} & 0 \end{pmatrix}, \tag{2.15}$$

where σ_k are the Pauli spin matrices. In the Dirac-Pauli representation, the γ matrices also have the following properties:

$$\gamma^T_1 = -\gamma_1, \quad \gamma^T_2 = \gamma_2, \quad \gamma^T_3 = -\gamma_3, \quad \gamma^T_4 = \gamma_4. \tag{2.16}$$

Using this plethora of definitions, we can Wick rotate the action from Minkowski to Euclidean spacetime. Suppressing flavour, spin, and colour indices then,

$$\begin{aligned} iS_M &= i\int \mathrm{d}x^0_M \int \mathrm{d}^3\mathbf{x}_M \Big[\overline{\psi}(i\gamma^0_M\mathcal{D}^M_0 + i\gamma^j_M\mathcal{D}^M_j - m)\psi - \frac{1}{4}G^M_{\mu\nu}G^{\mu\nu}_M\Big] \\ &= i\int(-i\mathrm{d}x_4)\int \mathrm{d}^3\mathbf{x}\Big[\overline{\psi}(i\gamma_4(i\mathcal{D}_4) + i(i\gamma_j)\mathcal{D}_j - m)\psi - \frac{1}{4}G_{\mu\nu}G_{\mu\nu}\Big] \\ &= -\int \mathrm{d}^4x\Big[\overline{\psi}(\gamma_\mu\mathcal{D}_\mu + m)\psi + \frac{1}{4}G_{\mu\nu}G_{\mu\nu}\Big] \\ &\equiv -S. \end{aligned} \tag{2.17}$$

For the spin-$\frac{1}{2}$ fermion fields, the Wick rotation involves some subtleties [51, 52]. Simultaneously requiring invariance under Euclidean transformations and equivalence of the two-point function in Euclidean spacetime with the two-point function in Minkowski spacetime analytically continued to imaginary time rules out the identification of $\overline{\psi} = \psi^\dagger\gamma^4$ or $\overline{\psi} = \psi$. Since, from a path integral viewpoint, we consider ψ and $\overline{\psi}$ as *independent* Grassmann integration variables, there is no issue with not having any particular relationship between the two. While the action is no longer

Hermitian[2], there is no issue with the physical interpretation of the theory as it has been engineered to reproduce the Green's function of the physically-sensible Minkowski theory, analytically continued to imaginary time. This point will be revisited in section 2.4.1.

Rescaling the gauge field for convenience:

$$\mathcal{A}_\mu(x) \to \frac{1}{g}\mathcal{A}_\mu(x), \tag{2.18}$$

since we will not consider the theory in which $g = 0$, the final form of the QCD action in Euclidean spacetime is

$$S[\psi, \overline{\psi}, G] = \int \mathrm{d}^4x \left[\sum_{i=f}^{N_f} \overline{\psi}^{(f)}_{a\alpha} \Big((\gamma_\mu)_{\alpha\beta} (\mathcal{D}_\mu)_{ab} + m^{(f)} \delta_{\alpha\beta}\delta_{ab} \Big) \psi^{(f)}_{b\beta} + \frac{1}{4g^2} G^a_{\mu\nu} G^a_{\mu\nu} \right] \tag{2.19}$$

where now

$$\mathcal{D}_\mu = \partial_\mu + i\mathcal{A}_\mu, \tag{2.20a}$$

$$G_{\mu\nu} = -i[\mathcal{D}_\mu, \mathcal{D}_\nu] = \partial_\mu \mathcal{A}_\nu - \partial_\nu \mathcal{A}_\mu + i[\mathcal{A}_\mu, \mathcal{A}_\nu]. \tag{2.20b}$$

2.2 Discretising Spacetime

Now we must discuss how to restrict the theory to a finite cubic lattice to facilitate numerical methods. Such a lattice can be represented by

$$\Lambda \equiv \{ n = (n_1, n_2, n_3, n_4) \mid n_1, n_2, n_3 = 0, 1, \ldots, N_s - 1;\ n_4 = 0, 1, \ldots, N_t - 1 \} \tag{2.21}$$

where N_s is the number of sites in the spatial directions, and N_t is the number of sites in the temporal direction. In general, these numbers need not be the same, and in fact the lattice spacing in the spatial, a_s, and temporal, a_t, directions also need not be the same. Without loss of generality, we can take the lattice to be isotropic ($a_s = a_t \equiv a, N_s = N_t \equiv N$) for the following discussion of discretisation, though later it will prove useful to introduce a different spacing in the temporal direction.

In Fourier space[3], the finite lattice spacing a naturally acts as a momentum cutoff or regulator for the theory, restricting momenta to the first Brillouin zone

$$p_\mu \in \left(\frac{-\pi}{a}, \frac{\pi}{a} \right]. \tag{2.22}$$

The finite volume periodic boundary conditions restricts the momenta to be discrete

$$\boldsymbol{p} = \frac{2\pi}{L}\boldsymbol{n}, \tag{2.23}$$

[2] γ^5-Hermiticity of D ($D^\dagger = \gamma_5 D \gamma_5$) in $S = \overline{\psi} D \psi + S_g$ guarantees that $\det D$ is real, since $\det \gamma_5 = 1$.

[3] See for example Appendix A.3 in Ref. [48] for a description of the Fourier transform on a hypercubic lattice.

where L is the spatial extent of the lattice, and $\boldsymbol{n}$ is a vector of integers: $\boldsymbol{n} = (n_1, n_2, n_3),\ n_i \in \mathbb{Z}$.

A point on the spacetime lattice is given by $x = an$, so, to define the QCD action on the lattice we begin with the following replacements

$$x \to n, \tag{2.24a}$$

$$\int \mathrm{d}^4 x \to a^4 \sum_{n \in \Lambda}. \tag{2.24b}$$

Crucially, the lattice discretisation must be performed in such a way as to recover the continuum theory in the limit $a \to 0$. Additionally, we require that the theory remain gauge invariant under the same gauge transformations as the continuum theory. For QCD, this amounts to $SU_c(3)$ gauge invariance, a property that is spoiled by simply applying eq. (2.24). Thus, care must be taken when formulating the lattice theory, ensuring that none of these properties are spoiled in the process.

We will begin with a naïve description of the fermionic sector of the theory which we then augment in such a way as to mitigate lattice artefacts. Importantly, we will see how the introduction of gluon fields differs on the lattice with respect to the continuum. On the lattice the gluon fields will appear as elements of the gauge *group* and not as elements of the *algebra* as in the continuum. The purely gluonic part of the action will then be discussed, also with improvements that help to minimise discretisation effects. Finally, specific details about how bare parameters for the theory are tuned to extract physics are outlined with some remarks on scale setting.

2.2.1 Naïve Discretisation of Fermions

In the continuum theory, it is the enforcement of local gauge invariance that prompts the introduction of gauge fields via the covariant derivative in eq. (2.4). Similarly, here we start from a discretised free fermion action S_F^0, and the appropriate gauge fields naturally emerge from the requirement of local gauge invariance under $SU_c(3)$ transformations. Suppressing quark field indices, the free Euclidean fermionic action in the continuum is

$$S_F^0[\psi, \overline{\psi}] = \int \mathrm{d}^4 x\, \overline{\psi}(x) \left(\gamma_\mu \partial_\mu + m\right) \psi(x). \tag{2.25}$$

Discretising the integral as in eq. (2.24) and the partial derivatives with the symmetric finite difference

$$\partial_\mu \psi(x) \to \frac{1}{2a} \left(\psi(n + \hat{\mu}), -\psi(n - \hat{\mu})\right) \tag{2.26}$$

we arrive at a lattice version of the free fermion action

$$S_F^0[\psi, \overline{\psi}] = a^4 \sum_{n \in \Lambda} \overline{\psi}(n) \left[\sum_{\mu=1}^{4} \gamma_\mu \frac{\psi(n + \hat{\mu}) - \psi(n - \hat{\mu})}{2a} + m\psi(n)\right]. \tag{2.27}$$

This however is not gauge invariant, so to make a locally gauge invariant action we need to use a gauge covariant version of the finite-difference operator. This gives us the following gauge invariant

Figure 2.1: Graphical representation of the gauge link variables, defined in eqs. (2.30) and (2.33).

action

$$S_F[\psi, \overline{\psi}, U] = a^4 \sum_{n\in\Lambda} \overline{\psi}(n) \left[\sum_{\mu=1}^{4} \gamma_\mu \frac{U_\mu(n)\psi(n+\hat{\mu}) - U_{-\mu}(n)\psi(n-\hat{\mu})}{2a} + m\psi(n) \right], \tag{2.28}$$

where $U_\mu(n)$ is an $SU_c(3)$ matrix associated with the gluon field on the link starting at lattice site n, and ending at $n+\hat{\mu}$, as shown in fig. 2.1. Under a local $SU_c(3)$ gauge transformation, the fermion fields and the so-called *link variables* U_μ transform according to

$$\psi(n) \to \psi\,' = \Omega(n)\psi(n), \tag{2.29a}$$

$$\overline{\psi}(n) \to \overline{\psi}\,' = \overline{\psi}(n)\Omega^\dagger(n), \tag{2.29b}$$

$$U_\mu(n) \to \Omega(n)U_\mu(n)\Omega^\dagger(n+\hat{\mu}), \tag{2.29c}$$

where $\Omega(n)$ is an element of $SU_c(3)$ chosen on each site n. For notational convenience we define the link variables pointing in the negative μ direction as

$$U_{-\mu}(n) \equiv U_\mu^\dagger(n-\hat{\mu}), \tag{2.30}$$

also shown in fig. 2.1. These reversed link variables transform as

$$U_{-\mu}(n) \to \Omega(n)U_{-\mu}(n)\Omega^\dagger(n-\hat{\mu}). \tag{2.31}$$

To ensure our discretised action produces a correct continuum action in the limit $a \to 0$, we first associate our link variables with the *gauge transporter* [53]

$$U(x,y) = P\exp\left(i\int_{\mathcal{C}_{xy}} \mathcal{A}(s)\cdot \mathrm{d}s \right) \tag{2.32}$$

where P denotes path-ordering and $\mathcal{C}_{xy}$ is some path connecting the points x and y. Each link variable is given in terms of the gluon field by

$$U_\mu(n) \approx \exp\left(ia\mathcal{A}_\mu(n)\right). \tag{2.33}$$

Expanding in the spacing a gives

$$U_\mu(n) \approx \mathbb{1} + ia\mathcal{A}_\mu(n) + \mathcal{O}(a^2), \tag{2.34a}$$

$$U_{-\mu}(n) \approx \mathbb{1} - ia\mathcal{A}_\mu(n-\hat{\mu}) + \mathcal{O}(a^2), \tag{2.34b}$$

so that eq. (2.28) becomes

$$
\begin{aligned}
S_F[\psi,\overline{\psi},U] &= a^4\sum_{n\in\Lambda}\overline{\psi}(n)\Bigg[\sum_{\mu=1}^{4}\gamma_\mu\Bigg[\frac{\psi(n+\hat{\mu})-\psi(n-\hat{\mu})}{2a} \\
&\qquad + \frac{ia\mathcal{A}_\mu(n)\psi(n+\hat{\mu})+ia\mathcal{A}_\mu(n-\hat{\mu})\psi(n-\hat{\mu})}{2a}\Bigg]+m\psi(n)+\mathcal{O}(a)\Bigg], \qquad (2.35)\\
&= a^4\sum_{n\in\Lambda}\overline{\psi}(n)\Big[\gamma_\mu\big(\partial_\mu+i\mathcal{A}_\mu(n)\big)\psi(n)+m\psi(n)+\mathcal{O}(a)\Big],
\end{aligned}
$$

which in the continuum limit becomes

$$
\begin{aligned}
\lim_{a\to 0}S_F[\psi,\overline{\psi},U] &= \lim_{a\to 0}a^4\sum_{n\in\Lambda}\overline{\psi}(n)\Big[\gamma_\mu\big(\partial_\mu+i\mathcal{A}_\mu(n)\big)\psi(n)+m\psi(n)+\mathcal{O}(a)\Big], \\
&= \int \mathrm{d}^4x\,\Big[\overline{\psi}(x)\big(\gamma_\mu D_\mu+m\big)\psi(x)+\mathcal{O}(a)\Big].
\end{aligned} \qquad (2.36)
$$

The naïve fermion action then reproduces the continuum action in the limit $a\to 0$ with discretisation errors of $\mathcal{O}(a)$. It is important to note at this stage that while the naïve fermion action (eq. (2.28)) seems to fulfil our basic requirements, the choice of discretised action is not unique, and in fact this naïve form has a serious weakness that requires careful fixing.

2.2.2 Fermion Doubling

Consider a generic fermion action with the following form,

$$
S_F[\psi,\overline{\psi},U]=\overline{\psi}D[U]\psi \qquad (2.37)
$$

where fermion indices are suppressed and we refer to $D[U]$ now as the Dirac matrix. With the full complement of quark indices, the Dirac matrix for the naïve lattice action (eq. (2.28)) is

$$
D_{a\alpha;b\beta}(n|m)=a^4\sum_{\mu=1}^{4}(\gamma_\mu)_{\alpha\beta}\,\frac{U_{\mu,ab}(n)\delta_{n+\hat{\mu},m}-U_{-\mu,ab}(n)\delta_{n-\hat{\mu},m}}{2a}+a^4m_f\delta_{\alpha\beta}\delta_{ab}\delta_{nm}, \qquad (2.38)
$$

where m_f is the mass of quarks with flavour f, and all quark indices are defined in section 2.1. The free lattice quark propagator then is obtained by setting $U_\mu(n)=1$ everywhere and inverting M. In Fourier space then,

$$
\widetilde{D}^0(p)=a^4\sum_{\mu=1}^{4}i\gamma_\mu\frac{\sin(ap_\mu)}{a}+a^4m_f, \qquad (2.39)
$$

so that the free lattice propagator then is given by

$$
a^4\widetilde{D}^0(p)^{-1}=\frac{-ia\sum_\mu\gamma_\mu\sin(ap_\mu)+a^2m_f}{\sum_\mu\sin^2(ap_\mu)+a^2m_f^2}. \qquad (2.40)
$$

As we would expect, there is a pole in this propagator at $p^2=m^2$. However the $\sin^2(ap_\mu)$ term gives 2^d-1 extra poles, referred to as *fermion doublers*, at the edges of the first Brillouin zone. If

for example we consider the case of massless fermions ($m = 0$), the lattice propagator will contain these unphysical modes at

$$p_\mu = (\pi/a, 0, 0, 0), (0, \pi/a, 0, 0), \ldots, (\pi/a, \pi/a, \pi/a, \pi/a). \tag{2.41}$$

Since the lattice action need only match the continuum QCD action for vanishing lattice spacing, we are free to add any number of terms to alleviate the doubling problem so long as they vanish as $a \to 0$. The particular choice of solution is not unique, and will belong to a larger class of additions to the action that we generically call *improvements*[4].

One such solution to the doubling problem was proposed by Wilson [54], where the so-called *Wilson term* is added to the fermionic action:

$$D(n|m) \to D(n|m) - a^4 \sum_{\mu=1}^{4} a \frac{U_\mu(n)\delta_{n+\hat{\mu},m} - 2\delta_{n,m} + U_{-\mu}(n)\delta_{n-\hat{\mu},m}}{2a^2}. \tag{2.42}$$

This term is a discretised version of $-\frac{a}{2}\partial_\mu\partial_\mu$, with the correct insertions of gauge links to preserve local gauge invariance. This term manifests in Fourier space as

$$\widetilde{D}(p) \to \widetilde{D}(p) + a^4 \sum_{\mu=1}^{4} \frac{1 - \cos(ap_\mu)}{a}. \tag{2.43}$$

For each momentum component with $p_\mu \neq 0$, the Wilson term acts like an additional mass term that is maximised for any momentum component with $p_\mu = \frac{\pi}{a}$. The total mass of the doublers then is $m + \frac{2l}{a}$, where l is the number of momentum components equal to $\frac{\pi}{a}$. In the limit $a \to 0$ the doublers become very heavy and will decouple from the theory so that only the physical pole ($p^2 = m^2$) will then remain in the corresponding momentum space propagator.

Unfortunately, this solution to the problem of the doubler states is not without its own drawbacks. Notice that even for the massless theory, ($m_f = 0$), where we would usually expect chiral symmetry in the QCD action, the Wilson term transforms like $\mathbb{1}$ in Dirac space. This explicitly breaks chiral symmetry by acting as a mass term in the (massless) theory. Furthermore, one might think that the Wilson term is simply a flawed solution to the doubler problem, yet in 1981 Nielson & Ninomiya proved a no-go theorem for regularising chiral fermions [49]. The theorem states that for lattice regularisations which respect Hermiticity, locality, and (lattice) translational invariance, it is not possible to lift the doubler degeneracy without breaking the chiral symmetry present in the QCD Lagrangian at vanishing bare quark mass. There exist several attempts to navigate the issue, though none can fully maintain chiral symmetry and solve the doubling problem concurrently. Examples include *Staggered* fermions [55–57], *Overlap* fermions [58, 59], *Domain-Wall* fermions [60, 61], and *Twisted-Mass* fermions [62–64]. In both the scattering and hadron spectrum analyses performed here, Wilson fermions have been used[5], with some systematic improvements to be discussed shortly.

[4]This freedom to add any irrelevant operators will be exploited beyond the doubling problem. For further details see section 2.3.

[5]On the CLS ensembles used in the scattering analysis, a small twisted-mass term is added to the action during the generation of gauge configurations to help to avoid instabilities in the simulations. See section 2.3.2 for details.

2.2.3 Gauge Action

At this stage it still remains to determine the purely gluonic part of the lattice action. The gauge link variables, U_μ, have already been established as the fundamental quantities with which we represent the gluon fields on the lattice, so it seems reasonable to consider gluon actions that depend only on those variables. As with the fermionic sector, the gluon action must be constructed in such a way as to maintain local gauge invariance, in addition to reproducing the continuum gluon action in the limit as $a \to 0$.

Consider first the product of k connected link variables that form a path $\mathcal{P}$ connecting lattice sites n and m

$$P(n|m) = U_{\mu_0}(n)U_{\mu_1}(n+\hat{\mu}_0)\dots U_{\mu_{k-1}}(m-\hat{\mu}_{k-1}) \equiv \prod_{(n,\mu)\in\mathcal{P}} U_\mu(n). \tag{2.44}$$

This product of links will transform under a gauge transformation as

$$P(n|m) \to \Omega(n)P(n|m)\Omega^\dagger(m), \tag{2.45}$$

so that a gauge invariant quantity can be formed by taking two quark fields at any two sites connected by $\mathcal{P}$:

$$\overline{\psi}(n)P(n|m)\psi(m). \tag{2.46}$$

Alternatively, consider a closed loop $\mathcal{L}$ of such a product of gauge links and take the trace

$$L[U] = \mathrm{Tr}\left[\prod_{(n,\mu)\in\mathcal{L}} U_\mu(n)\right], \tag{2.47}$$

where the trace ensures the object is gauge invariant. Such closed loops can serve many purposes as physical observables and we will use them in construction of the gauge action. Depending on the particular path chosen, these objects are sometimes called *Wilson loops* or *Polyakov loops*.

The smallest non-trivial closed loop we can construct is the *plaquette*:

$$\begin{aligned} U_{\mu\nu} &\equiv U_\mu(n)U_\nu(n+\hat{\mu})U_{-\mu}(n+\hat{\mu}+\hat{\nu})U_{-\nu}(n+\hat{\nu}), \\ &= U_\mu(n)U_\nu(n+\hat{\mu})U_\mu^\dagger(n+\hat{\nu})U_\nu^\dagger(n). \end{aligned} \tag{2.48}$$

Similarly to the closed loop above, taking the trace of the plaquette will result in a gauge invariant object. Wilson presented the first discretisation of the gauge action using a collection of all plaquettes [46]

$$S_G[U] = \frac{\beta}{3}\sum_{n\in\Lambda}\sum_{\mu<\nu}\mathrm{Re}\ \mathrm{Tr}\left[1 - U_{\mu\nu}(n)\right], \tag{2.49}$$

where $\beta = 2N_c/g^2 = 6/g^2$. The continuum limit can be checked by first looking at small a expansion of the plaquette in terms of gauge fields

$$\begin{aligned} U_{\mu\nu}(n) &= \exp\left(ia^2G_{\mu\nu}(n) + \mathcal{O}(a^3)\right), \\ &\xrightarrow{a\to 0} \mathbb{1} + ia^2G_{\mu\nu}(n) - \frac{1}{2}a^4G_{\mu\nu}^2(n) + \mathcal{O}(a^6), \end{aligned} \tag{2.50}$$

so that in the continuum limit, the Wilson gauge action reproduces the continuum gluon action in eq. (2.1) with leading discretisation errors of $\mathcal{O}(a^2)$. It is important to remember that this choice of discretised gauge action is not unique, and in fact many different discretisations exist that improve on discretisation errors over Wilson's construction. Our choice of action in both the fermionic and gluonic sectors with some discussion of discretisation errors will be discussed next.

2.3 Action Improvement and Scale Setting

When introducing the QCD action on the lattice we stressed that the particular discretisation of the continuum theory is not unique, and we can add any terms to the action that will vanish in the continuum limit. The Symanzik improvement program [65–67] is a systematic implementation of such additions that aims to reduce discretisation errors both in the action used and in the observables themselves. For example, consider the kinetic term in the action for a real scalar field [68],

$$\int \mathrm{d}^D x\, \partial_\mu \phi\, \partial_\mu \phi = \int \mathrm{d}^D x\, \partial_\mu \left(\phi\, \partial_\mu \phi\right) - \int \mathrm{d}^D x\, \phi\, \partial_\mu^2 \phi = -\int \mathrm{d}^D x\, \phi\, \partial_\mu^2 \phi. \tag{2.51}$$

A naïve discretisation of this term would invoke the Taylor expansion of the second derivative,

$$f''(x) = a^{-2}\left(f(x+a) + f(x-a) - 2f(x)\right) + \mathcal{O}(a^2), \tag{2.52}$$

whereas a simple improvement one could make is to use a higher order approximation like

$$f''(x) = a^{-2}\left(\frac{4}{3}\left(f(x+a) + f(x-a)\right) - \frac{1}{12}\left(f(x+2a) + f(x-2a)\right) - \frac{5}{2}f(x)\right) + \mathcal{O}(a^4). \tag{2.53}$$

While perhaps an obvious or trivial way to remove the leading $\mathcal{O}(a^2)$ correction, using this finite difference expression is essentially equivalent to using a tree-level $\mathcal{O}(a^2)$ Symanzik improved action. For a less trivial theory the improvement program is significantly more involved, yet the basic aim of constructing a lattice action with an improved continuum limit remains the same. By adding some number of terms that vanish in the continuum limit, the leading order corrections in a can be treated. For a quantum field theory, this must be done with care. Quantum corrections must be accounted for in the coefficients attached to each improvement term. Hence, such coefficients can be determined either order-by-order in perturbation theory (e.g. c_{SW}, defined below in eq. (2.54), is calculated to one loop order in Ref. [69]), or non-perturbatively (e.g. see Ref. [70] where c_{SW} is determined non-perturbatively for $N_f = 3$ lattice QCD).

As the gauge field ensembles used in the two sets of analyses in this thesis differ somewhat, we will outline the action improvements for each separately; first in some detail for the anisotropic ensemble used in chapter 7, followed by the isotropic ensembles used in the scattering analysis in chapter 8.

2.3.1 Anisotropic HadSpec Ensembles

For the glueball spectrum study in chapter 7, we use an anisotropic ensemble generated by the Hadron Spectrum (HadSpec) collaboration [71,72]. Here, we detail the improvements to the standard Wilson action of eqs. (2.42) and (2.49). In the fermionic sector, we add the Sheikholeslami-Wohlert *clover* term [73, 74],

$$ac_{\mathrm{SW}} \sum_{\mu<\nu} \overline{\psi}(n) \frac{i}{4} \sigma_{\mu\nu} \hat{F}_{\mu\nu}(n) \psi(n), \tag{2.54}$$

where $\sigma_{\mu\nu} = \frac{1}{2i}[\gamma_\mu, \gamma_\nu]$, and $\hat{F}_{\mu\nu}$ is a lattice representation of the gluon field strength tensor [75]. The coefficient c_{SW} can then be determined non-perturbatively, for example as in Ref. [70], though the tree-level estimate of Ref. [74] is used for the anisotropic ensembles. In addition to improving the $\mathcal{O}(a)$ convergence of the fermionic action, this term also seems to partially alleviate the chirality-breaking effects of Wilson fermions [76].

In the gauge sector, explicit $\mathcal{O}(a)$ convergence is treated, though we must also make modifications to deal with contributions from tadpole diagrams[6] that arise in lattice perturbation theory [77]. Tadpole improvement is implemented by rescaling the gauge links using tuneable tadpole improvement factors

$$U \to \frac{U}{u}, \qquad \text{where} \qquad u = \left\langle \frac{1}{3} \operatorname{Re} \operatorname{Tr} U_{\mu\nu} \right\rangle^{1/4}. \tag{2.55}$$

Lattice artefacts in the gauge sector are dealt with by introducing additional 2×1 planar Wilson loops $\mathcal{R}_{\mu\nu}$, where μ is the direction of length 2, ν the direction of length 1.

Positivity of the lattice transfer matrix is an important point that we must keep in mind throughout the construction of the lattice action. A positive definite transfer matrix will guarantee a Hermitian Hamiltonian, which is vital in the variational analysis we employ to extract excited hadronic states [33]. We must ensure that positivity is maintained in the action while reducing the effects of lattice artefacts as much as possible. To do this, the action must not contain terms which extend more than a single site in the temporal direction [78, 79]. For example, only 2×1 planar Wilson loops $\mathcal{R}_{\mu\nu}$ that contain length-two gauge links in a spatial direction will be used. This restriction on temporal gauge links will also need to be taken into account when we discuss gauge field smearing and operator construction in chapter 3.

Temporal correlation functions, the primary observable we use for spectrum extraction, generally have signal-to-noise ratios that decrease as the time separation increases. A large a_t will therefore reduce the number of viable data points before the time separation at which noise takes over is reached. The obvious solution is simply to use a lattice spacing that is very small. However, for smaller lattice spacing, the computational cost of the calculations grows rapidly. In order to circumvent this issue, increase the temporal resolution of correlation functions, and further reduce

[6] These are generated by the expansion of $e^{iag\mathcal{A}_\mu}$ where higher order terms in the expansion contain additional factors that generate ultraviolet divergences which precisely cancel the additional powers of a.

temporal lattice artefacts while maintaining positivity, we employ an anisotropic lattice [33, 80] with anisotropy $\xi \equiv a_s/a_t > 1$.

Let's now summarise the final form of the anisotropic action used here. For the gauge action, we use a Symanzik-improved Lüscher-Weisz action [67, 81] with tree-level tadpole-improved coefficients [33, 71, 72, 80]

$$\begin{aligned} S_G^\xi[U] = \frac{\beta}{3\gamma_g}\Bigg\{ &\sum_{x,i\neq j}\left[\frac{5}{6u_s^4}\Omega_{\mathcal{P}_{ij}}(x) - \frac{1}{12u_s^6}\Omega_{\mathcal{R}_{ij}}(x)\right] \\ &+ \sum_{x,i}\gamma_g^2\left[\frac{4}{3u_s^2u_t^2}\Omega_{\mathcal{P}_{it}}(x) - \frac{1}{12u_s^4u_t^2}\Omega_{\mathcal{R}_{it}}(x)\right]\Bigg\}, \end{aligned} \tag{2.56}$$

where $\Omega_W = \mathrm{Re}\,\mathrm{Tr}(1-W)$, $\mathcal{P}$ is a plaquette, and $\mathcal{R}_{\mu\nu}$ is the 2×1 planar Wilson loop defined above. The parameters u_s and u_t are the spatial and temporal tadpole coefficients, indices $i, j \in \{x, y, z\}$ always run over the spatial directions, and γ_g is the bare gauge anisotropy. This action has leading discretisation error at $\mathcal{O}(a_s^4, a_t^2, g^2a_s^2)$, and has a positive definite transfer matrix since no length-two gauge links in time are used. In the fermionic sector we use the anisotropic clover-improved action [74], which for some number of quark flavours f is given by

$$S_F^\xi[U,\overline{\psi},\psi] = a_s^3 a_t \sum_f \sum_x \overline{\psi}(x) D_W^\xi(m_{0,f})\psi(x), \tag{2.57}$$

with the tree-level clover-improved, anisotropic Wilson Dirac matrix

$$\begin{aligned} D_W^\xi(m_0) = \frac{1}{\tilde{u}_t}\Bigg\{ &\tilde{u}_t\hat{m}_0 + \gamma_t\hat{W}_t + \frac{1}{\gamma_f}\sum_i \gamma_i\hat{W}_i \\ &- \frac{1}{2}\left[\frac{1}{2}\left(\frac{\gamma_g}{\gamma_f} + \frac{1}{\xi}\right)\frac{1}{\tilde{u}_t\tilde{u}_s^2}\sum_i \sigma_{ti}\hat{F}_{ti} + \frac{1}{\gamma_f}\frac{1}{\tilde{u}_s^3}\sum_{i<j}\sigma_{ij}\hat{F}_{ij}\right]\Bigg\} \end{aligned} \tag{2.58}$$

where $\tilde{u}_s$ and $\tilde{u}_t$ are the spatial and temporal tadpole factors for the fermion action, $\hat{m}_0$ is the dimensionless bare quark mass, γ_f is the bare fermion anisotropy, $\xi = a_s/a_t$ is the renormalised anisotropy, and

$$\hat{W}_\mu = \nabla_\mu - \frac{a_\mu}{2}\gamma_\mu\Delta_\mu, \tag{2.59a}$$

$$\nabla_\mu f(x) = \frac{1}{2a_\mu}\Big[U_\mu(x)f(x+\mu) - U_\mu^\dagger(x-\mu)f(x-\mu)\Big], \tag{2.59b}$$

$$\Delta_\mu f(x) = \frac{1}{a_\mu^2}\Big[U_\mu(x)f(x+\mu) + U_\mu^\dagger(x-\mu)f(x-\mu) - 2f(x)\Big]. \tag{2.59c}$$

This action has leading discretisation error at $\mathcal{O}(g^2a_s, g^2a_t, a_s^2, a_t^2)$.

2.3.2 Isotropic CLS Ensembles

For the $K\pi$ scattering analysis in chapter 8, we use a subset of isotropic ensembles generated by the Coordinated Lattice Simulations (CLS) initiative, initially presented in Refs. [82, 83]. Like the anisotropic HadSpec ensemble described in the previous section, in the gauge sector the tree-level improved Lüscher-Weisz gauge action [67, 81] is used, given by (cf. eq. (2.56))

$$S_G^{\mathrm{CLS}}[U] = \frac{\beta}{6}\left(c_0 \sum_{\mathcal{P}} \mathrm{Tr}(1-\mathcal{P}) + c_1 \sum_{\mathcal{R}} \mathrm{Tr}(1-\mathcal{R})\right), \tag{2.60}$$

where the plaquette and rectangle coefficients are $c_0 = 5/3$ and $c_1 = -1/12$ respectively, and the sums run over all plaquettes $\mathcal{P}$, and rectangles $\mathcal{R}$ contained in the lattice. In the fermion sector, the same Sheikholeslami-Wohlert clover term [73] is added to the Wilson action, though here with the coefficient c_{SW} determined non-perturbatively in Ref. [70]. The fermion action is then given by, for any number of quark flavours f (cf. eq. (2.57))

$$S_F^{\mathrm{CLS}}[U, \overline{\psi}, \psi] = a^4 \sum_f \sum_x \overline{\psi}_f(x) D_W(m_{0,f}) \psi_f(x), \tag{2.61}$$

with clover-improved Wilson Dirac matrix (cf. eq. (2.58))

$$D_W^{\mathrm{CLS}}(m_0) = m_0 + \frac{1}{2}\sum_{\mu=0}^{3}\{\gamma_\mu(\nabla_\mu^* + \nabla_\mu) - a\nabla_\mu^*\nabla_\mu\} + ac_{\mathrm{SW}} \sum_{\mu,\nu=0}^{3} \frac{i}{4}\sigma_{\mu\nu}\hat{F}_{\mu\nu}. \tag{2.62}$$

While the choice of action is relatively standard, there are additional improvements included in the simulation of these ensembles, most notably the use of open temporal boundary conditions, and twisted-mass reweighting in the fermion determinant. Other improvements, including a reweighting factor that compensates for the RHMC approximation, see section 2.5.2, are detailed in Ref. [82].

Twisted-Mass Reweighting

As the Wilson Dirac matrix is not protected against having zero eigenvalues, during the Monte Carlo simulation such zeros can lead to numerical instabilities. Lüscher and Palombi suggested in Ref. [84] to add a small twisted-mass [62] term to the light quark action during the Monte Carlo simulation, and then to compensate by reweighting the measured observables. The details of the implementation by the CLS effort are outlined in Ref. [82, 85], so here we review the basic idea behind reweighting in the context of a Monte Carlo simulation.

Generally, reweighting is a method for "extending" the results from an original simulation, say at inverse temperature β, to any other β' sufficiently close to the simulation point without performing any additional simulations. The idea stems from the fact that the canonical probability of a configuration ϕ at inverse temperature β, $p_\beta(\phi)$, is easily related to the distribution at β':

$$p_{\beta'}(\phi) \propto e^{-\beta' E_\phi} = C e^{-(\beta'-\beta)E_\phi} p_\beta(\phi), \tag{2.63}$$

where E_ϕ is the total energy for configuration ϕ, C depends on β and β', and is generally unknown. For some operator $\mathcal{O}(\phi)$ then

$$\begin{aligned}\langle\mathcal{O}\rangle_{\beta'} &\equiv \frac{1}{Z_{\beta'}}\int \mathrm{d}\phi\, \mathcal{O}(\phi)\, p_{\beta'}(\phi) \\ &= \frac{C}{Z_{\beta'}}\int \mathrm{d}\phi\, \mathcal{O}(\phi) e^{-(\beta'-\beta)E_\phi}\, p_\beta(\phi) \\ &= \frac{Z_\beta}{Z_{\beta'}} C\langle \mathcal{O}\, e^{-(\beta'-\beta)E}\rangle_\beta.\end{aligned} \tag{2.64}$$

If we look at the trivial observable $\mathcal{O}(\phi) = 1$, we get the ratio of partition functions

$$\frac{Z_{\beta'}}{Z_\beta} = C\langle e^{-(\beta'-\beta)E}\rangle_\beta, \tag{2.65}$$

so that the final result is

$$\langle\mathcal{O}\rangle_{\beta'} = \frac{\langle \mathcal{O}\, e^{-(\beta'-\beta)E}\rangle_\beta}{\langle e^{-(\beta'-\beta)E}\rangle_\beta}. \tag{2.66}$$

In principle then, we should be able to get the expectation value of an observable at inverse temperature β' given a simulation at inverse temperature β. In reality, the finite statistics of a real simulation becomes a limiting factor. For a Monte Carlo simulation at coupling β that gives us a (finite) series of configurations $\phi_1, \ldots, \phi_N$, and measurements of some observable $\mathcal{O}_i = \mathcal{O}(\phi_i)$, the reweighting formula becomes

$$\langle\mathcal{O}\rangle_{\beta'} = \frac{\sum_i \mathcal{O}_i\, e^{-(\beta'-\beta)E_i}}{\sum_i e^{-(\beta'-\beta)E_i}} = \frac{\langle \mathcal{O}\, e^{-(\beta'-\beta)E}\rangle_\beta}{\langle e^{-(\beta'-\beta)E}\rangle_\beta}, \tag{2.67}$$

where E_i and $\mathcal{O}_i$ are measured on the same configuration at inverse temperature β. This is the exact procedure that is followed when treating observables from the CLS ensembles; the expectation values of some primary observable A in the target theory (e.g. without the twisted-mass term) can be computed from expectation values in the theory with the modified action $\langle\ldots\rangle_W$, according to

$$\langle A\rangle = \frac{\langle AW\rangle_W}{\langle W\rangle_W}, \tag{2.68}$$

where the reweighting factor W in this case contains ratios of fermion determinants and is described in Ref. [82].

Temporal Boundary Conditions

The gauge field configurations we integrate over when calculating observables in QCD (see section 2.5) can be classified according to their topological charge [86]. Since in lattice QCD we randomly generate a representative set of such gauge configurations using Monte Carlo methods, it is crucial to sample field configurations from many different topological sectors (i.e. regions with different topological charge) to avoid biasing the calculations [87]. For smaller and smaller lattice

spacings (i.e. towards the continuum limit) however, these simulations tend to get "trapped" in the topologically frozen sectors of field space[7], potentially biasing the results [88, 89]. In practical simulations, the emergence of such topological sectors can induce very long autocorrelation times in certain observables, e.g. the global topological charge. To combat this, the CLS effort has enforced open boundary conditions as follows [89]. As the description of the boundary conditions is independent of lattice discretisation, we will proceed in the continuum theory. At time 0 and T, i.e. the temporal boundary, the conditions imposed on the gauge potential $\mathcal{A}_\mu(x)$ are

$$G_{0k}(x)|_{x_0=0} = G_{0k}(x)|_{x_0=T} = 0, \qquad \forall \quad k = 1, 2, 3, \tag{2.69}$$

where the gauge field strength tensor $G_{\mu\nu}(x)$ is defined in eq. (2.8). Note that since these conditions preserve the gauge symmetry of the action, and therefore do not constrain the gauge field degrees of freedom, we have not fixed the gauge here. For the quark and anti-quark fields, imposing the temporal boundary conditions requires

$$P_+\psi(x)|_{x_0=0} = P_-\psi(x)|_{x_0=T} = 0, \qquad P_\pm = \frac{1}{2}(1 \pm \gamma_0), \tag{2.70a}$$

$$\overline{\psi}(x)P_-|_{x_0=0} = \overline{\psi}(x)P_+|_{x_0=T} = 0. \tag{2.70b}$$

The primary concern in choosing these boundary conditions, from our point of view, is the influence on the finite-temporal-extent effects in the temporal correlation functions we calculate [20, 82, 85, 90]. Detailed in section 5.2, the use of open temporal boundary conditions limits the number of time slices that we can use for source and sink times in our correlation functions, as times sufficiently far away from the boundary are needed to avoid corrections due to boundary effects. Thankfully, the temporal extent of these lattices is relatively large, and this restriction, while limiting, does not preclude us from proceeding in our scattering studies. Importantly, in [82] for example, the accuracy of hadron mass results using these boundary conditions is comparable to studies where periodic boundary conditions are used, with the leading boundary effects shown to be parametrically similar to $e^{-m_\pi L}$, where m_π is the mass of the pion (i.e. the lightest state in/the inverse correlation length of the theory), the leading order finite-volume correction.

2.3.3 Tuning the Action and Scale Setting

To wrap up our discussion on the lattice discretisation of QCD and set the stage for a discussion on Monte Carlo integration, we now discuss the tuning of bare lattice parameters and scale setting. The bare masses, anisotropies, and gauge coupling β must all be tuned by imposing some set of renormalisation conditions on the parameters, done by matching to some desired physical results. The Schrödinger functional formalism [91] allows for efficient simulations at small quark masses, allowing for such tuning to remain computationally feasible.

[7] i.e. regions where the topological charge does not fluctuate.

Anisotropic HadSpec Ensembles

Both of the bare anisotropies, γ_g and γ_f, are set by adjusting their values until the desired renormalised anisotropy $\xi \approx 3.5$ is achieved. For the bare gauge anisotropy, the following ratios of Wilson loops are measured

$$R_{ii}(x,y) = \frac{W_{ii}(x,y)}{W_{ii}(x+1,y)}, \tag{2.71a}$$

$$R_{it}(x,y) = \frac{W_{it}(x,t)}{W_{it}(x+1,t)}, \tag{2.71b}$$

where $W_{\mu\nu}(x_\mu, x_\nu) = \langle 0| \operatorname{Tr} \mathcal{C}_{\mu\nu}(x_\mu, x_\nu)|0\rangle$ is the expectation value of the trace of a product of link variables around a rectangle of length x_μ in the $\hat{\mu}$-direction and x_ν in the $\hat{\nu}$-direction. For a given desired renormalised anisotropy ξ then we require $R_{ii}(x,y) = R_{it}(x,\xi t)$. The fermion anisotropy is tuned by imposing for the pseudoscalar and vector mesons the dispersion relation

$$a_t^2 E^2(\boldsymbol{p}) = a_t^2 m^2 + \frac{a_s^2 \boldsymbol{p}^2}{\xi^2}. \tag{2.72}$$

The bare light and strange quark masses, m_l, m_s, are tuned by requiring the dimensionless ratios of hadron masses

$$s_\Omega = \frac{9\,(2m_K^2 - m_\pi^2)}{4m_\Omega^2}, \qquad l_\Omega = \frac{9m_\pi^2}{4m_\Omega^2}, \tag{2.73}$$

are close to their physical values. These ratios are inspired by expanding the pseudoscalar meson masses to leading order in chiral perturbation theory [72].

Often in $N_f = 2+1$ lattice QCD simulations with two degenerate light quarks and a heavier strange quark, the strange quark mass is kept approximately fixed to its physical value, while reducing the light quark masses towards their physical value. Hence, on the HadSpec ensemble that we use in chapter 7, the kaon and pion masses are heavier than their physical values, but the omega (sss) baryon mass is taken to have its physical value. The correlation length of the system is given by the lightest state in the theory which for QCD is m_π. In order to mitigate finite volume effects that appear suppressed by factors of $e^{-m_\pi L}$, where L is the length of the lattice in the spatial directions, we require that $m_\pi L$ is at the very least greater than one. In lattice QCD, a general rule of thumb is to keep $m_\pi L \gtrsim 4$. While it might seem straightforward to use bare parameters such that the pion mass is at its physical value and increase L, we will see later that when calculating quark propagators, smaller pion masses lead to a higher likelihood of ill-conditioned Dirac matrices.

The renormalisation group equations tell us that the gauge coupling β is a function of the cutoff scale of the theory, or more specifically, that the gauge coupling has non-trivial dependence on the lattice spacing. The lattice spacing then can be set by tuning β. A continuum limit extrapolation would then seem straightforward, changing β towards its continuum value should allow for probing smaller a. For spectroscopy however, this is not a very big issue. The temporal lattice spacing a_t cancels in any mass ratios that we extract and the leading discretisation error is at $\mathcal{O}(a^2)$. Hence, we require β to be tuned such that we are insensitive to the difference between lattice and continuum dispersion relations.

Isotropic CLS Ensembles

The general tuning and scale setting strategies employed by the CLS effort are detailed in full in Refs. [82, 90], so we shall just summarise them here. For the tuning of lattice parameters, the scale is set using t_0, defined by the Wilson flow [92], as described in sec. (6.1) of Ref. [82]. As t_0 is not an experimentally accessible observable however, lattice calculations must be used for comparison. Furthermore, the quantity is observed to have significant flavour content dependence [93, 94], so in fact comparing our $N_f = 2+1$ simulation to a calculation with the same flavour content is not only desirable, but necessary. Each of the ensembles we use then is determined to have lattice spacing $a \approx 0.064$ fm for $\beta = 3.55$.

The particular subset of CLS ensembles that we use employ a somewhat unusual quark mass trajectory, proposed in Ref. [95], in which

$$\operatorname{tr} M_q = m_u + m_d + m_s = 2m_l + m_s = \text{const.}, \tag{2.74}$$

where M_q is the bare quark mass matrix, i.e. $M_q = \operatorname{diag}(m_u, m_d, m_s)$. The authors of Ref. [95] advocate for this trajectory as many observable quantities, such as the centre of meson/baryon mass multiplets, depend much more strongly on the trace of the mass matrix than on $m_s - m_l$. As seen in Ref. [90] however, it should be noted that this is not equivalent to fixing the sum of renormalised quark masses. There, an extra Taylor expansion is used to slightly shift the quark masses such that $\phi_4 = 8t_0(m_K^2 + \frac{1}{2}m_\pi^2) = \text{const}$, though we do not do this here. As discussed in Ref. [20], this small deviation from the desired chiral trajectory is presumed to have little effect on the observables we consider. At the $SU(3)$ flavour symmetric point, i.e. $m_u = m_d = m_s$, particle masses are determined to be $m_\pi = m_K \approx 420$ MeV, so that as the light quark/pion mass is lowered towards the physical point, the strange quark/kaon mass will increase towards its physical mass. Again, this is unlike what is traditionally done (e.g. the HadSpec anisotropic lattice) where the kaon is held at its physical value while the pion mass is lowered.

2.4 Euclidean Two-Point Functions

Throughout this thesis, we focus on the computation of Euclidean time ordered two-point temporal correlation functions of the form

$$\mathcal{C}(t) = \langle 0 | T\, \mathcal{O}(t + t_0) \overline{\mathcal{O}}(t_0) | 0 \rangle, \tag{2.75}$$

where $\overline{\mathcal{O}}(t), \mathcal{O}(t)$ are hadronic creation and annihilation operators respectively, and T is the time ordering operator. In what follows, time ordering will always be assumed so the time ordering symbol is suppressed for brevity. Designing, calculating, and analysing matrices of such correlation functions will saturate many of the subsequent chapters in this document; in chapter 3 we discuss designing the interpolating operators $\overline{\mathcal{O}}(t), \mathcal{O}(t)$, then in chapter 4 our method of stochastically estimating these functions is presented, followed by the extraction of stationary state energies from large matrices of these functions in chapter 5.

To motivate the usefulness of these temporal correlation functions for spectroscopy, consider the spectral decomposition of eq. (2.75) by inserting a complete set of energy eigenstates

$$\begin{aligned}
\mathcal{C}(t) &= \sum_n \langle 0|\mathcal{O}(t+t_0)|n\rangle\langle n|\overline{\mathcal{O}}(t_0)|0\rangle \\
&= \sum_n \langle 0|e^{H(t+t_0)}\mathcal{O}(0)e^{-H(t+t_0)}|n\rangle\langle n|e^{Ht_0}\overline{\mathcal{O}}(0)e^{-Ht_0}|0\rangle \\
&= \sum_n e^{E_0(t+t_0)}\langle 0|\mathcal{O}(0)|n\rangle e^{-E_n(t+t_0)}e^{E_n t_0}\langle n|\overline{\mathcal{O}}(0)|0\rangle e^{-E_0 t_0} \\
&= \sum_n \langle 0|\mathcal{O}(0)|n\rangle\langle n|\overline{\mathcal{O}}(0)|0\rangle e^{-\Delta E_n t},
\end{aligned} \tag{2.76}$$

where $\Delta E_n \equiv E_n - E_0$, and we assume the energies are ordered such that $E_{n+1} > E_n$. We can also assume that the spectrum is appropriately shifted such that $E_0 = 0$, so that we can replace ΔE_n with E_n without any loss of generality. Note that since we are in finite-volume with periodic boundary conditions, the insertion of a complete set of energy eigenstates contains a discrete sum of states rather than an integral over a continuous energy variable. Since the finite-volume energies, E_n, are the observables we wish to extract, we define the effective energy/mass through the logarithmic derivative

$$E^{\text{eff}}(t) \equiv -\frac{1}{\Delta t}\ln\left(\frac{\mathcal{C}(t+\Delta t)}{\mathcal{C}(t)}\right), \tag{2.77}$$

where Δt is some time-step, usually taken to be $\Delta t \leq 3a_t$. For large times then

$$\lim_{t\to\infty} E^{\text{eff}}(t) = E_1, \tag{2.78}$$

so that if we plot eq. (2.77), the function should plateau to E_1 at some (large) t, giving some measure of the excited state contamination of the particular operator used in the correlation function. As the signal-to-noise ratio for these correlators quickly deteriorates for large time separations, carefully designed interpolating operators are vital in ensuring accurate energy determinations.

One could, in principle, perform a fit to eq. (2.75) using some number, k, of decaying exponentials, over some time range $(t_{\text{min}}, t_{\text{max}})$ for which t_{min} is large enough that the terms with $n > k$ have died off. This, however, is largely impractical for a number of reasons. For any given interpolating operator, the overlaps onto the low-lying energy eigenstates $\langle 0|\mathcal{O}|n\rangle$ may be small compared to the overlaps for higher-lying states, increasing the risk of a fit "missing" the energy associated with that low-lying level. To avoid this problem, we consider matrices of these correlation functions using large bases of various interpolating operators with similar symmetry properties. Using these then, we solve a generalised eigenvalue problem [12–14], from which we can confidently extract the low-lying states in the spectrum. This is discussed in detail in chapter 5.

2.4.1 Hermiticity

In section 2.1.1, we saw that the action in Euclidean spacetime is no longer Hermitian, but stressed that this does not have an adverse impact on the physical interpretation of results from our theory.

In fact, we only require that any Euclidean space Green's functions of our theory reproduce the physically sensible Minkowski space functions analytically continued to imaginary time. Ultimately, while the action may be non-Hermitian it is important for us to construct correlation matrices that are Hermitian, or perhaps even real-symmetric. This is not a physically mandated restriction, but it greatly simplifies the analysis needed to extract finite-volume energies and leads to somewhat improved statistics.

Whether a correlation function is Hermitian or not will depend on the operators used, and so we will now see what must be done to ensure Hermiticity. Consider a correlation matrix in *Minkowski* space

$$\begin{aligned}\mathcal{C}_{ij}(t) &= \langle 0|\mathcal{O}_i(t)\,\mathcal{O}_j^\dagger(0)|0\rangle \\ &= \sum_n \langle 0|\mathcal{O}_i|n\rangle\langle n|\mathcal{O}_j^\dagger|0\rangle^* e^{-iE_n t}.\end{aligned} \tag{2.79}$$

Provided that the operators $\{\mathcal{O}_i\}$ all behave in the expected way under time reversal

$$T\mathcal{O}_t(t)T^\dagger = \mathcal{O}_i(-t), \tag{2.80}$$

where the anti-linear time reversal operator T satisfies unitarity, $TT^\dagger = 1$, then we can show that the correlation matrix is Hermitian. Assuming $T^\dagger|0\rangle = |0\rangle$,

$$\begin{aligned}\mathcal{C}_{ji} &= \langle 0|\mathcal{O}_j(t)\mathcal{O}_i^\dagger(0)|0\rangle \\ &= \langle 0|T\,\mathcal{O}_j(t)\,TT^\dagger\,\mathcal{O}_i^\dagger(0)\,T^\dagger|0\rangle \\ &= \langle 0|\mathcal{O}_j(-t)\mathcal{O}_i^\dagger(0)|0\rangle \\ &= \langle 0|e^{-iHt}\mathcal{O}_j(0)e^{iHt}\mathcal{O}_i^\dagger(0)|0\rangle \\ &= \sum_n \langle 0|\mathcal{O}_j(0)|n\rangle\langle n|\mathcal{O}_i^\dagger(0)\langle 0|e^{i(E_n-E_0)t} \\ &= \left(\sum_n \langle 0|\mathcal{O}_j(0)|n\rangle^*\langle 0|\mathcal{O}_i(0)\langle n|e^{-i(E_n-E_0)t}\right)^* \\ &= \mathcal{C}_{ij}(t)^*.\end{aligned} \tag{2.81}$$

Then, provided our operators transform as above under time reversal, the correlation matrices should remain Hermitian.

Additionally, we must take care to ensure that in the Wick rotation to Euclidean spacetime, the Euclidean correlation matrix remains Hermitian. For example, consider meson annihilation and creation operators in Minkowski space given by

$$\begin{aligned}M^{(M)}(t) &= \delta_{ab}\,\psi_{a\alpha}^\dagger(x)\,\psi_{b\beta}(x) \\ &= \delta_{ab}\,\overline{\psi}_{a\alpha'}(x)\gamma^0_{\alpha'\alpha}\,\psi_{b\beta}(x),\end{aligned} \tag{2.82a}$$

$$\begin{aligned}M^{(M)\dagger}(t) &= \delta_{ab}\,\psi_{b\beta}^\dagger(x)\,\psi_{a\alpha}(x) \\ &= \delta_{ab}\,\overline{\psi}_{b\beta'}(x)\gamma^0_{\beta'\beta}\,\psi_{a\alpha}(x),\end{aligned} \tag{2.82b}$$

where flavour indices have been suppressed, and we have used $\overline{\psi} \equiv \psi^\dagger \gamma^0$, which is true in Minkowski space. Then, in the Wick rotation to imaginary time:

$$\begin{aligned} \psi &\to \psi \\ \overline{\psi} &\to \overline{\psi} \\ \gamma^0 &\to \gamma_4. \end{aligned} \tag{2.83}$$

Hence, to ensure that our Euclidean space operators lead to Hermitian correlation matrices, each $\overline{\psi}$ field must be accompanied by a γ_4. For convenience, we do this by defining the field $\chi \equiv \overline{\psi}\gamma_4$. We do this in the following chapter on operator design by defining our basic building blocks in terms of the ψ and χ fields.

2.5 Monte Carlo Integration

The path integral approach to Quantum Field Theory (QFT) expresses connected vacuum expectation values as a weighted sum over histories, that is, as a sum over field configurations. A Euclidean correlation function can then be expressed as

$$\langle \mathcal{O} \rangle_T = \frac{1}{Z_T} \int \mathcal{D}[\psi, \overline{\psi}] \mathcal{D}[U] \, \mathcal{O}[\psi, \overline{\psi}, U] \, e^{-S[\psi, \overline{\psi}, U]}, \tag{2.84}$$

where $\mathcal{O}$ is some generic operator or product of operators, the subscript T denotes the finite temporal extent of length T, and the partition function Z_T is given by

$$Z_T = \int \mathcal{D}[\psi, \overline{\psi}] \mathcal{D}[U] \, e^{-S[\psi, \overline{\psi}, U]}. \tag{2.85}$$

Note that the measures

$$\mathcal{D}[\psi, \overline{\psi}] \equiv \prod_{n \in \Lambda} \prod_{f, \alpha, a} \mathrm{d}\psi^{(f)}_{a\alpha}(n) \, \mathrm{d}\overline{\psi}^{(f)}_{a\alpha}(n), \tag{2.86a}$$

$$\mathcal{D}[U] \equiv \prod_{n \in \Lambda} \prod_{\mu=1}^{4} \mathrm{d}U_\mu(n), \tag{2.86b}$$

are a product of all integration measures for the quark field variables at all points n, m of the lattice Λ, and the product of integration measures for all link variables respectively and should not be confused with the gauge-covariant derivative defined in eq. (2.4). Using a convenient parameterisation of a general $SU(3)$ matrix in terms of 8 real Euler angles α_b [96]

$$U(\alpha) = e^{i\lambda_3\alpha_1} e^{i\lambda_2\alpha_2} e^{i\lambda_3\alpha_3} e^{i\lambda_5\alpha_4} e^{i\lambda_3\alpha_5} e^{i\lambda_2\alpha_6} e^{i\lambda_3\alpha_7} e^{i\lambda_8\alpha_8}, \tag{2.87}$$

where the λ_i's are the Gell-Mann matrices defined in eq. (2.6), the Haar measure is found to be

$$\mathrm{d}U = \frac{1}{2} \sin(2\alpha_2) \sin(2\alpha_6) \sin(2\alpha_4) \sin^2(\alpha_4) \, \mathrm{d}\alpha_8 \, \mathrm{d}\alpha_7 \, \mathrm{d}\alpha_6 \, \mathrm{d}\alpha_5 \, \mathrm{d}\alpha_4 \, \mathrm{d}\alpha_3 \, \mathrm{d}\alpha_2 \, \mathrm{d}\alpha_1, \tag{2.88}$$

where the ranges of integration are

$$0 \leq \alpha_1, \alpha_5 \leq \pi, \quad 0 \leq \alpha_3, \alpha_7 \leq 2\pi, \quad 0 \leq \alpha_2, \alpha_4, \alpha_6 \leq \frac{\pi}{2}, \quad 0 \leq \alpha_8 \leq \sqrt{3}\pi. \tag{2.89}$$

The group volume is found to be $\sqrt{3}\pi^5$. Euler-angle parametrisations for $SU(N)$ elements can also be found in Ref. [96].

Recall that while constructing the lattice action, we only considered fermionic actions that were quadratic in the quark fields. Since these fermionic degrees of freedom must anti-commute with one another and as such are represented by Grassmann variables, the integration over the quark fields may be performed exactly if the action is quadratic in those fields. Then for an action of the form

$$S[\psi, \overline{\psi}, U] = \overline{\psi} D[U] \psi + S_G[U], \tag{2.90}$$

where $D[U]$ is the improved Dirac matrix, and $S_G[U]$ is the improved gauge action, the integration over the Grassmann degrees of freedom yields

$$\langle \mathcal{O} \rangle_T = \frac{\int \mathcal{D}[U]\, F(D^{-1}[U]) \det D[U]\; e^{-S_G[U]}}{\int \mathcal{D}[U]\; \det D[U]\; e^{-S_G[U]}}, \tag{2.91}$$

where F is some function of D^{-1} resulting from the Wick contractions required in evaluating $\mathcal{O}$.

We are now left with the integration over the gauge link variables. However, there is no way to do this exactly and we need some method to represent the integral numerically. Standard quadrature techniques for approximating integrals numerically become exponentially impractical for high dimensional integrals. Thus, we resort to Monte Carlo methods for evaluating the integrals over gauge link variables.

While Monte Carlo methods vary wildly in their use and implementation, the main result that we need is the estimate for a highly-multidimensional integral of the form

$$I_g = \int \mathcal{D}[U]\, p(U)\, g(U), \tag{2.92}$$

where U is a collection of variables, $p(U)$ is a probability density, and $g(U)$ is some function of the integration variables U. For an ensemble of the variables U sampled according to $p(U)$, $\{U_1, U_2, \ldots, U_{N_C}\}$ consisting of N_C configurations, an estimate for I_g can be given by

$$I_g \approx \frac{1}{N_C} \sum_{k=1}^{N_C} g(U_k). \tag{2.93}$$

By the central limit theorem the error in this estimate is given by

$$\sigma_I = \sqrt{\frac{\mathrm{Var}(g(U))}{N_C}}, \tag{2.94}$$

where $\mathrm{Var}(g(U))$ is the variance of g with respect to the probability density p.

By setting

$$p(U) = \frac{\det D[U]\, e^{-S_G[U]}}{\int \mathcal{D}[U'] \det D[U']\, e^{-S_G[U']}}, \tag{2.95}$$

we can put the integrals over gauge link variables, eq. (2.91), in the form of eq. (2.92). To evaluate these integrals then we need some method for generating an ensemble of gauge link configurations. While the configurations could be generated according to a uniform probability distribution, this however is very inefficient when evaluating the integral due to a large number of gauge configurations that will lead to exponentially suppressed contributions. Specifically, field configurations that are associated with particularly large actions are effectively irrelevant. The estimate can be improved by using a process known as *importance sampling* where a non-uniform probability density is used in order to pick out configurations that contribute most.

In order to generate gauge link configurations according to eq. (2.95) we use a Markov chain method. The idea of a Markov chain is to stochastically generate a sequence of configurations in which the current element in the chain is obtained by making a random change to the previous element. The process requires some transition probability $T(U_j|U_i)$ to go from configuration U_i to U_j. Provided that this transition probability satisfies detailed balance

$$p(U_i)T(U_j|U_i) = p(U_j)T(U_i|U_j), \qquad \forall\, i, j \tag{2.96}$$

then it can be shown that the transition probability will generate configurations that approach the desired distribution $p(U)$ for each update in the chain [97]. Then, by performing sufficient number of updates until the Markov chain has reached equilibrium, subsequent configurations in the chain will be distributed according to $p(U)$. Performing an initial set of such updates in order to approach the limiting stationary distribution is referred to as *thermalisation* of the ensemble.

Many methods exist for practically constructing a Markov chain that approaches a given probability distribution, each with their advantages and disadvantages depending on the distribution in question. One such method that is simple to both implement and understand is the Metropolis-Hastings algorithm [98,99] which proposes an accept-reject step for each proposed new configuration. Generally the method involves proposing local changes to the system configuration so that the probability of acceptance does not become too low. Due to the non-local nature of the fermion determinant ($\det D$) however, an algorithm that uses global updates to the gauge configuration at each step is preferred. In addition, the extremely large dimension of the Dirac matrix D makes recalculating this determinant prohibitively expensive after each proposal step. Instead, the quark determinant is written as an integral over *pseudofermion* fields

$$\det D = \int \mathcal{D}[\phi^\dagger]\mathcal{D}[\phi] e^{-\phi^\dagger D^{-1}\phi}, \tag{2.97}$$

where ϕ is a complex valued (non-Grassmann) field with the same indices as the quark fields. The fermion determinant dependence has then been eliminated by introducing an additional field with a non-local action. The mass-degenerate light u and d quark determinants can then be straightforwardly combined and simulated using the Hamiltonian/Hybrid Monte Carlo (HMC)

algorithm [100], while the strange quark poses additional difficulties that are addressed with the Rational Hamiltonian/Hybrid Monte Carlo (RHMC) algorithm [101, 102].

2.5.1 Hybrid Monte Carlo

For an even number of mass-degenerate quark flavours, the HMC (Hamiltonian/Hybrid Monte Carlo) algorithm addresses the additional care that the fermion determinant requires, using *global* updates, in which all elements of U and ϕ are changed simultaneously. The method uses the evolution of an artificially introduced set of Hamiltonian equations to propose such global changes to the gauge and pseudofermion fields, akin to molecular dynamics simulations. First, let's combine the light quark determinants. Exploiting the γ_5-Hermiticity of the (Euclidean) Dirac matrix we can write the up (u) and down (d) quark fermion determinants as

$$\begin{aligned} \det D^{(u)} \det D^{(d)} &= \det[D^{(l)\dagger} D^{(l)}], \\ &= \int \mathcal{D}[\phi^{(l)\dagger}]\mathcal{D}[\phi^{(l)}] e^{-\phi^{(l)\dagger}[D^{(l)\dagger}D^{(l)}]^{-1}\phi^{(l)}}, \end{aligned} \tag{2.98}$$

where the up and down quarks are treated as two degenerate light (l) quarks. We can then rewrite the integrand of eq. (2.95) by introducing an effective action

$$S_{\text{eff}}[U, \phi^{(l)\dagger}, \phi^{(l)}] = \phi^{(l)\dagger}[D^{(l)\dagger}D^{(l)}]^{-1}\phi^{(l)} + S_G[U]. \tag{2.99}$$

Now, an integral over a momentum field $\pi_\mu(x)$, canonically conjugate to the gauge links $U_\mu(x)$, is introduced with gaussian integrand. In other words, a clever unity factor is introduced for each link. We obtain the fictitious Hamiltonian

$$H[U, \phi^{(l)\dagger}, \phi^{(l)}] = \frac{1}{2}\sum_{x,\mu} \pi_\mu^\dagger(x)\pi_\mu(x) + S_{\text{eff}}[U, \phi^{(l)\dagger}, \phi^{(l)}], \tag{2.100}$$

and the gauge links and momenta are now updated according to Hamilton's equations of motion

$$\frac{\mathrm{d}f}{\mathrm{d}\tau} = \{f, H\}, \tag{2.101}$$

where $f = (U, \pi)$, and τ is a fictitious time coordinate, sometimes referred to as molecular dynamics time, using some symplectic integration scheme. While the process is intended to change U and π such that the Hamiltonian H is conserved, to mitigate errors due to the finite time step-size $\delta\tau$, a Metropolis-Hastings accept-reject step is included after evolving for some fixed length in τ with acceptance probability

$$P_{\text{acc}} = \min(1, e^{-\delta H}) \tag{2.102}$$

where δH is the change in H after the new configuration is proposed. To guarantee ergodicity, where it is possible to eventually get from every state to every other state with positive probability, the conjugate momenta also need to be changed periodically; this is achieved by updating the momenta from a Gaussian distribution after each update [103]. Note that conjugate momenta for the pseudofermion fields ϕ are not introduced and they must be refreshed periodically just as the conjugate momenta are. This is achieved by drawing a vector η from a Gaussian distribution with variance $\frac{1}{2}$ and then calculating $\phi = D^\dagger\eta$ for the refreshed pseudofermion field.

2.5.2 Rational Hybrid Monte Carlo

Since the HMC method assumes an even number of degenerate quarks, we need to adjust our method when including the strange quark. We use the RHMC (Rational Hamiltonian/Hybrid Monte Carlo) method that extends HMC to single quarks [101, 102]. For the strange quark determinant we write

$$\begin{aligned} \det D^{(s)} &= \det[D^{(s)\dagger} D^{(s)}]^{\frac{1}{2}}, \\ &= \int \mathcal{D}[\phi^{(s)\dagger}]\mathcal{D}[\phi^{(s)}]\; e^{-\phi^{(s)\dagger}[D^{(s)\dagger}D^{(s)}]^{-1/2}\phi^{(s)}}. \end{aligned} \tag{2.103}$$

Note that this is only valid if $\det D^{(s)}$ is positive. Since the physical strange quark mass is relatively high, the strange sector of the Dirac matrix is relatively well conditioned and the negative fluctuation of its eigenvalues is not an issue. We are then fortunate that in nature the u and d quark masses are so similar and that treating them as degenerate is a good approximation since simulating a single light quark is incredibly difficult. Their small masses lead to Dirac matrices that are at risk of being ill-conditioned, making the RHMC method inapplicable. The extension of the HMC method is in treating the $[D^{(s)\dagger}D^{(s)}]^{-1/2}$ term, for which a low-order rational approximation is made

$$\left[D^{(s)\dagger}D^{(s)}\right]^{-1/2} \approx \alpha_0 \mathbb{1} + \sum_i \alpha_i \left[D^{(s)\dagger}D^{(s)} + \beta_i\right]^{-1}, \tag{2.104}$$

where the coefficients α_i, β_i specify the particular rational approximation. To refresh the pseudo-fermion fields, a vector η is again drawn according to a Gaussian distribution with variance $\frac{1}{2}$ and $\phi = [D^\dagger D]^{1/4}\eta$ is calculated. The rest of the algorithm proceeds much the same way as the HMC algorithm. Note that in the generation of the CLS ensembles used in the scattering analysis in chapter 8, a reweighting factor has been included in the strange sector where RHMC is used [82].

Chapter 3

Constructing Hadron Operators

Careful construction of hadronic interpolating operators for use in correlation matrices proves to be a crucial step in the extraction of excited states from lattice QCD. There are a number of considerations to be made when constructing such objects. First, to extract the low-lying states in the theory, operators which couple minimally to high-lying modes of the theory should be used. By smearing the quark fields and gauge links, mixing with higher frequency modes of the theory can be dramatically reduced. As hadron resonances are expected to be large objects, spatially extended operators can be included to capture the orbital and radial structure of such states. Then, having settled on the base components for constructing operators, we ensure that the operators we use transform appropriately under irreducible representations (irreps) of the relevant symmetry groups categorising the states of interest.

In this chapter we outline our approach to the above considerations; first discussing the basic building blocks with which we design hadron operators. The meson and baryon elemental operators are then summarised, including our procedure for obtaining linearly independent sets of these operators. Then, the role of symmetry transformations is discussed, first with an outline of the general transformation properties for operators under the irreps of a given symmetry group, followed by properties of the symmetry group of a finite, cubic lattice, and the projection of our hadron operators onto irreps of that group. Since a significant number of two hadron states lie below the resonant states of interest, the inclusion of two hadron interpolating operators is essential for our calculations. Finally, following the construction of two-hadron operators, the construction of some exotic operators will be discussed, including the scalar glueball operator that will be used in chapter 7. Much of the discussion here follows Ref. [104].

3.1 Basic Building Blocks

We begin by describing the basic building blocks to be used in constructing all of our hadronic operators. Since hadrons are composite objects of quarks and gluons, quark fields and gauge links make up these basic components. At this level both smearing and quark displacements are

performed. Smearing involves replacing a field at a given point with a carefully tuned local average of neighbouring fields in such a way as to preserve all of the symmetries of the original field. Note that any operator we create must remain a gauge invariant object.

3.1.1 Gauge Link Smearing

Gauge-link smearing is important not just in operator construction, but is also used for improving the gauge links in the QCD action. In operator construction for example, it has a dramatic effect in reducing the statistical uncertainty for displaced operators, while also reducing the mixing from high frequency modes in the theory. In both our operator construction and improved lattice action, we employ *stout smearing* as described in Ref. [105]. This method has the advantage of being an analytic method of link smearing in which the stout smeared links remain in $SU(3)$, retaining the differentiability that is often lost is other forms of smearing.

Let $C_\mu(x)$ denote the following weighted sum of perpendicular staples beginning at x, and terminating at $x+\hat{\mu}$:

$$C_\mu(x) = \sum_{\nu\neq\mu} \rho_{\mu\nu} \left(U_\nu(x) U_\mu(x+\hat{\nu}) U_\nu^\dagger(x+\hat{\mu}) + U_\nu^\dagger(x) U_\mu(x-\hat{\nu}) U_\nu(x-\hat{\nu}+\hat{\mu}) \right), \tag{3.1}$$

where $\hat{\mu}, \hat{\nu}$ represent vectors in directions μ, ν respectively, with length of one lattice spacing in that direction, and the weights $\rho_{\mu\nu}$ are real, tuneable parameters. Our choice of these parameters is

$$\rho_{jk} = \rho, \qquad \rho_{4\mu} = \rho_{\mu 4} = 0, \tag{3.2}$$

yielding a scheme in which only the spatial links are smeared. We define then the following matrix

$$Q_\mu(x) = \frac{i}{2}\left(\Omega_\mu^\dagger(x) - \Omega_\mu(x)\right) - \frac{i}{2N}\,\mathrm{Tr}\left(\Omega_\mu^\dagger(x) - \Omega_\mu(x)\right), \tag{3.3a}$$

$$\Omega_\mu(x) = C_\mu(x) U_\mu^\dagger(x), \qquad \text{(no summation over } \mu\text{)}, \tag{3.3b}$$

which is Hermitian and traceless, and hence, is an element of $\mathfrak{su}(N)$ (so then $e^{iQ_\mu(x)}$ is an element of $SU(N)$). We define with this an iterative, analytic smearing process in which the link $U_\mu^{(n)}(x)$ at step n is mapped to $U_\mu^{(n+1)}(x)$ using

$$U_\mu^{(n+1)}(x) = \exp\left(iQ_\mu^{(n)}(x)\right) U_\mu^{(n)}(x), \tag{3.4}$$

with closure ensuring that $U_\mu^{(n+1)}(x)$ remains in $SU(N)$. This fuzzing is iterated n_ρ times to produce the so-called *stout* links denoted by $\tilde{U}_\mu(x)$:

$$U \to U^{(1)} \to U^{(2)} \to \cdots \to U^{(n_\rho)} \equiv \widetilde{U}. \tag{3.5}$$

Since we only smear the spatial links and leave the links in the temporal direction unsmeared, we ensure that the transfer matrix remains positive definite [71].

3.1.2 Quark Field Smearing

The goal in smearing the fermionic quark fields is to reduce the excited state contamination to our correlation functions. We want the smeared fields to have the same symmetry properties as the original fields. A natural choice for such a symmetry preserving smoothing function is the three-dimensional covariant Laplacian, defined on the lattice as follows:

$$\widetilde{\Delta}^{ab}_{xy}(\widetilde{U}) = \sum_{k=1}^{3} \left\{ \widetilde{U}^{ab}_{k}(x)\delta_{x+\hat{k},y} + \widetilde{U}^{\dagger ab}_{k}(y)\delta_{x-\hat{k},y} - 2\delta_{x,y}\delta^{ab} \right\}, \tag{3.6}$$

where we note the dependence on smeared gauge links, $\widetilde{U}$, and lack of dependence on Dirac spin indices. We now must find an appropriate way to use this operator to smear our quark fields. First, let's consider the popular covariant form of Gaussian smearing [106]

$$\widetilde{\psi}(x) = \left(\delta_{x,y} + \frac{\sigma_s^2}{4n_\sigma} \widetilde{\Delta}_{xy} \right)^{n_\sigma} \psi(y), \tag{3.7a}$$

$$\widetilde{\chi}(x) = \chi(y) \left(\delta_{y,x} + \frac{\sigma_s^2}{4n_\sigma} \widetilde{\Delta}_{yx} \right)^{n_\sigma}, \tag{3.7b}$$

where σ_s and n_σ are parameters used to tune the smearing. Looking at the covariant Laplacian, it is straightforward to show that, under this smearing scheme, the quark fields retain their original gauge transformation properties. The effect of using this smearing scheme (along with stout smeared gauge links), is shown in fig. 3.1, where the dramatic reduction of excited state contamination from quark field smearing is clear. Now, as we seek a simpler strategy for quark field smearing, by expressing the smearing operators of eq. (3.7) in terms of the eigenvalues and eigenvectors of $\widetilde{\Delta}$, we can glean a deeper understanding of the smearing process.

From eq. (3.7), define the smearing operator

$$K_{ab}(x,y) = \left(\delta_{x,y} + \frac{\sigma_s^2}{4n_\sigma} \widetilde{\Delta}^{ab}_{xy} \right)^{n_\sigma}. \tag{3.8}$$

Using the properties of the gauge links, it is straightforward to show that the covariant Laplacian is Hermitian, and hence, that its eigenvalues are real and that the eigenvectors can be chosen to be orthonormal. As it can also be shown that $-\widetilde{\Delta}$ is positive semi-definite, we denote its (non-negative) eigenvalues by $\lambda^{(k)}$, where $\lambda^{(k+1)} \geq \lambda^{(k)} \geq \cdots \geq 0$. Writing the eigenvectors of $-\widetilde{\Delta}$ as $v^{(k)}$, we have

$$\sum_j \widetilde{\Delta}_{ij} v_j^{(k)} = -\lambda(k) v_i^{(k)}, \tag{3.9}$$

where the Latin indices i, j span the initial spatial and colour indices. The smearing operator can then be decomposed in terms of these eigenvectors as

$$K_{ab}(x,y) = \delta_{x_4,y_4} \sum_k \left(1 - \frac{\sigma_s^2}{4n_\sigma} \lambda^{(k)} \right)^{n_\sigma} v_a^{(k)}(x)\, v_b^{(k)\,*}(y). \tag{3.10}$$

By taking the limit $n_\sigma \to \infty$, the action of this smearing operator becomes clear; the larger eigenmodes of $-\widetilde{\Delta}$ are suppressed by the Gaussian in

$$\lim_{n_\sigma \to \infty} K_{ab}(x,y) = \delta_{x_4,y_4} \sum_k e^{-\frac{1}{4}\sigma_s^2 \lambda^{(k)}} v_a^{(k)}(x)\, v_b^{(k)\,*}(y). \tag{3.11}$$

Now that we have established how smearing the quark fields reduces excited state contamination, the form of eq. (3.11) leads to considering a more straightforward alternative: simply exclude the exponentially suppressed eigenmodes in the sum over k. This idea was introduced in Refs. [15, 107] and is referred to as Laplacian Heaviside (LapH) smearing. Aside from the smearing properties we discuss here, the method offers an additional crucial advantage for correlator estimation that we will discuss in chapter 4. Define now the smearing kernel

$$\begin{aligned} \mathcal{S}_{ab}(x,y) &= \Theta\left(\sigma_s^2 + \widetilde{\Delta}\right) \\ &= V_{\widetilde{\Delta}}\, \Theta\left(\sigma_s^2 + \Lambda_{\widetilde{\Delta}}\right) V_{\widetilde{\Delta}}^\dagger, \end{aligned} \tag{3.12}$$

where $\Lambda_{\widetilde{\Delta}}$ is the diagonal matrix, diagonalised by $V_{\widetilde{\Delta}}$, whose entries are the eigenvalues of $\widetilde{\Delta}$, i.e. $\widetilde{\Delta} = V_{\widetilde{\Delta}} \Lambda_{\widetilde{\Delta}} V_{\widetilde{\Delta}}^\dagger$, and the Heaviside function ensures that $\mathcal{S}$ includes only the eigenmodes satisfying $\lambda^{(k)} < \sigma_s^2$. As in eq. (3.9), we write the eigendecomposition

$$\mathcal{S}_{ab}(x,y) \approx \delta_{x_4,y_4} \sum_{k=1}^{N_v} v_a^{(k)}(x)\, v_b^{(k)\,*}(y), \tag{3.13}$$

where the number of retained eigenvectors, N_v, will depend on the value chosen for σ_s. For constant N_v this expression for $\mathcal{S}$ is approximate as we do not expect N_v to remain constant across gauge configurations. Also, since $\mathcal{S}$ is block-diagonal in time, each eigenvector is non-zero only on a single time slice, meaning that N_v may also vary across different times. Thankfully, explicit calculations with a number of values for N_v show that these variations are quite small and that using a constant value for N_v has a negligible effect on any final results [107]. Similarly, the numerical value for σ_s was chosen by considering the effective energy of nucleon operators for different values of σ_s [15].

Assuming that errors in using a constant value for N_v are negligible, we find

$$\mathcal{S} = \left(V_s V_s^\dagger\right) \otimes I_4^d, \tag{3.14}$$

where V_s is the matrix whose columns are the eigenvectors corresponding to the N_v lowest eigenmodes of $-\widetilde{\Delta}$ on each time slice, and I_4^d is the identity matrix in the Dirac spin subspace; so that the smearing matrix does not act on the quark field spin indices. This is the final form of the smearing operator that we use in our calculations. Finally, note that V_s has dimension $N_s^3 N_t N_c \times N_v N_t$, where N_s is the number of spatial sites in each direction, N_t the number of temporal sites/time slices, and $N_c = 3$ is the number of colours. The $N_v N_t N_d$ vectors that comprise $V_s \otimes I_4^d$ form what we call the LapH subspace, where $N_d = 4$ is the number of Dirac spin indices. We will revisit the importance of the LapH subspace in chapter 4 when we show the significant computational advantage of working solely in this much smaller subspace.

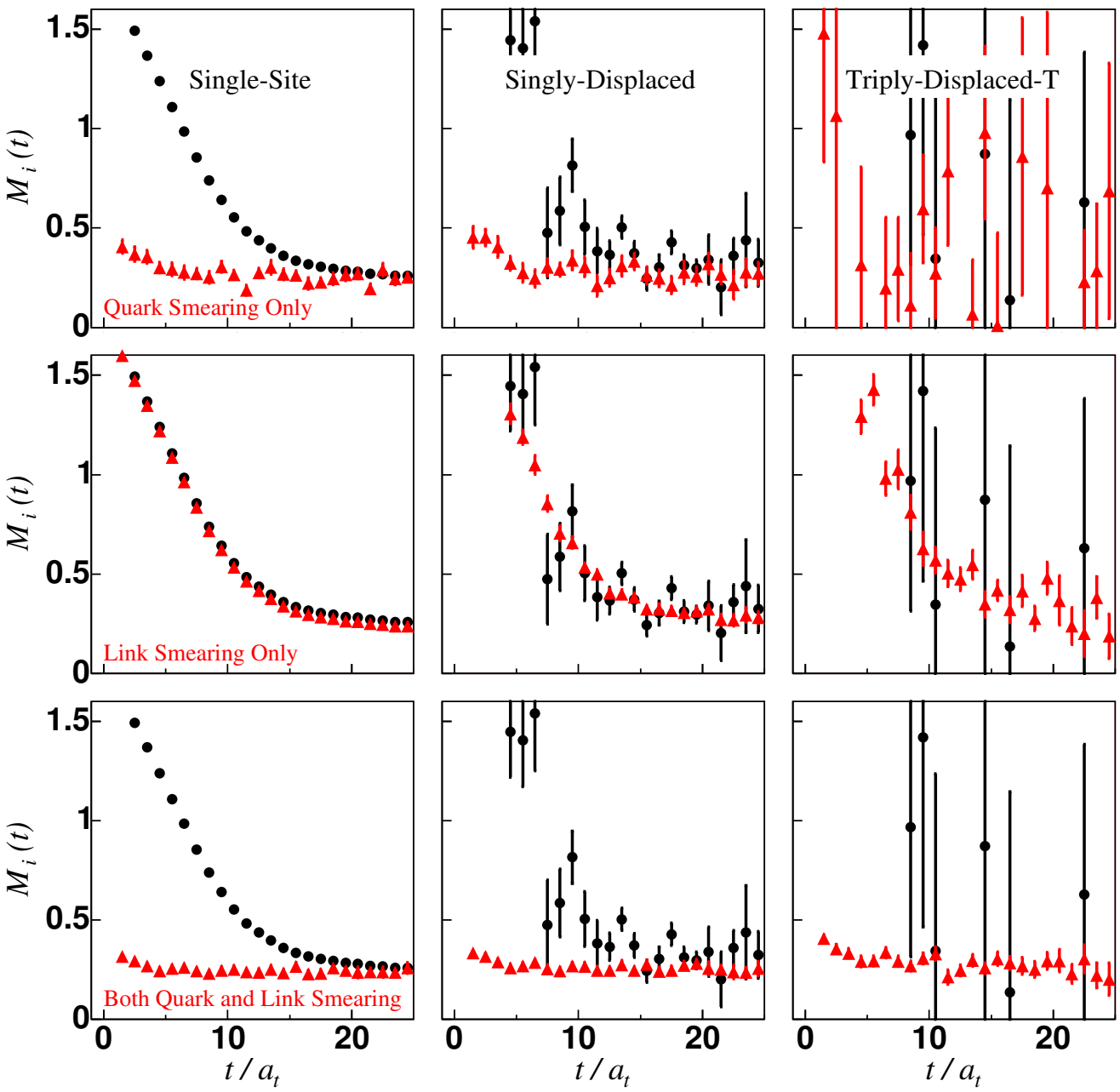

Figure 3.1: Effective masses $M(t)$ for unsmeared (black circles) and smeared (red triangles) nucleon operators with different covariant displacements. Top row: only quark-field smearing (see eq. (3.7)) is used. Middle row: only link-variable smearing (see eq. (3.5)) is used. Bottom row: both quark and link smearing are used, dramatically improving the signal for all three operators. Results are based on 50 quenched configurations on a $12^3 \times 48$ anisotropic lattice using the Wilson action with $a_s \sim 0.1$ fm, $a_s/a_t \sim 3.0$. Figure from Ref. [103].

3.1.3 Covariant Displacements

Since many of the hadron resonances we want to study are expected to be large objects, it is important that we include spatially extended operators in our calculations. Orbital structure can be probed by displacing the quarks in different directions, whereas radial structure is captured by using displacements over various distances [108]. As we require our operators to remain gauge invariant, covariant displacements are constructed using the (smeared) gauge link variables. Therefore, if, for simplicity, we restrict the displacements to the six directions along the axes of the cubic lattice, the p-link gauge-covariant displacement operator in the jth direction is given by [103, 108, 109]

$$D^{(j)}(x,x') = \widetilde{U}_j(x)\widetilde{U}_j(x+\hat{j})\ldots\widetilde{U}_j(x+(p-1)\hat{j})\,\delta_{x',x+p\hat{j}}, \tag{3.15}$$

where $j = 0, \pm1, \pm2, \pm3$, so that $D^{(j=0)}(x,x') = \delta_{x,x'}$ corresponds to no displacement.

We can now write the final form for the basic building blocks used in the construction of all our hadron operators. The gauge covariantly displaced, LapH-smeared quark and anti-quark fields are defined by

$$q^A_{a\alpha j} \equiv D^{(j)}\widetilde{\psi}^{(A)}_{a\alpha}, \qquad \overline{q}^A_{a\alpha j} \equiv \widetilde{\chi}^{(A)}_{a\alpha} D^{(j)\dagger}, \tag{3.16}$$

where A is a flavour index, a is the colour index, α is the Dirac spin index, and recall that $\chi \equiv \overline{\psi}\gamma_4$ is used to ensure Hermiticity of our correlation matrices. We will occasionally use, instead of a flavour index, explicit symbols for the different quarks, e.g. $u = q^u, \overline{d} = \overline{q}^d$, etc. In sections 3.2 and 3.5 we will show then how these building blocks are assembled into the single- and multi-hadron interpolating operators we use.

3.2 Single-Hadron Operators

Now that the basic building blocks have been identified, we can construct sets of linearly independent, gauge-invariant elemental hadron operators. Each operator set will be identifiable by hadron type (i.e. meson, baryon, etc.), flavour structure, and displacement type. Imposing the desired behaviour under various symmetry transformations is then the final step; within each set of elemental operators, appropriate linear combinations of the basis elemental operators can be used to form operators that transform irreducibly under rotations of the lattice symmetry group. Here, we consider the construction of such elemental operator sets for single meson and baryon type operators.

3.2.1 Flavour Structure: Isospin, and G-Parity

In our simulations we work in the approximation $m_u = m_d$, giving an exact $SU(2)$ flavour symmetry, also known as isotopic spin or isospin symmetry. Hence, we base the flavour structure of our operators on $SU(2)$ flavour irreps such that we avoid mixing between states of definite isospin. The u and d quarks can be viewed as two states of an $SU(2)$ multiplet, with $I_3 = +\frac{1}{2}$ and $I_3 = -\frac{1}{2}$ respectively. As the s (and c, b, and t) quark(s) have vastly different masses from those of the u

and d quarks, and from each other, this is the only flavour symmetry we need to consider. We then demand the following transformation properties of our creation and annihilation operators under an isospin rotation R_τ

$$U_{R_\tau}\mathcal{O}^{II_3S}(t)U^\dagger_{R_\tau} = \mathcal{O}^{II'_3S}(t)D^{(I)}_{I'_3I_3}(R_\tau)^* \tag{3.17a}$$

$$U_{R_\tau}\overline{\mathcal{O}}^{II_3S}(t)U^\dagger_{R_\tau} = \overline{\mathcal{O}}^{II'_3S}(t)D^{(I)}_{I'_3I_3}(R_\tau), \tag{3.17b}$$

where I is the isospin, I_3 its projection onto the z-axis in isospin space, S is the strangeness, and $D(R)$ are the Wigner D-matrices. Also, as the exact isospin symmetry means the spectrum must be independent of isospin projection I_3, the operators we construct are chosen to have maximal total $I_3 = I$.

Defining the generators, τ_1, τ_2, and τ_3, of isospin by $[\tau_i, \tau_j] = i\varepsilon_{ijk}\tau_k$, an annihilation operator $\mathcal{O}^{(I)}_{I_3}$ transforms appropriately under the isospin irrep I if it satisfies

$$\left[\tau_3, \mathcal{O}^{(I)}_{I_3}\right] = -I_3\mathcal{O}^{(I)}_{I_3}, \tag{3.18a}$$

$$\left[\tau_+, \mathcal{O}^{(I)}_{I_3}\right] = -\sqrt{(I-I_3)(I+I_3+1)}\mathcal{O}^{(I)}_{I_3+1}, \tag{3.18b}$$

$$\left[\tau_-, \mathcal{O}^{(I)}_{I_3}\right] = -\sqrt{(I+I_3)(I-I_3+1)}\mathcal{O}^{(I)}_{I_3-1}, \tag{3.18c}$$

where $\tau_\pm = \tau_1 \pm i\tau_2$. These relations also imply

$$\left[\tau_3, \left[\tau_3, \mathcal{O}^{(I)}_{I_3}\right]\right] + \frac{1}{2}\left[\tau_+, \left[\tau_-, \mathcal{O}^{(I)}_{I_3}\right]\right] + \frac{1}{2}\left[\tau_-, \left[\tau_+, \mathcal{O}^{(I)}_{I_3}\right]\right] = I(I+1)\mathcal{O}^{(I)}_{I_3}, \tag{3.19}$$

with similar relations for the creation operators. For the barred quark fields, we have the following commutation relations

$$\begin{aligned} &[\tau_3, \overline{u}] = \frac{1}{2}\overline{u}, && [\tau_3, \overline{d}] = -\frac{1}{2}\overline{d}, && [\tau_3, \overline{s}] = 0, \\ &[\tau_+, \overline{u}] = 0, && [\tau_+, \overline{d}] = \overline{u}, && [\tau_+, \overline{s}] = 0, \\ &[\tau_-, \overline{u}] = \overline{d}, && [\tau_-, \overline{d}] = 0, && [\tau_-, \overline{s}] = 0, \end{aligned} \tag{3.20}$$

with similar relations for the un-barred fields. Then by writing down all relevant combinations of quark fields, and applying all of the commutation relations above, we end up with the elemental operators for a given isospin channel. Explicit examples of the flavour structure for some baryonic states are given in table 3.1.

Now that we have introduced isospin as a good symmetry, we can introduce for bosonic systems with zero strangeness an additional symmetry, G-parity, resulting from a generalisation of C-parity for multiplets of particles. Charge conjugation, or C-parity, is a good symmetry for some electrically/flavour neutral states, e.g. $\mathcal{C}|\pi^0\rangle = +|\pi^0\rangle$. In fact, the symmetry gives us a good quantum number for any electrically/flavour neutral meson state[1]. However, since QCD alone

[1]Since baryons are comprised of three quarks, charge conjugation is not a good symmetry; $\mathcal{C}$ acting on $|qqq\rangle$ will produce an anti-baryon state $|\overline{qqq}\rangle$.

is blind to electric charge, the strong interaction does not distinguish among π^+, π^0, and π^-. It is natural then to generalise C-parity such that it applies to all of the charged states of a given multiplet with average charge zero. We are led to the symmetry known as G-parity, whose operation is defined by

$$U_{\mathcal{G}} = \mathcal{C} e^{-i\pi\tau_2}, \tag{3.21}$$

where $\mathcal{C}$ is the charge conjugation operator, and τ_2 is the second component of the isospin operator. G-parity is then simply a combination of charge conjugation and a particular rotation in isospin space. The transformation properties of the basic building blocks under G-parity are straightforward to deduce from the transformation of the quark fields and gauge links under charge conjugation, combined with isospin rotations using the Wigner D-matrix in the $I = 1/2$ representation in eq. (3.17). With explicit flavour labels then

$$\begin{aligned} U_{\mathcal{G}} \overline{u}_{a\alpha j} U_{\mathcal{G}}^\dagger &= -\Gamma^{\mathcal{G}}_{\alpha\beta} d_{a\beta j}, & U_{\mathcal{G}} u_{a\alpha j} U_{\mathcal{G}}^\dagger &= -\overline{d}_{a\beta j} \Gamma^{\mathcal{G}}_{\beta\alpha}, \\ U_{\mathcal{G}} \overline{d}_{a\alpha j} U_{\mathcal{G}}^\dagger &= \Gamma^{\mathcal{G}}_{\alpha\beta} u_{a\beta j}, & U_{\mathcal{G}} d_{a\alpha j} U_{\mathcal{G}}^\dagger &= \overline{u}_{a\beta j} \Gamma^{\mathcal{G}}_{\beta\alpha}, \\ U_{\mathcal{G}} \overline{s}_{a\alpha j} U_{\mathcal{G}}^\dagger &= -\Gamma^{\mathcal{G}}_{\alpha\beta} s_{a\beta j}, & U_{\mathcal{G}} s_{a\alpha j} U_{\mathcal{G}}^\dagger &= -\overline{s}_{a\beta j} \Gamma^{\mathcal{G}}_{\beta\alpha}, \end{aligned} \tag{3.22}$$

where the $\Gamma^{\mathcal{G}}$ matrices are representation dependant, and $\Gamma^{\mathcal{G}} = \gamma_2$ in the Dirac-Pauli, Weyl, and DeGrand-Rossi conventions.

3.2.2 Elemental Baryons

Having established the basic building blocks, we now turn to explicit forms for the gauge-invariant elemental baryon operators. Annihilation operators with definite three-momentum $\boldsymbol{p}$ consist of flavour combinations of

$$\Phi^{ABC}_{\alpha\beta\gamma;ijk}(\boldsymbol{p}, t) = \sum_{\boldsymbol{x}} e^{-i\boldsymbol{p}\cdot\boldsymbol{x}} \varepsilon_{abc}\, q^A_{a\alpha i}(\boldsymbol{x}, t)\, q^B_{b\beta j}(\boldsymbol{x}, t)\, q^C_{c\gamma k}(\boldsymbol{x}, t), \tag{3.23}$$

that transform appropriately for a given isospin irrep. The corresponding elemental creation operators take the form

$$\overline{\Phi}^{ABC}_{\alpha\beta\gamma;ijk}(\boldsymbol{p}, t) = \sum_{\boldsymbol{x}} e^{i\boldsymbol{p}\cdot\boldsymbol{x}} \varepsilon_{abc}\, \overline{q}^C_{c\gamma k}(\boldsymbol{x}, t)\, \overline{q}^B_{b\beta j}(\boldsymbol{x}, t)\, \overline{q}^A_{a\alpha i}(\boldsymbol{x}, t), \tag{3.24}$$

where, for both operators, gauge invariance is assured using the colour space Levi-Civita tensor ε_{abc}. The different displacement patterns we use for these operators are shown in fig. 3.2, and flavour structures for the different hadron annihilation operators are listed in table 3.2.

Assembling the final operator sets involves taking the appropriate linear combinations of these elemental basis operators that transform appropriately under isospin transformations and under the lattice symmetry group (see section 3.4). Such linear combinations take the form

$$B_l(t) = c^{(l)}_{\alpha\beta\gamma} \Phi^{ABC}_{\alpha\beta\gamma}(\boldsymbol{p}, t), \tag{3.25a}$$

$$\overline{B}_l(t) = c^{(l)*}_{\alpha\beta\gamma} \overline{\Phi}^{ABC}_{\alpha\beta\gamma}(\boldsymbol{p}, t), \tag{3.25b}$$

Table 3.1: Flavour combinations of three quarks (baryons) with definite isospin I, isospin projection I_3, and strangeness S.

I	I_3	S	$SU(2)$ flavour
$\frac{1}{2}$	$\frac{1}{2}$	0	$\sqrt{\frac{1}{2}}(\lvert udu\rangle - \lvert duu\rangle)$
$\frac{1}{2}$	$\frac{1}{2}$	0	$\sqrt{\frac{1}{6}}(2\lvert uud\rangle - \lvert udu\rangle - \lvert duu\rangle)$
$\frac{1}{2}$	$-\frac{1}{2}$	0	$\sqrt{\frac{1}{2}}(\lvert udd\rangle - \lvert dud\rangle)$
$\frac{1}{2}$	$-\frac{1}{2}$	0	$\sqrt{\frac{1}{6}}(-2\lvert ddu\rangle + \lvert udd\rangle + \lvert dud\rangle)$
$\frac{3}{2}$	$\frac{3}{2}$	0	$\lvert uuu\rangle$
$\frac{3}{2}$	$\frac{1}{2}$	0	$\sqrt{\frac{1}{3}}(\lvert uud\rangle + \lvert udu\rangle + \lvert duu\rangle)$
$\frac{3}{2}$	$-\frac{1}{2}$	0	$\sqrt{\frac{1}{3}}(\lvert ddu\rangle + \lvert dud\rangle + \lvert udd\rangle)$
$\frac{3}{2}$	$-\frac{3}{2}$	0	$\lvert ddd\rangle$
0	0	-1	$\sqrt{\frac{1}{2}}(\lvert uds\rangle - \lvert dus\rangle)$
0	0	-1	$\sqrt{\frac{1}{2}}(\lvert usd\rangle - \lvert dsu\rangle)$
0	0	-1	$\sqrt{\frac{1}{2}}(\lvert sud\rangle - \lvert sdu\rangle)$

I	I_3	S	$SU(2)$ flavour
1	1	-1	$\lvert uus\rangle$
1	1	-1	$\lvert usu\rangle$
1	1	-1	$\lvert suu\rangle$
1	0	-1	$\sqrt{\frac{1}{2}}(\lvert uds\rangle + \lvert dus\rangle)$
1	0	-1	$\sqrt{\frac{1}{2}}(\lvert usd\rangle + \lvert dsu\rangle)$
1	0	-1	$\sqrt{\frac{1}{2}}(\lvert sud\rangle + \lvert sdu\rangle)$
1	-1	-1	$\lvert dds\rangle$
1	-1	-1	$\lvert dsd\rangle$
1	-1	-1	$\lvert sdd\rangle$
$\frac{1}{2}$	$\frac{1}{2}$	-2	$\lvert uss\rangle$
$\frac{1}{2}$	$\frac{1}{2}$	-2	$\lvert sus\rangle$
$\frac{1}{2}$	$\frac{1}{2}$	-2	$\lvert ssu\rangle$
$\frac{1}{2}$	$-\frac{1}{2}$	-2	$\lvert dss\rangle$
$\frac{1}{2}$	$-\frac{1}{2}$	-2	$\lvert sds\rangle$
$\frac{1}{2}$	$-\frac{1}{2}$	-2	$\lvert ssd\rangle$
0	0	-3	$\lvert sss\rangle$

where l is a compound label including the momentum $\boldsymbol{p}$, little group irrep Λ, irrep row λ, isospin I, isospin projection I_3, strangeness S, and an identifier labelling the different operators in each symmetry channel.

Time Reversal

As a final remark on our baryon operators, we note that the creation operators will create a particle state with a given parity P, and annihilate an anti-particle state with the same parity P (likewise for the annihilation operators). Then, in the temporal correlation functions containing baryon operators, we create a baryon state with given parity that propagates forward in time, while also creating an anti-baryon state that propagates backwards in time. Since baryons are fermions, and hence have opposite parity to their corresponding anti-fermion, the backwards propagating anti-baryon state in the correlator is not the anti-baryon of the forward propagating baryon. Instead, the backwards propagating state is the antiparticle of the parity partner of the forward propagating baryon state of interest [108]. Moreover, the masses of the two states propagating in opposite temporal directions differ due to chiral symmetry breaking. We can take advantage of this fact by

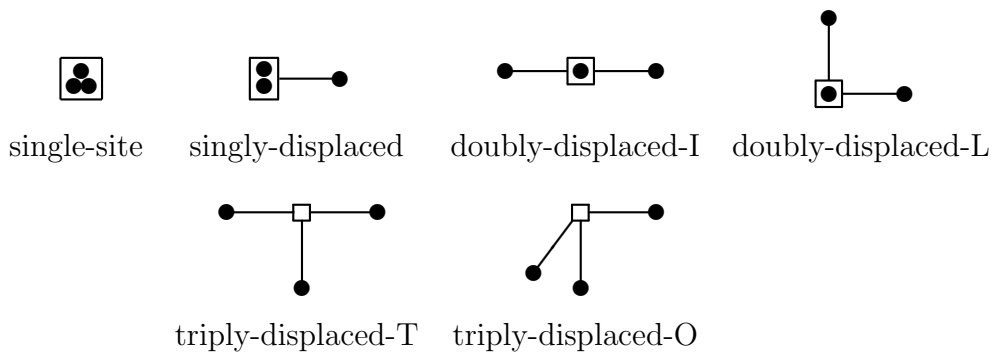

Figure 3.2: The displaced baryon operators we use. In the illustrations, the smeared quarks fields are depicted by solid circles, solid line segments indicate covariant displacements, and each box indicates the location of a colour ε_{abc} coupling. For simplicity, the displacements all have the same length in each operator. Figure from Ref. [103].

relating correlators of opposite parity to one another in order to increase statistics. This works by first constructing the odd-parity operators from the even-parity operators using charge conjugation such that the correlators are related by

$$C^{g}_{ij}(t) = C^{u}_{ij}(N_t - t)^*, \tag{3.26}$$

where N_t is the temporal extent of the lattice, and g, u label even- and odd-parity respectively. We can then average over the even- and odd-parity correlators using

$$\bar{C}^{g/u}_{ij}(t) = \frac{1}{2}\left(C^{g/u}_{ij}(t) + C^{u/g}_{ij}(N_t - t)^*\right) \tag{3.27}$$

to increase statistics. This procedure works only for correlators of baryons at-rest, since parity is no longer well-defined for baryons with non-zero momentum. We will revisit the issue of backwards propagating states both in the following discussion on meson operators, and in the discussion on temporal wrap-around effects in section 5.2.

3.2.3 Elemental Mesons

For a meson consisting of a quark field and "barred" anti-quark field, there is one way to construct a locally gauge-invariant object: using a Kronecker δ_{ab} to contract the colour indices. Hence, the elemental annihilation and creation operators are formed from appropriate flavour combinations (see table 3.2) of

$$\Phi^{AB}_{\alpha\beta;ijk}(\boldsymbol{p}, t) = \sum_{\boldsymbol{x}} e^{-i\boldsymbol{p}\cdot(\boldsymbol{x}+\frac{1}{2}(\boldsymbol{d}_\alpha+\boldsymbol{d}_\beta))}\delta_{ab}\,\overline{q}^{A}_{a\alpha i}(\boldsymbol{x}, t)\,q^{B}_{b\beta jk}(\boldsymbol{x}, t), \tag{3.28a}$$

$$\overline{\Phi}^{AB}_{\alpha\beta;ijk}(\boldsymbol{p}, t) = \sum_{\boldsymbol{x}} e^{i\boldsymbol{p}\cdot(\boldsymbol{x}+\frac{1}{2}(\boldsymbol{d}_\alpha+\boldsymbol{d}_\beta))}\delta_{ab}\,\overline{q}^{B}_{b\beta jk}(\boldsymbol{x}, t)\,q^{A}_{a\alpha i}(\boldsymbol{x}, t), \tag{3.28b}$$

where $\boldsymbol{d}_\alpha$ and $\boldsymbol{d}_\beta$ denote the spatial displacements for the quark/anti-quark fields from $\boldsymbol{x}$. These spatial displacements are included in the phase factor for the momentum projection to ensure

Table 3.2: Flavour structure of the elemental hadron operators we use. Each is characterised by total isospin I, maximal $I_3 = I$, strangeness S, and G-parity where applicable. $U_{\mathcal{G}}$ denotes a G-parity transformation. Table from Ref. [109].

Hadron	$I = I_3$	S	G	Annihilation Operators
Δ^{++}	$\frac{3}{2}$	0		$\Phi^{uuu}_{\alpha\beta\gamma}$
Σ^{+}	1	-1		$\Phi^{uus}_{\alpha\beta\gamma}$
N^{+}	$\frac{1}{2}$	0		$\Phi^{uud}_{\alpha\beta\gamma} - \Phi^{ddu}_{\alpha\beta\gamma}$
Ξ^{0}	$\frac{1}{2}$	-2		$\Phi^{ssu}_{\alpha\beta\gamma}$
Λ^{0}	0	-1		$\Phi^{uds}_{\alpha\beta\gamma} - \Phi^{dus}_{\alpha\beta\gamma}$
Ω^{-}	0	-3		$\Phi^{sss}_{\alpha\beta\gamma}$
f, f', η, η'	0	0	1	$\Phi^{uu}_{\alpha\beta} + \Phi^{dd}_{\alpha\beta} + U_{\mathcal{G}}\left(\Phi^{uu}_{\alpha\beta} + \Phi^{dd}_{\alpha\beta}\right)U^{\dagger}_{\mathcal{G}}$ $\Phi^{ss}_{\alpha\beta} + U_{\mathcal{G}}\Phi^{ss}_{\alpha\beta}U^{\dagger}_{\mathcal{G}}$
h, h', ω, ϕ	0	0	-1	$\Phi^{uu}_{\alpha\beta} + \Phi^{dd}_{\alpha\beta} - U_{\mathcal{G}}\left(\Phi^{uu}_{\alpha\beta} + \Phi^{dd}_{\alpha\beta}\right)U^{\dagger}_{\mathcal{G}}$ $\Phi^{ss}_{\alpha\beta} - U_{\mathcal{G}}\Phi^{ss}_{\alpha\beta}U^{\dagger}_{\mathcal{G}}$
b^{+}, ρ^{+}	1	0	1	$\Phi^{du}_{\alpha\beta} + U_{\mathcal{G}}\Phi^{du}_{\alpha\beta}U^{\dagger}_{\mathcal{G}}$
a^{+}, π^{+}	1	0	-1	$\Phi^{du}_{\alpha\beta} - U_{\mathcal{G}}\Phi^{du}_{\alpha\beta}U^{\dagger}_{\mathcal{G}}$
K^{+}, K^{*+}	$\frac{1}{2}$	1		$\Phi^{su}_{\alpha\beta}$
$\bar{K}^{0}, \bar{K}^{*0}$	$\frac{1}{2}$	-1		$\Phi^{ds}_{\alpha\beta}$

correct behaviour of the meson operators under G-parity. Note also that one of the fields carries two displacement direction indices, this is required to account for the different meson displacement patterns that we consider, illustrated in fig. 3.3.

The final meson operator sets then are formed in much the same way as the baryon operator sets, so that the linear combinations of elemental meson operators that transform irreducibly under irreps of the lattice symmetry group (along with isospin, G-parity, etc.) take the form

$$M_l(t) = c^{(l)}_{\alpha\beta}\Phi^{AB}_{\alpha\beta}(\boldsymbol{p}, t), \tag{3.29a}$$

$$\overline{M}_l(t) = c^{(l)*}_{\alpha\beta}\overline{\Phi}^{AB}_{\alpha\beta}(\boldsymbol{p}, t), \tag{3.29b}$$

where l now includes G-parity when relevant. Note that the operator coefficients here serve the purpose of both ensuring our operators transform irreducibly under irreps of the lattice and now under G-parity transformations in the isoscalar and isovector sectors.

Time Reversal

The treatment of our meson operators under time reversal proves to be similar, but more straightforward, than for the baryons. As bosons, the meson states share the same intrinsic parity with their corresponding anti-meson states, and hence, the backwards propagating states have the same

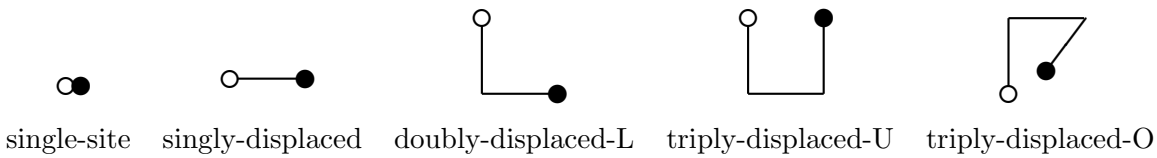

Figure 3.3: The displaced meson operators we use. In the illustrations, the smeared quarks fields are depicted by solid circles, each hollow circle indicates a smeared "barred" antiquark field, and the solid line segments indicate covariant displacements. For simplicity, the displacements all have the same length in each operator. Figure from Ref. [103].

energy as those that propagate forward in time. This allows for an increase in statistics if we design our meson operators such that

$$C_{ij}(t) = C_{ij}(N_t - t), \tag{3.30}$$

which is easily guaranteed for meson operators satisfying

$$M_i(t) = \eta M_i(N_t - t), \qquad \text{for} \quad |\eta|^2 = 1. \tag{3.31}$$

This restricted behaviour under time reversal turns out to only offer a statistically significant improvement to the lightest meson states for which temporal wrap-around effects are non-negligible. This will be discussed in more detail in section 5.2.

3.3 Symmetry Channels

Before we discuss the role that rotational symmetry plays in the construction of our operators, it is useful to discuss some general transformation properties of our operators, and of the correlation matrices we compute. Since hadronic states can be identified by their momentum $\boldsymbol{p}$, total spin J, spin projection, parity P, and their flavour structure, we can group these quantum numbers together and refer to such a set of quantum numbers that a set of states may share generically as a symmetry *channel*. To create states in a given channel then, we demand that our operators transform under the irreps corresponding to the quantum numbers of that channel. Denoting our creation and annihilation operators by $\overline{\mathcal{O}}_i^{\Lambda\lambda F}(t)$ and $\mathcal{O}_i^{\Lambda\lambda F}(t)$ respectively, where Λ denotes the irrep of the symmetry group, λ is the row of the Λ representation, F labels all other quantum numbers, and i labels the different operators in this $\Lambda\lambda F$ symmetry sector. Under a symmetry operation R, much like for isospin transformations in eq. (3.17), these operators transform like

$$U_R\, \mathcal{O}_i^{\Lambda\lambda F}(t)\, U_R^\dagger = \sum_\mu \mathcal{O}_i^{\Lambda\mu F}(t) \Gamma_{\mu\lambda}^{(\Lambda)}(R)^*, \tag{3.32a}$$

$$U_R\, \overline{\mathcal{O}}_i^{\Lambda\lambda F}(t)\, U_R^\dagger = \sum_\mu \overline{\mathcal{O}}_i^{\Lambda\mu F}(t) \Gamma_{\mu\lambda}^{(\Lambda)}(R), \tag{3.32b}$$

where U_R is the quantum operator for the symmetry transformation R, and $\Gamma_{\mu\lambda}^{(\Lambda)}(R)$ is a Λ representation matrix for R. The importance of using operators that transform under the irreps

of the symmetry groups of our system can be seen by looking at correlation functions containing these operators:

$$\begin{aligned}
\langle 0|T\,\mathcal{O}_i^{\Lambda\lambda F}(t)\overline{\mathcal{O}}_j^{\Lambda'\lambda' F}(0)|0\rangle &= \frac{1}{g_{\mathcal{G}}}\sum_{R\in\mathcal{G}}\langle 0|T\,U_R\,\mathcal{O}_i^{\Lambda\lambda F}(t)U_R^\dagger U_R\,\overline{\mathcal{O}}_j^{\Lambda'\lambda' F}(0)U_R^\dagger|0\rangle \\
&= \frac{1}{g_{\mathcal{G}}}\sum_{R\in\mathcal{G}}\sum_{\mu\mu'}\Gamma^{(\Lambda)}_{\mu\lambda}(R)^*\Gamma^{(\Lambda')}_{\mu'\lambda'}(R)\langle 0|T\,\mathcal{O}_i^{\Lambda\mu F}(t)\overline{\mathcal{O}}_j^{\Lambda'\mu' F}(0)|0\rangle \\
&= \sum_{\mu\mu'}\frac{1}{d_\Lambda}\delta_{\Lambda\Lambda'}\delta_{\lambda\lambda'}\delta_{\mu\mu'}\langle 0|T\,\mathcal{O}_i^{\Lambda\mu F}(t)\overline{\mathcal{O}}_j^{\Lambda'\mu' F}(0)|0\rangle \\
&= \delta_{\Lambda\Lambda'}\delta_{\lambda\lambda'}\sum_{\mu}\frac{1}{d_\Lambda}\langle 0|T\,\mathcal{O}_i^{\Lambda\mu F}(t)\overline{\mathcal{O}}_j^{\Lambda\mu F}(0)|0\rangle,
\end{aligned} \tag{3.33}$$

where $\mathcal{G}$ is the symmetry group, $g_{\mathcal{G}}$ is the order of $\mathcal{G}$, we require the vacuum to be invariant under all relevant transformations, and the so-called great orthogonality theorem is used:

$$\frac{1}{g_{\mathcal{G}}}\sum_{R\in\mathcal{G}}\Gamma^{(\Lambda)}_{\mu\lambda}(R)^*\Gamma^{(\Lambda')}_{\mu'\lambda'}(R) = \frac{1}{d_\Lambda}\delta_{\Lambda\Lambda'}\delta_{\lambda\lambda'}\delta_{\mu\mu'}. \tag{3.34}$$

As eq. (3.33) shows that the correlation matrix elements must vanish unless $\Lambda = \Lambda'$ and $\lambda = \lambda'$, we are motivated to divide our calculations into different symmetry sectors/channels. Furthermore, we can label our correlation functions using the irrep and irrep row:

$$C_{ij}^{\Lambda\lambda F}(t) \equiv \langle 0|T\,\mathcal{O}_i^{\Lambda\lambda F}(t)\overline{\mathcal{O}}_j^{\Lambda\lambda F}(0)|0\rangle. \tag{3.35}$$

Finally, we can arrive at another useful relation between correlators labelled by different irrep rows using the orthogonality of eq. (3.33), and the invariance of the vacuum:

$$\begin{aligned}
C_{ij}^{\Lambda\lambda F}(t) &= \langle 0|T\,\mathcal{O}_i^{\Lambda\lambda F}(t)\overline{\mathcal{O}}_j^{\Lambda\lambda F}(0)|0\rangle \\
&= \langle 0|T\,U_R\,\mathcal{O}_i^{\Lambda\lambda F}(t)U_R^\dagger U_R\,\overline{\mathcal{O}}_j^{\Lambda\lambda F}(0)U_R^\dagger|0\rangle \\
&= \sum_{\mu\mu'}\Gamma^{(\Lambda)}_{\mu\lambda}(R)^*\Gamma^{(\Lambda)}_{\mu'\lambda}(R)\langle 0|T\,\mathcal{O}_i^{\Lambda\mu F}(t)\overline{\mathcal{O}}_j^{\Lambda\mu' F}(0)|0\rangle \\
&= \sum_{\mu\mu'}\Gamma^{(\Lambda)}_{\mu\lambda}(R)^*\Gamma^{(\Lambda)}_{\mu'\lambda}(R)\,\delta_{\mu\mu'}C_{ij}^{\Lambda\mu F}(t) \\
&= \sum_{\mu}|\Gamma^{(\Lambda)}_{\mu\lambda}(R)|^2\,C_{ij}^{\Lambda\mu F}(t).
\end{aligned} \tag{3.36}$$

This result will be used shortly to show how we can enforce equivalence of correlators across irrep rows to increase statistics.

3.4 Rotational Symmetry on the Lattice

As states in infinite-volume are generally classified by their spin/total angular momentum, one may be inclined to design hadron operators that transform irreducibly under the spin irreps of $SU(2)$

i.e. operators with definite total angular momentum J. For continuum operators in infinite-volume, this strategy is the norm, and naturally works well, so we might seek to begin with these continuum operators, and then discretise them for use in lattice QCD. However, this strategy has several shortcomings: efficiently constructing spin states with large values of J quickly becomes unwieldy; imposing these continuum transformation properties for extended hadron operators also quickly becomes tedious; and, most importantly, since we are restricted to the reduced rotational symmetry of the hypercubic box, the discretised operators will mix different values of J. We are naturally led then to construct our operators so that they transform irreducibly under irreps of the rotational symmetry group of our lattice, the octahedral point group, which we denote by O_h^1. This group consists of the semidirect product of the Abelian group of allowed translations on a simple cubic lattice and the orthogonal point group O_h, which itself contains the proper spatial rotations of a cube, O, and a spatial inversion element I_s, such that $O_h = O \otimes \{E, I_s\}$, where E is an identity element. In what follows we shall provide an overview of how such transformation properties are imposed on our operators, leaving most of the details to Ref. [109], and references therein.

3.4.1 The Octahedral Group and Point Group

First we discuss the group of rotations that leave a three-dimensional, spatially isotropic cube invariant, the octahedral group O. The group has 24 elements, occurring in five conjugacy classes, for which we use the standard notation:

$$\begin{aligned} E &= \text{identity element} \\ C_{nj} &= \text{proper rotation through an angle } \frac{2\pi}{n} \text{ about the axis } Oj \\ I_s &= \text{spatial inversion (see point group } O_h) \end{aligned} \tag{3.37}$$

with the rotation axes Oj illustrated in fig. 3.4. Following the Mulliken convention [110,111], we label the (single-valued) irreps of O by A_1, A_2, E, T_1, T_2, which have dimension $1, 1, 2, 3, 3$ respectively. The incorporation of spatial parity leads to the cubic point group O_h, which is accomplished by taking the direct product $O_h = O \otimes \{E, I_s\}$, doubling the number of conjugacy classes, and hence number of irreps. As such, we add an additional label (g/u) to the (single-valued) irreps indicating behaviour under spatial inversions:

$$A_{1g/u}, A_{2g/u}, E_{g/u}, T_{1g/u}, T_{2g/u}, \tag{3.38}$$

where again, the subscripts g, u indicate even and odd parity respectively[2]. Where relevant, we will use the superscripts $+, -$ to denote even and odd G-parity respectively.

So far, since these representations are all single-valued, we have only accounted for integer values of spin. We can construct spinorial (double-valued) representations by extending the group elements to form to so-called "double octahedral group" O^D and "double point group" O_h^D. This is done

[2]These labels come from the German words *gerarde* and *ungerade* for even and odd.

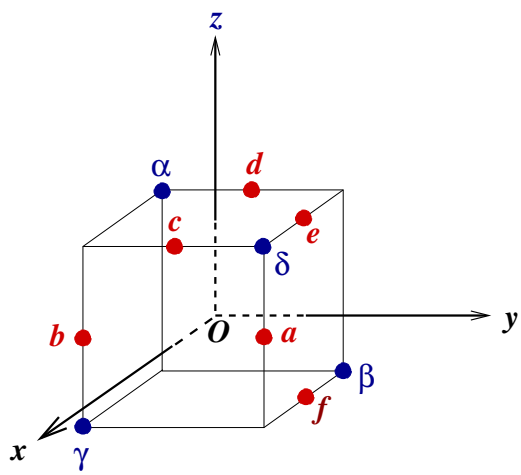

Figure 3.4: The rotation axes corresponding to the group elements C_{nj} of O. Figure from Ref. [109].

by introducing a new generator, denoted by $\overline{E}$, which represents a rotation by 2π about any axis. This doubles the number of group elements since, for each element G of the original group O, there is an extra element $\overline{G} = \overline{E}G$. Hence, O^D now has 48 group elements, in eight conjugacy classes, yielding three extra irreps which we label G_1, G_2, H, with dimension $2, 2, 4$ respectively. These single-valued representations of O^D then include both the single- and double-valued representations we need of the original group O. When we include parity, we consider the double point group $O_h^D = O^D \otimes \{E, I_s\}$, which has 96 elements, and six extra irreps:

$$G_{1g/u}, G_{2g/u}, H_{g/u}, \tag{3.39}$$

where we use the notation of ref [112]. For a good reference discussing the properties of these crystallographic space groups, see Ref. [113]. We refer to table XI of Ref. [109] for our choices for the representation matrices of the single- and double-valued irreps.

Ultimately, since we are interested in infinite-volume, continuum physics, the obvious question one asks is, which J irreps of the $SO(3)$ continuous group of rotations map into which irreps of O? Since O is a subgroup of $SO(3)$, we can answer this by looking at the *subduction* of the $SO(3)$ irreps onto the irreps of O. The number of times n_Γ^J that the irrep Γ of O appears in the reducible subduction of the J irrep of $SO(3)$ is given by

$$n_\Gamma^J = \frac{1}{g_O} \sum_p N_p \chi_{\downarrow O}^J(\mathcal{C}_p) \chi^\Gamma(\mathcal{C}_p)^*, \tag{3.40}$$

where g_O is the order of the group O, the sum is over the classes $\mathcal{C}_p$ of the group, N_p is the number of elements in class p, $\chi_{\downarrow O}^J$ is the character vector for the J irrep of $SO(3)$ subduced to O, and χ^Γ is the character vector for the irrep Γ of O. The same procedure, changing $O \to O^D$ and $SO(3) \to SU(2)$, is used for the half-integer J representations of $SU(2)$ subduced to O^D, with the results for all $J < 8$ shown in table 3.3.

Table 3.3: The number of times, n_Γ^J, that the irrep Γ of O occurs in the reducible subduction of the J irrep of $SO(3)/SU(2)$ for $J < 8$.

J	$n_{A_1}^J$	$n_{A_2}^J$	n_E^J	$n_{T_1}^J$	$n_{T_2}^J$
0	1	0	0	0	0
1	0	0	0	1	0
2	0	0	1	0	1
3	0	1	0	1	1
4	1	0	1	1	1
5	0	0	1	2	1
6	1	1	1	1	2
7	0	1	1	2	2

J	$n_{G_1}^J$	$n_{G_2}^J$	n_H^J
$\frac{1}{2}$	1	0	0
$\frac{3}{2}$	0	0	1
$\frac{5}{2}$	0	1	1
$\frac{7}{2}$	1	1	1
$\frac{9}{2}$	1	0	2
$\frac{11}{2}$	1	1	2
$\frac{13}{2}$	1	2	2
$\frac{15}{2}$	1	1	3

3.4.2 Moving Frames

For operators with non-zero momentum $\boldsymbol{p}$, the symmetry group we must consider is the little group of rotations that leaves $\boldsymbol{p}$ invariant. To simplify matters, we only consider three classes of momenta: on-axis $\boldsymbol{p}_{\text{oa}} = (0, 0, \pm n)$; planar-diagonal $\boldsymbol{p}_{\text{pd}} = (0, \pm n, \pm n)$; and cubic-diagonal $\boldsymbol{p}_{\text{cd}} = (\pm n, \pm n, \pm n)$ momentum directions. The three little groups we must consider then are: C_{4v} for on-axis momenta, C_{2v} for planar-diagonal momenta, and C_{3v} for cubic-diagonal momenta. Again, conjugacy classes and representation matrices for these little groups are given in Ref. [109].

When designing an operator to create/annihilate a particular particle state of interest, particle identification at-rest is reasonably straightforward using table 3.3 along with the other (flavour, etc.) relevant quantum numbers. For creating states with non-zero momentum however, the identification for each little group irrep is not quite as straightforward. We can make this identification easier for moving frames by considering the subductions of the O_h^D irreps onto the little group in question. These subductions are listed in table 3.4.

3.4.3 Projection onto Symmetry Groups

We will now outline the procedure that we use for obtaining a set of linearly independent operators that transform according to a particular symmetry channel. This essentially amounts to computing the coefficients in eqs. (3.25) and (3.29), following the procedure detailed in [108]. The key part of this process involves projecting a set of operators with given quantum numbers, which initially transform reducibly under the little group, to a set of operators that transform irreducibly under that little group. The key formula for projecting an operator $\mathcal{O}_i^F$, where F denotes all other relevant

Table 3.4: The subductions of the single- and double-valued irreps of O_h^D onto the irreps of the little groups C_{4v}, C_{3v}, and C_{2v}. Table from Ref. [109].

$\Lambda(O_h)$	$\downarrow C_{4v}$	$\downarrow C_{3v}$	$\downarrow C_{2v}$
A_{1g}	A_1	A_1	A_1
A_{1u}	A_2	A_2	A_2
A_{2g}	B_1	A_2	B_2
A_{2u}	B_2	A_1	B_1
E_g	$A_1 \oplus B_1$	E	$A_1 \oplus B_2$
E_u	$A_2 \oplus B_2$	E	$A_2 \oplus B_1$
T_{1g}	$A_2 \oplus E$	$A_2 \oplus E$	$A_2 \oplus B_1 \oplus B_2$
T_{1u}	$A_1 \oplus E$	$A_1 \oplus E$	$A_1 \oplus B_1 \oplus B_2$
T_{2g}	$B_2 \oplus E$	$A_1 \oplus E$	$A_1 \oplus A_2 \oplus B_1$
T_{2u}	$B_1 \oplus E$	$A_2 \oplus E$	$A_1 \oplus A_2 \oplus B_2$
$G_{1g/u}$	G_1	G	G
$G_{2g/u}$	G_2	G	G
$H_{g/u}$	$G_1 \oplus G_2$	$F_1 \oplus F_2 \oplus G$	$2G$

quantum numbers, to row λ of the irrep Λ of the little group $\mathcal{G}$ is

$$\mathcal{O}_{Pi}^{\Lambda\lambda F}(t) = \frac{d_\Lambda}{g_\mathcal{G}} \sum_{R\in\mathcal{G}} \Gamma_{\lambda\mu}^{(\Lambda)}(R) U_R \, \mathcal{O}_i^F(t) U_R^\dagger, \tag{3.41}$$

where R denotes the elements of $\mathcal{G}$, d_Λ is the dimension of the Λ representation, $g_\mathcal{G}$ is the order of $\mathcal{G}$, U_R is the operator which effects the symmetry transformation corresponding to group element R, $\Gamma_{ij}^{(\Lambda)}(R)$ is a Λ unitary representation matrix for element R, and the subscript P specifies that the operator has been projected onto the Λ irrep. Where relevant, projections for definite G-parity can also be done. Note that the choice of index μ on $\Gamma_{\lambda\mu}^{(\Lambda)}$ is somewhat arbitrary, so we choose $\mu = \lambda$ such that the projection itself remains idempotent (i.e. $P^2 = P$). This can be seen by applying the projection formula twice, observing that for $\mu \neq \lambda$ the operator will vanish. It is also straightforward to convince ourselves that the projected operators do in fact transform as desired

by transforming such a projected operator by a group element $G \in \mathcal{G}$:

$$
\begin{aligned}
U_G\, \mathcal{O}_{Pi}^{\Lambda\lambda F}(t)\, U_G^\dagger &= \frac{d_\Lambda}{g_\mathcal{G}} \sum_{R\in\mathcal{G}} \Gamma^{(\Lambda)}_{\lambda\mu}(R) U_G U_R\, \mathcal{O}_i^F(t) U_R^\dagger U_G^\dagger \\
&= \frac{d_\Lambda}{g_\mathcal{G}} \sum_{GR\in\mathcal{G}} \Gamma^{(\Lambda)}_{\lambda\mu}(G^{-1}GR) U_{GR}\, \mathcal{O}_i^F(t) U_{GR}^\dagger \\
&= \frac{d_\Lambda}{g_\mathcal{G}} \sum_{R\in\mathcal{G}} \Gamma^{(\Lambda)}_{\lambda\mu}(G^{-1}R) U_R\, \mathcal{O}_i^F(t) U_R^\dagger \\
&= \frac{d_\Lambda}{g_\mathcal{G}} \sum_{\lambda'} \sum_{R\in\mathcal{G}} \Gamma^{(\Lambda)}_{\lambda\lambda'}(G^{-1}) \Gamma^{(\Lambda)}_{\lambda'\mu}(R) U_R\, \mathcal{O}_i^F(t) U_R^\dagger \\
&= \sum_{\lambda'} \Gamma^{(\Lambda)}_{\lambda\lambda'}(G^{-1})\, \mathcal{O}_{Pi}^{\Lambda\lambda' F}(t) \\
&= \sum_{\lambda'} \mathcal{O}_{Pi}^{\Lambda\lambda' F}(t)\, \Gamma^{(\Lambda)}_{\lambda'\lambda}(G)^*,
\end{aligned}
\tag{3.42}
$$

showing that the projected operators $\mathcal{O}_{Pi}^{\Lambda\lambda F}(t)$ do in fact transform appropriately according to the irreps of the little group $\mathcal{G}$.

Since eq. (3.41) does not uniquely fix the normalisations and overall phase factors for a given operator, and where a given irrep occurs more than once in the basis set of operators $\{\mathcal{O}_i^F\}$, it does not uniquely specify relative weights, we cannot use this formula to construct operators for *all* rows of a given irrep Λ. Instead, we construct operators for only one of the rows, then construct partner operators for the remaining irrep rows, μ, using the transfer operation

$$
\mathcal{O}_{Pi}^{\Lambda\mu F}(t) = \frac{d_\Lambda}{g_\mathcal{G}} \sum_{R\in\mathcal{G}} \Gamma^{(\Lambda)}_{\mu\lambda}(R) U_R\, \mathcal{O}_{Pi}^{\Lambda\lambda F}(t) U_R^\dagger. \tag{3.43}
$$

In the absence of any external applied fields, the stationary state energies should not depend on the row λ of a given irrep Λ (cf. Zeeman effect: splitting of m_j degenerate energy levels of the hydrogen atom in a static magnetic field). Using eq. (3.36) and the particular representation matrices $\Gamma^{(\Lambda)}$ chosen in Ref. [109], it can be shown that our correlation matrices satisfy

$$
C_{ij}^{\Lambda\lambda F}(t) = C_{ij}^{\Lambda\mu F}(t), \tag{3.44}
$$

for all irrep rows λ, μ. Therefore, we have an economic way to increase statistics on each gauge configuration by averaging correlation functions over irrep row. Finally, the numerical implementation of the above ideas for determining the coefficients in eqs. (3.25) and (3.29) using software written in `Maple` is detailed explicitly in section V of Ref. [108].

3.5 Multi-Hadron Operators

As the majority of hadron resonant states we wish to study will lie above two-particle thresholds, it is crucial to include two-hadron operators in our basis. Since we find only stationary states in

finite-volume with periodic boundary conditions, many of the low-lying states can be what we refer to as mixed states (i.e. linear combinations of single- and two-particle states). Additionally, when we wish to study infinite-volume hadron-hadron scattering using the formalism described in chapter 6, it is vital that we include the finite-volume energies corresponding to two-particle stationary states. The construction of multi-particle operators involves the same procedure as the single-hadron operators, except the basic building blocks are now single-hadron operators rather than the elemental three-quark and quark-antiquark operators for the baryons and mesons. These two-hadron basis operators take the form

$$\mathcal{O}^{I_a I_{3a} S_a}_{\boldsymbol{p}_a \Lambda_a \lambda_a i_a} \mathcal{O}^{I_b I_{3b} S_b}_{\boldsymbol{p}_b \Lambda_b \lambda_b i_b}, \tag{3.45}$$

where a and b distinguish between the two constituent hadrons, and i consists of all other relevant labels (e.g. displacement type and index). The process for constructing the final two-hadron operators then proceeds using the same methods as we used for the single-hadrons. First, appropriate linear combinations of these building blocks are found that transform irreducibly under isospin using eqs. (3.18) and (3.19), then the group theoretical projections described in section 3.4.3 are used to ensure that the two-hadron operators transform irreducibly under a given irrep of the little group of $\boldsymbol{p} = \boldsymbol{p}_a + \boldsymbol{p}_b$, along with a projection for definite G-parity where appropriate.

Local Two-Hadron Operators

A key feature of our two-hadron operators is the need for all-to-all quark propagators (quark propagators from all spatial lattice sites to all other spatial lattice sites) in the calculation of correlation functions. This is due the loss of the ability to use translational invariance to remove a sum over the spatial lattice sites. This is in contrast to the so-called "local" two-hadron operators in which both constituent hadrons individually do not have definite momentum but are instead located together at a single lattice site. For local two-hadron operators, we could take advantage of translational invariance and use the significantly cheaper point-to-all quark propagators (quark propagators from a single site to all other spatial lattice sites). This presents some practical issues as, for example in section V and fig. 4 of Ref. [109], the excited state contamination we wish to avoid is seen to be much more severe in the local two-hadron operators compared to our operators with definite constituent momenta. Additionally, for many of our calculations, the use of all-to-all quark propagation is completely unavoidable (e.g. isoscalar mesons), and so we are doubly incentivised to seek out computational techniques that facilitate the efficient computation of all-to-all quark propagation. Thankfully then, we are able to use the stochastic LapH method (described in chapter 4), which provides a very efficient way to include all-to-all quark propagators, and therefore multi-particle operators with definite constituent momenta.

3.6 Exotic Operators

So far, we have only considered gauge invariant objects comprised of a covariantly displaced quark and antiquark, known as mesons, and three covariantly displaced quarks, known as baryons. However, there is no reason for there not to exist gauge invariant states containing greater numbers of valence (anti)quarks, or even, gauge invariant combinations of gluon fields and no valence (anti)quarks. Here, we will very briefly discuss the operators we use to study two types of these exotic objects, for both of which there exist multiple experimental candidates.

3.6.1 Tetraquarks

After discussing meson and baryon states, with two and three valence (anti)quarks respectively, it is natural to then consider what sort of gauge invariant combinations we can form using four (anti)quarks. Consider then combining four $SU(3)$ colour vectors together; the various Clebsch-Gordan series are

$$\mathbf{3} \otimes \mathbf{3} \otimes \mathbf{3} \otimes \mathbf{3} = \mathbf{3} \oplus \mathbf{3} \oplus \mathbf{3} \oplus \overline{\mathbf{6}} \oplus \overline{\mathbf{6}} \oplus \mathbf{15} \oplus \mathbf{15} \oplus \mathbf{15} \oplus \mathbf{15}, \tag{3.46a}$$

$$\mathbf{3} \otimes \mathbf{3} \otimes \mathbf{3} \otimes \overline{\mathbf{3}} = \overline{\mathbf{3}} \oplus \overline{\mathbf{3}} \oplus \overline{\mathbf{3}} \oplus \mathbf{6} \oplus \mathbf{6} \oplus \mathbf{6} \oplus \overline{\mathbf{15}} \oplus \overline{\mathbf{15}} \oplus \mathbf{24}, \tag{3.46b}$$

$$\mathbf{3} \otimes \mathbf{3} \otimes \overline{\mathbf{3}} \otimes \overline{\mathbf{3}} = \mathbf{1} \oplus \mathbf{1} \oplus \mathbf{8} \oplus \mathbf{8} \oplus \mathbf{8} \oplus \mathbf{8} \oplus \mathbf{10} \oplus \overline{\mathbf{10}} \oplus \mathbf{27}. \tag{3.46c}$$

The only way to form a gauge invariant object ($\mathbf{1}$ colour vector) out of four colour vectors then is with two $\mathbf{3}$ vectors and two $\overline{\mathbf{3}}$ vectors, i.e. with two quarks ($\mathbf{3}$ representation) and two antiquarks ($\overline{\mathbf{3}}$ representation). For colour vectors p, q, r, s in the fundamental $\mathbf{3}$ representation, p^*, q^*, r^*, s^* will transform in the $\overline{\mathbf{3}}$ representation. It is straightforward to show then that the following two linear combinations of these colour vectors are gauge invariant:

$$T_S = (\delta_{ac}\delta_{bd} + \delta_{ad}\delta_{bc}) p^*_a(x) q^*_b(x) r_c(x) s_d(x), \tag{3.47a}$$

$$T_A = (\delta_{ac}\delta_{bd} - \delta_{ad}\delta_{bc}) p^*_a(x) q^*_b(x) r_c(x) s_d(x). \tag{3.47b}$$

Since these are linearly independent, we have exhausted the gauge invariant combinations of two quarks and two antiquarks. Note that these differ slightly from the meson-meson operators described in section 3.5 as the individual gauge invariant quark-antiquark objects in eq. (3.47) are not required to transform irreducibly under any symmetry transformation other than gauge symmetry. We will of course project the final operators to transform irreducibly under all appropriate symmetry groups. The elemental tetraquark operators (including displacements) we consider then are

$$\Phi^{ABCD\pm}_{\alpha\beta\mu\nu;ijkl}(\boldsymbol{p}, t) = \sum_{\boldsymbol{x}} e^{-i\boldsymbol{p}\cdot\boldsymbol{x}} (\delta_{ab}\delta_{cd} \pm \delta_{ad}\delta_{bc})\, \overline{q}^A_{a\alpha i}(\boldsymbol{x}, t)\, q^B_{b\beta j}(\boldsymbol{x}, t)\, \overline{q}^C_{c\mu k}(\boldsymbol{x}, t)\, q^D_{d\nu l}(\boldsymbol{x}, t), \tag{3.48a}$$

$$\overline{\Phi}^{ABCD\pm}_{\alpha\beta\mu\nu;ijkl}(\boldsymbol{p}, t) = \sum_{\boldsymbol{x}} e^{i\boldsymbol{p}\cdot\boldsymbol{x}} (\delta_{ab}\delta_{cd} \pm \delta_{ad}\delta_{bc})\, \overline{q}^D_{d\nu l}(\boldsymbol{x}, t)\, q^C_{c\mu k}(\boldsymbol{x}, t)\, \overline{q}^B_{b\beta j}(\boldsymbol{x}, t)\, q^A_{a\alpha i}(\boldsymbol{x}, t), \tag{3.48b}$$

with the displacement types we include shown in fig. 3.5. At the time of writing, calculations in which we include these operators in the light, scalar meson sectors in search of "missing" tetraquark dominated levels are underway and will appear in an upcoming publication [114].

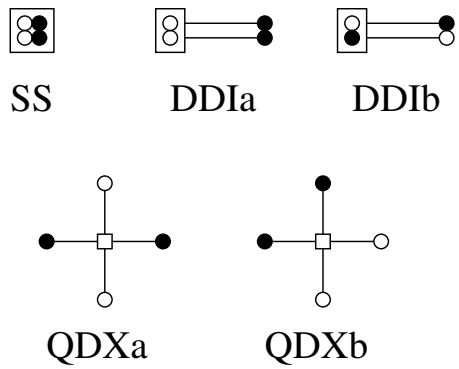

Figure 3.5: The tetraquark operator displacements we plan to use, consisting of two gauge-covariantly displaced quarks (open circles) and two displaced antiquarks (solid circles). Hollow boxes denote colour couplings of the form $\delta_{ab}\delta_{cd} \pm \delta_{ad}\delta_{bc}$.

3.6.2 Glueballs

The gluon self-coupling in QCD suggests the existence of glueballs, states which consist primarily of bound gluons, having no valence quarks. Experimental evidence for such states is sparse and ambiguous, with many candidate states significantly mixing with and difficult to distinguish from hadronic resonances and hadron-hadron scattering states. These issues will be discussed further in chapter 7, where we motivate the need for lattice studies of glueball candidates and present the first study of the light scalar glueball including the mixing with meson and meson-meson states using fully dynamical quarks. Here we will discuss the gluonic operators that are used to probe glueball states non-perturbatively in lattice QCD, including our construction of a scalar glueball operator used in the aforementioned analysis in chapter 7.

As objects consisting solely of bound gluons, glueball operators are usually constructed using sums of gauge invariant loops of smeared spatial gauge link variables on a single time slice (i.e. the Wilson loops defined in eq. (2.47)), which are invariant under translations, rotations, and charge conjugation. See for example, Ref. [80], where various closed-loop operators are constructed to transform irreducibly under different representations of O_h to study various glueball states in $SU(3)$ pure gauge theory. However, presumably any purely gluonic quantity with the same symmetry properties could be used to probe potential glueball states. For example, the eigenvalues of the gauge covariant spatial Laplacian $\widetilde{\Delta}$ are invariant under rotations and gauge transformations, and so, are seemingly appropriate for a scalar glueball operator. As the LapH quark-field smearing that we use involves $\widetilde{\Delta}$, a scalar glueball operator constructed from its eigenvalues is a natural choice for us to use. This idea was proposed in section VI of Ref. [109] where it was found that essentially any combination of the low-lying eigenvalues worked well for studying the scalar glueball. Two such operators were considered, the so-called TrLapH operator:

$$G_\Delta = -\operatorname{Tr}[\Theta(\sigma_s^2 + \widetilde{\Delta})\widetilde{\Delta}], \tag{3.49}$$

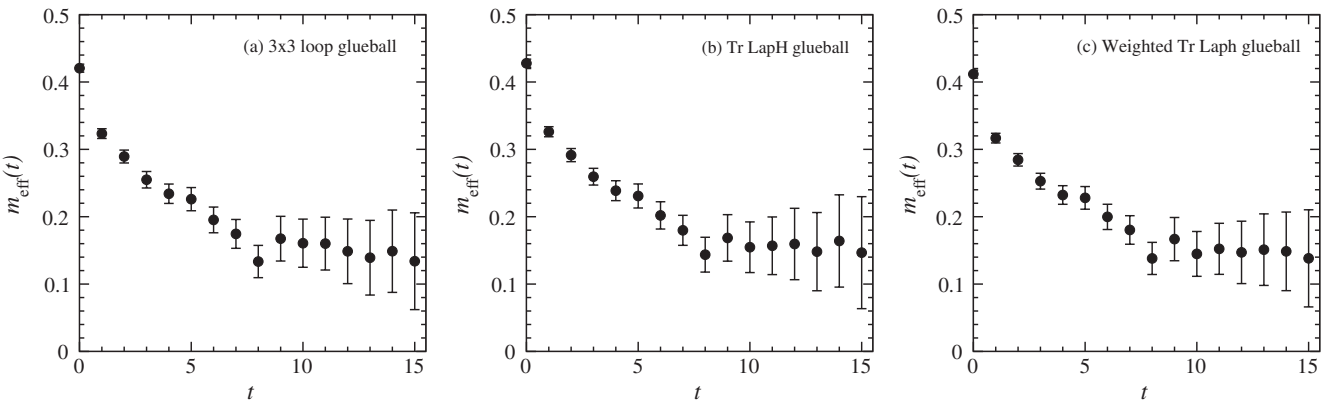

Figure 3.6: Comparison of the effective masses, $m_{\rm eff}(t)$ using $\Delta t = 3$, for three different scalar glueball operators on the $(24^3|390)$ ensemble described in chapter 7. (a) The leftmost plot shows the effective mass using an operator defined by a sum of 3×3 Wilson loops of smeared gauge link variables that is rotationally and translationally invariant. (b) The middle plot uses the TrLapH glueball operator G_Δ, defined in eq. (3.49). (c) The rightmost plot shows the results using the weighted TrLapH glueball operator G_W, defined in eq. (3.50). One observes very little difference between these plots, suggesting that these operators are comparable in usefulness for studying the scalar glueball. Each effective mass eventually tends toward the energy of two pions at rest, demonstrating non-negligible coupling of these operators to $\pi\pi$ states. Figure from Ref. [109].

and the so-called weighted TrLapH operator

$$G_W = -\operatorname{Tr}[\Theta(\sigma_s^2 + \widetilde{\Delta})\widetilde{\Delta}\,\exp(-W\widetilde{\Delta}^2)], \tag{3.50}$$

where W is a weighting factor used so that only a certain number of the low-lying eigenvalues contribute. Using $W = 64$ for the weighted operator, the effective mass for both of these operators were obtained on the same $24^3 \times 128$ ensemble we use in chapter 7, and compared to that obtained using a standard glueball operator consisting of a sum of 3×3 Wilson loops. As is shown in fig. 3.6, there is very little difference between the three effective masses, suggesting the comparable usefulness of each for studying the scalar glueball. This motivates our use of the TrLapH operator (eq. (3.49)) for studying the scalar glueball and the mixing between glueball and meson-meson states in finite-volume. Since we calculate the low-lying eigenvalues of the covariant spatial Laplacian for smearing the quark fields, we obtain this operator without additional cost by computing the eigenvalues of $\widetilde{\Delta}$.

Chapter 4

Stochastic Estimation of Correlation Functions

Recall from section 2.4 that in order to extract the finite-volume spectrum of QCD (or any other theory) we need to calculate two-point temporal correlation functions. Such correlation functions are easily written in terms of Euclidean path integrals over quark fields and gauge link variables:

$$\langle \mathcal{O}_i(t+t_0)\overline{\mathcal{O}}_j(t_0)\rangle = \frac{1}{Z}\int \mathcal{D}[\chi,\psi]\mathcal{D}[U]\mathcal{O}_i(t+t_0)\overline{\mathcal{O}}_j(t_0)e^{-\chi\Omega[U]\psi-S_G[U]}, \tag{4.1}$$

where $\chi = \overline{\psi}\gamma_4$, $\Omega = \gamma_4 D$, and D is the Dirac matrix. As the action is quadratic in the quark fields, the Grassmann fields χ, ψ can be integrated exactly (see eq. (2.91)), resulting in the integration over gauge link variables that we describe in section 2.5, and some number of fermion propagators, which we describe in section 4.1. Calculating these propagators involves products of the inverse of the Dirac matrix Ω^{-1} which, as Ω is very large, are prohibitively expensive to perform exactly. Hence, for computing these matrix inversions, we use the stochastic LapH method [15], in which quark lines are estimated using diluted noise vectors in the so-called LapH subspace, defined in section 4.1.1. We will describe this method for matrix inversion in section 4.2, followed by the application to quark line estimates in section 4.3, defining the crucial quark source and sink functions. Then we close out the chapter by showing in section 4.4 how the temporal correlation functions we are ultimately interested in can be factorised into the quark source/sink functions which themselves are expressed in terms of stochastically estimated quark lines.

4.1 Quark Lines

While we will refer the reader to their favourite field theory textbook for more detail on the integration of Grassmann variables in the context of fermion integration, we recall here some illustrative results. For the Grassmann valued fields $\psi_a, \overline{\psi}_b$:

$$\int \mathcal{D}[\psi,\overline{\psi}]\,\psi_a\overline{\psi}_b \exp\left(\overline{\psi}^T D\psi\right) = D^{-1}_{ab}\det D, \tag{4.2}$$

where for Dirac matrix D, we can identify the Feynman propagator D^{-1}_{ab}. A typical meson correlation function then would look (schematically) like

$$\begin{aligned}\langle \psi_a \psi_b \overline{\psi}_c \overline{\psi}_d \rangle &= \int \mathcal{D}[\psi, \overline{\psi}]\, \psi_a \psi_b \overline{\psi}_c \overline{\psi}_d \exp\left(\overline{\psi}^T D \psi\right) \\ &= \left(D^{-1}_{ad} D^{-1}_{bc} - D^{-1}_{ac} D^{-1}_{bd}\right) \det D,\end{aligned} \tag{4.3}$$

where we have suppressed the integration over gauge fields (i.e. the above result holds for a single gauge configuration)[1]. Now, since we use (anti)quark fields that are both smeared and spatially displaced, we need integrals in the following form

$$\int \mathcal{D}[\chi, \psi] \sum_{cd} f_{ac} \psi_c \chi_d g_{db} \exp\left(-\chi^T \Omega \psi\right) = \sum_{cd} f_{ac} \Omega^{-1}_{cd} g_{db} \det \Omega, \tag{4.4}$$

where f_{ac} and g_{db} are c-number coefficients, and we have replaced $\overline{\psi}$ with χ in the interest of ensuring Hermiticity. For each coupling (i.e. Wick contraction) of a ψ and χ field, the integration over quark fields leads to a factor of Ω^{-1}. We will refer to each such coupling as a *quark line* which can be drawn as a directed line originating at the χ field, and terminating at the ψ field. We can then classify the three different types of such quark lines that appear in hadronic correlation functions by the relative time ordering of their beginning and end:

- *forward-time*: quark line starting (χ) at early time t_0 and ending (ψ) at later time t (i.e. $t_0 < t$),
- *backward-time*: quark line starting (χ) at later time t_0 and ending (ψ) at earlier time t (i.e. $t_0 > t$),
- *same-time*: quark line starting (χ) and ending (ψ) at the same time, either t or t_0 (i.e. $t_0 = t$).

These different types of quark lines are illustrated in fig. 4.1.

Let's now write the quark-antiquark contraction for a single quark line in eq. (4.4) more explicitly. Including the smearing and displacement of the two fields, and using a single compound index to denote colour, spin, flavour, space, and time a forward-time line looks like

$$(D_j)_{ab} \mathcal{S}_{bc} \Omega^{-1}_{ch} \mathcal{S}_{hg} (D^\dagger_k)_{gf} = \left(D_j \mathcal{S} \Omega^{-1} \mathcal{S} D^\dagger_k\right)_{af}, \tag{4.5}$$

which, for convenience we denote by $\mathcal{Q}$:

$$\mathcal{Q}_{jk}(t, t_0) = D_j \mathcal{S} \Omega^{-1}(t, t_0) \mathcal{S} D^\dagger_k. \tag{4.6}$$

An important integral where this appears then is

$$\int \mathcal{D}[\chi, \psi] \left(D_j \mathcal{S} \psi\right)_a (t) \left(\chi \mathcal{S} D^\dagger_k\right)_b (t_0) \exp\left(-\chi^T \Omega \psi\right) = \mathcal{Q}_{jk}(t, t_0)_{ab} \det \Omega. \tag{4.7}$$

[1]Recall that the fermion determinant $\det D$ is included in the Monte Carlo integration over the gauge fields, so we need not worry about it here.

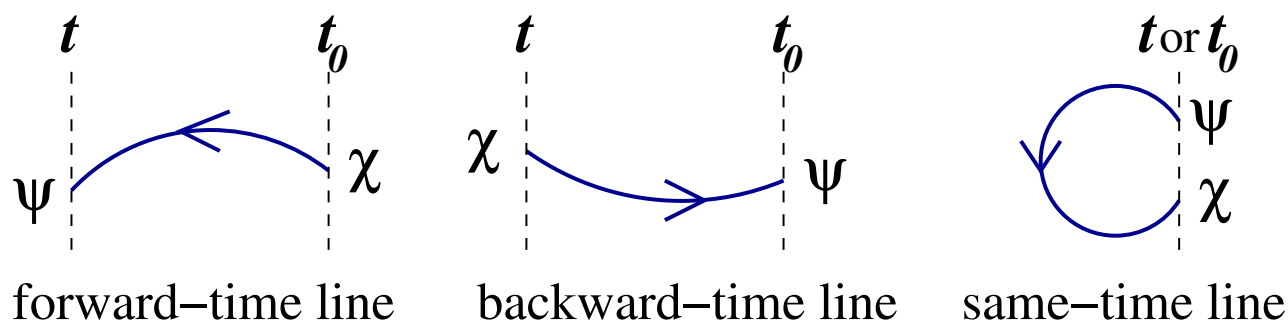

Figure 4.1: The three types of quark lines we must consider in the evaluation of hadronic temporal correlation functions. A quark line stares at an antiquark (χ) field and ends at a quark (ψ) field. In the above diagrams, time t_0 is assumed to be the early time (source) and t is the later time (sink), i.e. $t > t_0$.

Same-time quark lines occur when the two time indices are identical, i.e. $\mathcal{Q}_{jk}(t,t)$, and backward-time lines can be written as

$$\overline{\mathcal{Q}}_{jk}(t,t_0) = \left(\gamma_5\gamma_4\mathcal{Q}_{jk}(t,t_0)\gamma_4\gamma_5\right)^* . \tag{4.8}$$

Any given correlation function then can be decomposed into these quark lines, each of which contains computationally expensive Dirac matrix inverses Ω^{-1}.

Translational Invariance

Before moving on with our discussion, it is important here to stress the importance of efficient computational techniques for evaluating quark lines, in particular for same-time lines. Performing the necessary Dirac matrix inversions can be very computationally expensive, so many calculations are designed to avoid directly inverting the matrix by solving the linear system of equations $Dx = y$ for a practical number of source vectors y. Consider the temporal correlator for a single hadron operator at rest

$$\begin{aligned} C(t) &= \langle 0|\mathcal{O}(\boldsymbol{p}=0, t+t_0)\overline{\mathcal{O}}(\boldsymbol{p}=0,t_0)|0\rangle \\ &= \frac{1}{V^2}\sum_{\boldsymbol{x},\boldsymbol{y}}\frac{1}{N_{t_0}}\sum_{t_0}\langle 0|\phi(\boldsymbol{x},t+t_0)\overline{\phi}(\boldsymbol{y},t_0)|0\rangle. \end{aligned} \tag{4.9}$$

As written, the above correlator requires the evaluation of the quark propagator from all spatial sites $\boldsymbol{y}$ at $t=0$ to all spatial sites $\boldsymbol{x}$ at time t, a so-called *all-to-all* propagator. A drastic reduction in the number of inversions required can be achieved by exploiting translational invariance to remove one of the spatial sums. The correlator will then look like

$$C(t) = \frac{1}{V}\sum_{\boldsymbol{x}}\langle 0|\phi(\boldsymbol{x},t)\overline{\phi}(0,0)|0\rangle, \tag{4.10}$$

where we have assumed only one source time t_0 (more of course can be used to increase statistics). Now, the quark propagator from the origin at time $t=0$ to all spatial sites $\boldsymbol{x}$ at time t is required,

reducing the number of inversions (for a single t_0) by a factor of V. These are referred to as *point-to-all* propagators.

Consider however, the temporal correlator for an isoscalar meson operator. Such operators will require same-time quark lines (i.e. internal loops/disconnected diagrams) for contractions on a single time slice. While we can still use translation invariance to fix the source operator at the origin, the sink operator must be summed over all lattice sites. Hence, the same-time quark lines for all spatial sites at the sink time to the same site at the sink time must be calculated, a significant number of Dirac matrix inversions (essentially the diagonal elements of Ω^{-1}). Even if we restrict ourselves to the flavour non-singlet sectors however, our use of two-hadron operators with definite constituent momenta necessitates the evaluation of all-to-all quark propagators. A typical two-hadron operator of total momentum zero then has the form

$$\mathcal{O}_1(\boldsymbol{p},t)\mathcal{O}_2(-\boldsymbol{p},t) = \frac{1}{V^2}\sum_{\boldsymbol{x},\boldsymbol{y}} \phi_1(\boldsymbol{x},t)\phi_2(\boldsymbol{y},t)e^{-i\boldsymbol{p}\cdot(\boldsymbol{x}-\boldsymbol{y})}. \tag{4.11}$$

With operators of this form, it is impossible to use translation invariance to remove all summations over spatial sites on the source time slice, and so all-to-all time slice propagators must be used. Local multi-particle operators of the form

$$(\mathcal{O}_1\mathcal{O}_2)(\boldsymbol{p}=0,t) = \frac{1}{V}\sum_{\boldsymbol{x}} \phi_1(\boldsymbol{x},t)\phi_2(\boldsymbol{x},t), \tag{4.12}$$

circumvent this issue, allowing for the exploitation of translation invariance to remove all summations over all spatial sites on the source time slice, and hence the use of point-to-all propagators. However, as stated in section 3.5, the excited state contamination present in these local two-hadron operators is significantly more troublesome than in our operators with definite constituent momentum.

4.1.1 The LapH Subspace

Inverting the Dirac matrix exactly is impractical for all but very small lattices[2]. Recall however from section 3.1.2 that, since we are ultimately interested in the low-lying spectrum/modes of QCD, we smear the quark fields by projecting into the subspace containing only these low-lying modes, the so-called *LapH subspace*. The subspace is that spanned by the N_v lowest eigenvectors of the covariant Laplacian on each time slice, forming the columns of the matrix $V_d \otimes I_4^d$. Using eq. (3.14) for the smearing matrices, the Dirac matrix inverses in a quark line are replaced with

$$\mathcal{S}\Omega^{-1}\mathcal{S} = V_s\left(V_s^\dagger\Omega^{-1}V_s\right)V_s^\dagger, \tag{4.13}$$

where, for the ease of notation, factors of the identity in Dirac space I_4^d have been suppressed. The term in parenthesis, $V_s^\dagger\Omega^{-1}V_s$, is referred to as a *perambulator* [107], and describes quark

[2]The Dirac matrix is of rank $N_s^3 N_t N_d N_c$, where N_s is the spatial extent, N_t the temporal extent, N_d the number of Dirac spin indices (usually 4), and N_c is the number of colour indices (usually 3). Then, for a typical lattice used in this work, the N200 CLS ensemble ($N_s = 48$, $N_t = 128$) say, the Dirac matrix has size $\sim 10^8 \times 10^8$.

propagation in the LapH subspace. This matrix then is significantly smaller than Ω^{-1}, and so inverting it in the calculation of quark lines is significantly easier. To solve for the inverse exactly, now $N_v N_t N_d$ linear systems are required compared to $N_s^3 N_t N_d$ for Ω^{-1}. In Ref. [107] the so-called *distillation* method for evaluating these perambulators exactly was proposed, the feasibility of which clearly relies on the size of N_v, shown to grow proportional to the spatial volume of the lattice in Ref. [15]. This then motivates finding an alternative method for application to larger spatial volumes. Since we approximate the path integral over gauge fields using the Monte Carlo method, evaluating the quark lines exactly proves to be quite wasteful. We need only determine the quark lines to within the precision of the Monte Carlo estimates, i.e. within the gauge noise limit. Hence, we explore the use of stochastic methods for such matrix inversion in the following sections.

4.2 Stochastic Matrix Inversion

For a large, albeit sparse, $N \times N$ matrix Ω, calculating exactly the inverse is impractical. Typical Dirac matrices in modern lattice calculations can contain on the order of $\sim 10^{14} - 10^{18}$ elements, growing proportional to the lattice volume. Therefore, computing, and even just storing in memory, the inverse of Ω exactly is impractical. Any matrix inverse Ω^{-1} can be estimated stochastically by introducing a set of N_R random noise vectors $\eta^{(r)}$, and solving the linear system of equations $\Omega X^{(r)} = \eta^{(r)}$ for each $X^{(r)}$, to get $X^{(r)} = \Omega^{-1}\eta^{(r)}$. If the noise vectors are chosen such that their expected values are given by $E(\eta_i) = 0$, and $E(\eta_i \eta_j^*) = \delta_{ij}$, then the elements of the matrix inverse Ω_{ij}^{-1} are given by

$$\begin{aligned} E(X_i \eta_j^*) &= E\left(\sum_k \Omega_{ik}^{-1} \eta_k \eta_j^*\right) \\ &= \sum_k \Omega_{ik}^{-1} E(\eta_k \eta_j^*) \\ &= \sum_k \Omega_{ik}^{-1} \delta_{kj} \\ &= \Omega_{ij}^{-1}. \end{aligned} \tag{4.14}$$

We can then find a Monte Carlo estimate of Ω_{ij}^{-1} using

$$\Omega_{ij}^{-1} \approx \lim_{N_R \to \infty} \frac{1}{N_R} \sum_{r=1}^{N_R} X_i^{(r)} \eta_j^{(r)*}. \tag{4.15}$$

However, this approximation only becomes exact in the limit $N_R \to \infty$, yet the linear system can be solved exactly using point sources with only N solution vectors. Therefore, we require a modification of this stochastic method to produce estimates of the quark propagators with drastically reduced variances.

We can significantly reduce the variance in the above estimate by projecting the noise vectors into distinct subspaces in a process known as noise *dilution* [115–117]. A given dilution scheme

proceeds as follows: for a complete set of projection operators $P^{(b)}$, define $\eta^{r[b]} = P^{(b)}\eta^r$, and $X^{r[b]}$ as the solution of $\Omega X^{r[b]} = \eta^{r[b]}$. Then, a much better Monte Carlo estimate of the matrix inverse Ω^{-1}_{ij} is given by

$$\Omega^{-1}_{ij} \approx \frac{1}{N_R}\sum_{r=1}^{N_R}\sum_b X_i^{r[b]}\eta_j^{r[b]*}. \tag{4.16}$$

The projection ensures exact zeros for many of the $E(\eta_i\eta_j^*)$ elements rather than estimates that are only statistically zero. This results in the dramatic reduction in the variance in the estimates of Ω^{-1}. Fully diluting the noise vectors should completely eliminate the variance in the matrix inverse estimate; this corresponding to the set of projectors $P^{(r)}_{ij} = \delta_{ir}\delta_{jr}$, which when applied to the noise vectors will return a set of basis vectors, i.e. an exact inversion scheme. A smaller set of projectors then allows for a reduction in computation time in exchange for increasing the variance in the estimates of Ω^{-1}. Different dilution schemes that we consider will be discussed shortly.

We can achieve a significant cost reduction by considering a smaller subspace in which to perform the dilution [15], i.e. we do not necessarily need to dilute the noise vectors in the full spin-colour-space-time vector space. Our use of LapH smeared quark fields suggests an alternative: noise vectors ρ that are introduced only in the LapH subspace, having only spin, time, and Laplacian eigenmode number as their indices, the last of which replaces the spatial and colour indices, found after diagonalising $\widetilde{\Delta}$. The dilution projectors $P^{(b)}$ are then matrices in the LapH subspace.

4.2.1 Dilution Schemes

The dilution projectors we use are products of time, spin, and LapH eigenvector dilution projectors. The compound projector index can then be written as the triplet $b = (b_T, b_S, b_L)$ of projector indices for time, spin, and LapH eigenvector. More explicitly, the projectors have the form

$$P^{(b)}_{t\alpha n;t'\alpha' n'} = P^{(b_T)}_{t;t'}P^{(b_S)}_{\alpha;\alpha'}P^{(b_L)}_{n;n'}, \tag{4.17}$$

where t, t' denote time slices, α, α' are Dirac spin incides, and n, n' are LapH eigenvector indices. The dilution schemes considered then are [15]:

$$P^{(b)}_{ij} = \delta_{ij}, \qquad b = 0, \qquad \text{(no dilution)} \tag{4.18a}$$

$$P^{(b)}_{ij} = \delta_{ij}\delta_{bi}, \qquad b = 0, \ldots, N-1, \qquad \text{(full dilution)} \tag{4.18b}$$

$$P^{(b)}_{ij} = \delta_{ij}\delta_{b,\lfloor Ji/N\rfloor}, \qquad b = 0, \ldots, J-1, \qquad \text{(block}-J\text{)} \tag{4.18c}$$

$$P^{(b)}_{ij} = \delta_{ij}\delta_{b,i \bmod J}, \qquad b = 0, \ldots, J-1, \qquad \text{(interlace}-J\text{)} \tag{4.18d}$$

where $N = N_t$ for time dilution, $N = N_d = 4$ for spin dilution, and $N = N_v$ for LapH eigenvector dilution, and N/J is assumed to be an integer. Explicit comparisons between the different schemes are studied in Ref. [15] on 16^3 and 20^3 lattices. We will often use the shorthand triplet (T,S,L) to denote a particular choice of dilution schemes, e.g. full time and spin dilution with interlace-16 LapH eigenvector dilution would be denoted by (TF,SF,LI16).

4.3 Stochastic Estimates of Quark Lines

Let's now collate these ideas and look at the factorisation of the all-important quark lines into distinct source and sink functions. In the stochastic LapH method, a quark line is evaluated on each gauge configuration by inserting the noise vectors described in the previous section as follows:

$$\begin{aligned}\mathcal{Q} &= D_j \mathcal{S}\Omega^{-1}\mathcal{S}D_k^\dagger \\ &= D_j \mathcal{S}\Omega^{-1}V_s V_s^\dagger D_k^\dagger \\ &= \sum_b D_j \mathcal{S}\Omega^{-1}V_s P^{(b)}P^{(b)\dagger}V_s^\dagger D_k^\dagger \\ &= \sum_b D_j \mathcal{S}\Omega^{-1}V_s P^{(b)}E(\rho\rho^\dagger)P^{(b)\dagger}V_s^\dagger D_k^\dagger \\ &= \sum_b E\left(D_j \mathcal{S}\Omega^{-1}V_s P^{(b)}\rho\left(D_k V_s P^{(b)}\rho\right)^\dagger\right).\end{aligned} \tag{4.19}$$

We define then the all-important displaced-smeared-diluted quark source and sink vectors by

$$\varrho^{[b]}(\rho) \equiv D_j V_s P^{(b)}\rho, \tag{4.20a}$$

$$\varphi^{[b]}(\rho) \equiv D_j \mathcal{S}\Omega^{-1}V_s P^{(b)}\rho, \tag{4.20b}$$

so that each quark line on a given gauge configuration can be estimated using

$$\mathcal{Q}_{uv}^{AB} \approx \frac{1}{N_R}\delta_{AB}\sum_{r=1}^{N_R}\sum_b \varphi_u^{[b]}(\rho^r)\varrho_v^{[b]}(\rho^r)^*, \tag{4.21}$$

where u, v are compound indices including space, time, colour, spin, and displacement type, B is the flavour of the source field, and A is the flavour of the sink field. As an aside, note that the above estimate takes the form of an outer product expansion. Similar estimates are often used in the processing/compression of digital images [118, 119], and so, the stochastic LapH estimate can be viewed as a lossy compression of the quark propagation [15].

When computing some quark lines needed for meson operators, it can sometimes be useful to exploit the γ_5-Hermiticity of the Dirac matrix. Recall from section 2.1.1 that $D^\dagger = \gamma_5 D\gamma_5$, and hence $(D^{-1})^\dagger = \gamma_5 D^{-1}\gamma_5$, so that the quark lines can also be estimated by

$$\mathcal{Q}_{uv}^{AB} \approx \frac{1}{N_R}\delta_{AB}\sum_{r=1}^{N_R}\sum_b \bar{\varrho}_u^{[b]}(\rho^r)\bar{\varphi}_v^{[b]}(\rho^r)^*, \tag{4.22}$$

where

$$\bar{\varrho} \equiv -\gamma_5\gamma_4\varrho, \qquad \bar{\varphi} \equiv \gamma_5\gamma_4\varphi. \tag{4.23}$$

This allows us to swap the quark source and sink by reversing a given quark line in what we call γ_5-*Hermiticity* mode. To see how this can be useful, first recall that we will need to calculate quark line estimates for same time (sink-to-sink and source-to-source) lines on (essentially) every time

slice (we sometimes refer to these as relative quark lines), requiring some temporal dilution to make the calculation feasible. On the other hand, many of the quark lines we need to estimate are from a source time t_0 to a different sink time t, and so we can use instead a smaller, manageable set of source times (we refer to these as slice-to-slice or fixed quark lines), and so we can use full time dilution for these. However, for a typical meson correlator for example, consider the contractions shown on the left in fig. 4.3. One of the quark lines needed begins on the meson source time and ends on the meson sink time, while the other line begins on the meson sink time and ends on the meson source time. Since we want only a manageable set of source times for our quark lines using the γ_5-Hermiticity mode formula above to swap the quark source and sink allows us to group all of the quark sinks at the meson sink time, and all of the quark sources at the meson source time, simplifying the computation and storage requirements.

4.4 Correlation Function Factorisation

We are now able to show how the quark source and sink functions can be used to evaluate hadronic temporal correlation functions via the stochastic LapH method. Following Ref. [15], here we will describe baryon-to-baryon, and meson-to-meson correlations in some detail, along with a brief discussion on how we generalise the procedure to more complicated correlations involving multiple hadrons at the source and/or sink times.

4.4.1 Baryon-to-Baryon Correlations

Recall from section 3.2.2 that our baryon source and sink operators are linear combinations of three-quark elemental operators of the form

$$\overline{B}_l(t) = c^{(l)*}_{\alpha\beta\gamma}\overline{\Phi}^{ABC}_{\alpha\beta\gamma}(\boldsymbol{p},t), \tag{4.24a}$$

$$B_l(t) = c^{(l)}_{\alpha\beta\gamma}\Phi^{ABC}_{\alpha\beta\gamma}(\boldsymbol{p},t), \tag{4.24b}$$

where l is a compound index including the baryon three-momentum $\boldsymbol{p}$, transformation under an irrep Λ of the lattice symmetry group, irrep row λ, any relevant flavour quantum numbers (e.g. isospin, G-parity, etc.), and an identifier labelling the different operators in each symmetry channel; and the elemental operators $\Phi, \overline{\Phi}$, are defined in eqs. (3.23) and (3.24). Temporal correlation matrix elements are then given by

$$\begin{aligned} C_{l\bar{l}}(t_F - t_0) &= \frac{1}{N_t}\sum_{t_0}\langle B_l(t_F)\overline{B}_{\bar{l}}(t_0)\rangle \\ &= c^{(l)}_{\alpha\beta\gamma}c^{(\bar{l})*}_{\bar{\alpha}\bar{\beta}\bar{\gamma}}\langle\Phi^{ABC}_{\alpha\beta\gamma}(t_F)\overline{\Phi}^{\bar{A}\bar{B}\bar{C}}_{\bar{\alpha}\bar{\beta}\bar{\gamma}}(t_0)\rangle \\ &= c^{(l)}_{\alpha\beta\gamma}c^{(\bar{l})*}_{\bar{\alpha}\bar{\beta}\bar{\gamma}}\sum_{\boldsymbol{x}\bar{\boldsymbol{x}}}\varepsilon_{abc}\varepsilon_{\bar{a}\bar{b}\bar{c}}\, e^{-i\boldsymbol{p}\cdot(\boldsymbol{x}-\bar{\boldsymbol{x}})} \\ &\qquad \times \langle q^A_{a\alpha}(\boldsymbol{x},t_F)q^B_{b\beta}(\boldsymbol{x},t_F)q^C_{c\gamma}(\boldsymbol{x},t_F)\,\overline{q}^{\bar{A}}_{\bar{a}\bar{\alpha}}(\boldsymbol{x},t_0)\overline{q}^{\bar{B}}_{\bar{b}\bar{\beta}}(\boldsymbol{x},t_0)\overline{q}^{\bar{C}}_{\bar{c}\bar{\gamma}}(\boldsymbol{x},t_0)\rangle, \end{aligned} \tag{4.25}$$

where $\langle \dots \rangle$ denotes the vacuum expectation value, and in the second line we have replaced the sum over source times by a single source time t_0 to simplify notation (we of course still compute the correlation functions for multiple source times to increase statistics), and have exploited time translation invariance. Evaluating the integration over quark fields then yields the rather unwieldy sum over products of quark lines:

$$\begin{aligned} C_{l\bar{l}}(t) = c^{(l)}_{\alpha\beta\gamma} c^{(\bar{l})*}_{\bar{\alpha}\bar{\beta}\bar{\gamma}} \sum_{\boldsymbol{x}\bar{\boldsymbol{x}}} \varepsilon_{abc}\varepsilon_{\bar{a}\bar{b}\bar{c}}\, e^{-i\boldsymbol{p}\cdot(\boldsymbol{x}-\bar{\boldsymbol{x}})} \\ \times \Big\langle \mathcal{Q}^{(A\overline{A})}_{a\alpha;\bar{a}\bar{\alpha}} \mathcal{Q}^{(B\overline{B})}_{b\beta;\bar{b}\bar{\beta}} \mathcal{Q}^{(C\overline{C})}_{c\gamma;\bar{c}\bar{\gamma}} - \mathcal{Q}^{(A\overline{A})}_{a\alpha;\bar{a}\bar{\alpha}} \mathcal{Q}^{(B\overline{C})}_{b\beta;\bar{c}\bar{\gamma}} \mathcal{Q}^{(C\overline{B})}_{c\gamma;\bar{b}\bar{\beta}} \\ - \mathcal{Q}^{(A\overline{B})}_{a\alpha;\bar{b}\bar{\beta}} \mathcal{Q}^{(B\overline{A})}_{b\beta;\bar{a}\bar{\alpha}} \mathcal{Q}^{(C\overline{C})}_{c\gamma;\bar{c}\bar{\gamma}} - \mathcal{Q}^{(A\overline{C})}_{a\alpha;\bar{c}\bar{\gamma}} \mathcal{Q}^{(B\overline{B})}_{b\beta;\bar{b}\bar{\beta}} \mathcal{Q}^{(C\overline{A})}_{c\gamma;\bar{a}\bar{\alpha}} \\ + \mathcal{Q}^{(A\overline{C})}_{a\alpha;\bar{c}\bar{\gamma}} \mathcal{Q}^{(B\overline{A})}_{b\beta;\bar{a}\bar{\alpha}} \mathcal{Q}^{(C\overline{B})}_{c\gamma;\bar{b}\bar{\beta}} + \mathcal{Q}^{(A\overline{B})}_{a\alpha;\bar{b}\bar{\beta}} \mathcal{Q}^{(B\overline{C})}_{b\beta;\bar{c}\bar{\gamma}} \mathcal{Q}^{(C\overline{A})}_{c\gamma;\bar{a}\bar{\alpha}} \Big\rangle_U, \end{aligned} \tag{4.26}$$

where time and spatial labels have been omitted, and $\langle \dots \rangle_U$ denotes the expectation value over the gauge fields only (i.e. eq. (2.91)). Each term in eq. (4.26) corresponds to one of the possible Wick contractions between a baryon creation and annihilation operator, shown diagrammatically in fig. 4.2. Remember that each quark line $\mathcal{Q}$ connecting the source site $\bar{\boldsymbol{x}}$ to sink site $\boldsymbol{x}$ also connects the colour and spin components between the sites, resulting in the summation over $\boldsymbol{x}, \bar{\boldsymbol{x}}$ being very costly to evaluate for every combination of baryon creation and annihilation operators.

A dramatic simplification, central to the stochastic LapH method, comes from instead expressing eq. (4.26) in terms of the quark source and sink vectors that make up our quark lines estimates. A key component of this is the following quantity:

$$\mathcal{B}^{[b_1 b_2 b_3]}_l(\varphi_1, \varphi_2, \varphi_3; t) = c^{(l)}_{\alpha\beta\gamma} \sum_{\boldsymbol{x}} e^{-i\boldsymbol{p}\cdot\boldsymbol{x}} \varepsilon_{abc} \varphi^{[b_1]}_{a\alpha\boldsymbol{x}t}(\rho_1) \varphi^{[b_2]}_{b\beta\boldsymbol{x}t}(\rho_2) \varphi^{[b_3]}_{c\gamma\boldsymbol{x}t}(\rho_3), \tag{4.27}$$

where b_i are noise dilution projector indices, and the short-hand notation $\varphi_k \equiv \varphi(\rho_k)$ has been introduced. The matrix element estimate of eq. (4.26) is then given by

$$\begin{aligned} C_{l\bar{l}}(t_F - t_0) = \Big\langle \mathcal{B}^{[b_1 b_2 b_3]}_l(\varphi_1, \varphi_2, \varphi_3; t_F) \\ \times \Big(\delta^{\overline{ABC}}_{ABC} \mathcal{B}^{[b_1 b_2 b_3]}_{\bar{l}}(\varrho_1, \varrho_2, \varrho_3; t_0) - \delta^{\overline{ACB}}_{ABC} \mathcal{B}^{[b_1 b_3 b_2]}_{\bar{l}}(\varrho_1, \varrho_3, \varrho_2; t_0) \\ - \delta^{\overline{BAC}}_{ABC} \mathcal{B}^{[b_2 b_1 b_3]}_{\bar{l}}(\varrho_2, \varrho_1, \varrho_3; t_0) - \delta^{\overline{CBA}}_{ABC} \mathcal{B}^{[b_3 b_2 b_1]}_{\bar{l}}(\varrho_3, \varrho_2, \varrho_1; t_0) \\ + \delta^{\overline{CAB}}_{ABC} \mathcal{B}^{[b_2 b_3 b_1]}_{\bar{l}}(\varrho_2, \varrho_3, \varrho_1; t_0) + \delta^{\overline{BCA}}_{ABC} \mathcal{B}^{[b_3 b_1 b_2]}_{\bar{l}}(\varrho_3, \varrho_1, \varrho_2; t_0) \Big)^* \Big\rangle_{U,\rho}, \end{aligned} \tag{4.28}$$

where $\delta^{DEF}_{ABC} \equiv \delta_{AD}\delta_{BE}\delta_{CF}$, and $\langle \dots \rangle_{U,\rho}$ denotes the expectation value taken over the gauge field U and over any noise vectors ρ_k. To increase statistics, the six different permutations of the $1, 2, 3$ noises (which we will refer to as noise orderings) can be calculated, and if the quark masses for each of the lines are the same, this doesn't require any more Dirac matrix inversions.

An important feature of eq. (4.28) is the complete factorisation of the baryon correlator into a function associated only with the sink time slice t_F, and another function associated only with the source time slice t_0. The summations over colour, spin, and spatial sites at the source have

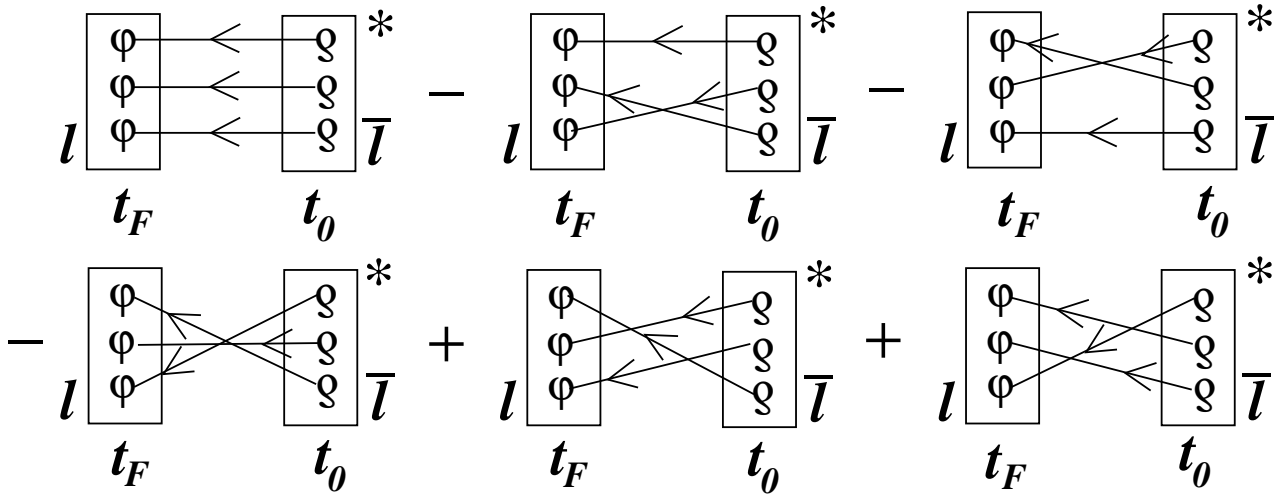

Figure 4.2: A diagrammatic depiction of eq. (4.28) for a baryon-to-baryon correlation function with source time t_0 and sink time t_F. Each box denotes a baryon function as defined in eq. (4.27), with the constituent quark source and sink functions connected by quark lines, indicating a summation over the dilution projector indices. Any line connecting quarks of different flavour gives zero. Each diagram corresponds to one of the possible Wick orderings for a baryon-to-baryon correlator. Diagram from Ref. [15].

been completely separated from the colour, spin, and spatial summations at the sink. The major advantage of this factorisation, and a key feature of the stochastic LapH method, is that for a large set of hadron operators, we can calculate the source and sink functions for each operator and then "tie them together" (i.e. contract over the relevant indices) as needed to form the final correlation matrix elements.

4.4.2 Meson-to-Meson Correlations

Factorising meson-to-meson correlation functions into hadron sources and sinks is done in the same way as for the baryon-to-baryon correlators. For the meson source and sink operators defined in eq. (3.29) in terms of the elemental meson operators defined in eq. (3.28), meson-to-meson correlation matrix elements are given by

$$\begin{aligned} C_{l\bar{l}}(t_F - t_0) &= \frac{1}{N_t}\sum_{t_0}\langle M_l(t_F)\overline{M}_{\bar{l}}(t_0)\rangle \\ &= c^{(l)}_{\alpha\beta}c^{(\bar{l})*}_{\bar{\alpha}\bar{\beta}}\langle \Phi^{AB}_{\alpha\beta}(t_F)\overline{\Phi}^{\bar{A}\bar{B}}_{\bar{\alpha}\bar{\beta}}(t_0)\rangle \\ &= c^{(l)}_{\alpha\beta}c^{(\bar{l})*}_{\bar{\alpha}\bar{\beta}}\sum_{\boldsymbol{x}\bar{\boldsymbol{x}}} e^{-i\boldsymbol{p}\cdot\left(\boldsymbol{x}+\frac{1}{2}(\boldsymbol{d}_\alpha+\boldsymbol{d}_\beta)\right)}e^{i\boldsymbol{p}\cdot\left(\bar{\boldsymbol{x}}+\frac{1}{2}(\boldsymbol{d}_\alpha+\boldsymbol{d}_\beta)\right)} \\ &\qquad\qquad \times\langle \overline{q}^{A}_{a\alpha}(\boldsymbol{x},t_F)q^{B}_{a\beta}(\boldsymbol{x},t_F)\,\overline{q}^{\bar{B}}_{\bar{a}\bar{\beta}}(\boldsymbol{x},t_0)q^{\bar{A}}_{\bar{a}\bar{\alpha}}(\boldsymbol{x},t_0)\rangle, \end{aligned} \tag{4.29}$$

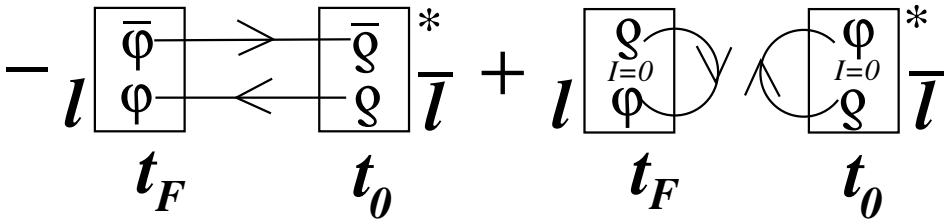

Figure 4.3: A diagrammatic depiction of eq. (4.32) for a meson-to-meson correlation function with source time t_0 and sink time t_F. Each box denotes a meson function as defined in eq. (4.31), with the constituent quark source and sink functions connected by quark lines, indicating a summation over the dilution projector indices. The second term, containing only same-time quark lines/meson internal lines, contributes only for isoscalar/flavour singlet mesons. Diagram from Ref. [15].

where again, $l, \bar{l}$ are taken to be compound indices, and the three-momenta associated with each is assumed to be the same $\boldsymbol{p}$. Then, following the integration over Grassmann fields, we obtain an expression in terms of quark lines:

$$\begin{aligned} C_{l\bar{l}}(t) = c^{(l)}_{\alpha\beta} c^{(\bar{l})*}_{\bar{\alpha}\bar{\beta}} \sum_{\boldsymbol{x}\bar{\boldsymbol{x}}} & e^{-i\boldsymbol{p}\cdot\left(\boldsymbol{x}+\frac{1}{2}(\boldsymbol{d}_\alpha+\boldsymbol{d}_\beta)\right)} e^{i\boldsymbol{p}\cdot\left(\bar{\boldsymbol{x}}+\frac{1}{2}(\boldsymbol{d}_\alpha+\boldsymbol{d}_\beta)\right)} \\ & \times \langle -\mathcal{Q}^{(\overline{A}A)}_{\bar{a}\bar{\alpha};a\alpha} \mathcal{Q}^{(B\overline{B})}_{a\beta;\bar{a}\bar{\beta}} + \mathcal{Q}^{(BA)}_{a\beta;a\alpha} \mathcal{Q}^{(\overline{AB})}_{\bar{a}\bar{\alpha};\bar{a}\bar{\beta}} \rangle_U, \end{aligned} \tag{4.30}$$

where $t = t_f - t_0$, and time and spatial labels have been omitted. As discussed in section 4.3, it is advantageous to use the γ_5-Hermiticity mode expression in eq. (4.22) for the B quark line, and the regular form in eq. (4.21) for the A line.

Define now the meson function:

$$\mathcal{M}^{[b_1 b_2]}_l(\varrho_1, \varphi_2; t) = c^{(l)}_{\alpha\beta} \sum_{\boldsymbol{x}} e^{-i\boldsymbol{p}\cdot\left(\boldsymbol{x}+\frac{1}{2}(\boldsymbol{d}_\alpha+\boldsymbol{d}_\beta)\right)} \varrho^{[b_1]}_{a\alpha\boldsymbol{x}t}(\rho_1)^* \varphi^{[b_2]}_{a\beta\boldsymbol{x}t}(\rho_2), \tag{4.31}$$

so that the factorised meson correlator is given by

$$\begin{aligned} C_{l\bar{l}}(t_F - t_0) = \Big\langle & -\delta^{\overline{AB}}_{AB} \mathcal{M}^{[b_1 b_2]}_l(\overline{\varphi}_1, \varphi_2; t_F) \mathcal{M}^{[b_1 b_2]}_{\bar{l}}(\overline{\varrho}_1, \varrho_2; t_0)^* \\ & + \delta^{B\overline{B}}_{A\overline{A}} \mathcal{M}^{[b_1 b_1]}_l(\varrho_1, \varphi_1; t_F) \mathcal{M}^{[b_2 b_2]}_{\bar{l}}(\varphi_2, \varrho_2; t_0)^* \Big\rangle_{U,\rho}, \end{aligned} \tag{4.32}$$

where $\delta^{CD}_{AB} \equiv \delta_{AC}\delta_{BD}$. This expression is depicted diagrammatically in fig. 4.3, with the second term contributing only for isoscalar/flavour singlet mesons.

4.4.3 More Complicated Correlation Functions

As we consider correlations involving more and more hadrons, writing down expressions for such correlation functions quickly becomes cumbersome. Using the diagrammatic representation of baryon and meson correlation functions in figs. 4.2 and 4.3 allows us to straightforwardly generalise our approach to more complicated correlation matrix elements involving multi-hadron operators.

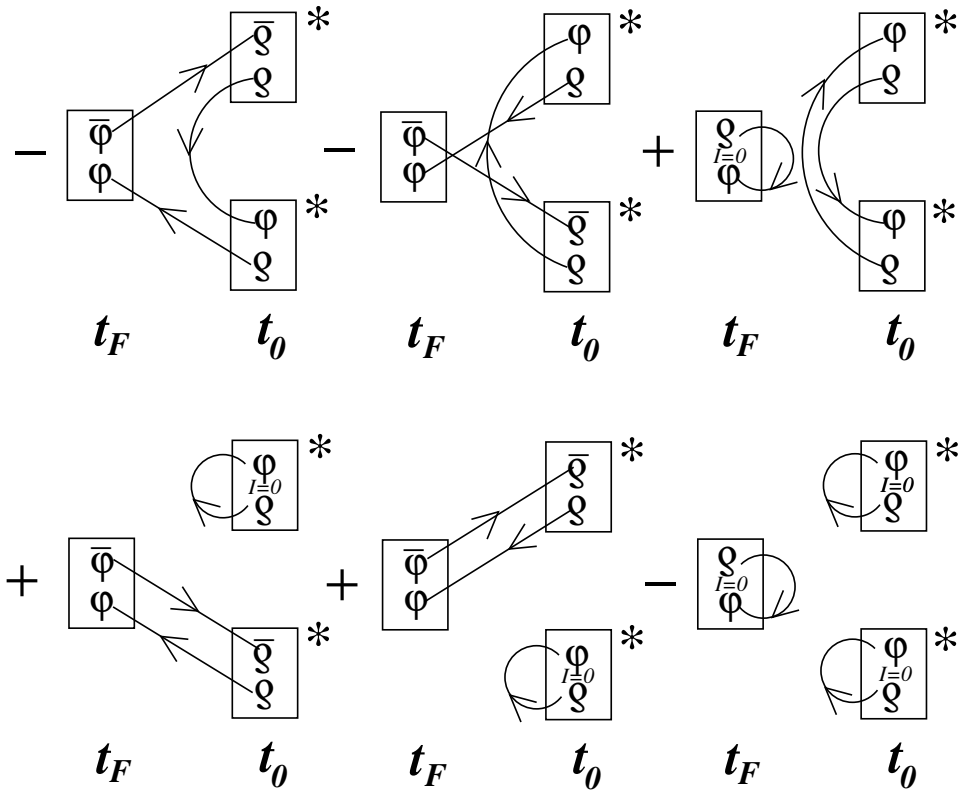

Figure 4.4: A diagrammatic depiction of the temporal correlation between a two-meson source at time t_0 and a single-meson sink at time t_F. Each box denotes a meson function as defined in eq. (4.31), with the constituent quark source and sink functions connected by quark lines, indicating a summation over the dilution projector indices. Boxes with an internal line contribute only for isoscalar/flavour singlet mesons. Swapping the sources and sinks also yields the same results for a single-meson source at time t_0 to a two-meson sink at t_F. Diagram from Ref. [15].

To evaluate a matrix of correlation functions, first the various hadron source and sink functions must be identified and calculated using eqs. (4.27) and (4.31). The factorisation of the correlation functions allows these to be evaluated for a large set of operators, and then stored on disk. For a given matrix element then, the appropriate diagrams (i.e. Wick contractions) must be determined, and then evaluated by contracting over the hadron functions over dilution indices. An example meson to two-meson correlator is shown in fig. 4.4.

Chapter 5

Extracting the Finite-Volume Spectrum

In section 2.4 we showed how the finite-volume energies are represented in a two-point Euclidean temporal correlation function by inserting a complete set of energy eigenstates. Here, we will discuss the process of extracting such a finite-volume energy spectrum from matrices of correlation functions, the estimation of which was outlined in chapter 4. First, in section 5.1 we discuss the analysis of a temporal correlation matrix, and how a generalised eigenvalue problem (GEVP) is solved in order to extract the lowest N energies from an $N \times N$ matrix. Then we will look at how thermal effects due to the finite temporal extent are accounted for in section 5.2, followed by the fit ansätze we use in section 5.3. Finally, we refer to appendix A for a discussion on how we fit correlated Monte Carlo data and the different resampling schemes used for error estimation.

5.1 Correlator Matrix Analysis

Looking at the spectral decomposition in eq. (2.76), we can see that all of the information about the finite-volume spectrum is contained within a given temporal correlation matrix. However, extracting the finite-volume energies directly from a matrix of such correlation functions is impractical. Instead, we use a variational method, proposed in Ref. [13], and studied further in Ref. [14], for extracting the stationary state energies and the overlaps of our interpolating operators onto the finite-volume energy eigenstates. In what follows, effects due to the finite temporal extent of the lattice are neglected, though will be addressed later on in section 5.2.

Consider then the matrix of temporal correlation functions

$$\mathcal{C}_{ij}(t) = \langle 0|\mathcal{O}_i(t+t_0)\overline{\mathcal{O}}_j(t_0)|0\rangle, \tag{5.1}$$

where an average over many source times t_0 is implicit, and the operators are designed such that $\mathcal{C}_{ij}$ is Hermitian (see section 2.4.1). To lessen the effects of differing normalisations among the operators, we rescale the correlation matrix by

$$C_{ij}(t) \equiv \frac{\mathcal{C}_{ij}(t)}{\sqrt{\mathcal{C}_{ii}(\tau_N)\mathcal{C}_{jj}(\tau_N)}}, \tag{5.2}$$

where the normalisation time τ_N is taken at an early time, usually $\tau_N = 1, 2, 3$. Following from eq. (2.76), a spectral decomposition can be written as

$$C_{ij}(t) = \sum_n \langle 0|\mathcal{O}_i|n\rangle\langle n|\overline{\mathcal{O}}_j|0\rangle e^{-E_n t}, \tag{5.3}$$

where the Hermiticity of $C(t)$ implies that

$$\langle 0|\mathcal{O}_i|n\rangle^* = \langle n|\overline{\mathcal{O}}_i|0\rangle. \tag{5.4}$$

Then, defining the overlap amplitudes (often referred to as *Z-factors*)

$$Z_j^{(n)} \equiv \langle 0|\mathcal{O}_j|n\rangle, \tag{5.5}$$

we have

$$C_{ij}(t) = \sum_n Z_i^{(n)} Z_j^{(n)*} e^{-E_n t}, \tag{5.6}$$

where the spectrum has been shifted such that $E_0 = 0$. As we expect degeneracies to rarely occur in the presence of interactions, the spectrum is assumed to be non-degenerate and the energies ordered according to $E_{n+1} > E_n$. Note also that, since the eigenvectors of $C(t)$ are defined only to within a constant, there is some ambiguity in the determination of the overlap Z-factors. While normalisation of the eigenvectors is fixed in the spectral decomposition, their phase is not. Hence, the matrix elements are invariant up to an arbitrary phase:

$$Z_i^{(n)} \to Z_i^{(n)} e^{i\phi_n}, \tag{5.7}$$

and we can determine only the magnitudes $|Z_i^{(n)}|$ of the overlap factors.

5.1.1 The Generalised Eigenvalue Problem

The idea of using variational methods to compute energy levels in lattice gauge theory dates back to the early days of the field [120]. First applied to finding the ground state in a particular symmetry channel, an approach which is equivalent to finding the largest eigenvalue in a generalised eigenvalue problem (GEVP). Following Refs. [13, 14], we will present this GEVP and how it is used to extract not only the ground state but also many excited energy eigenstates from a matrix of temporal correlation functions. To begin consider the following theorem from Ref. [13]:

Theorem. *For every $t \geq 0$, let $\lambda_n(t)$ be the eigenvalues of an $N \times N$ Hermitian correlation matrix $C(t)$, ordered such that $\lambda_0 \geq \lambda_1 \geq \cdots \geq \lambda_{N-1}$. Then,*

$$\lim_{t\to\infty} \lambda_n(t) = b_n e^{-E_n t}\left(1 + \mathcal{O}(e^{-t\Delta_n})\right), \qquad b_n > 0, \qquad \Delta_n = \min_{m\neq n} |E_n - E_m|. \tag{5.8}$$

This gives us a basis for the determination of the energies E_n from a Hermitian correlation matrix $C(t)$. However, simply diagonalising $C(t)$ at large times proves to be impractical. The

correlation matrix elements are difficult to determine accurately for large times, and so the leading error $\mathcal{O}(e^{-t\Delta_n})$ is often not negligible for the time range where the statistical errors on $C(t)$ are manageable. Alternatively, in Ref. [13] Lüscher and Wolff propose solving the following GEVP, which they show to have smaller leading errors:

$$C(t)v_n(t,\tau_0) = \lambda_n(t,\tau_0)C(\tau_0)v_n(t,\tau_0), \qquad n = 1,\ldots,N-1, \qquad t > \tau_0, \tag{5.9}$$

where τ_0 is fixed and referred to as the metric time. Excited state energies can then be systematically determined using the effective mass:

$$E_n^{\text{eff}}(t,\tau_0) \equiv \frac{1}{\Delta t}\ln\left(\frac{\lambda_n(t+\Delta t,\tau_0)}{\lambda_n(t,\tau_0)}\right), \tag{5.10}$$

where the time-step Δt is generally taken $\Delta t \leq 3a_t$ This is motivated by truncating the sum in eq. (5.6) to contain only the N lowest terms, giving eigenvalues that are exactly

$$\lambda_n^{(0)}(t,\tau_0) = e^{-E_n(t-\tau_0)}. \tag{5.11}$$

This however neglects contributions from states with $E \geq E_N$. The authors of Ref. [14] address this by taking a perturbative expansion of the correlation functions, finding that if $\tau_0 \geq t/2$, the leading order corrections to $\lambda_n^{(0)}(t,\tau_0)$ are of order $\mathcal{O}(e^{-(E_N-E_n)t})$, a significant improvement over eq. (5.8) for the low-lying states. We are therefore motivated to solve the GEVP rather than simply diagonalise $C(t)$ to extract the spectrum, while crucially keeping N and τ_0 large in order to reduce systematic errors. As the leading correction grows as $n \to N$, we find it is often important to keep N larger than the number of states you wish to extract, using $N \sim \frac{3}{2}n$, where n is the number of desired levels, as a rough guide (see fig. 5.1(c)).

It is straightforward to see that solving the GEVP is equivalent to diagonalising

$$G(t) \equiv C^{-1/2}(\tau_0)C(t)C^{-1/2}(\tau_0), \tag{5.12}$$

where we emphasise the difference between metric time τ_0 and the normalisation time τ_N used in eq. (5.2). The eigenvalues of $G(t)$ then obey [14]

$$\lim_{t\to\infty}\lambda_n(t) = |Z_n'|^2\, e^{-E_n t}, \tag{5.13}$$

with the overlap factors approximated by

$$Z_j^{(n)} \approx C_{jk}(\tau_0)^{1/2}V_{kn}(t)Z_n', \tag{5.14}$$

where $V(t)$ is the unitary matrix containing the orthonormal eigenvectors of $G(t)$ as its columns. This expression becomes exact as t and τ_0 become large, with non-negligible contributions from states with $n \geq N$ appearing otherwise. To illustrate the importance of the GEVP, in fig. 5.1 we show the effective energies for a 12×12 correlator matrix using the methods described above for a toy model whose energies are given by

$$E_0 = 0.20, \qquad E_n = E_{n-1} + \frac{0.08}{\sqrt{n}}, \qquad n = 1,\ldots,N-1. \tag{5.15}$$

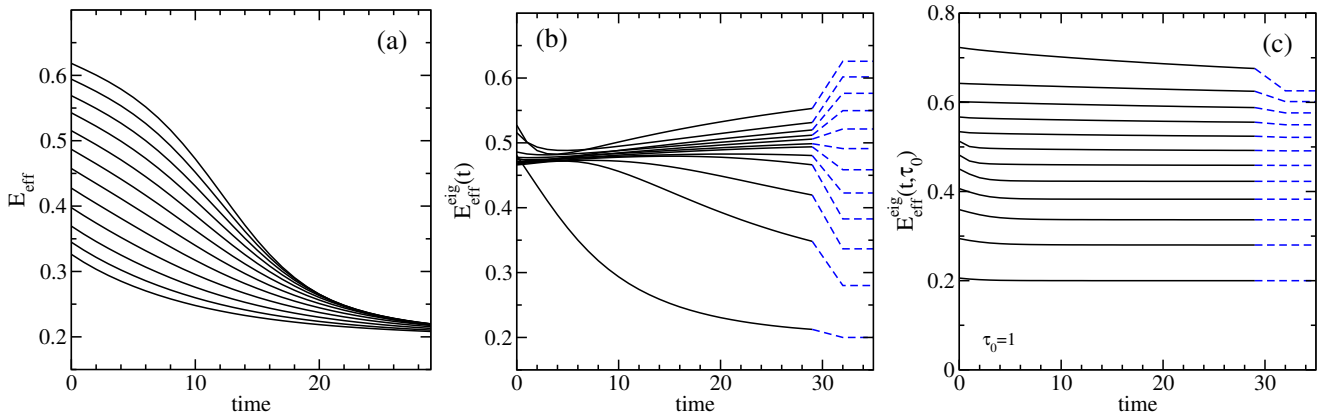

Figure 5.1: (a) Effective energies associated with the diagonal elements of the original raw correlator matrix $C(t)$ of the toy model, whose energies are defined in eq. (5.15). (b) Effective energies associated with the GEVP eigenvalues of the original correlator matrix $C(t)$. (c) Effective energies associated with the GEVP eigenvalues of $C(\tau_0)^{-1/2}C(t)C(\tau_0)^{-1/2}$ for $\tau_0 = 1$. Dashed blue lines indicate exact values for the lowest 12 energies.

Note the significant improvement gained by rescaling the correlation matrix via eq. (5.2). The highest lying levels in fig. 5.1(c) also give an indication that in order to reliably extract n levels, we require matrices with $N > n$ operators. Increasing N is much more effective than increasing t, especially as statistical errors grow significantly with t.

5.1.2 The Single Pivot

From the assumption of Hermiticity and eq. (5.13), we expect both $C(t)$ and $G(t)$ to be positive definite matrices. However, if the N operators used create N states that are not sufficiently distinct from one another, statistical noise in the correlator estimates can cause the matrices to become ill-conditioned by having eigenvalues very close to zero, or even to have negative eigenvalues, spoiling the assumed positive definiteness. While a careful pruning of the operator set is a crucial step in maintaining well-conditioned correlator matrices, this can be an imprecise process, and a method of tackling the GEVP for initially ill-conditioned matrices, but that ultimately produces a well-conditioned matrix, is desirable.

The condition number of a matrix gives a measure of how well- (or ill-)conditioned a matrix is. Given by the ratio of the largest and smallest eigenvalues of the matrix

$$\xi^{\mathrm{cn}} = \left| \frac{\lambda_{\max}}{\lambda_{\min}} \right|, \tag{5.16}$$

where $\lambda_{\max}, \lambda_{\min}$ are the largest and smallest eigenvalues respectively, a matrix is said to be ill-conditioned if ξ^{cn} is too high (for us, generally this means $> 100 - 200$), and well-conditioned if it is low enough (i.e. below ~ 100). Since the eigenvalues are expected to be asymptotically of the form in eq. (5.13), the largest eigenvalues will correspond to the lowest energies, and so, it is the

smallest eigenvalues we will look to discard when the correlator matrix is ill-conditioned. Then, we set the threshold for the lowest eigenvalue by choosing a maximum accepted condition number $\xi_{\max}^{\mathrm{cn}}$, so that at time t

$$\lambda_{\mathrm{thres}}^{(t)} = \frac{\lambda_{\max}^{(t)}}{\xi_{\max}^{\mathrm{cn}(t)}}, \tag{5.17}$$

where $1/\xi_{\max}^{\mathrm{cn}(t)}$ is generally chosen to be on the order of the statistical error in $C(t)$. Then, we form the $N \times N_0$ matrix P_0 that contains the $N_0 \leq N$ eigenvectors of $C(\tau_0)$ with eigenvalues larger than $\lambda_{\mathrm{thres}}^{(\tau_0)}$. Using this, we define

$$\widetilde{C}(t) = P_0^\dagger \, C(t) P_0, \tag{5.18}$$

with which we can form $\widetilde{G}(t)$:

$$\widetilde{G}(t) = \widetilde{C}^{-1/2}(\tau_0)\widetilde{C}(t)\widetilde{C}^{-1/2}(\tau_0), \tag{5.19}$$

where we note that $\widetilde{C}(\tau_0)$ is a diagonal matrix. Next, using the $N_p \leq N_0$ eigenvectors of $\widetilde{G}(\tau_D)$ with eigenvalues larger than $\lambda_{\mathrm{thres}}^{(\tau_0)}$ to form the $N_0 \times N_p$ matrices $\widetilde{V}(\tau_D)$, where τ_D is referred to as the diagonalisation time[1]. Finally then, we form the $N_p \times N_p$ diagonal matrix

$$\widetilde{D}(t) = \widetilde{V}^\dagger(\tau_D)\widetilde{G}(t)\widetilde{V}(\tau_D), \tag{5.20}$$

whose diagonal elements will tend to $\lambda_n \propto e^{-E_n t}$ (i.e. eq. (5.13)). Thus, by fitting the diagonal elements, we can obtain estimates for E_n and $|\widetilde{Z}_n'|$. Note that, for the full ensemble of gauge configurations $\widetilde{D}(\tau_0) = 1$, and $\widetilde{D}(\tau_D)$ is diagonal. On different bootstrap/jackknife resamplings this may not be true, and at later times, $\widetilde{D}(t)$ may not be diagonal. We must then check for non-zero off-diagonal elements of $\widetilde{D}(t)$, and adjust the parameters τ_0, and τ_D until none remain.

We call this the *single pivot* method for solving the GEVP, as the diagonalisation is performed only for one choice of metric time τ_0, and only one other time $t = \tau_D$. The main advantage of performing the diagonalisation in this way is the avoidance of diagonalising the correlator matrix at large times, which, due to the increased statistical errors, can lead to a significant bias in the final results. Additionally, alternative methods which require significantly more diagonalisations require the use of the cumbersome and time-consuming eigenvector pinning. As no significant differences in the final spectrum determination are seen using other techniques, we exclusively use the single pivot method in our analyses.

5.2 Temporal Wrap-Around Effects

At this point, we will take a brief aside to consider the effects of the finite temporal extent of the lattice. While there are two scenarios to consider here, distinguished by the differing temporal boundary conditions used on the HadSpec and CLS gauge ensembles (see sections 2.3.1 and 2.3.2),

[1] A single diagonalisation time is chosen satisfying $\tau_0 < \tau_D \leq 2\tau_0$, following the findings of Ref. [14] in which they find the leading order corrections to the eigenvalues of the GEVP are $\mathcal{O}(e^{-(E_n - E_n)t})$ for $\tau_0 \geq t/2$.

we will begin with a general discussion assuming periodic boundary conditions (used on the HadSpec ensembles), followed by some comments on the subtleties involved with the open temporal boundary conditions (used on the CLS ensembles).

In Euclidean space and finite-volume with periodic boundary conditions, the path integral expressions that we compute are in fact equivalent to quantum statistical mechanical expectation values, at a temperature given by the inverse temporal extent. Explicitly, for finite temporal extent T (not to be confused with temperature), and assuming periodic boundary conditions

$$\begin{aligned}\mathcal{C}_{ij} &= \langle \mathcal{O}_i(t)\overline{\mathcal{O}}_j(0)\rangle_T \\ &= \frac{1}{Z_T}\,\mathrm{Tr}\left[e^{-HT}\mathcal{O}_i(t)\overline{\mathcal{O}}_j(0)\right] \\ &= \frac{1}{Z_T}\sum_n \langle n|e^{-H(T-t)}\mathcal{O}_i(0)e^{-Ht}\overline{\mathcal{O}}_j(0)|n\rangle \\ &= \frac{1}{Z_T}\sum_{n,m} e^{-E_n(T-t)}e^{-E_m t}\langle n|\mathcal{O}_i(0)|m\rangle\langle m|\overline{\mathcal{O}}_j(0)|n\rangle,\end{aligned} \tag{5.21}$$

where $H|n\rangle = E_n|n\rangle$, we assume the energies have been shifted such that $E_0 = 0$, and the partition function is given by

$$\begin{aligned}Z_T &\equiv \mathrm{Tr}\, e^{-HT} \\ &= \sum_n \langle n|e^{-HT}|n\rangle \\ &= \sum_n e^{-E_n T}.\end{aligned} \tag{5.22}$$

For large T, the contributions from $n = 0$ will dominate (as the energies are assumed to be ordered $E_{n+1} > E_n$), with contributions from $n > 0$ states existing solely due to the finite time extent. We refer to such extraneous states as *thermal states*. Taking the large time limit then, i.e. $T \to \infty$, the Euclidean correlation function of eq. (5.21) will approach the vacuum expectation value $\langle 0|\mathcal{O}_i(t)\overline{\mathcal{O}}_j(0)|0\rangle$.

The effects of these thermal states are generally small, but often non-negligible and so must be accounted for. For bosonic correlation functions (e.g. the mesonic correlators considered in this work), the backwards (in time) propagating modes associated with the thermal states, $e^{-E_n(T-t)}$ in the last line of eq. (5.21), have the same energy as the forwards propagating modes. We took advantage of this when designing our mesonic operators in section 3.2.3, and so in these cases use a fit form that is symmetric under time reversal, or simply add a constant term, to take the thermal effects into account. Such fit forms are discussed in more detail in the next section. For baryon correlation functions the energy of the backwards propagating modes is not the same as for the propagating modes but in fact corresponds to the parity partner of the forwards propagating mode (see section 3.2.2). Thankfully, these thermal effects are, in general, quite small and appear in a statistically significant fashion only for the lightest states, suppressed by the finite temporal extent of the lattice. Hence, we observe thermal effects only on the $24^3 \times 128$ anisotropic lattice used in the glueball study, and there only in the correlation functions for a single pion or kaon.

Adopted to reduce autocorrelation times of the global topological charge [89], the open temporal boundaries employed in the CLS gauge configurations influence the finite temporal extent effects in a different manner that must be considered carefully (see section 2.3.2 and references therein for more details). Here, for large T, and if both the source and sink time (t_0, t_F) are sufficiently far from the boundaries, the correlation functions have the form [20] (cf. eq. (5.21))

$$\lim_{\substack{T\to\infty \\ t_0,(T-t_F)\to\infty}} \mathcal{C}_T(t_0, t_F) = \mathcal{C}(t_F - t_0) \times \left(1 + \mathcal{O}(e^{-E_0^{\text{vac}} t_{\text{bnd}}})\right), \tag{5.23}$$

where $\mathcal{C}_T(t_0, t_F) = \langle \mathcal{O}(t_F)\overline{\mathcal{O}}(t_0)\rangle_T$ is the Euclidean correlation function with open temporal boundary conditions, $\mathcal{C}(t) = \langle 0|\mathcal{O}(t)\overline{\mathcal{O}}(0)|0\rangle$ is the correlator in the $T \to \infty$ limit, E_0^{vac} is the lightest state with vacuum quantum numbers, and $t_{\text{bnd}} = \min(t_0, T - t_F)$ is the minimum distance from one of the interpolating operators to the temporal boundary. Since we roughly expect $E_0^{\text{vac}} \approx 2m_\pi$, at least on this subset of CLS ensembles, if we choose source and sink times such that $m_\pi t_{\text{bnd}} \geq 2$, then the corrections in eq. (5.23) are similar to the exponentially suppressed finite-volume effects that contribute to single-hadron states. These effects are discussed in more detail in Ref. [20], including a check for discrepancies between source times that may indicate a loss of Hermiticity in correlation matrices. Ultimately in the correlator construction for the scattering analysis in chapter 8, we use only source and sink times such that $m_\pi t_{\text{bnd}} \geq 2$ so that these effects are negligible.

5.3 Fitting Diagonal Correlators

Once the elements of $\widetilde{D}(t)$ have been determined, we are ready to fit the diagonal correlator elements to extract the energy spectrum and operator overlaps. The large time behaviour (eq. (5.13)) suggests the simplest fit ansatz we consider, a single "time-forward" exponential

$$C(t) = Ae^{-Et}, \tag{5.24}$$

with fit parameters A and E. This can also be symmetrised in time, following the discussion in the previous section, to include the thermal effects of backwards propagating (bosonic) modes, giving the "time-symmetric" single exponential fit form:

$$C(t) = A\left(e^{-Et} + e^{-E(T-t)}\right), \tag{5.25}$$

where T is the temporal extent of the lattice, and no new fit parameters are introduced. In the absence of temporal wrap-around effects, the time-forward and time-symmetric fit forms should produce the same results, offering a simple check for such effects. Additionally, we can add an extra constant (in time) fit parameter to both fit forms to account for potential higher lying contributions that vary slowly in time. In the context of thermal effects, such a constant term is only seen to be non-zero for lattices with a small temporal extent where we have high statistics.

A single exponential fit form of course assumes negligible contributions from excited state contamination that we see for early times, even after solving the GEVP. We must then use eqs. (5.24)

and (5.25) only over time ranges for which eq. (5.10) is seen to plateau to a constant value. The significant increase in statistical noise at later times leads us to also seek out fit forms that are valid also for early times. We introduce then a time-forward two exponential fit form:

$$C(t) = Ae^{-Et}\left(1 + Be^{-\Delta^2 t}\right), \tag{5.26}$$

with fit parameters A, B, E, Δ^2, where we use Δ^2 to ensure a positive decay constant. The aim here is that the second term will parameterise the effects of the leading order excited state contributions. We can then also make this form time-symmetric, and add a constant term where we expect thermal effects to contribute. Another fit ansatz for capturing excited state contamination that we consider is the time-forward geometric series:

$$C(t) = Ae^{-Et}\left(1 + Be^{-\Delta^2 t} + B^2 e^{-\Delta^4 t} + \dots\right) = \frac{Ae^{-Et}}{1 - Be^{-\Delta^2 t}}, \tag{5.27}$$

with fit parameters A, B, E, Δ^2, and can also be made time-symmetric.

A comparison of the different methods for accounting for the thermal effects on the $24^3 \times 128$ anisotropic ensemble is shown in fig. 5.2, including the time-subtracted correlator

$$C_{\text{sub}}(t) \equiv C(t+1) - C(t). \tag{5.28}$$

This serves as an alternative to adding an additional constant (in time) fit parameter that proves to be useful not just in removing thermal effects, but also in the subtraction of vacuum expectation values (VEVs) in symmetry channels with vacuum quantum numbers. The presence of thermal effects is apparent in the time-forward effective mass points in fig. 5.2a where, for large time separations, the effective mass drops below the plateau seen at earlier times. We find in our analyses that, when thermal effects are non-negligible, using eq. (5.28) increases the statistical errors somewhat, especially for later times, and so is used sparingly.

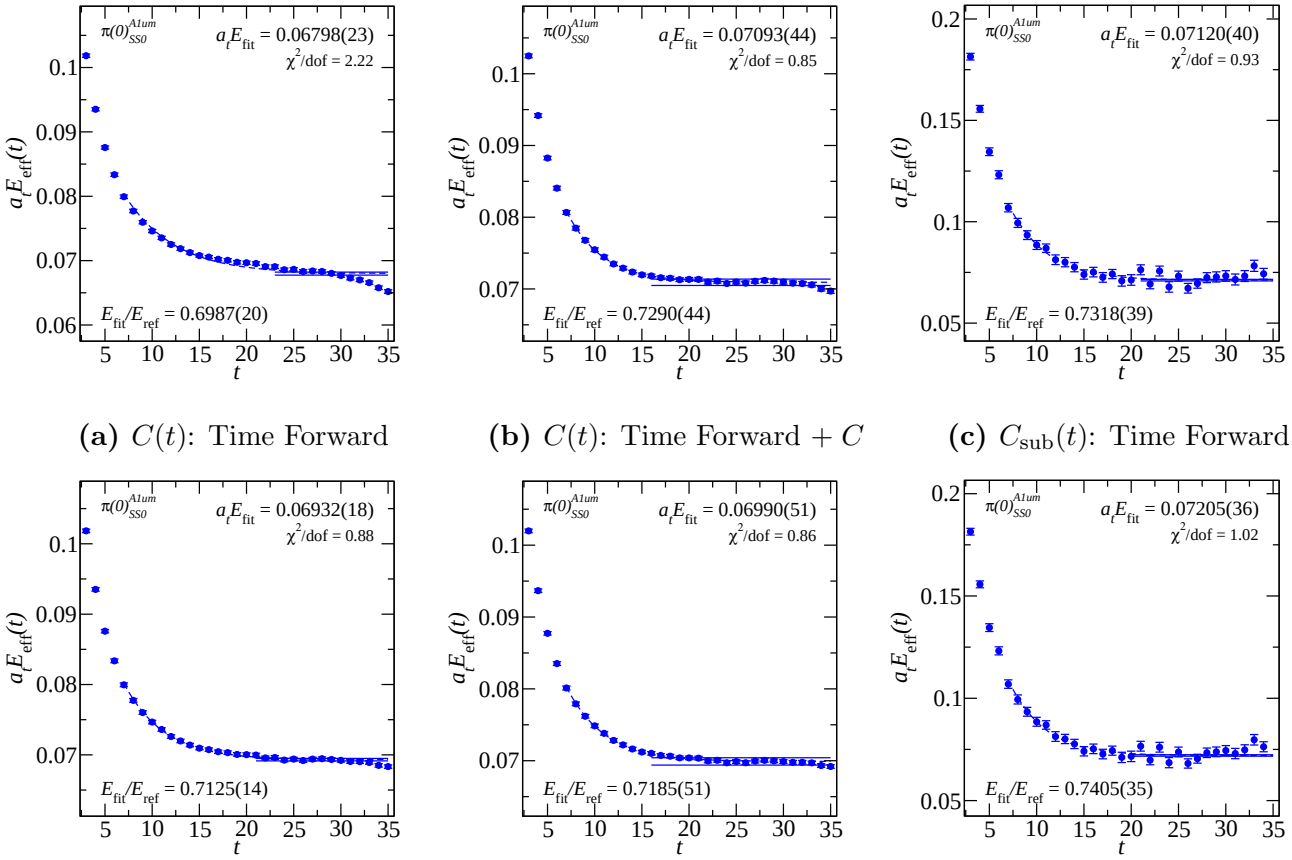

(a) $C(t)$: Time Forward **(b)** $C(t)$: Time Forward + C **(c)** $C_{\rm sub}(t)$: Time Forward

(d) $C(t)$: Time Symmetric **(e)** $C(t)$: Time Symmetric + C **(f)** $C_{\rm sub}(t)$: Time Symmetric

Figure 5.2: Comparison of two exponential (eq. (5.26)) fits to a single pion at rest correlator on a $24^3 \times 128$ anisotropic ensemble with $m_\pi \approx 390$ MeV. The fit plateaus are overlaid on the effective energies for $C(t)$ and $C_{\rm sub}(t) = C(t+1) - C(t)$ using $t_{\rm min} = 7$, $t_{\rm max} = 35$ and bootstrap resampling. Where a time symmetric fit form and/or an added constant fit parameter is used an appropriately time symmetrised and/or constant shifted version of eq. (5.10) is used to determine the effective energy points. Recall that we fit to the correlator itself and so the fits are overlaid here to guide the eye only. The reference energy used is the kaon mass, i.e. $E_{\rm ref} = m_K$.

Chapter 6

Scattering Observables from the Lattice

At this point, it is important for us to think about what observable physics we can extract from lattice calculations. The discrete, finite-volume to which we are necessarily restricted must be carefully distinguished from the continuous, infinite-volume of the physical world. Even solely within QCD, most of the excited hadrons we want to study are unstable resonances, manifesting as complex poles in a scattering amplitude. In finite-volume with periodic boundary conditions, the allowed momenta are restricted such that the eigenstates of a Hamiltonian will be discrete. Diagonalising this Hamiltonian will then give access to these discrete stationary states. In infinite-volume, a continuum of momenta are allowed and unstable excited states decay into multi-hadron asymptotic states. In finite-volume however, there are no decays; instead there is only quantum mechanical mixing between Fock states. Additionally, even in an infinite-volume calculation, it is now well known that on-shell scattering amplitudes away from threshold cannot be obtained from the asymptotic temporal separation of infinite-volume Euclidean correlation functions. That is, simply taking the infinite-volume limit of the Euclidean correlation functions that we calculate in lattice QCD is insufficient for the study of scattering phenomena. In this chapter we will look at a formalism for embracing the finite-volume restriction, by relating the finite-volume stationary states to infinite-volume scattering amplitudes, from which resonance parameters can be extracted.

6.1 Quantisation Condition

The idea that finite-volume energies can be related to infinite-volume scattering processes is not a new one, dating back to the 1950's [121, 122]. Beginning in the 1980's, Lüscher first suggested applying this idea to gauge field theories in Ref. [123]. In Refs. [124, 125] Lüscher then studied for massive quantum field theories, the volume dependence of stable particle states and of scattering states. This culminated in [16] where Lüscher found, in the case of two identical spinless particles with zero total momentum interacting via a central potential, relationships between finite-volume energies and infinite-volume scattering phase shifts. Rummukainen and Gottlieb in 1995 then generalised Lüscher's result to frames with non-zero total momentum [126]. While these results

were all obtained from a relativistic quantum mechanical approach, the calculations were revisited in 2005 using an entirely field theoretic approach in a seminal work by Kim, Sachrajda, and Sharpe [127]. This work focuses on the case of a single channel with the scattering of identical, spinless particles. While numerical applications to that point had been restricted to simplified models, such as a scalar theory in the Ising limit in Refs. [68, 126], as lattice QCD computations matured to the stage where it is now possible to calculate scattering phase shifts with reasonable accuracy, the results of Ref. [127] were generalised in Refs. [128–134], among others, to include multiple decay channels, different particles masses, and non-zero spin.

A key limitation of this formalism is the restriction to energies that lie below the three or more particle thresholds. Development of a formalism to treat three-body scattering channels is currently underway [135–146], with the first application to QCD appearing in Ref. [147]. Once this formalism is fully developed, it will then be possible to calculate scattering amplitudes below four-particle thresholds. From the point of view of future directions, it's also important to keep in mind the increasing difficulty of using these methods with the developments made in cutting-edge lattice calculations. A current concern is the lowering of the relevant three- and four-particle thresholds as we progress towards physical particle masses, resulting in smaller energy ranges in which scattering amplitudes can be extracted. More critical however, is the trend towards larger and larger spatial volumes. In a large spatial volume, the determination of individual finite-volume energies quickly becomes cumbersome. For example, on one ensemble with $m_\pi L = 6.1$ used in the $\pi\pi$ scattering analysis in Ref. [20], 43 energies are determined. While this is manageable, various groups are generating ensembles with $m_\pi L \geq 10$, resulting in very dense low-lying spectra at close to physical quark masses. Hence, alternative methods for extracting scattering amplitudes, for example from finite-volume spectral functions [148], have been proposed, though most are still in the very early stages of development.

6.1.1 Quantum Mechanics in One Dimension

Before diving into deriving the full field theoretic quantisation condition, it is useful to think about a more pedagogical example of how a finite-volume interacting spectrum can be related to infinite-volume scattering phase shifts. To this end, consider a system consisting of two identical (non-relativistic) bosons in one dimension. In the absence of interactions, the total energy is given by

$$E_{\text{non}} = \frac{k_1^2}{2m_1} + \frac{k_2^2}{2m_2}. \tag{6.1}$$

Introducing a finite-range, separation dependent potential

$$\begin{aligned} V(|x_1 - x_2|) &\equiv V(x) \\ V(x) &= 0 \ \text{ for } \ |x| > R, \end{aligned} \tag{6.2}$$

at a given separation x, the wave-function can be written

$$\psi(x) = A\left(e^{-ikx} + e^{i(kx+2\delta(k))}\right), \tag{6.3}$$

where the outgoing/scattered wave has been shifted by $\delta(k)$, the *scattering phase shift*. Restricting to a finite-volume L, where $L > 2R$, then with periodic boundary conditions (such that $k_i = \frac{2\pi}{L} n_i$, where $n_i \in \mathbb{Z}$)

$$\psi(x + L) = \psi(x), \tag{6.4}$$

imposing continuity of the wavefunction and its derivative yields

$$\frac{B}{A} = e^{-ikL} \qquad \Rightarrow e^{2i\delta} = e^{-ikL}, \tag{6.5}$$

giving us the *quantisation condition*

$$\delta(k) + \frac{kL}{2} + n\pi = 0. \tag{6.6}$$

The finite-volume energy spectrum for the interacting system with identical particles is then given by

$$E_n^{\text{int}} = \frac{k_n^2}{m}, \qquad k_n = \frac{2\pi}{L}\left(n - \frac{\delta}{\pi L}\right), \tag{6.7}$$

so that the interaction energy is

$$\begin{aligned} \Delta E_n &\equiv E_n^{\text{int}} - E_n^{\text{non}} \\ &= \frac{1}{m}\left(\frac{2\pi}{L}\right)^2 \left[\left(n - \frac{\delta}{\pi L}\right)^2 - n^2\right] \\ &= \frac{\delta}{\pi L m}\left(\frac{2\pi}{L}\right)^2 \left(\frac{\delta}{\pi L} - 2n\right), \end{aligned} \tag{6.8}$$

yielding a direct relationship between the interaction energies in finite-volume, ΔE_n, and the infinite-volume scattering phase shifts, δ. In fig. 6.1 we show the interacting and non-interacting energies as a function of box size L for a typical weak interaction, $\delta(k) = ak$, $-1 < a < 0$.

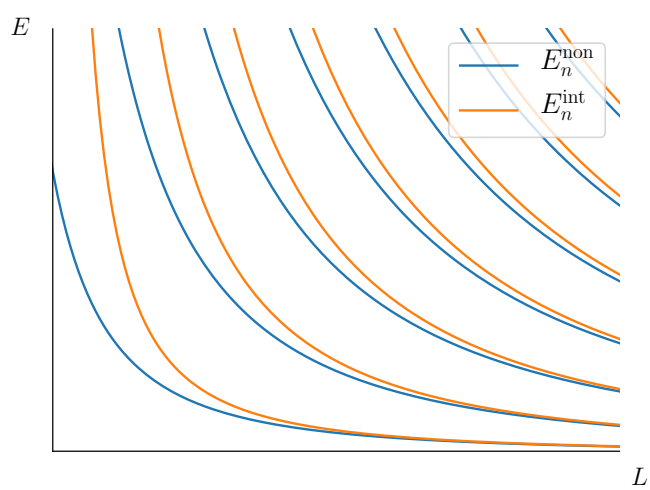

Figure 6.1: Typical interacting and non-interacting energy levels as a function of volume L for a weak interaction: $\delta(k) = ak$, $-1 < a < 0$. At smaller L, the energy difference due to interactions, ΔE, is more pronounced, and so with finite statistics, easier to resolve.

The relation in eq. (6.7) gives us an indication of how the finite-volume to which we are necessarily restricted in lattice QCD may be exploited to study infinite-volume phenomena. In fact, if we look at the large-L behaviour in fig. 6.1, we can see that there will be a sweet spot in which the finite-volume is best used; for small L finite-volume corrections will tend to be large, and so energy determination is difficult, but also for very large L the shift ΔE of the energies away from their non-interacting values becomes smaller and smaller, and so more difficult to resolve with finite statistics. This leads us to consider a method which is more rigorous, yet in the same vein, for extracting observable infinite-volume physics from a finite-volume calculation that takes advantage of the finite-volume.

6.1.2 Lüscher Quantisation Condition - Overview

The infinite-volume scattering matrix S can be related to finite-volume stationary state energies with total momentum $\boldsymbol{P}$ by

$$\det[1 + F^{(\boldsymbol{P})}(S - 1)] = 0, \tag{6.9}$$

where $F^{(\boldsymbol{P})}$ is a known function of energy, defined shortly in eq. (6.13) and derived in section 6.1.3. This determinant allows for a relationship between the S-matrix and each discrete finite-volume energy[1]. In the case of a single scattering channel in a single partial wave, the matrices F and S are one dimensional and the scattering amplitude is uniquely defined at each finite-volume energy. Including multiple decay channels, and/or multiple partial waves however, S is no longer 1×1 and contains multiple independent elements, so each finite-volume energy gives a single condition to the entire matrix. Hence, some parameterisation of S is required with some number of parameters that can be determined using a fit to a set of finite-volume energies. The details of the scattering amplitude parameterisation and fit procedures we use are detailed in sections 6.2 and 6.3 respectively.

Each finite-volume energy, E_{lab}, determined in the "lab" frame from a correlator matrix analysis at some total momentum $\boldsymbol{P}$, is boosted to the centre-of-momentum frame using a continuum dispersion relation[2]

$$E_{\text{cm}} = \sqrt{E_{\text{lab}}^2 - \boldsymbol{P}^2}, \tag{6.10}$$

where the total momentum takes only discrete values given by $\boldsymbol{P} = \frac{2\pi}{L}\boldsymbol{d}$, where $\boldsymbol{d}$ is a vector of integers and L^3 is the spatial volume of the lattice. Note also that for anisotropic lattices, a determination of the lattice anisotropy $\xi = a_s/a_t$ is also required here. We label open two-particle scattering channels with the index a, with the spins and masses of the scattered particles denoted by s_{ia} and m_{ia}, with $i = 1, 2$, respectively. In each channel we then define the following kinematic

[1] Keeping in mind the relevant many-particle thresholds.

[2] We assume here that discretisation effects that manifest in the dispersion relation are negligible. If this were not the case, one needs only use a modified "lattice" dispersion relation, for example as in [126].

quantities

$$u_a^2 = \frac{L^2 \boldsymbol{q}_{\mathrm{cm},a}^2}{(2\pi)^2}, \qquad \boldsymbol{s}_a = \left(1 + \frac{(m_{1a}^2 - m_{2a}^2)}{E_{\mathrm{cm}}^2}\right)\boldsymbol{d}, \qquad \gamma = \frac{E_{\mathrm{lab}}}{E_{\mathrm{cm}}}, \tag{6.11a}$$

$$\boldsymbol{q}_{\mathrm{cm},a}^2 = \frac{1}{4}E_{\mathrm{cm}}^2 - \frac{1}{2}(m_{1a}^2 + m_{2a}^2) + \frac{(m_{1a}^2 - m_{2a}^2)}{4E_{\mathrm{cm}}^2}, \tag{6.11b}$$

where $\boldsymbol{q}_{\mathrm{cm}}$ is a solution to

$$E_{\mathrm{cm},a} = \sqrt{\boldsymbol{q}_{\mathrm{cm},a}^2 + m_{1a}^2} + \sqrt{\boldsymbol{q}_{\mathrm{cm},a}^2 + m_{1a}^2}. \tag{6.12}$$

In the typical JLS basis, we can write an explicit expression for $F^{(\boldsymbol{P})}$. Each basis state will be labelled by $|Jm_JLSa\rangle$, where J is the total angular momentum of the two particles, with m_J its projection onto the z-axis, L (not to be confused with the lattice length) is the orbital angular momentum in the centre-of-momentum frame, S is the total spin of the scattering particles (not to be confused with the S-matrix), and a is an index containing all other necessary labels: particle species, individual intrinsic spins, isospin, isospin projection, G-parity (where relevant), etc. In this basis elements of $F^{(\boldsymbol{P})}$ are given by

$$\begin{aligned}\langle J'm_{J'}L'S'a'|F^{(\boldsymbol{P})}|Jm_JLSa\rangle = \delta_{a'a}\delta_{S'S}\frac{1}{2}\Big[&\langle J'm_{J'}|L'm_{L'}Sm_S\rangle\langle Lm_LSm_S|Jm_J\rangle W^{(\boldsymbol{P})}_{L'm_{L'};Lm_L} \\ &+ \delta_{J'J}\delta_{m_{J'}m_J}\delta_{L'L}\Big],\end{aligned} \tag{6.13}$$

where $\langle Lm_LSm_S|Jm_J\rangle$ are Clebsch-Gordan coefficients. The matrix $W^{(\boldsymbol{P})}_{L'm_{L'};Lm_L}$ is given by

$$\begin{aligned}-iW^{(\boldsymbol{P}a)}_{L'm_{L'};Lm_L} = \sum_{l=|L'-L|}^{L'+L}\sum_{m=-l}^{l}&\frac{\mathcal{Z}_{lm}(\boldsymbol{s}_a,\gamma,u_a^2)}{\pi^{3/2}\gamma u_a^{l+1}}\sqrt{\frac{(2L'+1)(2l+1)}{(2L+1)}} \\ &\times\langle L'0,l'0|L0\rangle\langle L'm_{L'},lm|Lm_L\rangle,\end{aligned} \tag{6.14}$$

where $\mathcal{Z}_{lm}$ are the Rummukainen-Gottleib-Lüscher (RGL) shifted zeta functions [16, 126], known but numerically complex functions of the finite-volume energies. Our method of evaluating these functions is described briefly in Ref. [29].

The above relations apply for both distinguishable and indistinguishable particles, since the associated symmetry factors cancel in the quantisation condition in general [131]. The only difference that occurs with indistinguishable particles is that certain combinations of L and S cannot occur. In the absence of isospin, $L + S$ must be even for identical particles. For identical particles with isospin I_1, $L + S + I - 2I_1$ must be even, where I is the total isospin.

6.1.3 Lüscher Quantisation Condition - Derivation

We will in this section sketch out a derivation of the Lüscher quantisation condition, mainly following the field theoretic presentation from Refs. [127, 131]. Analogous to the QM example in section 6.1.1, we focus on the difference between correlation functions in finite- and infinite-volume.

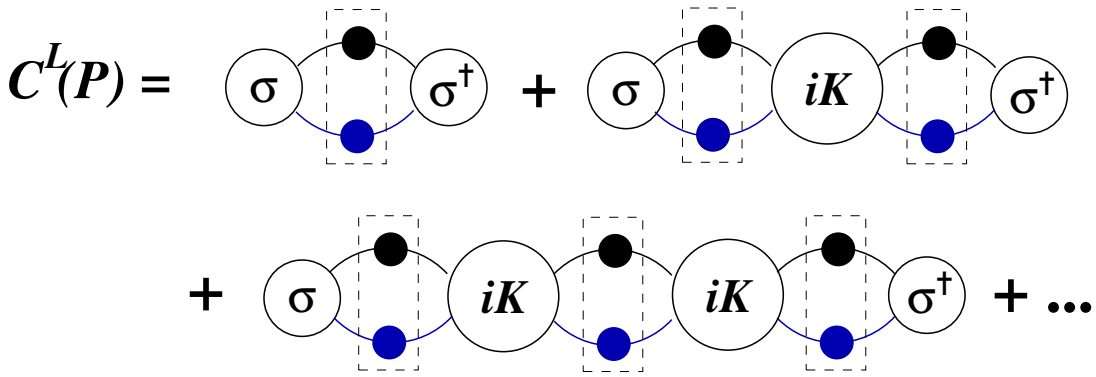

Figure 6.2: Diagrammatic expansion of $C^L(P)$ in terms of Bethe-Salpeter kernels iK (eq. (6.16)) connected by fully dressed propagators, and the two-body interpolators σ. The dashed rectangles indicate finite-volume loop momentum sums. Initial and final states are on the right and left respectively.

Typically the differences between such quantities fall into two broad classes: those that fall off slowly with some power of $1/L$, and those that are exponentially suppressed as $e^{-L/r}$ where the finite-volume theory is defined in an L^3 cubic spatial volume and r is the range of interactions in the theory, here the interactions between hadrons. Here, we assume that $L \gg r$ such that $e^{-L/r}$ corrections can be neglected. Additionally, note that while we shall assume periodic spatial boundary conditions for the fields, $\psi(\boldsymbol{x} + \boldsymbol{n}L) = \psi(\boldsymbol{x})$ for $\boldsymbol{n} \in \mathbb{Z}^3$, others such as twisted boundary conditions, $\psi(\boldsymbol{x} + \boldsymbol{n}L) = e^{i\theta\cdot\boldsymbol{n}}\psi(\boldsymbol{x})$ for $0 \leq \theta_j \leq 2\pi$, can instead be used[3]. Finally, we restrict ourselves to energies and momenta below all three- and four-particle thresholds.

Consider the two-body interpolating operator $\sigma(x)$, that couples to all open two-body channels. The operator need not be local, though we must be able to associate it with a single spatial site x (e.g. it could be spatially extended). Define then

$$C^L(P) \equiv \int_L \mathrm{d}^4x \; e^{i(Ex_0 - \boldsymbol{P}\cdot\boldsymbol{x})} \langle 0|\sigma(x)\sigma^\dagger(0)|0\rangle, \tag{6.15}$$

where $P = (E, \boldsymbol{P})$ is the total four-momentum of the system, and the spatial integration is over the L^3 cubic volume. In infinite-volume, $C^\infty(P)$ will have branch-cuts where each two-particle threshold begins, but the quantisation of momenta in finite-volume means that these cuts will be replaced by a series of poles. The poles in $C^L(P)$ will correspond to stationary states in the finite-volume spectrum that couple to $\sigma(x)$, so that the condition that $C^L(P)$ diverges will be central to the quantisation condition we are after.

We rewrite $C^L(P)$ in terms of the Bethe-Salpeter kernel K (not to be confused with the

[3]On the CLS ensembles used for the $K\pi$ scattering analysis presented in chapter 8, open temporal boundary conditions are imposed. For further discussion, see section 2.3.2 and Refs. [88, 89].

scattering K-matrix), as illustrated in fig. 6.2,

$$\begin{aligned} C^L(P) &= \frac{1}{L^3}\sum_{\boldsymbol{q}}\int\frac{\mathrm{d}q^0}{2\pi}\,\sigma_a(q)B_a^L(q)\sigma_a^\dagger(q) \\ &+\frac{1}{L^6}\sum_{\boldsymbol{q},\boldsymbol{q}'}\int\frac{\mathrm{d}q^0}{2\pi}\frac{\mathrm{d}q'^0}{2\pi}\,\sigma_a(q)B_a^L(q)iK_{ab}(q,q')B_b^L(q')\sigma_b^\dagger(q')+\cdots\,, \end{aligned} \tag{6.16}$$

where a, b label two-particle channels, and $\sigma_a(q)$ and $\sigma_a^\dagger(q)$ are related to the Fourier transforms of $\sigma(x)$ and $\sigma^\dagger(x)$ and describe the coupling of the operators to the two-particle channel a. Their exact form is not important, all that is necessary is that they are regular functions of q. Note that tensor indices that appear when the scattering particles have non-zero spin have been suppressed. In each momentum sum the allowed momenta for periodic boundary conditions are $\boldsymbol{q} = (2\pi/L)\boldsymbol{n}$. If the two hadrons in channel a are a_1 and a_2, then

$$B_a^L(q) = \zeta_a[z_{a_1}(q)\Delta_{a_1}(q)][z_{a_2}(P-q)\Delta_{a_2}(P-q)], \tag{6.17}$$

where ζ_a is a symmetry factor, and $z_\alpha(q)\Delta_\alpha(q)$ is the fully dressed propagator for particle of type α:

$$z_\alpha(q)\Delta_\alpha(q) = \int \mathrm{d}^4x\, e^{iq\cdot x}\langle\phi_\alpha(x)\phi_\alpha^\dagger(0)\rangle, \qquad \text{(no summation over } \alpha), \tag{6.18a}$$

$$\Delta_\alpha(q) = \frac{i}{q^2 - m_\alpha^2 + i\epsilon}. \tag{6.18b}$$

Here, ϕ_α is an interpolating field for hadron type α, chosen such that $z_\alpha = 1$ when the hadron is on-shell. In eq. (6.16) both the Bethe-Salpeter kernels, iK, and residues, z_α, can be shown to have exponentially decaying finite-volume corrections which we assume are negligible [124,125]. We can therefore replace these quantities with their infinite-volume counterparts. The finite-volume loop momentum sums however cannot be replaced by momentum integrals in infinite-volume, the finite-volume corrections having a power-law dependence on the finite volume. To make this more explicit we write $B^L = B^\infty + \mathcal{F}$, where $\mathcal{F}$ captures the finite-volume corrections to B^L, shown diagrammatically in fig. 6.3. Using this then we can write the difference between our correlation function in finite- and infinite-volume as

$$\begin{aligned} C_{\text{sub}}(P) &\equiv C^L(P) - C^\infty(P) \\ &= A\mathcal{F}\sum_{n=0}^{\infty}(i\mathcal{M}\mathcal{F})^n\,A', \end{aligned} \tag{6.19}$$

where

$$A \equiv \sigma\sum_{n=0}^{\infty}(BiK)^n\,, \qquad A' \equiv \sum_{n=0}^{\infty}(iKB)^n\,\sigma^\dagger, \tag{6.20}$$

and $i\mathcal{M}$ is the usual infinite-volume scattering amplitude, here defined by

$$i\mathcal{M} \equiv iK\sum_{n=0}^{\infty}(BiK)^n\,. \tag{6.21}$$

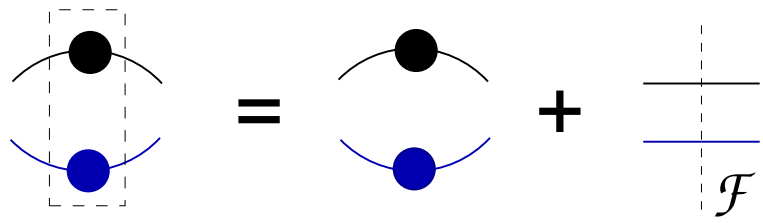

Figure 6.3: The finite-volume momentum sum/integration (indicated by the dashed rectangle) over the two single-particle fully-dressed propagators (shown on the left) equals the infinite-volume integration (first term on right with no dashed rectangle) plus a finite-volume correction $\mathcal{F}$ (the second term on the right).

These definitions are all represented diagrammatically in fig. 6.4.

Recall that the poles of $C^L(P)$ correspond to the finite-volume spectrum of interest, so then $C_{\text{sub}}(P)$ must also contain these poles, as well as cuts which must cancel those in $C^\infty(P)$. These poles can then be used to find the infinite-volume scattering amplitude at each of the discrete finite-volume energies. Noticing the appearance of a geometric series we can write

$$\begin{aligned} C_{\text{sub}}(P) &= A\mathcal{F}\sum_{n=0}^{\infty}\left(i\mathcal{M}\mathcal{F}\right)^n A' \\ &= A\mathcal{F}\left(1 - i\mathcal{M}\mathcal{F}\right)^{-1} A' \\ &= A\left(\mathcal{F}^{-1} - i\mathcal{M}\right)^{-1} A'. \end{aligned} \tag{6.22}$$

Now, the value of $\mathcal{M}$ that makes C_{sub} singular for each energy in the finite-volume spectrum gives us the relationship between finite-volume energies and the infinite-volume amplitude $\mathcal{M}$. Since the factors A and A' do not contain any singularities and have no finite-volume corrections [127], the poles in C_{sub} will correspond to the zero eigenvalues of $\mathcal{F}^{-1} - i\mathcal{M}$. This condition can be written as

$$\det[\mathcal{F}^{-1} - i\mathcal{M}] = 0. \tag{6.23}$$

This is equivalent to the determinant in eq. (6.9) where $\mathcal{F}$ and $F^{(\boldsymbol{P})}$ are related by a multiplicative kinematic factor:

$$F^{(\boldsymbol{P})} = -\frac{16\pi^2 E_{\text{cm}}}{\sqrt{\boldsymbol{q}_{\text{cm}}^2}}\mathcal{F}. \tag{6.24}$$

What remains is to find an explicit expression for calculating $\mathcal{F}$ by isolating the finite-volume corrections to the loop summations appearing in fig. 6.2, the explicit details of which are contained in Ref. [127]. From eqs. (6.16) to (6.18), we can convince ourselves that $\mathcal{F}$ will involve integrals/sums of the form

$$I \equiv \frac{1}{L^3}\sum_{\boldsymbol{k}}\int\frac{\mathrm{d}k_0}{2\pi}\frac{f(k_0,\boldsymbol{k})}{(k^2 - m_1^2 + i\epsilon)((P-k)^2 - m_2^2 + i\epsilon)}, \tag{6.25}$$

where f is a function containing no singularities for real $\boldsymbol{k}$, and has appropriate ultraviolet behaviour as to render the integral and sum convergent. By replacing certain momentum sums with integrals,

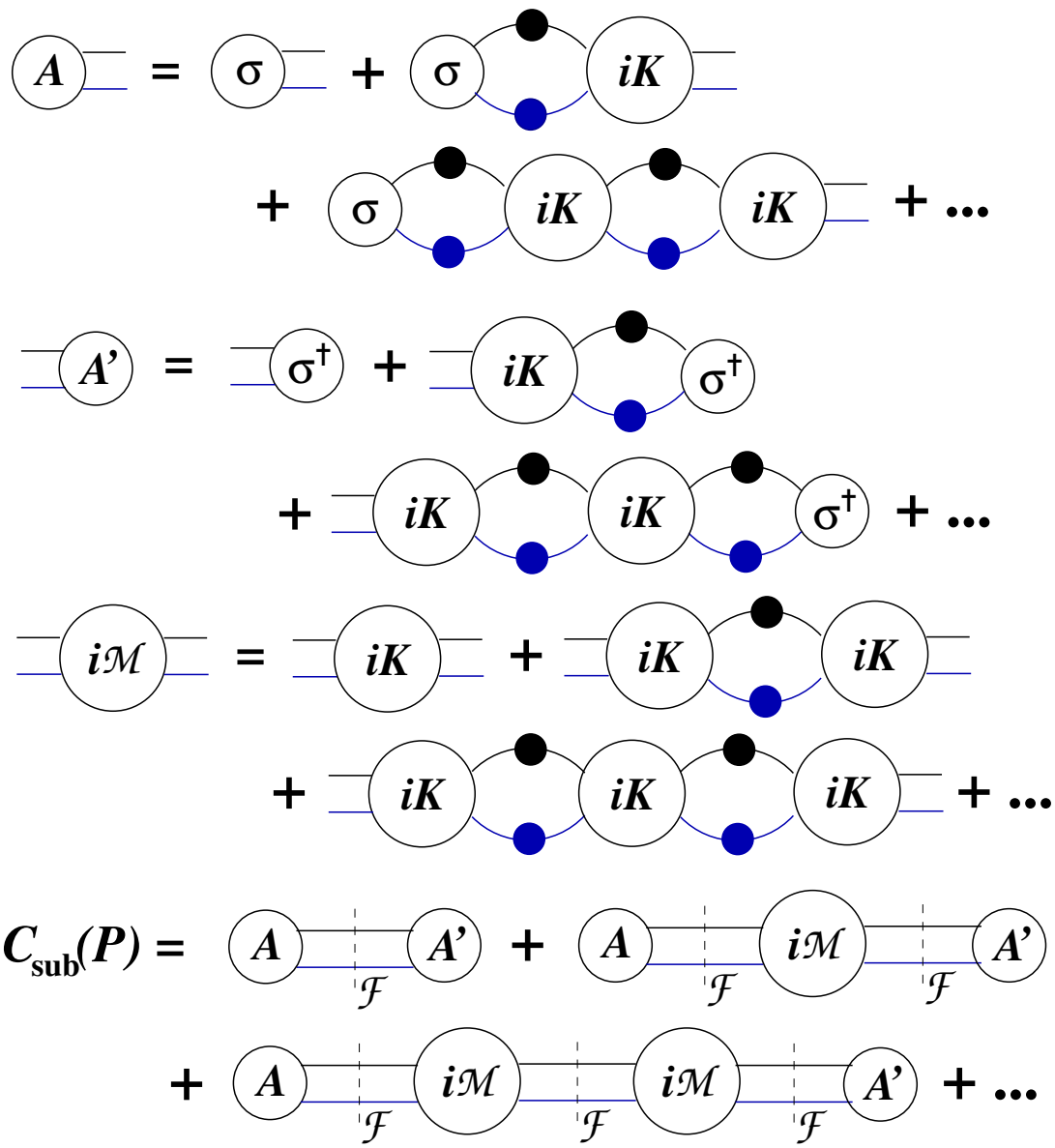

Figure 6.4: Diagrammatic expansion of $C_{\text{sub}}(P) \equiv C^L(P) - C^\infty(P)$ in terms of the quantities $A, A', i\mathcal{M}$, and $\mathcal{F}$.

etc. and ignoring contributions of $\mathcal{O}(e^{-mL})$, where m is the (lowest) mass scale of the theory/mass gap (in QCD this is the pion mass), these integrals can be written in the form

$$I = I^{\infty} + I^{\mathrm{FV}}. \tag{6.26}$$

Now that the finite-volume corrections have been isolated we can write $\mathcal{F}$ in terms of expressions like I^{FV} in which appear the RGL shifted zeta functions introduced in section 6.1.2.

6.2 Box Matrix and Block Diagonalisation

The quantisation condition as written in eqs. (6.9) and (6.23) gives us a direct relationship between the infinite-volume scattering matrix S and energies in a finite-volume spectrum. However, this only gives us a single relation between the entire scattering matrix and an energy E determined in finite-volume. In the limited case of a single scattering channel with a single partial wave we can directly extract the scattering phase shift for each energy. When multiple partial waves/decay channels are included, this single relation is not sufficient. In this case then, the S-matrix must be parameterised using some physically motivated functions of E, with some number of parameters that can be determined using a fit using a large set of finite-volume energies[4]. Historically, lattice calculations of scattering phase shifts avoided this by restricting to processes where the S matrix has a single entry. The canonical example is of $I = 1$ $\pi\pi$ scattering to study resonance parameters of the ρ resonance, where waves other than $\ell = 1$ are neglected; our analysis of which is contained in Ref. [18]. In a subsequent publication [29], we outlined our implementation of the Lüscher quantisation condition with a practical procedure for estimating the scattering matrix for multiple partial waves and decay channels, and as a first test revisited the study of ρ-meson decay including for the first time, $\ell = 3$ and $\ell = 5$ partial waves. We shall now highlight some details of that publication, in particular our use of the scattering K-matrix and the introduction of a quantity we call the *box matrix*.

6.2.1 The K-Matrix and Box Matrix

As the S-matrix is dimensionless and unitary, and it is usually easier to parameterise a real symmetric matrix than a unitary one, using the real and symmetric K-matrix is often preferred. Before introducing K, we shall review some properties of S. In a standard angular momentum basis,

$$\langle J' m_{J'} L' S' a' | S | J m_J L S a \rangle = \delta_{JJ'} \delta_{m_J m_{J'}} s^{(J)}_{L'S'a';LSa}(E), \tag{6.27}$$

[4]Note that since (usually) we are ultimately interested in the extraction of resonance parameters, decay masses/widths, etc., at some stage a parameterisation of the scattering amplitudes is unavoidable, even in the case of a 1×1 S-matrix.

where $s^{(J)}(E)$ is unitary, and $SO(3)$ rotational invariance has been assumed. Assuming invariance under spatial parity implies

$$s^{(J)}_{L'S'a';LSa}(E) = 0 \quad \text{if} \quad \eta^P_{1a}\eta^P_{1a'}\eta^P_{2a}\eta^P_{2a'}(-1)^{L+L'} = -1, \tag{6.28}$$

where η^P_{ia} is the intrinsic parity of scattering particle i in channel a. For a single elastic scattering channel involving spinless particles then, S is diagonal in J/L and typically parameterised by

$$s^{(J)} = s^{(L)} = e^{2i\delta_L(E)}, \tag{6.29}$$

where δ_L is the scattering phase shift for the L-th partial wave. Including a second channel of spinless particles leads to three parameters being needed to describe S. A typical parameterisation looks like

$$s^{(L)} = \begin{pmatrix} \eta e^{2i\delta_a^{(L)}} & i\sqrt{1-\eta^2}e^{i(\delta_a^{(L)}+\delta_b^{(L)})} \\ i\sqrt{1-\eta^2}e^{i(\delta_a^{(L)}+\delta_b^{(L)})} & \eta e^{2i\delta_b^{(L)}} \end{pmatrix}, \tag{6.30}$$

where δ_i is the scattering phase shift for channel i, and $\eta \in [0,1]$ is an inelasticity parameter. Clearly, the parameterisation of S quickly becomes tedious with the inclusion of more channels and partial waves. Also, recall that with more than one decay channel and partial wave, each of the parameters in S cannot be exactly determined from the quantisation condition. Additionally, these parameters (phase shifts, inelasticities, etc.) are often not the physical quantities that we wish to extract (resonance masses, decay widths, scattering lengths, etc.). Hence, we are incentivised to seek an alternative that simplifies the parameterisation.

Defining the transition operator T using $S = 1 + iT$, the K-matrix [149,150] can be defined by

$$K = (2T^{-1} + i)^{-1}, \qquad K^{-1} = 2T^{-1} + i, \tag{6.31}$$

so that

$$S = (1 + iK)(1 - iK)^{-1} = (1 - iK)^{-1}(1 + iK), \tag{6.32}$$

where the unitarity and invariance under time reversal of S implies that K is real and symmetric. Similar to the S-matrix, K is invariant under rotations

$$\langle J'm_{J'}L'S'a'|K|Jm_JLSa\rangle = \delta_{J'J}\delta_{m_{J'}m_J}K^{(J)}_{L'S'a';LSa}(E), \tag{6.33}$$

and under parity

$$K^{(J)}_{L'S'a';LSa}(E) = 0 \quad \text{if} \quad \eta^P_{1a}\eta^P_{1a'}\eta^P_{2a}\eta^P_{2a'}(-1)^{L+L'} = -1. \tag{6.34}$$

Following eq. (6.32) then, in the case of single channel, elastic scattering of particles without spin

$$K^{(J)} = K^{(L)} = \tan\delta_L, \tag{6.35}$$

so that the pole at $\delta_L = \frac{\pi}{2}$ is indicative of a resonance. For a short-ranged potential one can derive the so-called effective range expansion [151]

$$q_{\text{cm}}^{2L+1}\cot\delta_L(q_{\text{cm}}) = q_{\text{cm}}^{2L+1}K_L^{-1} = \sum_{n=0} c_{2n}q_{\text{cm}}^{2n} = -\frac{1}{a_L} + \frac{r_L}{2}q_{\text{cm}}^2 + \mathcal{O}(q_{\text{cm}}^4), \tag{6.36}$$

where $q_{\rm cm} = \sqrt{\boldsymbol{q}_{\rm cm}^2}$, the constants a_L are referred to as scattering lengths[5], and r_L as the effective ranges. The generalisation to multiple channels [152, 153] and the way in which K^{-1} appears in eq. (6.36) suggests the convenience of writing

$$K^{-1}_{L'S'a';LSa}(E_{\rm cm}) = \left(\frac{\boldsymbol{q}_{{\rm cm},a'}}{m_{\rm ref}}\right)^{-L'-\frac{1}{2}} \widetilde{K}^{-1}_{L'S'a';LSa}(E_{\rm cm}) \left(\frac{\boldsymbol{q}_{{\rm cm},a}}{m_{\rm ref}}\right)^{-L-\frac{1}{2}}, \tag{6.37}$$

where $\widetilde{K}^{-1}(E_{\rm cm})$ is a real, symmetric, and analytic function of the centre-of-momentum energy $E_{\rm cm}$, and $m_{\rm ref}$ is some reference mass, typically the pion mass, used to make $\widetilde{K}^{-1}$ dimensionless. Note the normalisation of $\widetilde{K}^{-1}$ here differs from eq. (19) of Ref. [29] and instead follows that of Ref. [19] where dependence on the dimension of the finite-volume, L, has been replaced by $m_{\rm ref}$. Using the new normalisation, the $\widetilde{K}$ matrix does not pick up a dependence on any finite-volume quantity, and a Breit-Wigner parameterisation for example will take its canonical form.

With these definitions, it is then straightforward to show that the quantisation condition of eqs. (6.9) and (6.23) can be written as

$$\det[1 - B^{(\boldsymbol{P})}\widetilde{K}] = \det[1 - \widetilde{K}B^{(\boldsymbol{P})}] = 0, \tag{6.38}$$

where we define the *box matrix* by

$$\begin{aligned}\langle J'm_{J'}L'S'a'|B^{(\boldsymbol{P})}|Jm_JLSa\rangle \equiv -i\delta_{a'a}\delta_{S'S}\left(\frac{\boldsymbol{q}_{{\rm cm},a}}{m_{\rm ref}}\right)^{L+L'+1} W^{(\boldsymbol{P})}_{L'm_{L'};Lm_L} \\ \times \langle J'm_{J'}|L'm_{L'}Sm_S\rangle\langle Lm_LSm_S|Jm_J\rangle.\end{aligned} \tag{6.39}$$

Again, note the slight change in normalisation from Ref. [29] to ensure that $\widetilde{K}$ contains no dependence on the finite-volume. When $\det\widetilde{K} \neq 0$, which is generally true in the presence of interactions, the quantisation can also be written as

$$\det[\widetilde{K}^{-1} - B^{(\boldsymbol{P})}] = 0. \tag{6.40}$$

Since the box matrix $B^{(\boldsymbol{P})}$ is Hermitian for real $\boldsymbol{q}^2_{{\rm cm},a}$, and $\widetilde{K}$ is real and symmetric for real $\boldsymbol{q}^2_{{\rm cm},a}$ ensures that each of these determinants are real. Note that since $\widetilde{K}$ and $B^{(\boldsymbol{P})}$ do not always commute, $1 - B^{(\boldsymbol{P})}\widetilde{K}$ and $1 - \widetilde{K}B^{(\boldsymbol{P})}$ will not be Hermitian. Despite this, it is straightforward to show that each of their determinants must be real.

6.2.2 Block Diagonalisation

So far, the matrices $F^{(\boldsymbol{P})}$ and $B^{(\boldsymbol{P})}$ have been expressed in terms of the orthonormal centre-of-momentum frame $|Jm_JLSa\rangle$ basis states. This presents difficulties when evaluating the determinants in eqs. (6.9), (6.23), (6.38), and (6.40) as the matrices in each of these expressions are of infinite dimension. If we can transform to a basis in which both $B^{(\boldsymbol{P})}$ and $\widetilde{K}$ are block diagonal, then

[5] Despite only the s-wave constant a_0 having units of length!

Table 6.1: Relationship between box matrix irrep Λ_B and full symmetry irrep Λ when $\eta^P_{1a}\eta^P_{2a} = -1$. When $\eta^P_{1a}\eta^P_{2a} = 1$, $\Lambda_B = \Lambda$. Recall that subscript g and u denote even and odd parity respectively. "LG" below denotes little group.

$\boldsymbol{d}$	LG	Λ_B relationship to Λ when $\eta^P_{1a}\eta^P_{2a} = -1$
$(0,0,0)$	O_h	Subscript $g \leftrightarrow u$
$(0,0,n)$	C_{4v}	$A_1 \leftrightarrow A_2;\ B_1 \leftrightarrow B_2;\ E, G_1, G_2$ unchanged
$(0,n,n)$	C_{2v}	$A_1 \leftrightarrow A_2;\ B_1 \leftrightarrow B_2;\ G$ unchanged
(n,n,n)	C_{3v}	$A_1 \leftrightarrow A_2;\ F_1 \leftrightarrow F_2;\ E, G$ unchanged

the determinant can be considered separately in each block[6]. Each block will still have infinite dimension, but we can truncate each block in orbital angular momentum, keeping only basis states with $L \leq L_{\max}$, so that each truncated block is finite and reasonably sized for our computations. An additional important motivation is that the finite-volume energies we extract are in a basis diagonal in irreps of the lattice symmetry group. Hence, to block diagonalise $B^{(\boldsymbol{P})}$, we apply the unitary change of basis

$$|\Lambda\lambda nJLSa\rangle = \sum_{m_J} c^{J\eta;\Lambda\lambda n}_{m_J} |Jm_JLSa\rangle, \tag{6.41}$$

where Λ and λ label the irrep and irrep row of the little group of $\boldsymbol{P}$, n is an integer identifying each occurrence of the irrep Λ in the $|Jm_JLSa\rangle$ reducible representation, and $\eta = (-1)^L$. Our procedure for computing the transformation coefficients is outlined in Ref. [29].

In this new basis then, the box matrix is diagonal in Λ, λ, but not in the occurrence index n, and takes the following form

$$\langle\Lambda'\lambda'n'J'L'S'a'|B^{(\boldsymbol{P})}|\Lambda\lambda nJLSa\rangle = \delta_{\Lambda'\Lambda}\delta_{\lambda'\lambda}\delta_{S'S}\delta_{a'a}B^{(\boldsymbol{P}\Lambda_B Sa)}_{J'L'n';JLn}(E). \tag{6.42}$$

The box matrix depends on a only through the kinematic quantities u_a and $\boldsymbol{s}_a$. Note that in eq. (6.42) the irrep label Λ_B is used instead of Λ to label the matrix elements of $B^{(\boldsymbol{P})}$. This distinction arises because the box matrix is insensitive to the intrinsic parities of the scattering particles in a given scattering channel a, whereas we include intrinsic parity in our choice of Λ irreps. If $\eta^P_{1a}\eta^P_{2a} = 1$, then $\Lambda_B = \Lambda$, however if $\eta^P_{1a}\eta^P_{2a} = -1$ then this is in general not true. The relationships between Λ_B and Λ in this case for various momenta $\boldsymbol{P}$ are summarised in table 6.1. Software to evaluate the box matrix elements for total momentum $\boldsymbol{P} = (0,0,0), (0,0,n)$ with $L \leq 6$, $S \leq 2$ and for $\boldsymbol{P} = (0,n,n), (n,n,n)$ with $L \leq 6$, $S \leq \frac{3}{2}$ is available [154] and described in Ref. [29].

Now we need to express the $\widetilde{K}$ matrix in the new basis. One can show that

$$\langle\Lambda'\lambda'n'J'L'S'a'|\widetilde{K}|\Lambda\lambda nJLSa\rangle = \delta_{\Lambda'\Lambda}\delta_{\lambda'\lambda}\delta_{n'n}\delta_{J'J}\widetilde{K}^{(J)}_{L'S'a';LSa}(E_{\mathrm{cm}}), \tag{6.43}$$

[6]Since $\det\begin{pmatrix} A_1 & & 0 \\ & \ddots & \\ 0 & & A_n \end{pmatrix} = \det A_1 \ldots \det A_n$, the quantisation condition is satisfied whenever any of the individual blocks has a zero determinant.

for $\eta = \eta'$ where $\eta = (-1)^L$ and $\eta' = (-1)^{L'}$. If $\eta = -\eta'$ the situation is much more complicated, but in QCD, we should never need such matrix elements. Since all meson-meson and baryon-baryon states of potential interest have $\eta_{1a}^P \eta_{2a}^P = 1$, and meson-baryon states of interest have $\eta_{1a}^P \eta_{2a}^P = -1$, and in QCD we should never need 2-to-2 K-matrix elements between states with differing products of intrinsic parities, the expression above is sufficient for our purposes. In other field theories, it may occur that $\eta_{1a}^P \eta_{2a}^P = -\eta_{1a}^{P'} \eta_{2a}^{P'}$, in which case eq. (6.43) must be generalised.

Finally, note that while the box matrix is diagonal in total spin S and channel a, $\widetilde{K}$ allows mixing between different spins and channels. Hence, the block structure of the box matrix alone differs from that of $1 - B^{(\boldsymbol{P})}\widetilde{K}$ and $\widetilde{K}^{-1} - B^{(\boldsymbol{P})}$. Looking at eqs. (6.42) and (6.43) we can show that, for a given $\boldsymbol{P}$, we can label the quantisation blocks of $1 - B^{(\boldsymbol{P})}\widetilde{K}$ and $\widetilde{K}^{-1} - B^{(\boldsymbol{P})}$ in the $|\Lambda\lambda nJLSa\rangle$ basis solely by the irrep label Λ, where Λ is the irrep associated with the K-matrix.

6.3 Fitting the K-Matrix

To close off this chapter, we now discuss some important details in implementing the quantisation condition of eqs. (6.9), (6.23), (6.38), and (6.40) for determining best fits to a given $\widetilde{K}$-matrix parameterisation. Two methods of fitting the elements of $\widetilde{K}$ are presented in Ref. [29], one of which we advocate for and use in our calculations. The main point stressed in this section is the impact that different choice of residuals can have in a χ^2 minimisation. If the model used has some dependence on the data (observables), then the covariance between the residuals which depend on model parameters must be computed. During the minimisation process then, as the fit parameters are adjusted, these covariances must be recomputed and the covariance matrix needs to be inverted. This can very quickly become computationally intensive, and so we seek models with no dependence on the observables so that the covariance matrix doesn't need to repeatedly be recomputed. For a review of correlated χ^2 fitting see section A.2.

Since the Lüscher quantisation condition relates a finite-volume spectrum to the infinite-volume $\widetilde{K}$-matrix, one may be inclined to choose as residuals the difference between the observed energy levels from a lattice calculation, and the predicted energies given by a particular parameterisation of $\widetilde{K}$. Explicitly,

$$r_k = E_{\mathrm{cm},k}^{(\mathrm{obs})} - E_{\mathrm{cm},k}^{(\mathrm{model})}, \qquad (k = 1, \ldots, N_E), \tag{6.44}$$

where $E_{\mathrm{cm},i}^{(\mathrm{obs})}$ are the measured energies determined from the lattice, and $E_{\mathrm{cm},i}^{(\mathrm{model})}$ are energies determined by inverting the quantisation condition for a given parameterisation of $\widetilde{K}$. We describe in detail this method, and a trick in the spirit of Lagrange multipliers for making the implementation slightly easier in Ref. [29]. However, as we outline in that paper, the complicated root finding involved in inverting the quantisation condition means that using this "spectrum method", while properly considering all covariances, remains quite an onerous task. As such, we are led to seek out a different choice of residuals for which the minimisation process may be more straightforward.

6.3.1 Determinant Residual Method and the Ω Function

In this alternative method, we introduce the quantisation determinant itself as the residual. The determinant uses the observed box matrix elements, containing the observed values for finite-volume energies, scattering particle masses, box size, and where relevant, the lattice anisotropy.

Recall from eqs. (6.22) and (6.23) that expressing the quantisation condition in terms of a vanishing determinant is just a convenient way of stating the appearance of a zero eigenvalue. In the case of very large matrices, the magnitude of the determinant can become very large, making it more difficult to find zeroes. This leads us to propose the following function of matrix A, with real determinant, and some scalar $\mu \neq 0$:

$$\Omega(\mu; A) \equiv \frac{\det(A)}{\det[(\mu^2 + AA^\dagger)^{\frac{1}{2}}]}. \tag{6.45}$$

When A has a zero eigenvalue this function will also be zero, replicating the quantisation condition. The advantage of using Ω is that, when the determinant is real, it should be bounded between -1 and 1. Therefore we can choose the residuals to be

$$r_k = \begin{cases} \Omega\left(\mu, 1 - B^{(\boldsymbol{P})}(E^{(\mathrm{obs})}_{\mathrm{cm},k})\widetilde{K}(E^{(\mathrm{obs})}_{\mathrm{cm},k})\right), \\ \qquad\qquad \text{or} \\ \Omega\left(\mu, \widetilde{K}^{-1}(E^{(\mathrm{obs})}_{\mathrm{cm},k}) - B^{(\boldsymbol{P})}(E^{(\mathrm{obs})}_{\mathrm{cm},k})\right), \end{cases} \qquad (k = 1, \ldots, N_E), \tag{6.46}$$

where μ can be chosen to optimise the numerical χ^2 minimisation. Since here the model predictions remain dependent on the observables, so the covariances between residuals must be recomputed and inverted during the minimisation as the fit parameters are adjusted. Despite this, the method remains much simpler than the root finding involved in the spectrum method above. The advantage lies in the box matrix elements being treated as observables; the complicated RGL zeta functions contained within need not be recomputed as the model parameters are adjusted. In Ref. [29] numerical tests of this determinant residual method are presented for $I = 1$ $\pi\pi$ scattering with the first inclusion of partial wave mixing up to $\ell = 5$. There we show the insensitivity in best fit parameters to choice of residual and for the Ω-function, to tuning of μ.

Chapter 7

The Scalar Glueball

In this chapter, we present the first of the two analyses in this thesis, a study of the low-lying hadronic spectrum in the scalar isoscalar zero-strangeness sector, with the main goal of addressing the issue of the scalar glueball. This is the first study to include the mixing between glueball, meson, and meson-meson operators in dynamical QCD. In chapter 1 we gave an overview of the current experimental and theoretical status of glueballs. In particular, since glueball spectroscopy in pure gauge theories is one of the first major successes of lattice field theory, we highlight the progress that has been made in lattice studies to date, along with the technical difficulties in making the jump from pure Yang-Mills theories to full QCD, including the effects of dynamical quarks. Details of the analysis are outlined then in section 7.1, followed by the spectrum results and further discussion in section 7.2.

7.1 Analysis Details

Correlation functions involving glueball operators are notoriously difficult to measure in lattice QCD, requiring prohibitively large computational resources to achieve even modest statistical precision. The signal-to-noise ratio for these quantities falls extremely rapidly with increasing separation between source and sink as the relevant interpolating operators have rather large vacuum expectation values. This prohibits the lattice from being too large, as the magnitude of these vacuum fluctuations will scale with the lattice volume. On the other hand, due to the large masses of these states, lattice studies of glueballs require very fine temporal lattice spacings so that a reliable signal can be measured. As both of these considerations have a significant effect on the required computational resources, we confront this difficulty by using an anisotropic lattice that is spatially coarse and temporally fine [80]. In this section we discuss the particular anisotropic ensemble of gauge configurations we use, along with discussions on the operators used, and on the subtleties of correctly dealing with the large vacuum fluctuations in the scalar sector.

Table 7.1: Details of the anisotropic ensemble used in the scalar glueball study. The anisotropy $\xi = a_s/a_t$ has been determined by enforcing the relativistic dispersion relation for the pion (eq. (2.72)), though the value is insensitive to the hadron used.

$(L/a_s)^3 \times (T/a_t)$	N_{cfgs}	a_s	ξ_π	$a_t m_\pi$	$a_t m_K$	$m_\pi L$
$24^3 \times 128$	551	0.12 fm	3.4464(71)	0.06901(17)	0.09689(15)	5.7

7.1.1 Ensemble Info

For this study we use a single anisotropic ensemble of $N_f = 2+1$ Wilson clover fermions generated by the Hadron Spectum collaboration [71,72], described in detail in sections 2.3.1 and 2.3.3. Various ensemble properties are listed in table 7.1. The dynamical quark parameters chosen, $a_t m_l = -0.084$ and $a_t m_s = -0.0743$, result in unphysically heavy hadron masses, with $m_\pi \sim 390$ MeV, and $m_K \sim 550$ MeV. Our results will primarily be presented as dimensionless ratios using a reference mass, $m_{\text{ref}} = 2m_K$. Note that this ensemble has been used in a previous study of the isoscalar $\pi\pi$ scattering in Ref. [155]. This will be discussed again in section 7.2 where we identify a stable σ meson state at these heavy quark masses.

7.1.2 Correlator Matrix Construction

The finite-volume stationary state energies are determined from a matrix of temporal correlation functions, $C_{ij}(t) = \langle 0|\mathcal{O}_i(t)\overline{\mathcal{O}}_j(0)|0\rangle$, using the methods described in chapter 5. The construction of operators $\mathcal{O}_i$ is described in chapter 3 and Ref. [109], here designed to transform irreducibly in the at-rest, isoscalar A_{1g}^+ irrep of the octahedral symmetry group and with zero total momentum. In order to include both the isoscalar single-hadron operators with disconnected quark annihilation diagrams, and two-hadron operators with definite constituent momenta, we need to calculate expensive all-to-all quark propagators between each spacetime point on the lattice. We use the stochastic LapH method [15] described in chapter 4 to evaluate these all-to-all quark propagators, allowing us to include for the first time meson and meson-meson operators with glueball operators. Here, using the stochastic LapH method also has the advantage of giving us a scalar glueball operator with no added cost as described in section 3.6.2.

The operator basis used is chosen such that as many single- and two-particle states < 2 GeV are extracted as possible. For the isoscalar single-hadron $\overline{q}q$ operators, we use operators with flavour structures $s\bar{s}$ and $(u\bar{u} + d\bar{d})$, including one of each for every expected $\overline{q}q$ level we wish to extract. This is detailed in Ref. [19] where, to extract the η meson mass, we include both $s\bar{s}$ and $(u\bar{u} + d\bar{d})$ interpolators in a 2×2 GEVP and identify the ground and first excited eigenstates as the η and η' meson respectively. This is in contrast to using definite $SU(3)_f$ eigenstates[1], though we expect our spectrum determination to be insensitive to this choice as solving the GEVP with either set of operators should yield the correct finite-volume eigenstates. We include $\pi\pi$, $\eta\eta$, and $K\overline{K}$

[1]Singlet: $\mathcal{O}_1 = \frac{1}{\sqrt{3}}\left(u\bar{u} + d\bar{d} + s\bar{s}\right)$, Octet: $\mathcal{O}_8 = \frac{1}{\sqrt{6}}\left(u\bar{u} + d\bar{d} - 2s\bar{s}\right)$.

two-hadron operators with various definite back-to-back momenta for each of the allowed two-body decay channels in this sector. Note that we do not include any 4π operators in our calculation. The inclusion of $\eta\eta$ interpolating operators introduces further computational complexity as additional diagrams containing internal loops (e.g. diagrams 3-6 in fig. 4.4) for each constituent isoscalar η meson increase the computational cost of, and statistical noise in our calculation.

Finally, we include the so-called TrLapH scalar glueball operator, described in section 3.6.2, constructed using the eigenvalues of the covariant Laplacian:

$$G_\Delta = -\operatorname{Tr}[\Theta(\sigma_s^2 + \widetilde{\Delta})\widetilde{\Delta}]. \tag{7.1}$$

While any purely gluonic quantity (with the appropriate transformation properties) could be used to describe the scalar glueball, in order to reliably extract a signal we must use optimal operators for which a signal is seen before being overwhelmed by statistical noise. Thankfully the TrLapH operator is shown in Ref. [109], and in fig. 3.6, to be comparable in usefulness to a standard 3×3 Wilson loop operator.

7.1.3 Correlator Matrix Analysis

We extract the low-lying spectrum of finite-volume stationary state energies by solving the GEVP in eq. (5.9) using the single pivot method detailed in chapter 5. We fit the diagonal elements of $\widetilde{D}(t)$ to single- or multi-exponential forms that tend to $A_n e^{-E_n t}$ for large times to obtain the finite-volume energies, E_n, and operator overlap Z-factors, $|Z_j^{(n)}| \equiv \langle 0|\mathcal{O}_j|n\rangle$. Jackknife resampling is used throughout to estimate errors on any fitted energies and Z-factors.

As the operators that transform irreducibly in the at-rest A_{1g}^+ irrep share quantum numbers with the vacuum, they are expected to have (sometimes very large) non-zero vacuum expectation values (VEVs). These must be subtracted when doing our analysis:

$$C_{ij}(t) \to \langle 0|\mathcal{O}_i(t)\overline{\mathcal{O}}_j(0)|0\rangle - \langle 0|\mathcal{O}_i(t)|0\rangle\langle 0|\overline{\mathcal{O}}_j(0)|0\rangle. \tag{7.2}$$

The need to subtract the vacuum expectation values $\langle 0|\mathcal{O}_i|0\rangle$ presents an additional difficulty when the glueball operator is included in the correlation matrix. Even in the moderately sized volume we employ here, the magnitude of $\langle 0|\mathcal{O}_{G_\Delta}|0\rangle$ is very large, and there is significant statistical noise in any of the correlation functions of G_Δ. For example, before VEV subtraction, the glueball correlation function at a time separation of $t = 5a_t$ is $C(5) = 4459(25)$, whereas subtracting the VEV as in eq. (7.2) gives $C(5) = 0.00540(21)$. To decrease computational costs, the gauge configurations used here were generated using single precision. We have checked that the VEV-subtracted glueball correlator can still be reliably estimated for temporal separations up to $t = 10a_t$ or so. The large statistical uncertainties which result upon including a glueball operator require us to use aggressive noise reduction techniques in order to reliably extract a signal.

Symmetry arguments tell us that the correlation matrix we are estimating should be real and symmetric. Our stochastic estimates of the matrix elements show that the imaginary parts are all

statistically consistent with zero, rather than exactly zero. Consider for example, the off-diagonal matrix elements with the glueball operator at the source/sink in fig. B.3. Here there are two important features of note. First, there is significant statistical noise in most of these matrix elements, and second there are some matrix elements (e.g. $\langle \mathcal{O}_{G_\Delta} \mathcal{O}_{\pi(2)\pi(2)} \rangle$) for which the mean value of our estimate of the imaginary part is systematically shifted away from zero. This hints at the difficulty in accurately estimating the VEVs for some of these operators. We find that in order to maintain a correlation matrix that is positive semi-definite when the glueball operator is included, we must explicitly set the imaginary parts of the correlation matrix to be zero. We observe that when the glueball operator is omitted, the finite-volume spectrum is unaffected by explicitly setting the imaginary components to be zero.

The significant statistical noise present in the VEV-subtracted correlators presents an additional problem when using the single pivot method described in section 5.1.2. As the diagonalisation is only performed on the full sample estimate of the correlator matrix (i.e. the matrix $\widetilde{V}$ in eq. (5.20) used to diagonalise the correlator matrix), statistical noise in the matrix elements is not taken into account here. This is usually not a problem since the single pivot is done at time separations where the statistical errors are very small, but in the presence of a glueball operator, even pivots done at small time separations can be adversely affected by the dramatically increased noise. See for example the $\langle \mathcal{O}_{G_\Delta} \mathcal{O}_{VV} \rangle$ matrix elements in figs. B.2b and B.2c, where $\mathcal{O}_{VV}$ is one of the vector-vector two-particle operators. We found that bias in the pivot from a few exceptionally noisy matrix elements could be prevented by setting these three $\langle \mathcal{O}_{G_\Delta} \mathcal{O}_{VV} \rangle$ matrix elements that are statistically zero to be exactly zero for our analysis.

Identifying a glueball state from a finite-volume study presents a major challenge for a number of reasons. First, as only a select few hadrons are stable under the strong force (i.e. π, K, N, etc.), any potential glueball or $\overline{q}q$ state in this sector would in infinite-volume manifest as an unstable resonance. We usually find that we can associate a "precursor" stationary state in finite volume with an infinite-volume quark-antiquark resonance, whereas with hadron-hadron molecular-type resonances this is not the case. This suggests that if a well-defined glueball resonance exists in infinite volume, we might expect the occurrence of an associated precursor state in finite volume predominantly created by a glueball operator, but given our lack of understanding of gluonic states, such an expectation cannot be fully justified. For a rigorous confirmation of a glueball resonance, an in-depth scattering analysis (see chapter 6) is required, but such calculations are currently not feasible. Furthermore, identifying the hadronic content of a particular finite-volume eigenstate is often difficult, in particular when we look at excited states in a given channel. In regions where finite-volume energies are expected to be shifted significantly from their non-interacting counterparts, i.e. where interactions are strong, we find the mixing between states to be more pronounced. This is seen in the operator overlap Z-factors, where multiple operators can create states with significant overlaps onto some of the same stationary states. Nevertheless, such mixing still offers a qualitative insight into the nature of potential resonant states. For example, a state with significant overlaps with those created by both $\overline{q}q$ and $\pi\pi$ interpolators might indicate a

Table 7.2: The single- and two-hadron interpolating operators we use in this study. Total integer momentum-squared for each individual hadron is shown in parentheses. Superscripts, where applicable, indicate displacement type for the individual hadrons, shown in fig. 3.3. Subscripts denote which irrep of the appropriate little group each individual hadron of definite momentum transforms under. We follow the notation established in chapter 3. The single-hadron operators listed in red are used only the operator pruning in fig. 7.1 for reasons discussed in the text.

Single-Hadron Operators	**Two-Hadron Operators**
$G_\Delta(0)_{A_{1g}^+}$	$\boldsymbol{\pi}(0)^{\mathtt{SS0}}_{A_{1u}^-} - \boldsymbol{\pi}(0)^{\mathtt{SS0}}_{A_{1u}^-}$
$(\bar{u}u + \bar{d}d)(0)^{\mathtt{SS0}}_{A_{1g}^+}$	$\boldsymbol{\pi}(1)^{\mathtt{SS1}}_{A_2^-} - \boldsymbol{\pi}(1)^{\mathtt{SS1}}_{A_2^-}$
$\bar{s}s\,(0)^{\mathtt{SS0}}_{A_{1g}^+}$	$\boldsymbol{\pi}(2)^{\mathtt{SS0}}_{A_2^-} - \boldsymbol{\pi}(2)^{\mathtt{SS0}}_{A_2^-}$
$(\bar{u}u + \bar{d}d)(0)^{\mathtt{SD2}}_{A_{1g}^+}$	$\boldsymbol{\rho}(0)^{\mathtt{SS0}}_{T_{1u}^+} - \boldsymbol{\rho}(0)^{\mathtt{SS0}}_{T_{1u}^+}$
$\bar{s}s\,(0)^{\mathtt{SD2}}_{A_{1g}^+}$	$\boldsymbol{\rho}(1)^{\mathtt{SS1}}_{A_1^+} - \boldsymbol{\rho}(1)^{\mathtt{SS1}}_{A_1^+}$
	$\boldsymbol{K}(0)^{\mathtt{SS0}}_{A_{1u}} - \boldsymbol{K}(0)^{\mathtt{SS0}}_{A_{1u}}$
	$\boldsymbol{K}(1)^{\mathtt{SS1}}_{A_2} - \boldsymbol{K}(1)^{\mathtt{SS1}}_{A_2}$
	$\boldsymbol{\eta}(0)^{\mathtt{SS0}}_{A_{1u}^+} - \boldsymbol{\eta}(0)^{\mathtt{SS0}}_{A_{1u}^+}$
	$\boldsymbol{\eta}(1)^{\mathtt{SS1}}_{A_2^+} - \boldsymbol{\eta}(1)^{\mathtt{SS0}}_{A_2^+}$
	$\boldsymbol{\omega}(0)^{\mathtt{SS0}}_{T_{1u}^-} - \boldsymbol{\omega}(0)^{\mathtt{SS0}}_{T_{1u}^-}$

resonance which in infinite-volume decays to two pions (e.g. $\rho \to \pi\pi$).

7.2 Results

As our aim is to study the mixing between glueball, conventional hadron, and hadron-hadron states, we will first look at the low-lying finite-volume spectrum obtained using only $\overline{q}q$, and meson-meson interpolating operators in the correlator matrix. We begin with a two-hadron operator for each expected two-hadron state in this sector, adding additional operators with various flavour, etc. structures until no new finite-volume states appear in the energy region of interest (i.e. below $\sim 2m_{\text{ref}}$). Single-hadron $\overline{q}q$ operators are chosen in a similar way, including one of each isoscalar flavour structure with various displacement types until the extra states lie well above the energy range of interest. We find that only two $\overline{q}q$ operators are necessary (one of each flavour type), as including any additional operators produce finite-volume states well outside the energy region of interest. This is shown in fig. 7.1 where the finite-volume levels from a 4×4 correlator matrix of $\overline{q}q$ operators produce only two states below $\sim 2m_{\text{ref}}$. We therefore need only include two $\overline{q}q$ operators in the final operator set. This has also been confirmed by adding a variety of additional $\overline{q}q$ operators to the 13×13 correlation matrix and observing no new finite-volume levels below $\sim 2m_{\text{ref}}$.

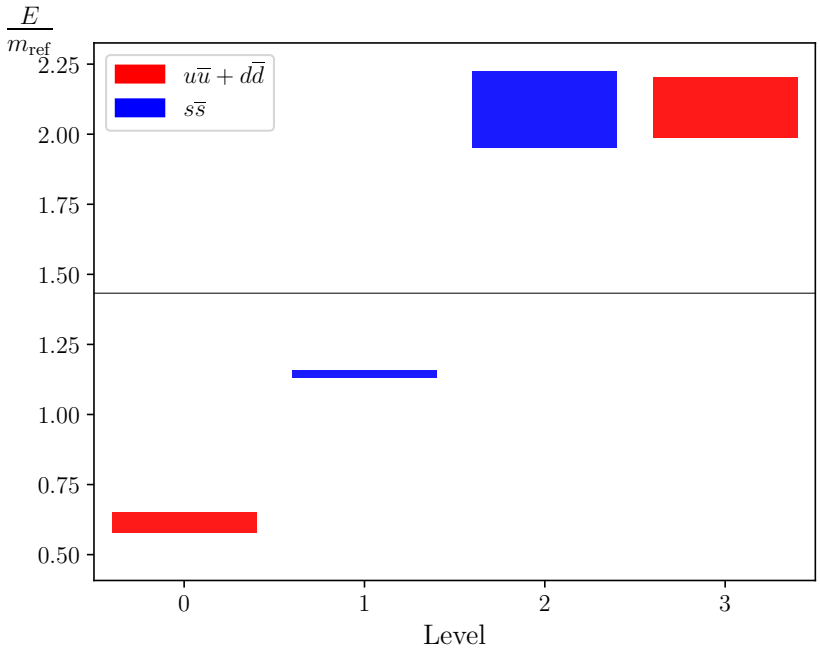

Figure 7.1: Finite-volume energies in the $I = 0$, $S = 0$, A_{1g}^{+} channel for levels with significant overlap onto states produced only by quark-antiquark operators. A 4×4 correlation matrix, including only $\overline{q}q$ operators, is used to extract these levels, with using the single-hadron operators listed in table 7.2. 1σ uncertainties are denoted by the box heights. Levels are coloured indicating the operator flavour type with maximal overlap onto that state. The solid horizontal black line indicates the 4π threshold. $m_{\text{ref}} = 2m_K$. These energies do not change appreciably when other $\overline{q}q$ operators are included in a larger correlation matrix with meson-meson operators and the glueball operator.

The final chosen operator set, including the glueball operator that we initially omit, is listed in table 7.2. Throughout, we normalise the correlator matrices using eq. (5.2), choosing $\tau_N = 3$. The severity of noise at early time separations in the $\eta\eta$ operators (and also in the glueball operator) necessitates rather early GEVP metric and diagonalisation times of $(\tau_0, \tau_D) = (3, 6)$. We have also used various combinations of times including $\tau_0 = 3, 4$, $\tau_D = 4, 5, 6, 7, 8$ to check that the results do not change. With these choices, the matrices remain well conditioned, with the condition numbers of $C(\tau_0)$ and $\widetilde{G}(\tau_D)$ being 3.53 and 2.42 respectively, and the off-diagonal elements of the resultant rotated correlator matrix $\widetilde{D}(t)$ being statistically consistent with zero for $t > \tau_D$. Fit results *excluding the glueball operator* are then listed in table 7.3, with effective mass plots for each level with best-fit curves overlaid shown in fig. 7.2. Overlap Z-factors are shown in fig. 7.3, and then the spectrum is shown in the staircase plot in fig. 7.6.

We then *include* a scalar glueball operator in the operator basis and extract the spectrum using the same GEVP parameters, $(\tau_0, \tau_D) = (3, 6)$. We find the condition numbers of $C(\tau_0)$ and $\widetilde{G}(\tau_D)$ to be 4.37 and 2.50 respectively, crucially indicating that the correlation matrix remains

Table 7.3: Fit results for a 12×12 correlation matrix in the A_{1g}^{+} channel excluding the glueball operator. Exponential fit forms are assumed to be *time-forward*, as described in section 5.3, unless otherwise stated. $m_{\text{ref}} = 2m_K$.

Level	**Model**	t_{min}	t_{max}	$a_t E_{\text{fit}}$	$E_{\text{fit}}/m_{\text{ref}}$	χ^2/d.o.f.
0	2-exp	3	25	0.1273(24)	0.657(13)	1.18
1	2-exp	4	25	0.1467(24)	0.757(12)	2.01
2	2-exp	4	25	0.2024(15)	1.0445(82)	1.61
3	1-exp	14	25	0.2090(27)	1.079(14)	2.05
4	1-exp	11	24	0.2350(37)	1.213(19)	1.20
5	2-exp	4	25	0.2647(30)	1.366(15)	1.22
6	1-exp	7	19	0.299(17)	1.545(87)	2.05
7	1-exp	5	20	0.323(28)	1.66(15)	1.20
8	1-exp	9	20	0.336(20)	1.73(10)	0.59
9	2-exp	3	14	0.3481(61)	1.797(31)	1.36
10	2-exp	4	20	0.3492(35)	1.802(19)	0.95
11	1-exp+C	9	20	0.3641(25)	1.879(13)	0.72

well-conditioned with the addition of the noisy glueball operator. Fit results are listed in table 7.4, with effective mass plots for each level including best-fit curves overlaid shown in fig. 7.4. Overlap Z-factors for each operator in the basis are shown in fig. 7.5, and the spectrum is shown in the staircase plot in fig. 7.7.

Looking first at the states below 4π in figs. 7.6 and 7.7, indicated by the horizontal dashed line, with the exception of some increased statistical noise, the spectrum below 4π is insensitive to the addition of the glueball operator. The overlap factors in figs. 7.3 and 7.5 show that there is minimal mixing in this region and so level identification is relatively straightforward and is indicated by the colouring of the energy levels. The overlap factors for the $(\overline{u}u + \overline{d}d)$ SS0 quark-antiquark operator in fig. 7.5(e) show that this operator very predominantly creates level 0. Scanning all of the other overlap factor plots, one sees that only the $s\overline{s}$ SS0 quark-antiquark operator in fig. 7.5(f) and, remarkably, the glueball operator in fig. 7.5(a) produce appreciable overlaps with level 0. Since level 0 is predominantly created by the $(\overline{u}u + \overline{d}d)$ SS0 quark-antiquark operator, we interpret this state as the finite-volume counterpart of the σ resonance. This is consistent with the $\pi\pi$ scattering study of Ref. [155] where a bound state σ meson is found below the $\pi\pi$ threshold. Similarly, from figs. 7.5(b) and 7.5(f), levels 1 and 2 are created by the $\pi(0)\pi(0)$ and $s\overline{s}$ SS0 quark-antiquark operators, respectively, where the integers indicate the square of the hadron momentum, in units of $2\pi/L$. As level 2 is predominantly created by a $\overline{q}q$ interpolating operator, we identify level 2 as the finite-volume counterpart of the $f_0(980)$ resonance, just above the $K\bar{K}$ threshold.

Making our way above the 4π threshold, we can assess the influence that the inclusion of the scalar glueball operator has on the spectrum. Note that the levels in this region have been reordered

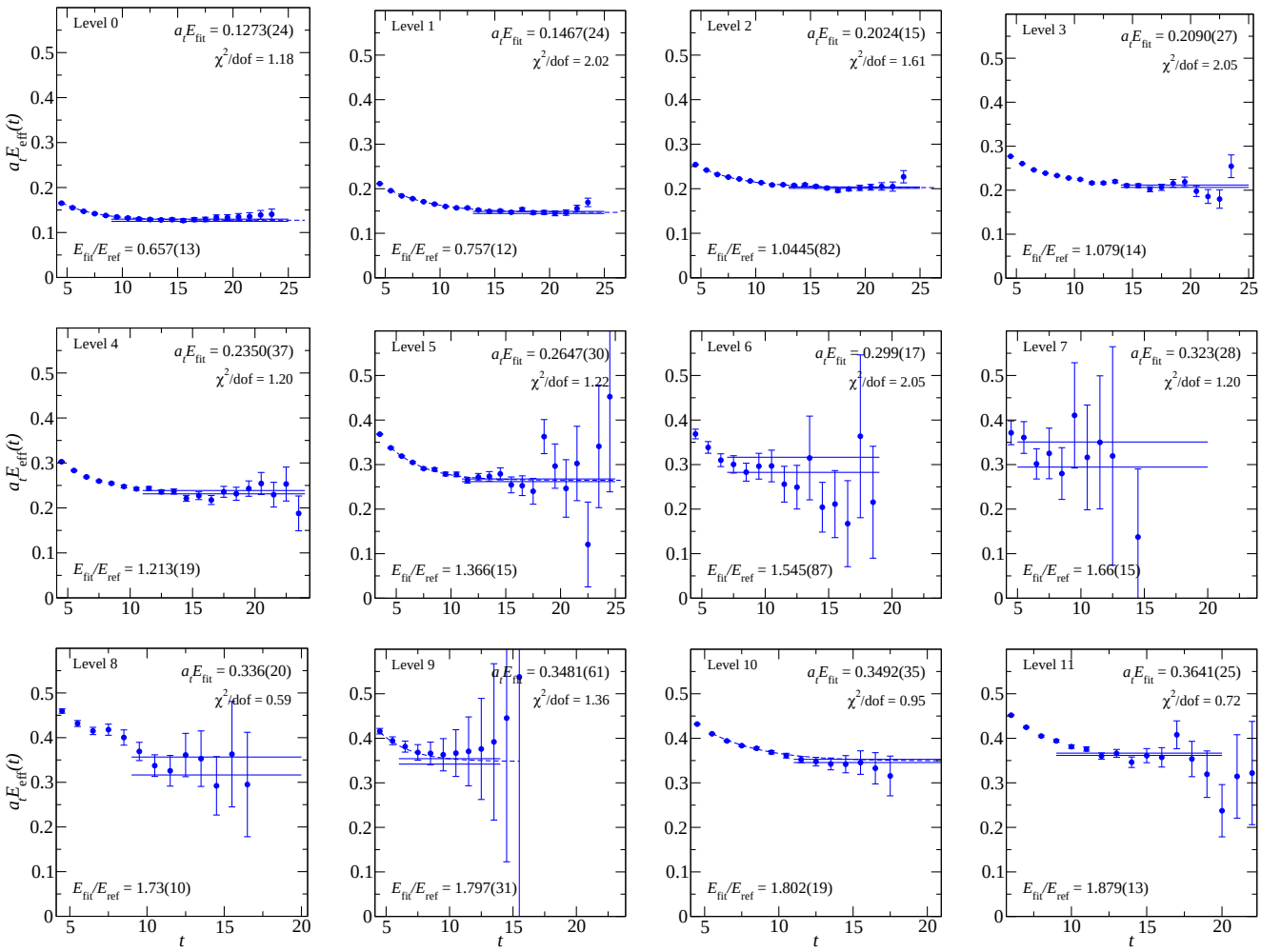

Figure 7.2: Effective masses for diagonal elements of the rotated A_{1g}^{+} correlation matrix, excluding the glueball operator. Recall that we fit to the temporal correlator directly. Best-fit plateaus are overlaid to guide the eye. $E_{\text{ref}} = 2m_K$.

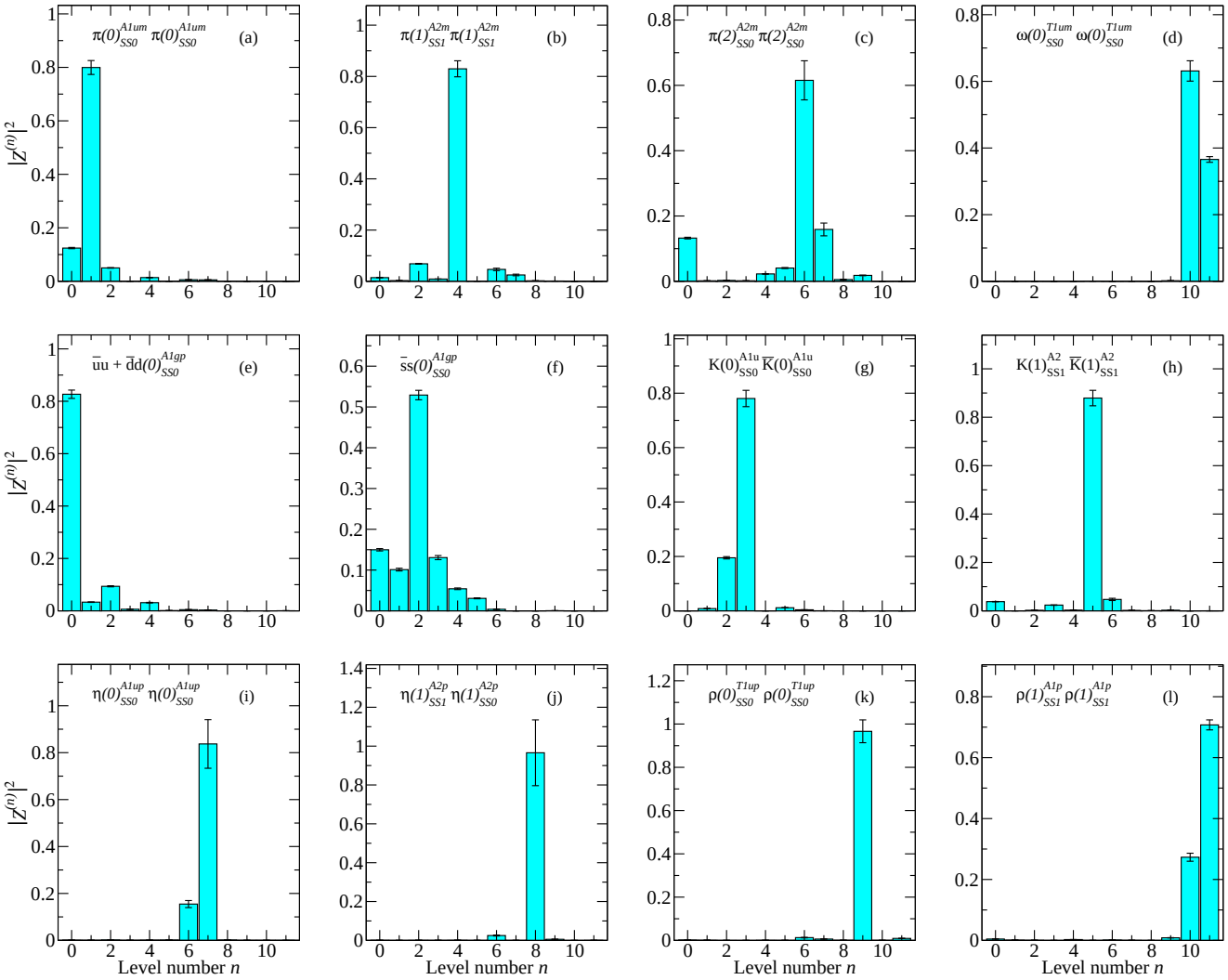

Figure 7.3: Overlaps $|Z^{(n)}|^2$ for the operators used in the A_{1g}^{+} correlation matrix excluding the scalar glueball operator.

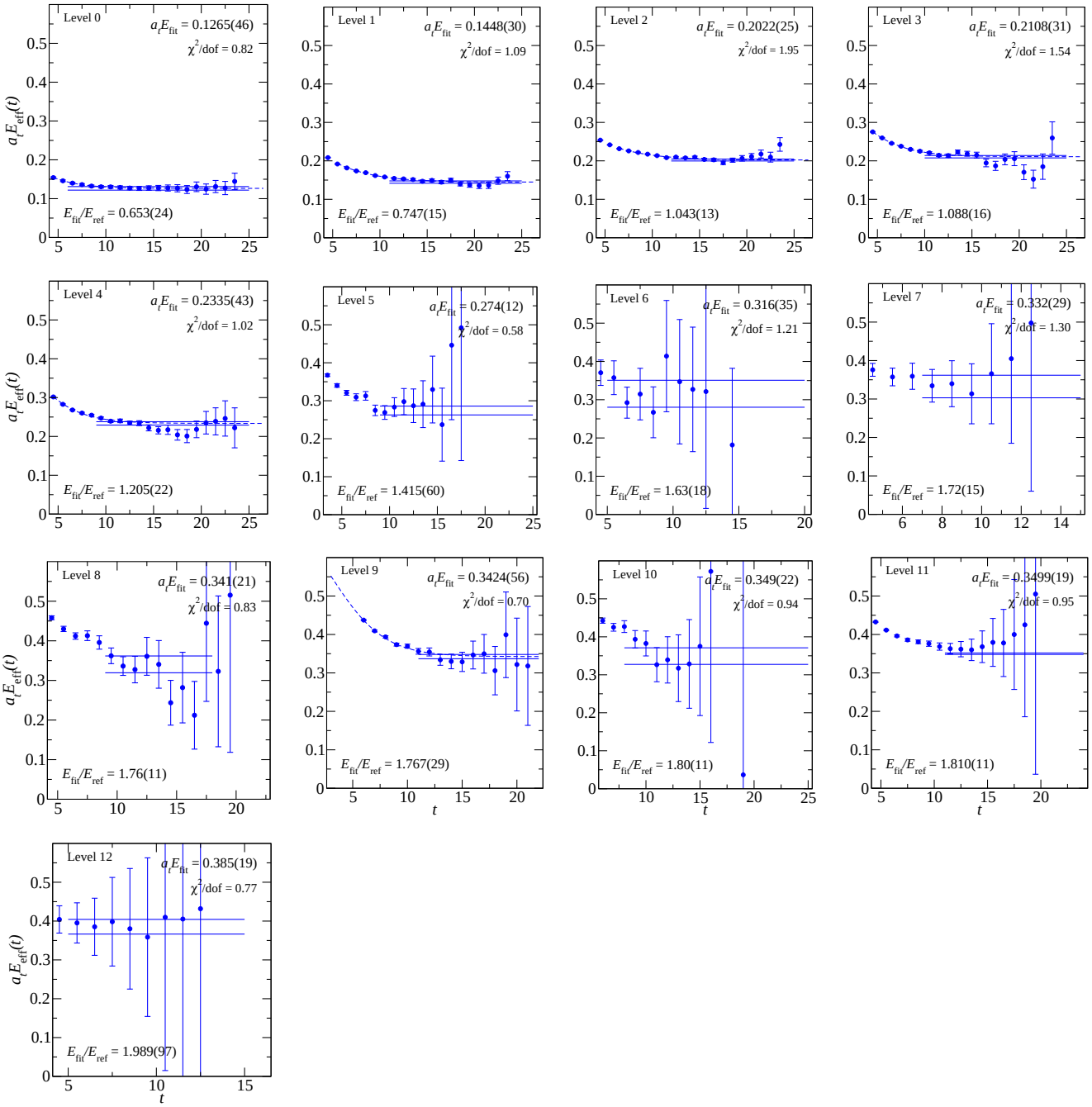

Figure 7.4: Effective masses for diagonal elements of the rotated A_{1g}^{+} correlation matrix, including the scalar glueball operator. Recall that we fit to the temporal correlator directly. Best-fit plateaus are overlaid to guide the eye. $E_{\text{ref}} = 2m_K$.

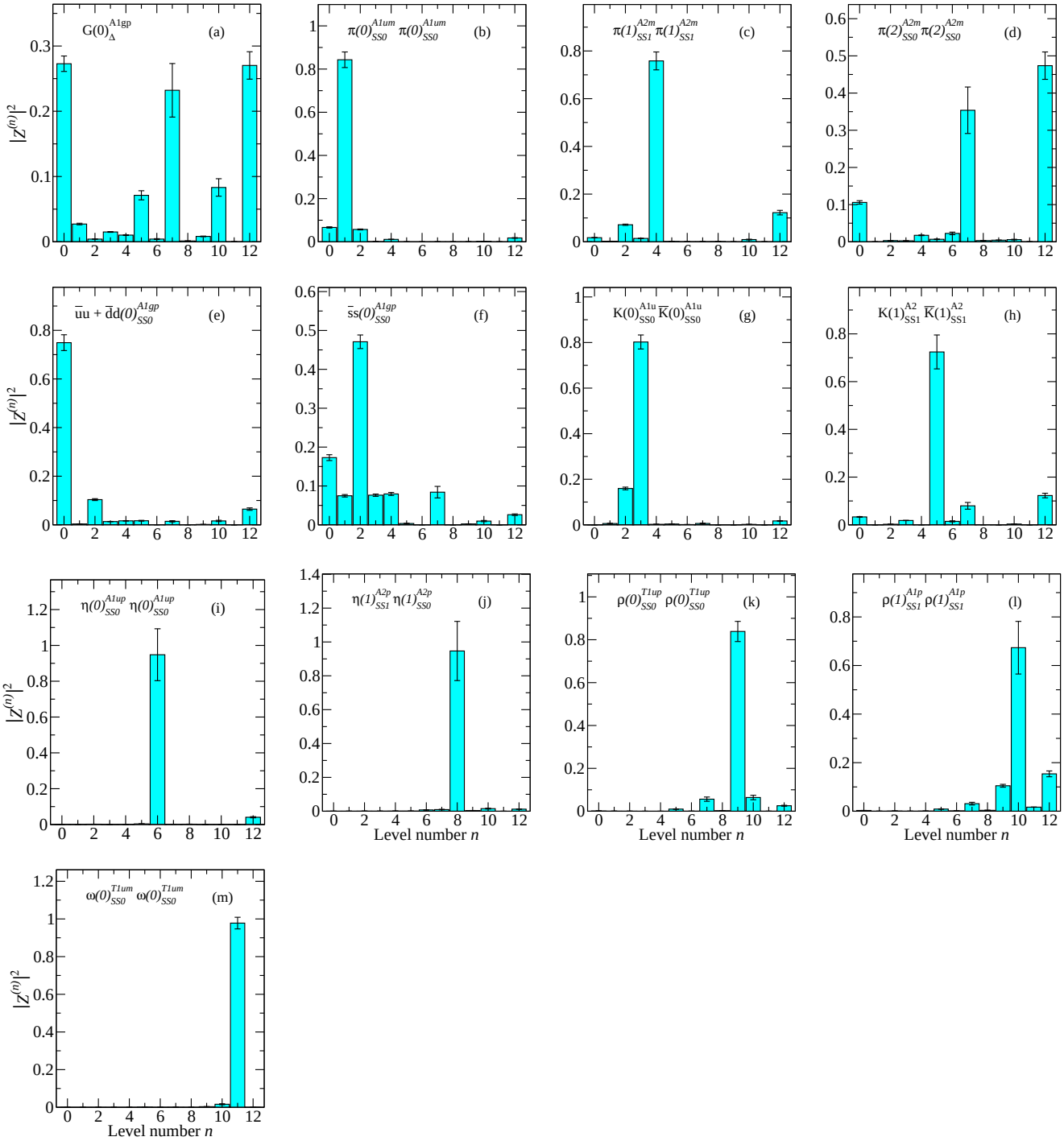

Figure 7.5: Overlaps $|Z^{(n)}|^2$ for the operators used in the A_{1g}^{+} correlation matrix including the scalar glueball operator.

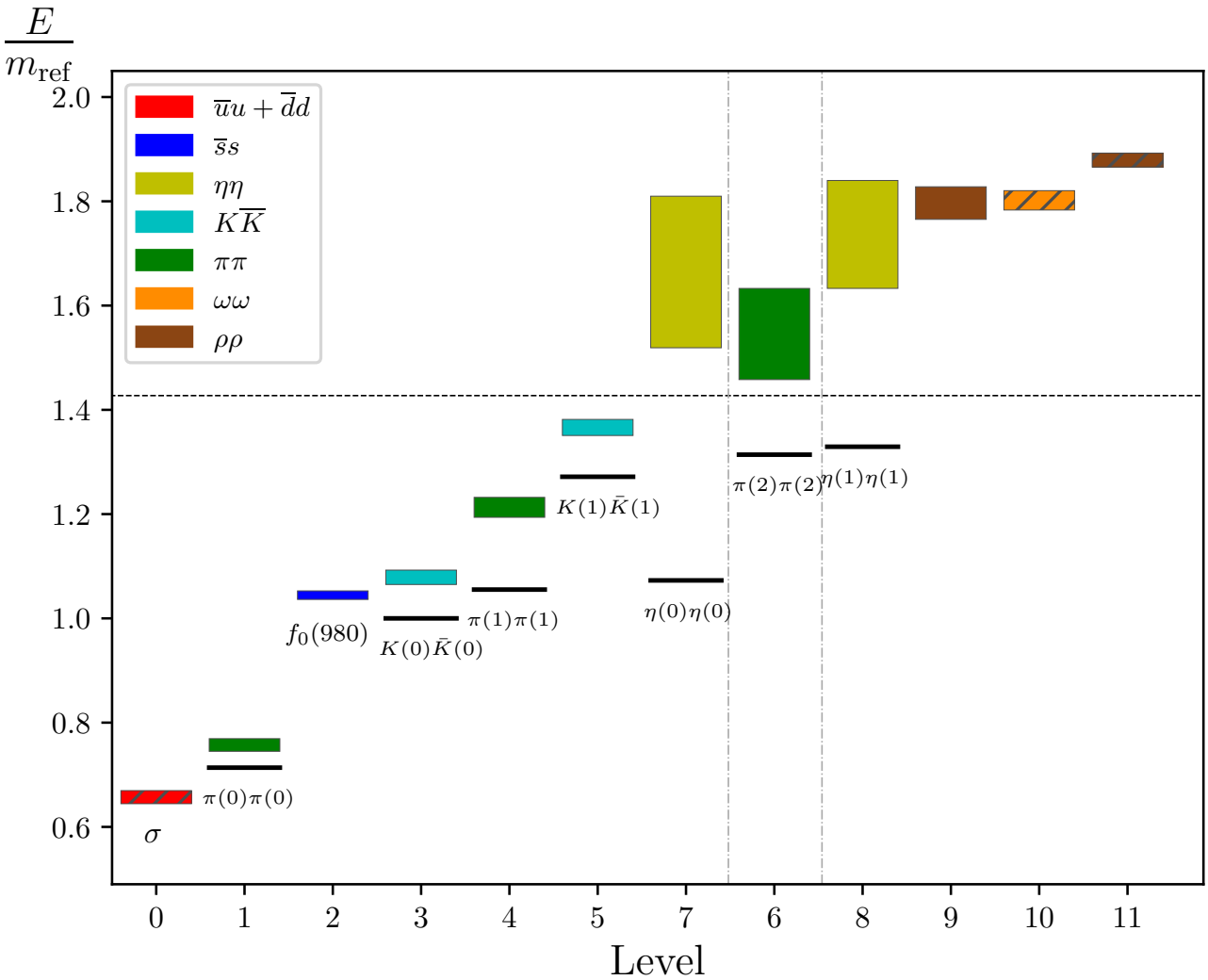

Figure 7.6: Finite-volume stationary state energies in the $I = 0$, $S = 0$, A_{1g}^{+} channel extracted using a 12×12 correlation matrix, *excluding* the scalar glueball operator. 1σ uncertainties are denoted by the box heights. If a level is created predominantly by a single operator, the level is colored to indicate the flavor content of that operator. If a level is created predominantly by more than one operator, a hatched box is used to denote the presence of operator overlaps within 75% of the maximum, indicating significant mixing. Level numbers indicate order in terms of increasing mean energy, but the levels have been rearranged horizontally to highlight the area of interest for the glueball operator we include in fig. 7.7. Note that these finite-volume energies should *not* be directly compared to the spectrum of experimental resonance states, in particular the two-hadron dominated levels. See text for further discussion. Short black lines indicate the non-interacting two-hadron levels, and the dashed horizontal black line indicates the 4π threshold. $m_{\text{ref}} = 2m_K$.

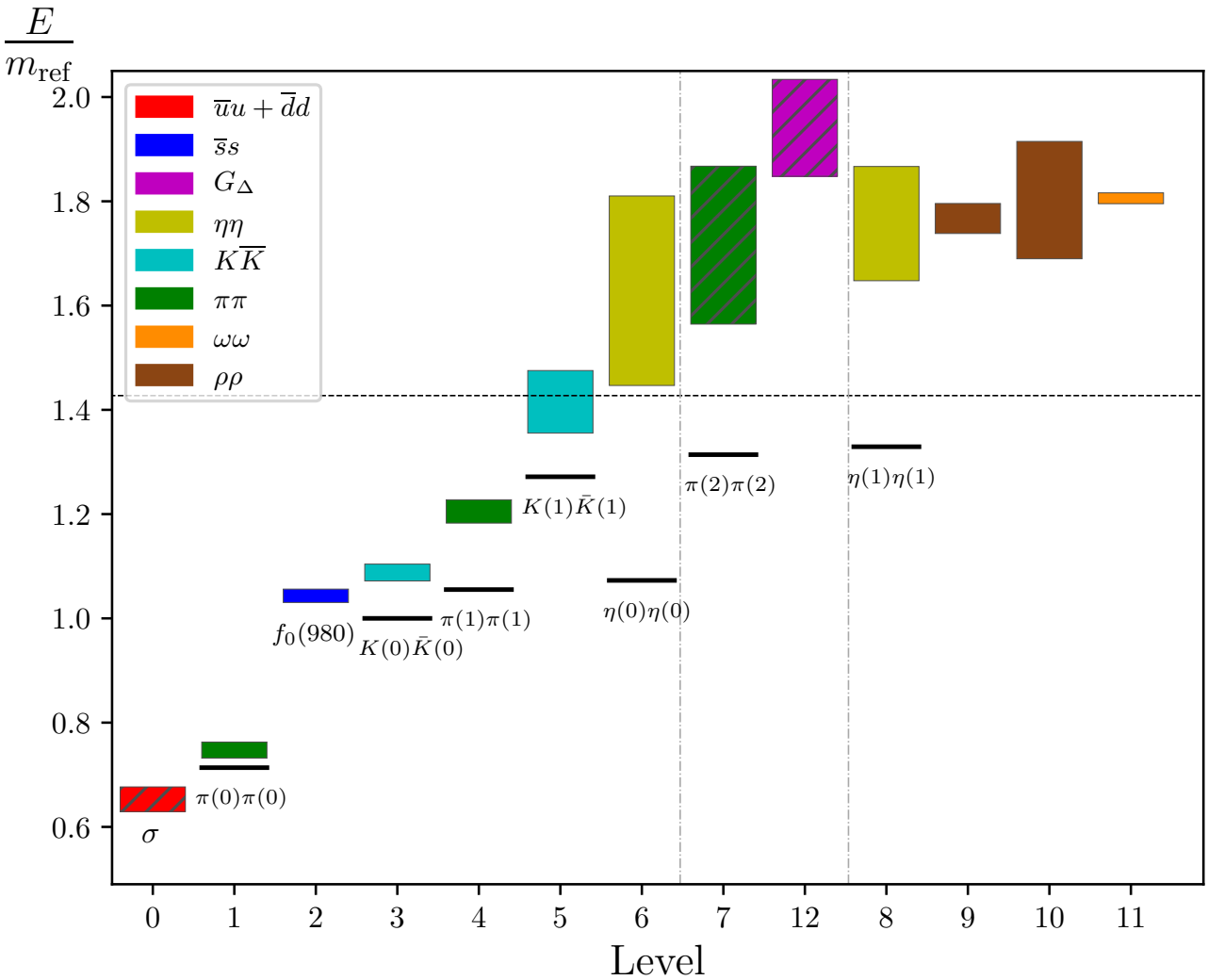

Figure 7.7: Finite-volume stationary state energies in the $I = 0$, $S = 0$, A_{1g}^{+} channel extracted using a 13×13 correlation matrix, *including* the scalar glueball operator. 1σ uncertainties are denoted by the box heights. If a level is created predominantly by a single operator, the level is colored to indicate the flavor content of that operator. If a level is created predominantly by more than one operator, a hatched box is used to denote the presence of operator overlaps within 75% of the maximum, indicating significant mixing. Level numbers indicate order in terms of increasing mean energy, but the levels have been rearranged horizontally to highlight the area of interest involving the glueball operator. Note that these finite-volume energies should *not* be directly compared to the spectrum of experimental resonance states, in particular the two-hadron dominated levels. See text for further discussion. Short black lines indicate the non-interacting two-hadron levels, and the dashed horizontal black line indicates the 4π threshold. $m_{\text{ref}} = 2m_K$.

Table 7.4: Fit results for a 13×13 correlation matrix in the A_{1g}^{+} channel including a scalar glueball operator. Exponential fit forms are assumed to be *time-forward*, as described in section 5.3, unless otherwise stated. $m_{\text{ref}} = 2m_K$.

Level	**Model**	t_{min}	t_{max}	$a_t E_{\text{fit}}$	$E_{\text{fit}}/m_{\text{ref}}$	χ^2/d.o.f.
0	2-exp	3	25	0.1265(46)	0.653(24)	0.82
1	2-exp	4	25	0.1448(30)	0.747(15)	1.09
2	2-exp	5	25	0.2022(25)	1.043(13)	1.95
3	2-exp	3	25	0.2108(31)	1.088(16)	1.54
4	2-exp	3	25	0.2335(43)	1.205(22)	1.02
5	1-exp	9	25	0.274(12)	1.415(60)	0.58
6	1-exp	5	20	0.316(35)	1.63(18)	1.21
7	1-exp	7	15	0.332(29)	1.72(15)	1.30
8	1-exp	9	18	0.341(21)	1.76(11)	0.83
9	2-exp+C	3	20	0.3424(56)	1.767(29)	0.70
10	1-exp+C	8	25	0.349(22)	1.80(11)	0.94
11	1-exp	11	23	0.3499(19)	1.810(11)	0.95
12	1-exp	5	15	0.385(19)	1.989(97)	0.77

slightly on the staircase plots. Hence, when referencing a particular level number, we are referring to the level numbers shown on the x-axis in fig. 7.7. From figs. 7.5(k-m) we can identify the rightmost three states as being predominantly created by the vector-vector operators, $\rho(0)\rho(0)$, $\rho(1)\rho(1)$, and $\omega(0)\omega(0)$. With the exception of, again an increase in statistical noise, and a slight reordering, these states too are unaffected by the addition of the glueball operator. A similar behaviour is seen in levels 6 and 8 which, based on figs. 7.5(i) and 7.5(j), are created dominantly by the $\eta(0)\eta(0)$ and $\eta(1)\eta(1)$ operators, respectively. Note however the significant shifts of these levels from their non-interacting levels, in particular as compared to the shifts of the lower-lying states.

The remaining finite-volume states have been highlighted in figs. 7.6 and 7.7 using the vertical dashed lines. Figure 7.5(a) shows that the glueball operator mainly creates levels 0, 7, and 12. Remarkably, it does *not* create a single new state near 1.5-1.7m_{ref}. When the glueball operator is included, there are two effects: the uncertainty in level 7 is greatly increased and *an additional state appears at a very high energy.* Based on both fig. 7.3(c) and fig. 7.5(d) we can identify level 7 as being dominantly created by the $\pi(2)\pi(2)$ operator before the addition of the glueball operator. When the glueball operator is included, it has significant overlap with this state. More notable is that the additional state we extract with the enlarged operator basis lies above all of the states extracted in fig. 7.6. This indicates that we have saturated the spectrum in this region without a glueball operator, with the exception of states dominated by three or more hadrons. Hence, we identify no finite-volume energy eigenstate predominantly created by a scalar glueball operator below $\sim 1.9m_{\text{ref}}$. Again, we emphasise that since this new energy occurs in a high region

above where our operator set is designed to create states, this level appears most likely just as a consequence of the enlarged operator basis. We cannot conclude that a pure glueball state has been created.

While these finite-volume results are insufficient to make any definitive statements regarding the infinite-volume resonances in this channel, we can make some qualitative comparisons to experiment. In finding only $\overline{q}q$ dominated states below $2m_{\text{ref}}$, we have observed no clearly identifiable counterpart finite-volume states to the $f_0(1370)$, $f_0(1500)$, or $f_0(1710)$ resonances in this region. This *suggests* thatthese resonances are not predominantly conventional $\overline{q}q$ states and are likely molecular in nature. Another important result is the absence of a state below 2 GeV predominantly created by a glueball operator in $N_f = 2 + 1$ QCD in finite-volume. While lattice calculations to date have long determined a scalar glueball mass near 1.7 GeV, these studies have exclusively used glueball-type interpolating operators in their analyses. Our result indicates, via the significant coupling of the glueball operator to the $\pi(2)\pi(2)$ and σ finite-volume states, that more extensive operator bases are crucial to a proper determination of the excited state spectrum in this sector of QCD.

In order to form definite conclusions regarding these states in infinite-volume, a rigorous determination of the coupled-channel scattering amplitudes in the scalar sector is required. Such calculations will be extremely challenging, requiring very large computational resources and the (ongoing) extension of the Lüscher formalism detailed in chapter 6 to amplitudes above the four-particle threshold. Correlator matrices including three- and four-hadron operators will need to be used. This has been done for example in Ref. [156] where the stochastic LapH method is used to compute correlation functions of three pion operators with maximal isospin. Additionally, as is now standard in scattering analyses, moving frames will need to be considered in order to accurately map out the scattering amplitudes. Partial wave mixing due to the finite volume will need to be accounted for here, requiring calculations in multiple volumes, especially when multiple decay channels are involved. Finally, in order to reliably compare such amplitudes to experimental results calculations at the physical quark masses are needed, increasing the difficulty of these calculations significantly.

Chapter 8

$K\pi$ Scattering

In this penultimate chapter, we will use the technology outlined in chapter 6 to connect finite-volume energies determined on the lattice to infinite-volume scattering amplitudes for elastic $K\pi$ scattering. As part of a larger project to map out s- and p-wave $I = \frac{1}{2}$ $K\pi$ scattering amplitudes, presented here is the finite-volume spectrum, and extraction of elastic scattering amplitudes on a single ensemble generated by the Coordinated Lattice Simulations (CLS) effort. This analysis is an early step in that project.

8.1 Analysis Details

The methods used for all stages of this analysis have been described in detail in previous chapters, so here they will only be briefly reviewed. Much of the analysis also follows Ref. [19], with the exception of not employing the so-called *ratio fits* used there to determine the finite-volume energy shifts due to interactions.

8.1.1 Ensemble Info

We employ here a single isotropic ensemble of $N = 2 + 1$ Wilson clover fermions generated by the CLS consortium, described in detail in sections 2.3.2 and 2.3.3. Various properties for the N200 ensemble used here are listed in table 8.1. Also listed in table 8.1 are details of the other ensembles intended to be used in the final amplitude analysis. On the N203 ensemble in particular, the low amount of statistics available at this time requires us to calculate correlation functions on a larger number of gauge configurations, currently underway on each of the three ensembles. We note also that the open temporal boundary conditions on these ensembles (see section 2.3.2 for details) restrict us to using source times in our temporal correlation functions that are sufficiently far away from the temporal boundary. As a result, we use only two source times in our correlation functions, $t_0 = 32, 53$.

Table 8.1: Details of the isotropic ensemble used in the $K\pi$ scattering study. After the ensemble ID in the first column, we list the gauge coupling, lattice spacing and dimensions, pseudoscalar meson masses, and number of gauge configurations used. Listed in red are the other ensembles which are not used in this thesis, which will be used in the future amplitude extraction.

ID	β	a (fm)	$L^3 \times T$	m_π, m_K (MeV)	N_{cfgs}
N200	3.55	0.064	$48^3 \times 128$	280, 460	427
N203	3.55	0.064	$48^3 \times 128$	340, 440	189
D200	3.55	0.064	$64^3 \times 128$	200, 480	1100

Table 8.2: Irreps Λ of the appropriate little group for various total momenta $\boldsymbol{p}_{\text{tot}} = (2\pi/L)\boldsymbol{d}$ (where $\boldsymbol{d}$ is a vector of integers) considered in this work. We consider $K\pi$ systems at rest as well as those with non-zero total on-axis, planar-diagonal, and cubic-diagonal momenta. These momentum classes are listed in the first column, where $n \in \mathbb{Z}$.

$\boldsymbol{d}$	Λ	ℓ
$(0,0,0)$	A_{1g}	0, 4, ...
	T_{1u}	1, 3, ...
$(0,0,n)$	A_1	0, 1, 2, ...
	E	1, 2, 3, ...
$(0,n,n)$	A_1	0, 1, 2, ...
	B_1	1, 2, 3, ...
	B_2	1, 2, 3, ...
(n,n,n)	A_1	0, 1, 2, ...
	E	1, 2, 3, ...

8.1.2 Spectrum Determination

Using the stochastic LapH method [15] outlined in chapter 4, we evaluate temporal correlation matrices in each of the irreps listed in table 8.2. We use an operator basis in each irrep composed of single- and two-hadron interpolating operators (described in chapter 3), including 1-4 $K\pi$ operators with various constituent momenta corresponding to the expected non-interacting energies in the elastic region, and 1-2 single-hadron, $\overline{q}q$-type operators allowing for the presence of a narrow $K^*(892)$ resonance along with the possibility of an additional s-wave resonance. The final operator set used is listed in table 8.3, and we find the finite-volume spectrum in the elastic region insensitive to the inclusion of additional operators.

The finite-volume spectrum is then extracted using the methods outlined in chapter 5. We solve the GEVP of eq. (5.9) using the single pivot method detailed in section 5.1.2. The diagonal elements of the rotated correlation matrix are then fit using single- or two-exponential fit forms that tend to $A_n e^{-E_n t}$ for large times to obtain the finite-volume energies E_n. Bootstrap resampling

Table 8.3: Single- and two-hadron operators included in the correlation matrix for each irrep. The single-hadron "kaon" operators are specified with a displacement type (i.e. SS = single-site), and a spatial identification number, with K referring only to the flavour structure. Integer momentum squared is shown in units of $2\pi/L$ in parenthesis.

$\boldsymbol{d}^2$	Λ	**operators**
0	A_{1g}	$K(0)_{\mathrm{SS0}}$, $K(0)\pi(0)$, $K(1)\pi(1)$
	T_{1u}	$K(0)_{\mathrm{SS1}}$, $K(1)\pi(1)$, $K(2)\pi(2)$
1	A_1	$K(1)_{\mathrm{SS2}}$, $K(0)\pi(1)$, $K(1)\pi(0)$, $K(1)\pi(2)$, $K(2)\pi(1)$
	E	$K(1)_{\mathrm{SS2}}$, $K(1)\pi(2)$, $K(2)\pi(1)$
2	A_1	$K(2)_{\mathrm{SS3}}$, $K(0)\pi(2)$, $K(1)\pi(1)$, $K(2)\pi(0)$, $K(3)\pi(1)$
	B_1	$K(2)_{\mathrm{SS1}}$, $K(3)\pi(1)$
	B_2	$K(2)_{\mathrm{SS3}}$, $K(1)\pi(1)$, $K(2)\pi(2)$
3	A_1	$K(3)_{\mathrm{SS0}}$, $K(3)_{\mathrm{SS3}}$, $K(0)\pi(3)$, $K(1)\pi(2)$, $K(2)\pi(1)$, $K(3)\pi(0)$
	E	$K(3)_{\mathrm{SS1}}$, $K(1)\pi(2)$, $K(2)\pi(1)$
4	A_1	$K(4)_{\mathrm{SS2}}$, $K(0)\pi(4)$, $K(1)\pi(1)$, $K(2)\pi(2)$, $K(4)\pi(0)$
	E	$K(4)_{\mathrm{SS2}}$, $K(2)\pi(2)$

is used to estimate uncertainties on the energies, using 1000 resamplings throughout.

8.1.3 K-Matrix Fits

Once the interacting finite-volume energies have been determined, we can use the formalism outlined in chapter 6 to extract the infinite-volume scattering K-matrix. The quantisation condition in eq. (6.40) gives us a relationship between each finite-volume energy and the $\widetilde{K}$-matrix, which for the scattering of spinless particles is given by

$$\widetilde{K}_\ell^{-1}(E_{\mathrm{cm}}) = \left(\frac{\boldsymbol{q}_{\mathrm{cm}}}{m_\pi}\right)^{2\ell+1} K_\ell^{-1}(E_{\mathrm{cm}}) = \left(\frac{\boldsymbol{q}_{\mathrm{cm}}}{m_\pi}\right)^{2\ell+1} \cot\delta_\ell(E_{\mathrm{cm}}). \tag{8.1}$$

When employing the quantisation condition to the irreps listed in table 8.2, care must be taken to account for the partial wave mixing induced by the reduced rotational symmetry of the finite, cubic volume. Here, we will neglect all partial waves with $\ell \geq 2$, justified by the analysis of Ref. [19] where d-wave contributions to $K\pi$ scattering in the elastic region were shown to be negligible.

After truncating the quantisation condition in ℓ, there are a number of irreps for which the box matrix element is one-dimensional, yielding a one-to-one relationship between energies in those irreps and scattering phase shift points. However, only the A_{1g} irrep at zero total momentum provides this direct relationship for s-wave amplitude points, and hence we proceed by fitting the energies across all listed irreps to determine both amplitudes simultaneously. For this we use the determinant residual method [29] described in section 6.3.1.

We now turn to the parameterisations of the $\widetilde{K}^{-1}$ for the s- and p-wave amplitudes. Since we expect a narrow p-wave $K^*(892)$ resonance, we use the relativistic Breit-Wigner

$$(\widetilde{K}_1^{-1})^{\mathrm{BW}}(E_{\mathrm{cm}}) = \frac{6\pi E_{\mathrm{cm}}}{g^2_{K^*K\pi} m_\pi}\left(\frac{m^2_{K^*}}{m^2_\pi} - \frac{E^2_{\mathrm{cm}}}{m^2_\pi}\right), \tag{8.2}$$

with two non-negative fit parameters $m^2_{K^*}/m^2_\pi$ and $g^2_{K^*K\pi}$. We explore a variety of parameterisations for the s-wave amplitude. Motivated by the analyticity of $\widetilde{K}^{-1}$ at threshold in both E_{cm} and $s = E^2_{\mathrm{cm}}$ [29], we consider polynomials in E_{cm}:

$$(\widetilde{K}_0^{-1})^{\mathrm{lin}}(E_{\mathrm{cm}}) = a_{\mathrm{lin}} + b_{\mathrm{lin}} E_{\mathrm{cm}}, \tag{8.3a}$$

$$(\widetilde{K}_0^{-1})^{\mathrm{quad}}(E_{\mathrm{cm}}) = a_{\mathrm{quad}} + b_{\mathrm{quad}} E^2_{\mathrm{cm}}, \tag{8.3b}$$

with unconstrained fit parameters a and b, along with a constant parameterisation, representing the lowest order effective range expansion:

$$(\widetilde{K}_0^{-1})^{\mathrm{ERE}}(E_{\mathrm{cm}}) = -\frac{1}{m_\pi a_0}, \tag{8.4}$$

with unconstrained fit parameter $m_\pi a_0$, where a_0 is known as the scattering length. Additionally, we allow for the presence of an s-wave resonance, employing an $\ell = 0$ relativistic Breit-Wigner

$$(\widetilde{K}_0^{-1})^{\mathrm{BW}}(E_{\mathrm{cm}}) = \frac{6\pi m_\pi E_{\mathrm{cm}}}{g^2_{K_0^*K\pi} m^2_{K_0^*}}\left(\frac{m^2_{K_0^*}}{m^2_\pi} - \frac{E^2_{\mathrm{cm}}}{m^2_\pi}\right), \tag{8.5}$$

with non-negative fit parameters $m^2_{K_0^*}/m^2_\pi$ and $g^2_{K_0^*K\pi}$.

8.2 Results

With the operator bases listed in table 8.3, we find the extracted energies to be largely insensitive to the choice of GEVP parameters, and so in each correlation matrix, we choose $(\tau_0, \tau_d) = (12, 24)$. Plots showing fitted energies for different values of t_{min}, but the same t_{max} are shown for each of the extracted levels in section C.1. These t_{min}-plots are helpful in determining the time separations for which a given fit ansatz best captures the signal, e.g. the time range over which a single exponential dominates. The finite-volume energies in the elastic scattering region (i.e. below the $K\eta$ threshold), boosted to the centre-of-mass frame, are shown in fig. 8.1 for total momenta $\boldsymbol{d}^2 \leq 4$. Note that, due to the quark mass trajectory used, the lighter than physical kaon mass results in the inelastic threshold on this ensemble being the $K\eta$ threshold, rather than the three-particle threshold ($K\pi\pi$) where the Lüscher formalism breaks down. As the s- and p-wave amplitudes we wish to study should lie in this elastic region, we consider only energies for which $E_{\mathrm{cm}} < m_K + m_\eta$.

Based on the operator overlap factors, $|Z_j^{(n)}| \equiv \langle 0|\mathcal{O}_j|n\rangle$, extracted from the rotated correlation matrix, the energies in fig. 8.1 are coloured to give a qualitative indication of the content of each level. Looking then at the irreps in which we expect only p-wave contributions (neglecting

$\ell \geq 2$), a $\overline{q}q$ dominated finite-volume state is seen around $3 - 3.2\ m_\pi$, perhaps indicative of a finite-volume counterpart to the $K^*(892)$ resonance. The finite-volume energies below the inelastic threshold are listed in table 8.4, along with their corresponding diagonal $\ell = 0, 1$ box matrix elements $B_{\ell\ell'} = B_{00}, B_{11}$. In irreps in which only a single partial wave is assumed to contribute, the quantisation condition is exactly solvable, and these matrix elements are equal to $(\boldsymbol{q}_{\rm cm}/m_\pi)\cot\delta_0$ and $(\boldsymbol{q}_{\rm cm}/m_\pi)^3\cot\delta_1$, respectively. We find 6 of the extracted energies, listed in italics in table 8.4 are not determined with sufficient accuracy to resolve their shifts away from the non-interacting energies. This is apparent in the box matrix elements for these levels which feature very large uncertainties, statistically consistent with zero. This occurs for energies that are very close to the non-interacting energies as the RGL zeta function contained in B diverges at each of the finite-volume non-interacting energies. Hence, these energies are excluded from the final amplitude fits.

We now proceed with fitting the s- and p-wave partial wave amplitudes simultaneously following the procedure outlined in section 8.1.3. The p-wave amplitude is parameterised by the relativistic Breit-Wigner in eq. (8.2), and we explore a variety of parameterisations for the s-wave amplitude. Best-fit parameters for each of these fits are listed in table 8.5. It is clear from these results that the p-wave $K^*(892)$ resonance parameters are insensitive to the particular s-wave parameterisation chosen. Additionally, the s-wave scattering length determined by interpolating a given s-wave parameterisation to the $K\pi$ threshold,

$$\lim_{q_{\rm cm}\to 0}\left(\frac{q_{\rm cm}}{m_\pi}\right)\cot\delta_0 = -\frac{1}{m_\pi a_0}, \tag{8.6}$$

is similarly insensitive to the parameterisation chosen. The p-wave amplitude and phase shift from the LO ERE fit are shown in figs. 8.2 and 8.3, respectively, along with points from irreps in which there is no $\ell = 0$ contribution which are seen to be consistent with the fit.

With $m_\pi = 280$ MeV here, our Breit-Wigner mass for the $K^*(892)$ resonance is $m_{K^*} \approx 848$ MeV, lighter than the experimental, physical point value, but also lighter than the results from various lattice calculations at both heavier and lighter pion masses, see e.g. fig. 6 from Ref. [19]. This can be attributed to the lighter than physical kaon/strange quark mass due to the atypical quark mass trajectory, in contrast to the more standard trajectory in which m_s, the strange quark mass, is fixed to its physical value as the light quark mass is lowered to the physical point. As such, a chiral extrapolation to the physical quark masses using amplitude analyses from the D200 and N203 ensembles listed in table 8.1 is desired (cf. fig. 6 of Ref. [20]). The coupling $g_{K^*K\pi} = 5.75^{+25}_{-35}$ is somewhat comparable to the physical value of $g_{K^*K\pi} \approx 5.39$ [9], though again, a chiral extrapolation is required.

Lattice calculations of the s-wave scattering length $m_\pi a_0$ are considerably more numerous than those of $K^*(892)$ resonance parameters [157–160]. As these calculations generally involve both a continuum and physical point extrapolation, a comparison with our result would be premature. Additionally, the relatively large uncertainties on our determination of $m_\pi a_0$ indicate the need for improvement of these results. Certainly, in addition to amplitude determinations on the D200 and

Table 8.4: Finite-volume two-hadron energies in the center-of-mass frame with corresponding box matrix diagonal elements, for $\ell < 2$. A vanishing matrix element is denoted by a dash. Levels in italics are not used in the final K-matrix fits.

$\boldsymbol{d}^2$	Λ	**level**	$E_{\rm cm}/m_\pi$	$\boldsymbol{q}^2_{\rm cm}/m^2_\pi$	B_{00}	B_{11}
0	A_{1g}	0	2.5576(99)	-0.0731(71)	1.22(21)	–
	T_{1u}	0	3.055(21)	0.595(29)	–	-0.257(10)
1	A_1	0	2.733(12)	0.147(11)	1.01(17)	0.92(12)
		1	2.915(14)	0.392(15)	-0.70(16)	-0.19(16)
		2	3.170(29)	0.769(43)	-1.06(19)	-1.96(25)
	E	0	3.034(20)	0.563(27)	–	-0.3158(53)
2	A_1	0	2.840(15)	0.289(16)	0.65(11)	0.83(12)
		1	3.016(29)	0.537(41)	-1.3(51)	-2.2(69)
		2	*3.254(17)*	*0.900(23)*	*4.4(67)*	*6(19)*
		3	*3.307(34)*	*0.986(53)*	*0.4(13)*$\times 10^2$	*-0.1(16)*$\times 10^2$
	B_1	0	3.104(25)	0.668(35)	–	-0.3342(87)
	B_2	0	2.928(41)	0.411(56)	–	0.171(89)
		1	3.387(24)	1.117(37)	–	-6.7(29)
3	A_1	0	2.883(24)	0.348(32)	0.32(10)	0.49(12)
		1	*3.061(28)*	*0.604(40)*	*0.1(83)*$\times 10^2$	*0.0(15)*$\times 10^3$
		2	*3.354(32)*	*1.062(50)*	*1.60(57)*	*0.72(86)*
	E	0	2.928(50)	0.412(70)	–	-0.046(43)
4	A_1	*0*	*2.615(29)*	*-0.004(36)*	*1(51)*	*0.3(74)*
		1	2.982(27)	0.488(37)	-0.08(11)	0.50(16)
		2	*3.219(40)*	*0.845(62)*	*-2(71)*	*-0.1(16)*$\times 10^2$
	E	0	3.147(38)	0.734(56)	–	-0.232(34)

N203 ensembles and a chiral extrapolation, increased statistics are needed here to improve the s-wave amplitude determination. With an increase in statistics, and results at both lighter and heavier pion masses, a careful analytic continuation of the amplitude can be performed, with the aim of searching for hints of a $K_0^*(700)$ resonance. Such calculations are currently ongoing.

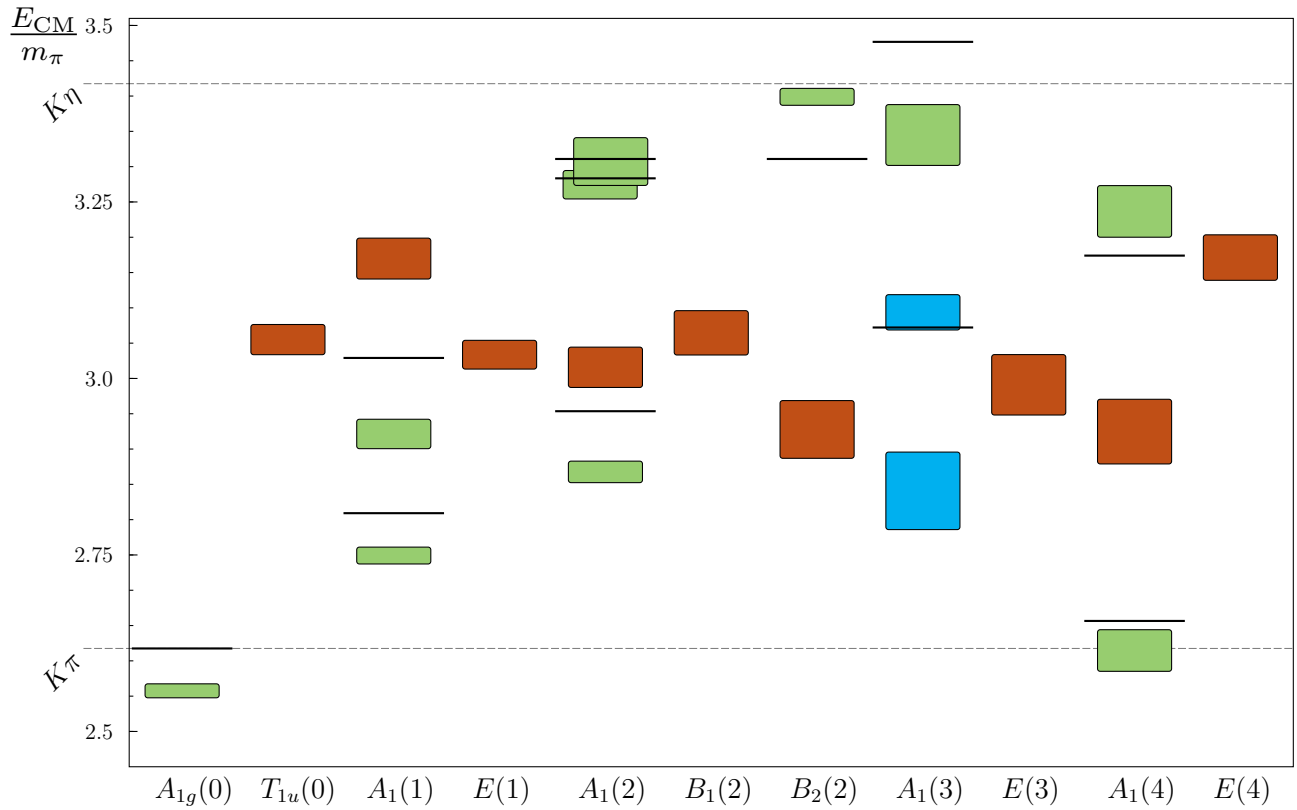

Figure 8.1: Finite-volume energies in the elastic regions in each of the irreps relevant for $K\pi$ scattering, boosted to the centre-of-mass frame. The allowed angular momenta that will appear in each irrep are listed in table 8.2. In each column, the statistical uncertainty is denoted by the height of the boxes, solid black lines indicate the non-interactive $K\pi$ energies, and the relevant thresholds delineating the elastic scattering region are denoted by the dashed grey lines. Levels are coloured according to maximal operator overlap factors: orange levels are created predominantly by $\overline{q}q$-type operators, green levels are created mainly by two-hadron $K\pi$ operators, and blue levels feature significant mixing between single- and two-hadron operators.

Table 8.5: $\widetilde{K}$-matrix fit results for the p-wave $K^*(892)$ resonance parameters and the s-wave scattering length $m_\pi a_0$ from simultaneous fits to both amplitudes. In each fit, the p-wave amplitude is described using the Breit-Wigner form in eq. (8.2), with the varyious s-wave parameterisations listed in the first column defined in eqs. (8.3) to (8.5). In all fits, the Ω function of eq. (6.45) with $\mu = 20$ is used as the residual.

s-wave	m_{K^*}/m_π	$g_{K^*K\pi}$	$m_\pi a_0$	χ^2/d.o.f.
lin	3.027^{+16}_{-15}	5.74^{+29}_{-56}	-0.93^{+14}_{-20}	2.05
quad	3.028^{+16}_{-15}	5.74^{+28}_{-56}	-0.93^{+14}_{-20}	2.05
LO ERE	3.027^{+16}_{-13}	5.75^{+25}_{-35}	-0.93^{+15}_{-19}	1.89
BW	3.028^{+16}_{-15}	5.75^{+26}_{-59}	-0.92^{+14}_{-20}	2.04

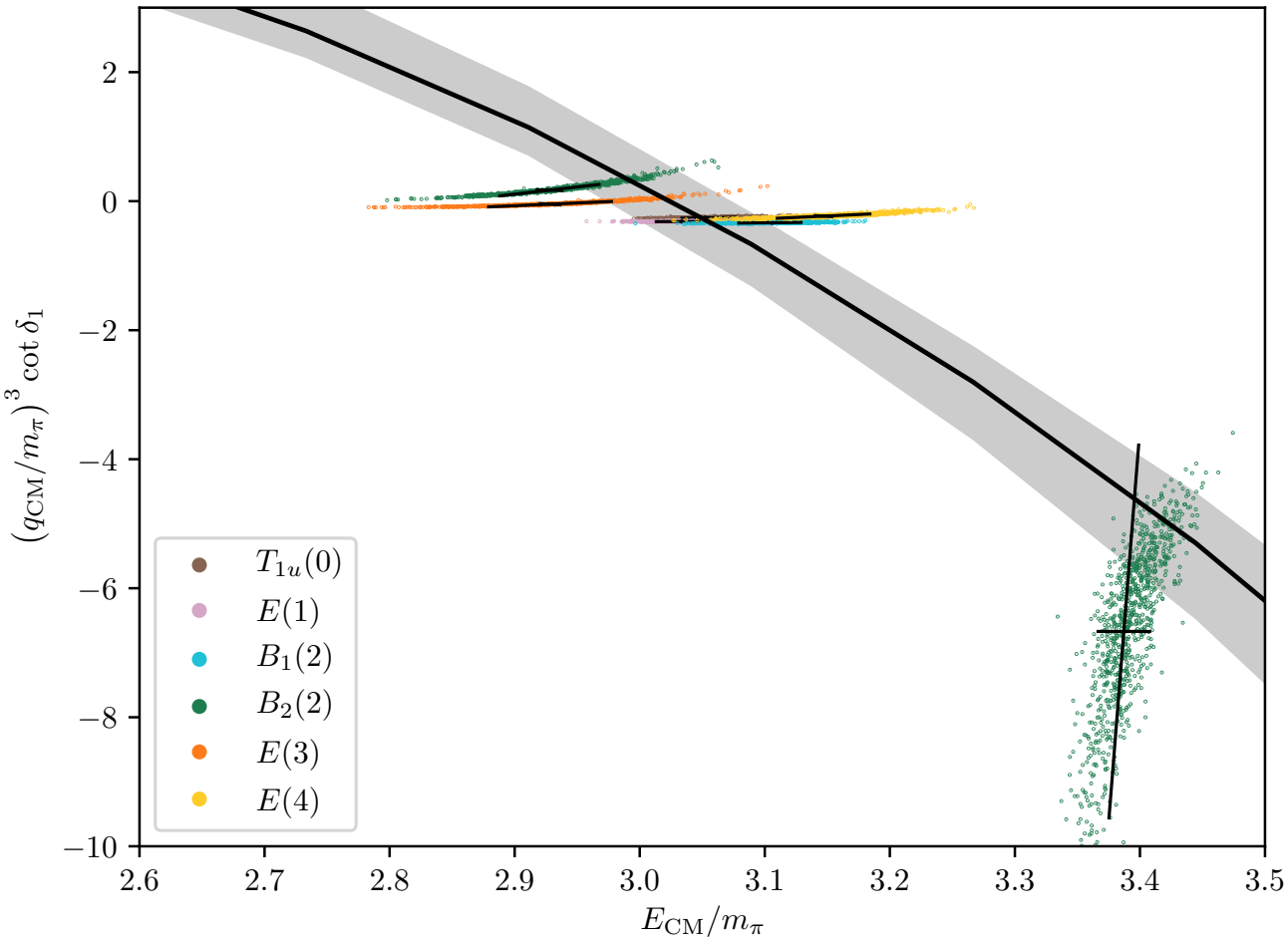

Figure 8.2: $(\boldsymbol{q}_{\mathrm{cm}}/m_\pi)^3 \cot\delta_1$ as a function of E_{cm}/m_π using the LO ERE fit from row 3 of table 8.5, with $\mu = 20$. All bootstrap resamplings for energies from irreps which do not mix the s- and p-waves are shown along with 1σ principal error bars to indicate the correlated uncertainty between the scattering phase shifts and finite-volume energies. We stress that the amplitude is constrained not just by these energies, but by the 15 energies listed in table 8.4. The black line indicates the best fit curve with the grey bands indicating $\pm 68\%$ asymmetric confidence intervals. The zero crossing where $\cot \pi/2 = 0$ indicates the presence of a $K^*(892)$ resonance at $3.027^{+16}_{-13}\ m_\pi$.

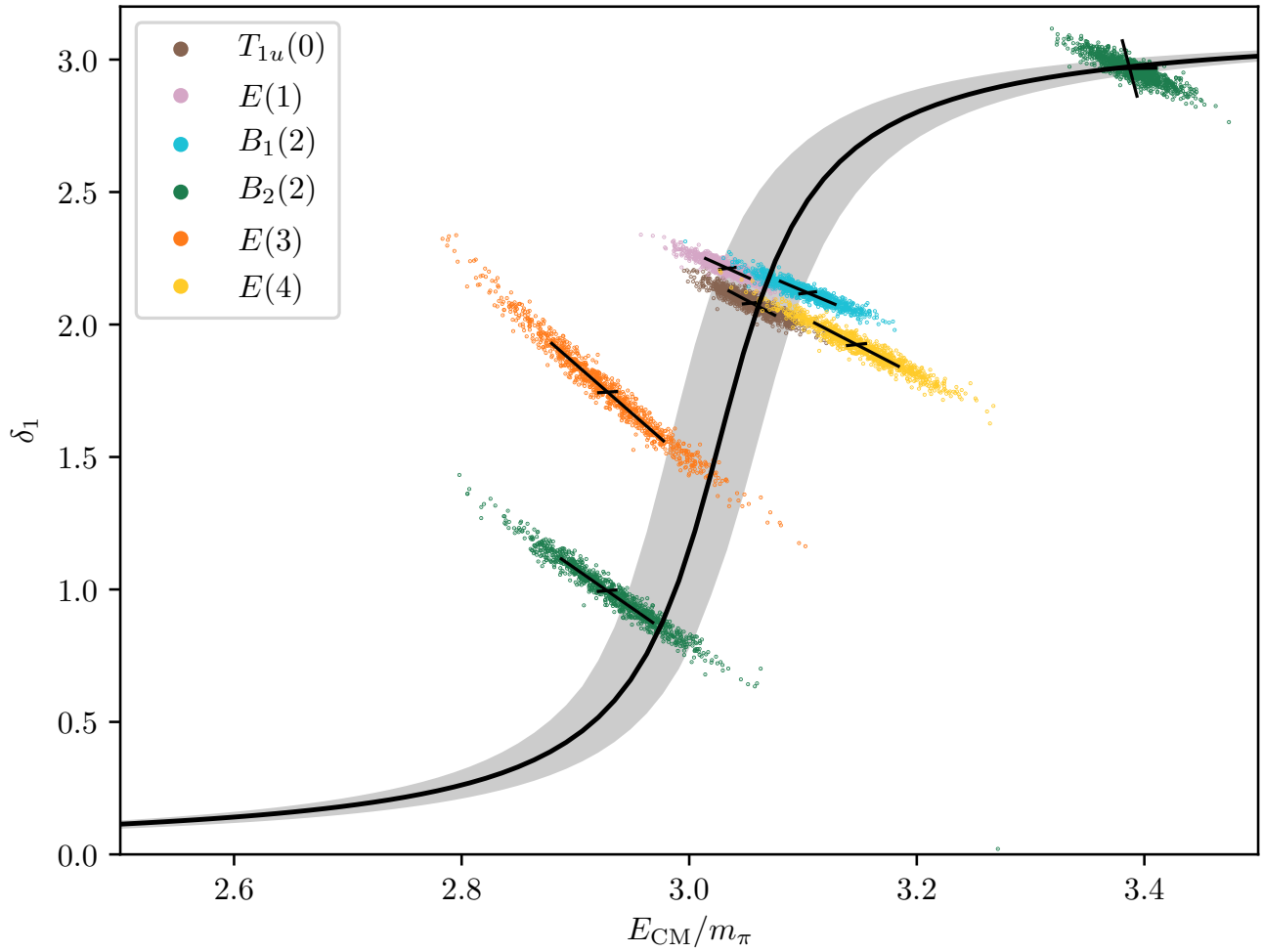

Figure 8.3: δ_1 as a function of E_{cm}/m_π using the LO ERE fit from row 3 of table 8.5, with $\mu = 20$. All bootstrap resamplings for energies from irreps which do not mix the s- and p-waves are shown along with 1σ principal error bars to indicate the correlated uncertainty between the box scattering phase shifts and finite-volume energies. We stress that the amplitude is constrained not just by these energies, but by the 15 energies listed in table 8.4. The black line indicates the best fit curve with the grey bands indicating $\pm 68\%$ asymmetric confidence intervals. The procession through $\pi/2$ indicates the presence of a $K^*(892)$ resonance at $3.027^{+16}_{-13}\ m_\pi$.

Chapter 9

Conclusions

We have presented here two studies in hadron spectroscopy using lattice QCD: the scalar channel below 2 GeV with an emphasis on the scalar glueball, and elastic, $I = 1/2$, $K\pi$ scattering. Applying Monte Carlo methods to sample the space of gluon field configurations and the stochastic LapH method for efficiently treating quark propagation, we were able to explore the excited-state spectrum of QCD in finite-volume with first-principles numerical calculations. In chapters 2 to 5 we described the framework required to perform such calculations, beginning with an introduction to the lattice regularisation of QCD, a description of the careful construction of optimal hadronic interpolating operators, the stochastic estimation of temporal correlation functions, statistical analysis of said correlation functions, followed by, in chapter 6, a formalism that allows for the extraction of infinite-volume scattering amplitudes from finite-volume stationary state energies.

The Scalar Glueball

In chapter 7 we tackled the notoriously troublesome scalar sector of QCD with vacuum quantum numbers, with the aim of assessing the glueball content of the spectrum below ~ 2 GeV. For the first time in lattice QCD, we studied the low-lying spectrum including quark-antiquark, meson-meson, and glueball interpolating operators so that we could capture the mixing patterns of finite-volume single- and two-hadron dominated states. Using first a basis of exclusively quark-antiquark interpolating operators, we found two low-lying finite-volume levels identifiable as finite-volume counterpart states to the σ and $f_0(980)$ mesons, but no further states below 2 GeV. Considering then the full operator basis listed in table 7.2, we extracted the finite-volume spectrum for two cases, with and without a glueball-type interpolating operator. The large vacuum expectation values associated with correlation functions of the glueball operator required much care to be taken in their removal, as their statistical errors were large. The spectrum in each scenario is shown in figs. 7.6 and 7.7, respectively. Our most striking observation was the absence of any additional finite-volume states below ~ 2 GeV with the inclusion of the glueball operator. As the spectrum in this region is, up to an increase in statistical noise, insensitive to the addition of the glueball operator (and additional meson-meson, and quark-antiquark operators), we concluded that we have

sufficiently saturated the spectrum below ~ 2 GeV, except for states dominated by three or more hadrons. In particular, we have not included any 4π interpolating operators.

These findings in finite-volume suggested that, in $N_f = 2+1$ fully dynamical QCD at $m_\pi \sim 390$ MeV, there is no pure scalar glueball below ~ 2 GeV. Additionally, considering the leading experimental glueball candidates in this region, the $f_0(1370)$, $f_0(1500)$, and $f_0(1710)$, we found no quark-antiquark dominated levels identifiable as finite-volume counterpart to these states, indicating that these states are likely to be molecular in nature. Forming definite infinite-volume conclusions about these states will require the determination of scattering amplitudes using the formalism detailed in chapter 6, along with extensions for determining amplitudes above the 4π threshold. Such computations will require very large computing resources and new calculational techniques, in particular as the physical point is approached. Additionally, moving frames will need to be considered.

Elastic $K\pi$ Scattering

In chapter 8 we presented an early study as part of a larger effort to map out elastic s- and p-wave $K\pi$ scattering amplitudes at varying quark masses from lattice QCD. Using an isotropic lattice with $(m_\pi, m_K) = (280, 460)$ MeV generated by the CLS consortium, we first mapped out the finite-volume spectrum of two-particle $K\pi$ states in the elastic region at total zero and non-zero momenta. Then, using the formalism in chapter 6 pioneered by Lüscher, we related those finite-volume stationary state energies to infinite-volume $K\pi$ scattering phase shifts. Despite the limited set of statistics available at this time, we were able to determine with reasonable accuracy, the $K^*(892)$ resonance mass and the $K^*(892) \to K\pi$ coupling, along with the s-wave $K\pi$ scattering length:

$$\frac{m_{K^*}}{m_\pi} = 3.027^{+16}_{-13}\,, \qquad g_{K^*K\pi} = 5.75^{+25}_{-35}\,, \qquad m_\pi a_0 = -0.93^{+15}_{-19}\,. \tag{9.1}$$

Efforts are ongoing to increase the statistics available on this ensemble, and on the two additional ensembles listed in table 8.1 with the same lattice spacing, but different quark masses. The end goal of this project is to map out these amplitudes on the atypical quark mass trajectory used in generating these lattices in which the trace of the quark mass matrix is kept constant, followed by a chiral extrapolation along this trajectory to the physical point, somewhat in the spirit of Ref. [20]. With this we hope to provide not just a high precision determination of resonance parameters of the well-established vector $K^*(892)$ meson, but also to provide an insight into the nature of the poorly understood scalar $K^*(700)$ meson.

At this point, calculations of these meson-meson scattering amplitudes from lattice QCD have matured significantly, and we are beginning to turn to more complicated processes, including meson-baryon scattering [21], baryon-baryon scattering [161], and the insertion of external currents [20]. With the advent of Exascale computing, and the continual development of improved algorithmic techniques, tackling yet more complicated nuclear processes is on the horizon.

Appendix A

Extracting Observables from Monte Carlo Data

The observable quantities we deal with can be classed into two categories; simple and non-simple observables. A simple observable is one that can be measured on a single configuration of gauge fields, or equivalently, one that coincides with the integrand of a single path integral. Estimates of such simple observables can then be estimated using standard Monte Carlo formulae: for a set of simple observables $\{b_i\}$, where $b_i^{(C)}$ is the value of b_i on a single configuration U_C, the sample mean and covariance are given by

$$\langle b_i \rangle = \frac{1}{N_C} \sum_{C=0}^{N_C-1} b_i^{(C)}, \tag{A.1a}$$

$$\mathrm{cov}(b_i, b_j) = \frac{1}{N_C - 1} \langle (b_i - \langle b_i \rangle)(b_j - \langle b_j \rangle) \rangle = \frac{\langle b_i b_j \rangle - \langle b_i \rangle \langle b_j \rangle}{N_C - 1}, \tag{A.1b}$$

where N_C is the number of gauge configurations. Note that we have used the factor $1/(N_C - 1)$ rather than $1/N_C$ as the former removes the bias due to estimating the mean by $\langle b_i \rangle$, though the difference is generally imperceptible. Additionally, to be pedantic, what we define here is the covariance for *our* estimates of b_i, b_j, i.e. the *sample* covariance, rather than the "true" or *population* covariance.

As the name may suggest, a non-simple observable is then any observable that is not simple. For non-simple observables the above formulae cannot be used, and so we need some way to estimate such quantities, and more importantly, the error in their estimates. In certain elementary cases, one could use a simple propagation of uncertainty, though for example in determining the error on parameters from a fit, it is unclear how to do this properly. Therefore we advocate the use of statistical resampling schemes for estimating the errors on our non-simple observables. In the following section, we will define the two resampling techniques that we use, followed by a description of the correlated χ^2 fitting procedure used to obtain best-fit estimates for the relevant model parameters we wish to extract.

A.1 Resampling Techniques

A resampling scheme involves determining a set of resamplings for an observable, where each resampling contains an estimate of the observable. We consider two schemes, the *jackknife* and *bootstrap* procedures [162]. In jackknife resampling, the n-th resampling is determined by taking an average for the observable over all configurations, omitting the n-th configuration, given by

$$\langle b_i \rangle_n^{\text{jack}} = \frac{1}{N_C - 1} \sum_{C \neq n} b_i^{(C)}. \tag{A.2}$$

From this, the so-called jackknife mean and covariance are then given by

$$\langle b_i \rangle^{\text{jack}} = \frac{1}{N_C} \sum_{n=0}^{N_C-1} \langle b_i \rangle_n^{\text{jack}}, \tag{A.3a}$$

$$\text{cov}^{\text{jack}}(b_i, b_j) = \frac{N_C - 1}{N_C} \sum_{n=0}^{N_C-1} (\langle b_i \rangle_n^{\text{jack}} - \langle b_i \rangle)(\langle b_j \rangle_n^{\text{jack}} - \langle b_j \rangle), \tag{A.3b}$$

and it can be shown that $\langle b_i \rangle = \langle b_i \rangle^{\text{jack}}$ and $\text{cov}(b_i, b_j) = \text{cov}^{\text{jack}}(b_i, b_j)$.

Alternatively, in *bootstrap* resampling, each resampling for a given observable is determined from an average of the values of that observable on N_C randomly chosen configurations *with replacement* (i.e. any configuration can be chosen multiple times). The total number of bootstrap resamplings N_B can then be set to any value, though if chosen too small we do not expect a good estimate for the covariances between observables. Hence, N_B should be chosen large enough that adding any further bootstrap resamplings does not effect the results significantly. The estimate for the n-th bootstrap resampling is then given by

$$\langle b_i \rangle_n^{\text{boot}} = \frac{1}{N_C} \sum_{\alpha=0}^{C-1} b_i^{(C_\alpha^{(n)})}, \tag{A.4}$$

where $C_\alpha^{(n)}$ denotes the α-th randomly chosen configuration for the n-th bootstrap resampling. Given a sufficiently large number N_B of these estimates, the bootstrap mean and covariance are then given by

$$\langle b_i \rangle^{\text{boot}} = \frac{1}{N_B} \sum_{n=0}^{N_B-1} \langle b_i \rangle_n^{\text{boot}}, \tag{A.5a}$$

$$\text{cov}^{\text{boot}}(b_i, b_j) = \frac{1}{N_B - 1} \sum_{n=0}^{N_B-1} (\langle b_i \rangle_n^{\text{boot}} - \langle b_i \rangle)(\langle b_j \rangle_n^{\text{boot}} - \langle b_j \rangle). \tag{A.5b}$$

Note finally that the jackknife scheme is simply a linear approximation to the bootstrap resampling procedure. Hence, since the bootstrap scheme provides information about the entire sampling distribution, for sufficient large values of N_B, should give either an equivalent or better estimate of the covariances. This is seen for example in App. A and Fig. 14 of Ref. [163] where, in studying

$\bar{D}D$ scattering in lattice QCD, the authors show how the non-linear nature of the phase shift analysis can result in a severe underestimation of errors when using jackknife resampling. Therefore, we choose to use bootstrap resampling in the scattering analysis in chapter 8.

A.2 Correlated χ^2 Fitting

Since the gauge configurations on which we measure our observables are generated using a Markov chain, there will be some residual correlations between observables on different configurations. We use autocorrelations as a measure of this correlation, and at various stages make efforts to reduce such correlations, so that we can assume at the fitting stage that autocorrelations are negligible. However, the correlations between different measurements must be accounted for when we fit a model function to our data. More concretely, the residual functions used in a fit minimisation are not statistically independent, having been measured on the same set of gauge configurations, and so their covariances should be included in the likelihood function we minimise.

Given a set of observables $\{b_i\}$, say a temporal correlation function $C(t)$, which constitute the components of the vector $\boldsymbol{b}$, and a set of best-fit parameters which constitute the components of the vector $\boldsymbol{\alpha}$, we denote the model function which we use to describe the data by $\boldsymbol{M}(\boldsymbol{\alpha}, \boldsymbol{b})$. We determine the best-fit estimates of the $\boldsymbol{\alpha}$ parameters as the values which minimise the correlated-χ^2 given by

$$\chi^2 = \sum_{i,j} \langle r_i \rangle \sigma_{ij}^{-1} \langle r_j \rangle, \tag{A.6}$$

where the vector of residuals is given by $\boldsymbol{r} = \boldsymbol{b} - \boldsymbol{M}(\boldsymbol{\alpha}, \boldsymbol{b})$, and $\sigma_{ij} = \mathrm{cov}(r_i, r_j)$. Note that if the model function does not depend on the observables, i.e. $\boldsymbol{M} = \boldsymbol{M}(\boldsymbol{\alpha})$, then it can be shown that $\mathrm{cov}(r_i, r_j) = \mathrm{cov}(b_i, b_j)$. This will then greatly simplify the minimisation as the covariance matrix needs only to be calculated once at the beginning of the minimisation. Otherwise, each time that one of the fit parameters in $\boldsymbol{\alpha}$ is changed, σ^{-1} needs to be recalculated.

While most minimisation software will often provide statistical uncertainties in the best-fit parameters, these generally assume Gaussian statistics. A better alternative, as alluded to in the previous sections, is the use a resampling scheme to solve the problem and calculate the covariances between best-fit parameters. To do this, we minimise

$$\chi_k^2 = \sum_{i,j} \langle r_i \rangle_k \sigma_{ij}^{-1} \langle r_j \rangle_k, \tag{A.7}$$

for each resampling k, and then obtain the covariances of the fit parameters $\mathrm{cov}(\alpha_i, \alpha_j)$ using either eq. (A.3b) or eq. (A.5b), depending on the resampling scheme used.

Appendix B

Correlator Matrices

Shown here are the normalised correlation matrix elements (eq. (5.2)) for the 13×13 matrix used in the scalar glueball study in chapter 7. Plots are arranged as shown in fig. B.1.

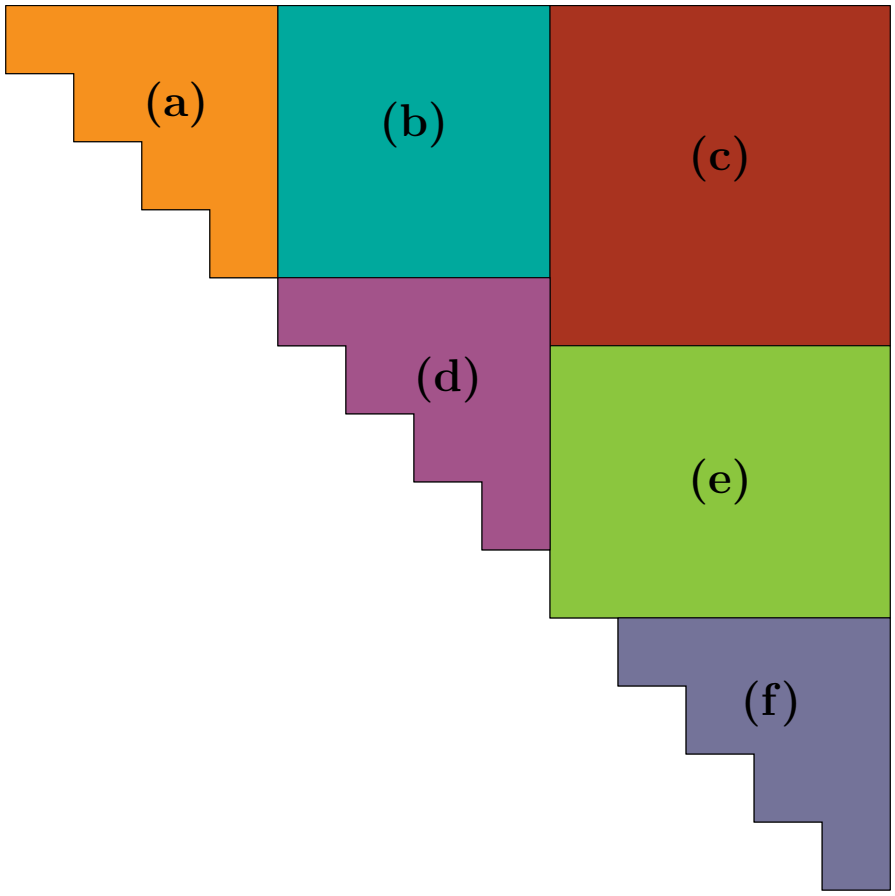

Figure B.1: The layout used here to display each element of the 13×13 symmetric correlation matrix. Labels in each block indicate the relevant subfigure where that block is shown in the rest of this appendix.

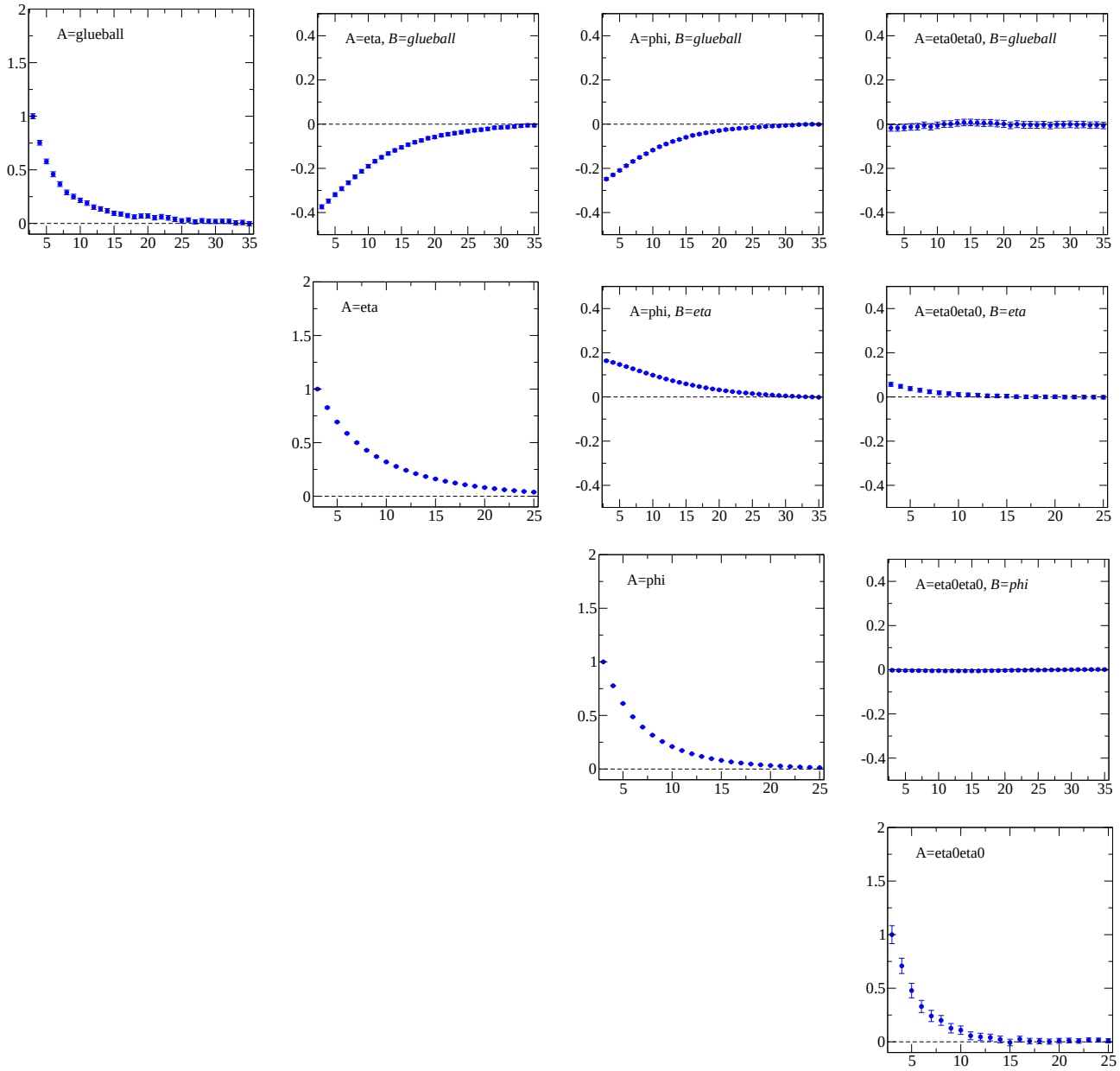

(a) $\mathrm{Re}\, C_{AB}(t)$ for block (a) of the A_{1g}^{+} correlation matrix.

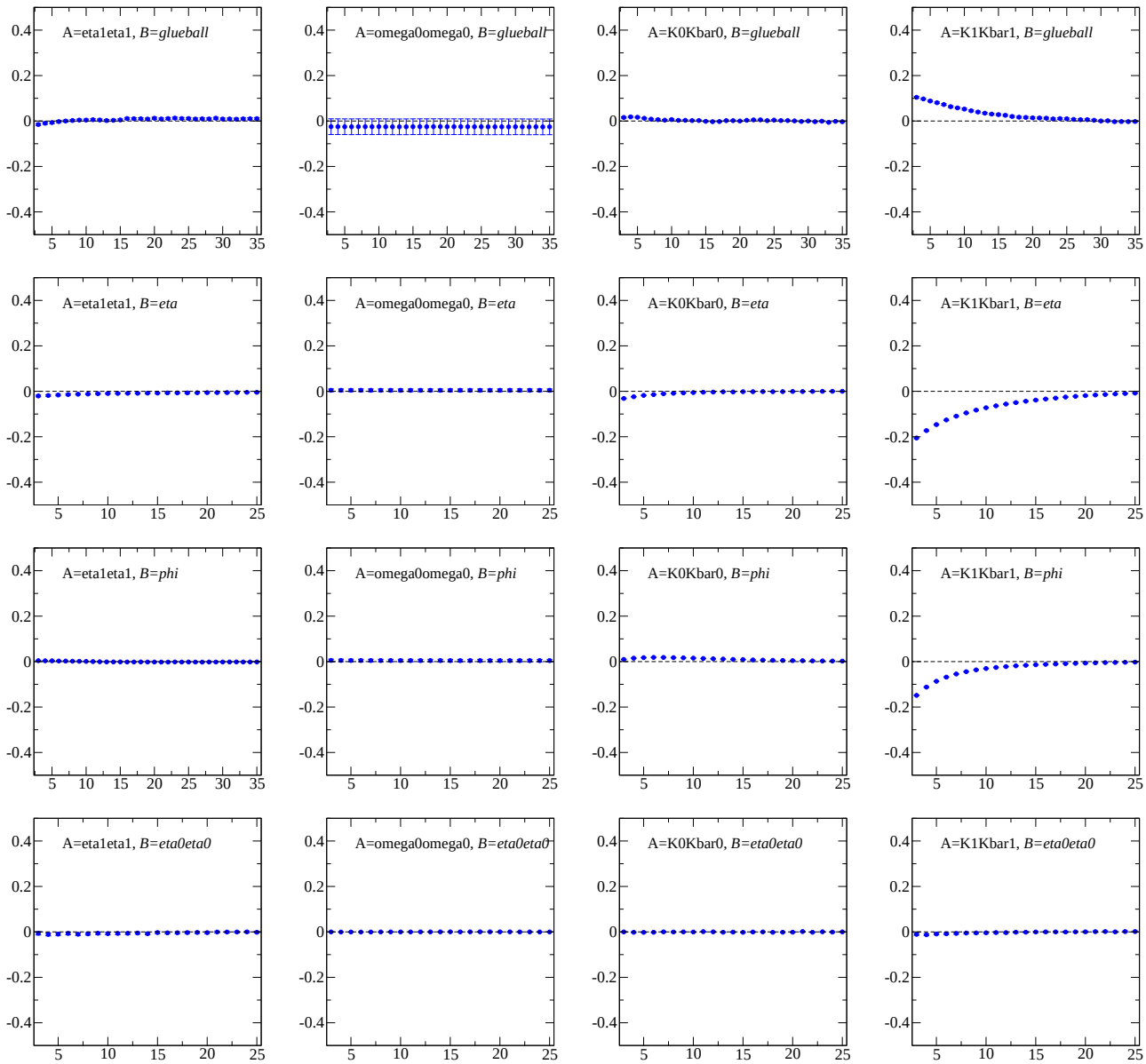

(b) $\mathrm{Re}\, C_{AB}(t)$ for block (b) of the A_{1g}^{+} correlation matrix.

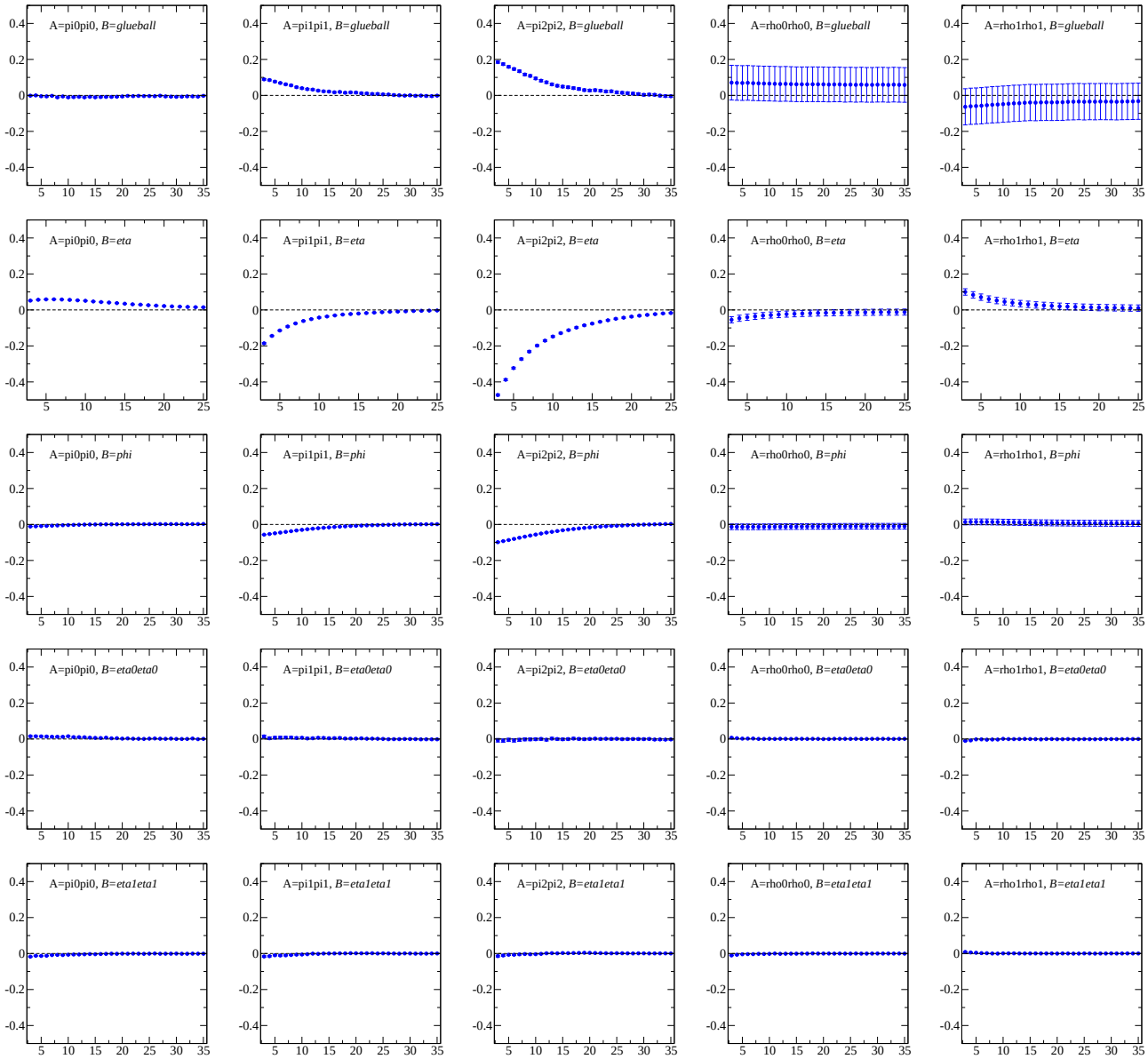

(c) $\mathrm{Re}\, C_{AB}(t)$ for block (c) of the A_{1g}^{+} correlation matrix.

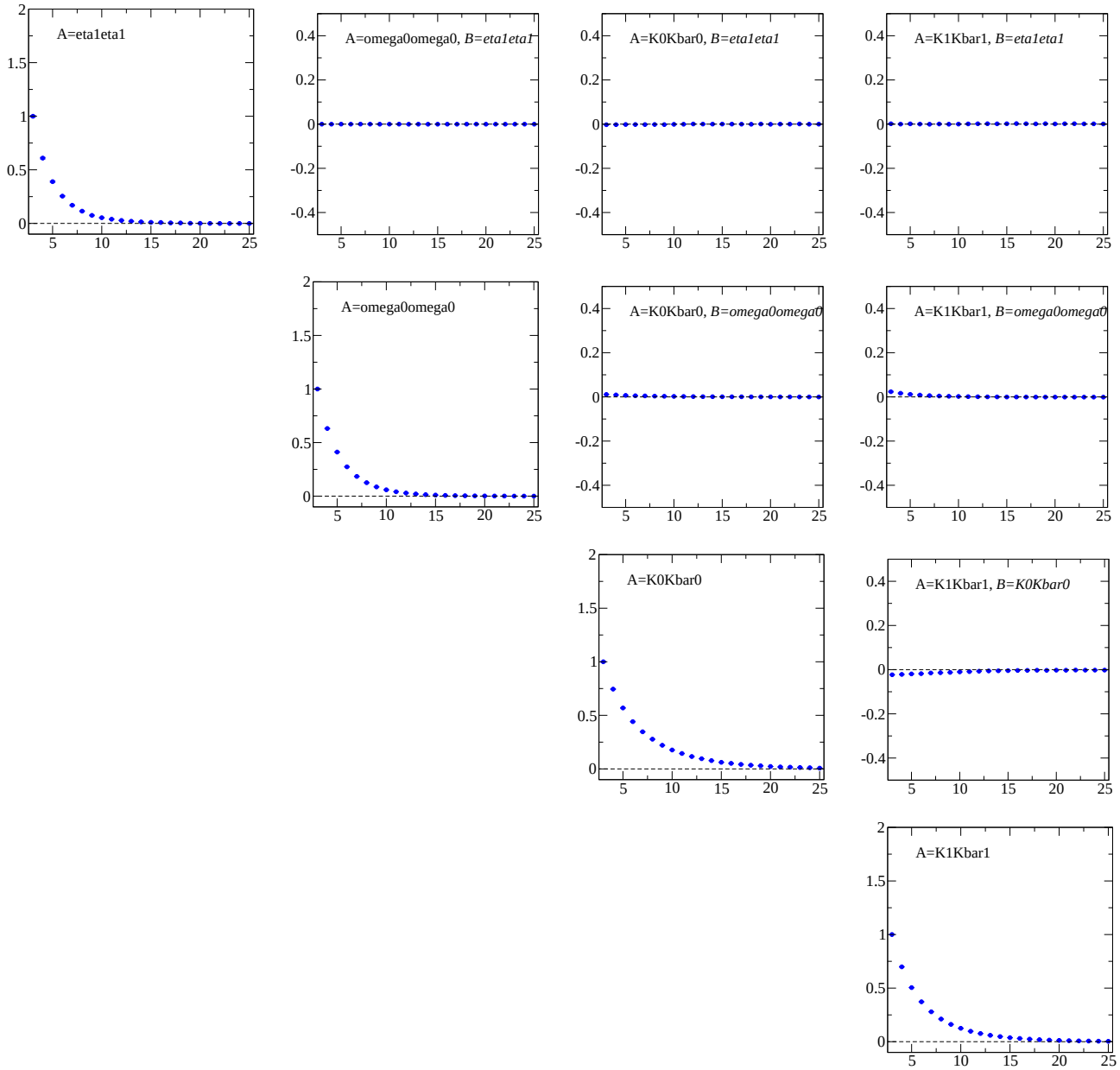

(d) $\mathrm{Re}\, C_{AB}(t)$ for block (d) of the A_{1g}^{+} correlation matrix.

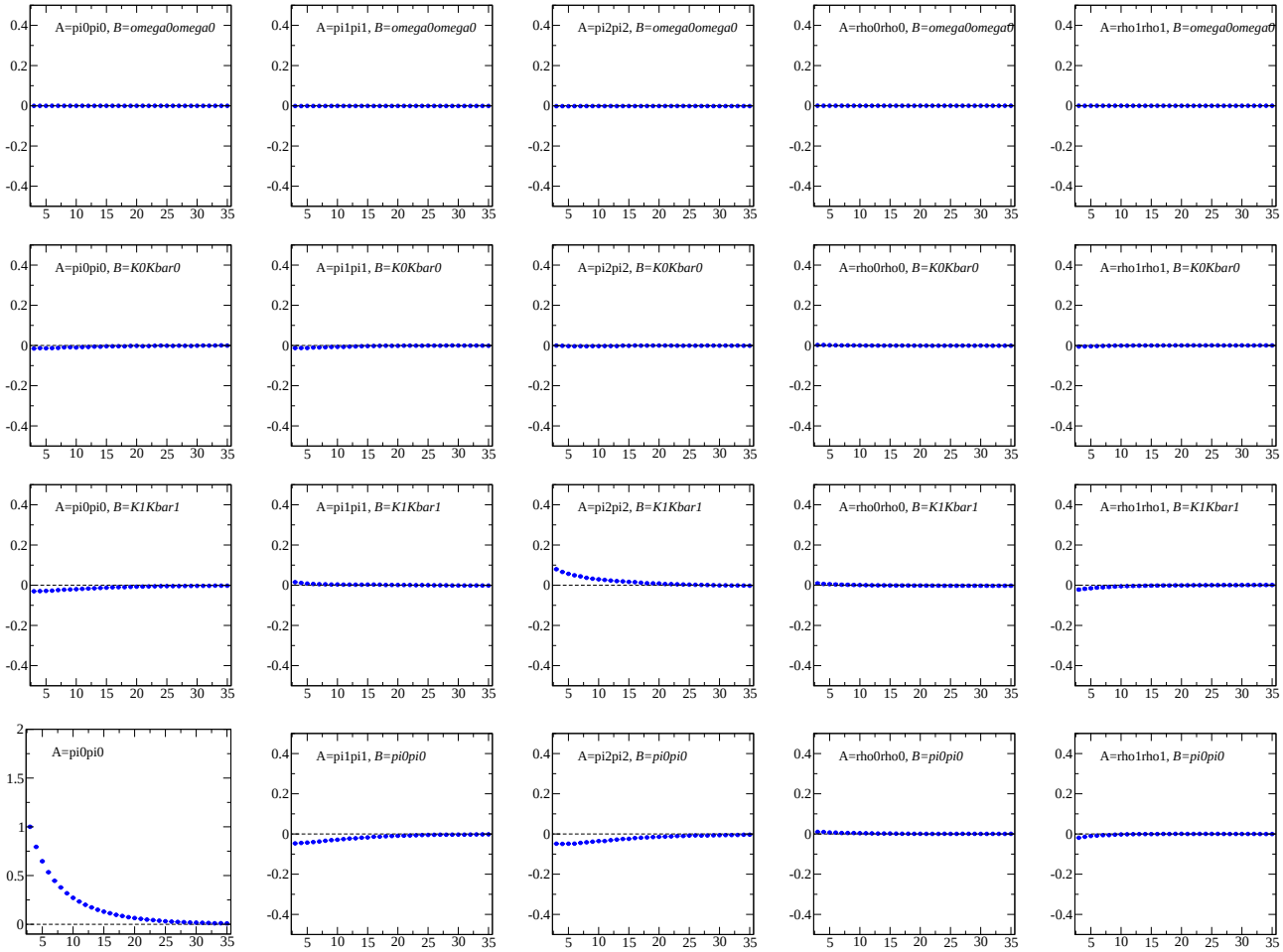

(e) $\mathrm{Re}\, C_{AB}(t)$ for block (e) of the A_{1g}^{+} correlation matrix.

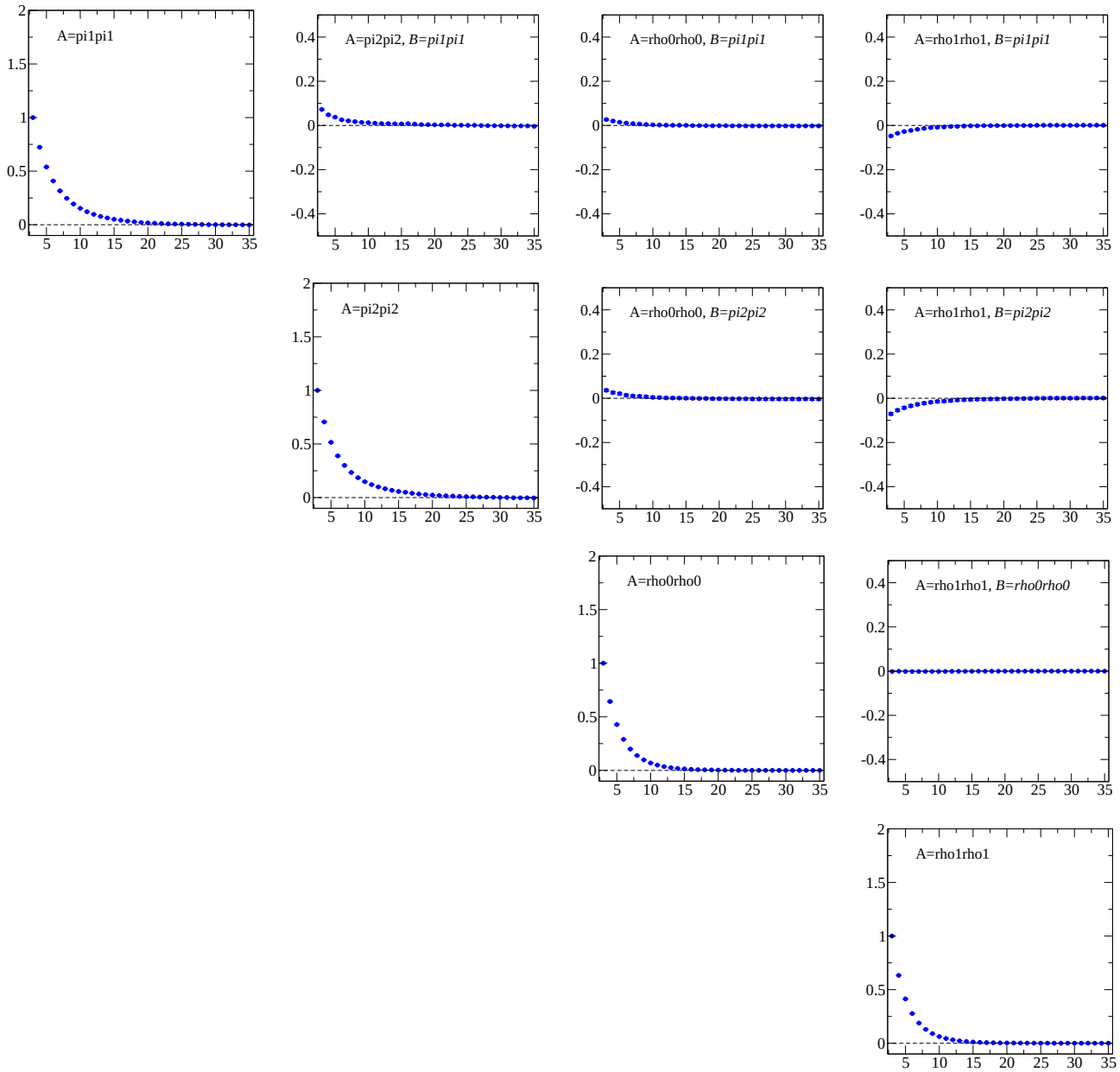

(f) $\mathrm{Re}\, C_{AB}(t)$ for block (f) of the A_{1g}^{+} correlation matrix.

Figure B.2: Real part of each matrix element of the 13×13 correlation matrix used in the analysis in chapter 7.

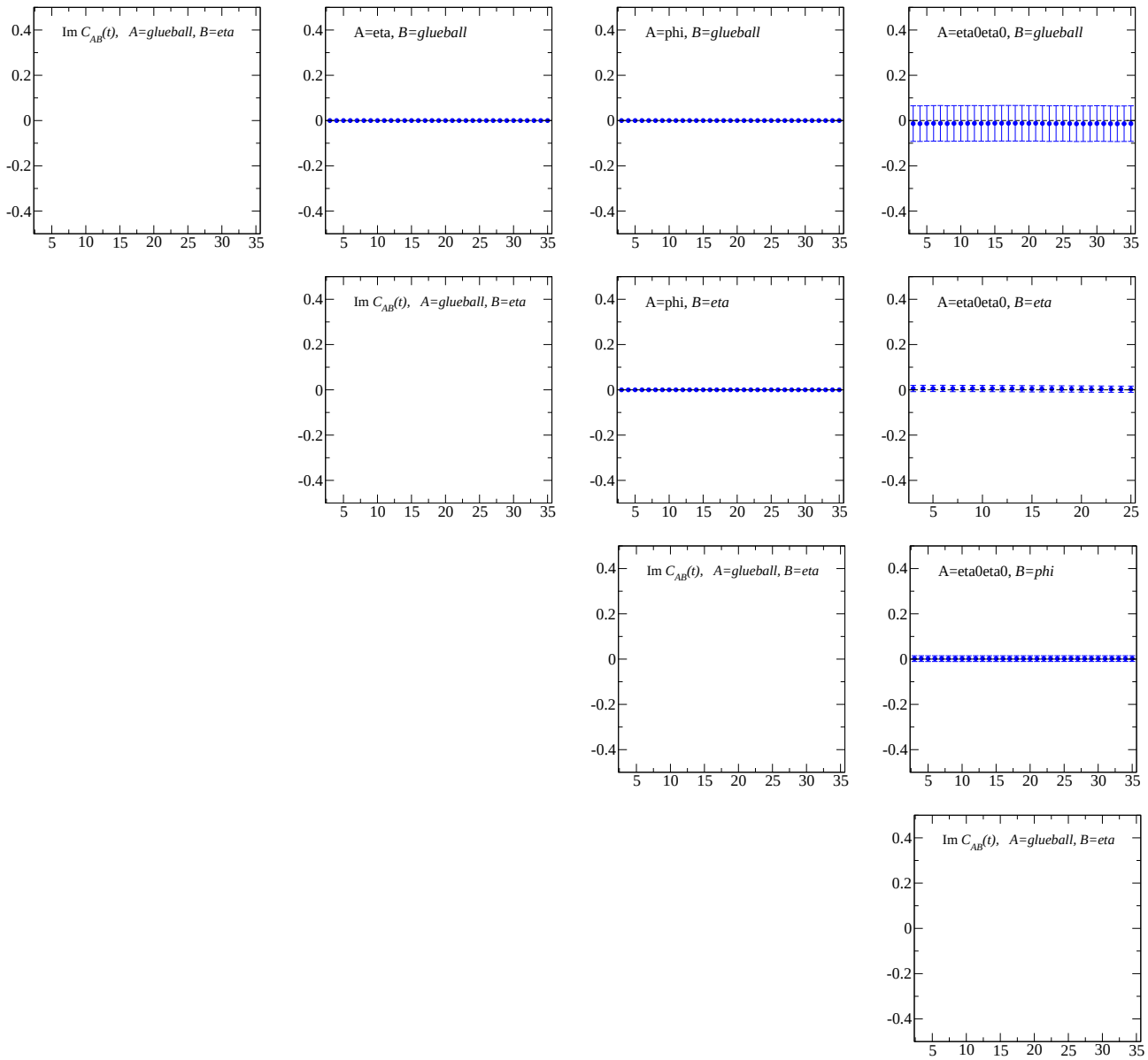

(a) $\mathrm{Im}\, C_{AB}(t)$ for block (a) of the A_{1g}^{+} correlation matrix.

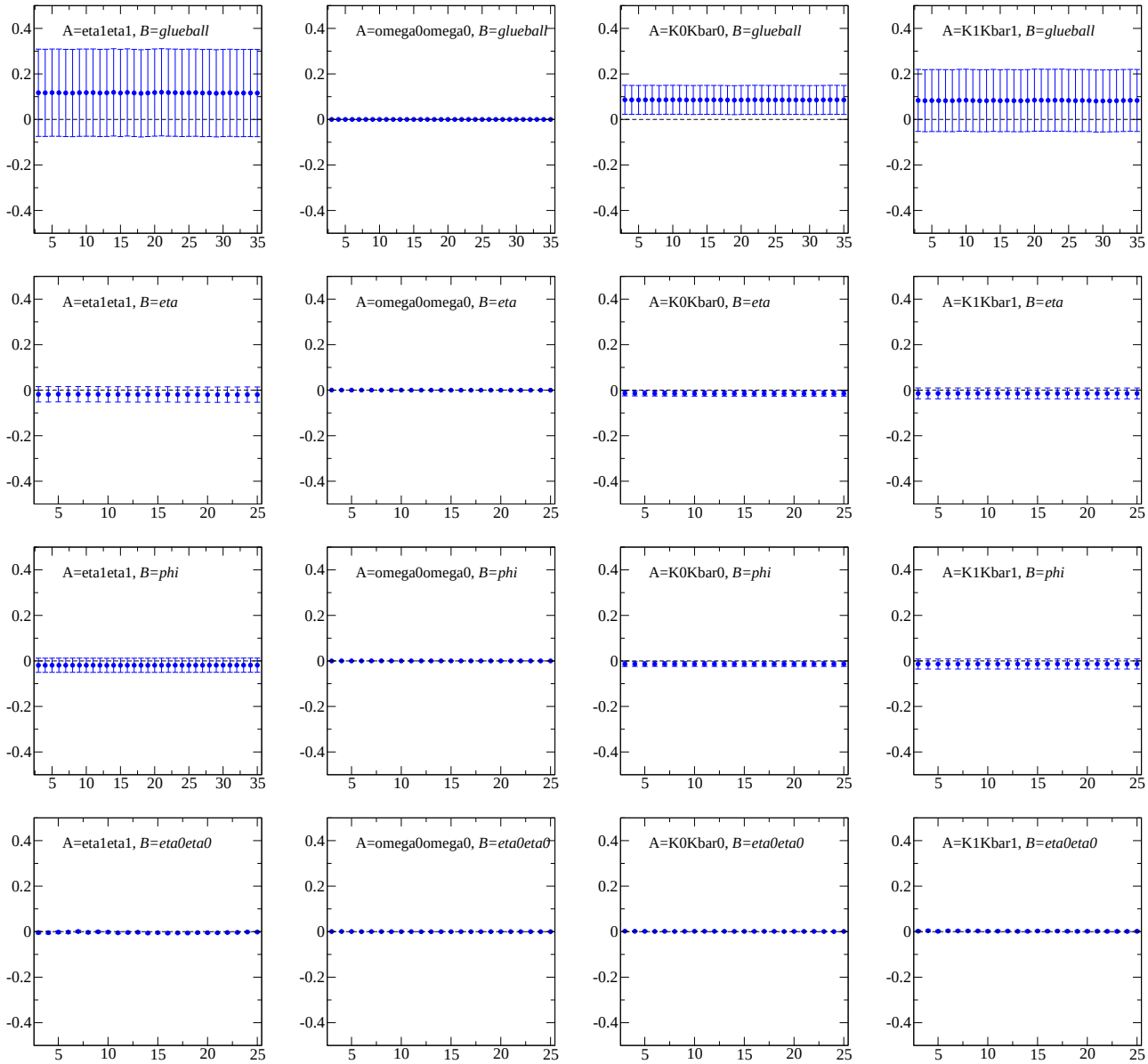

(b) $\mathrm{Im}\, C_{AB}(t)$ for block (b) of the A_{1g}^{+} correlation matrix.

(c) $\mathrm{Im}\, C_{AB}(t)$ for block (c) of the A_{1g}^{+} correlation matrix.

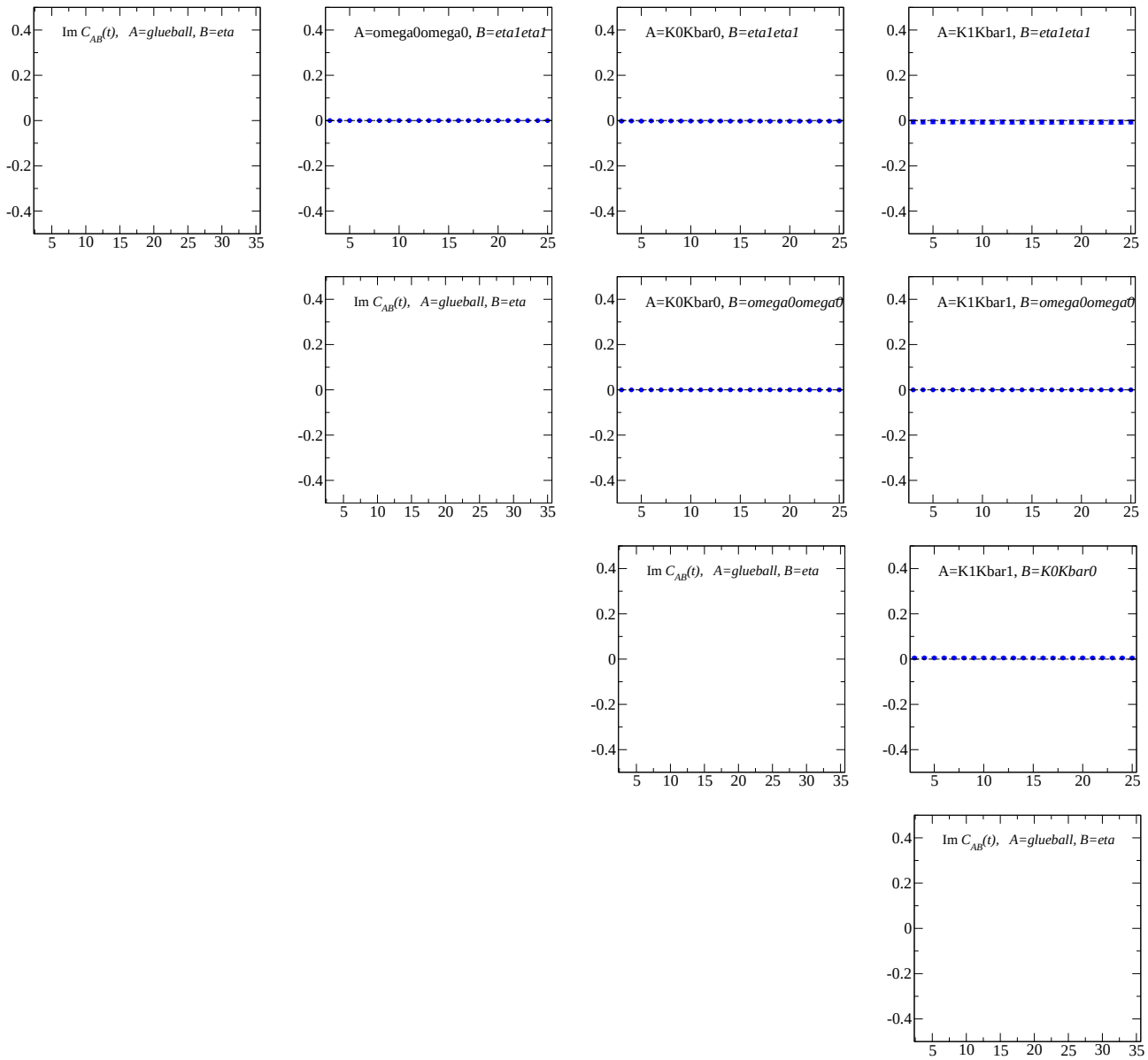

(d) $\mathrm{Im}\, C_{AB}(t)$ for block (d) of the A_{1g}^{+} correlation matrix.

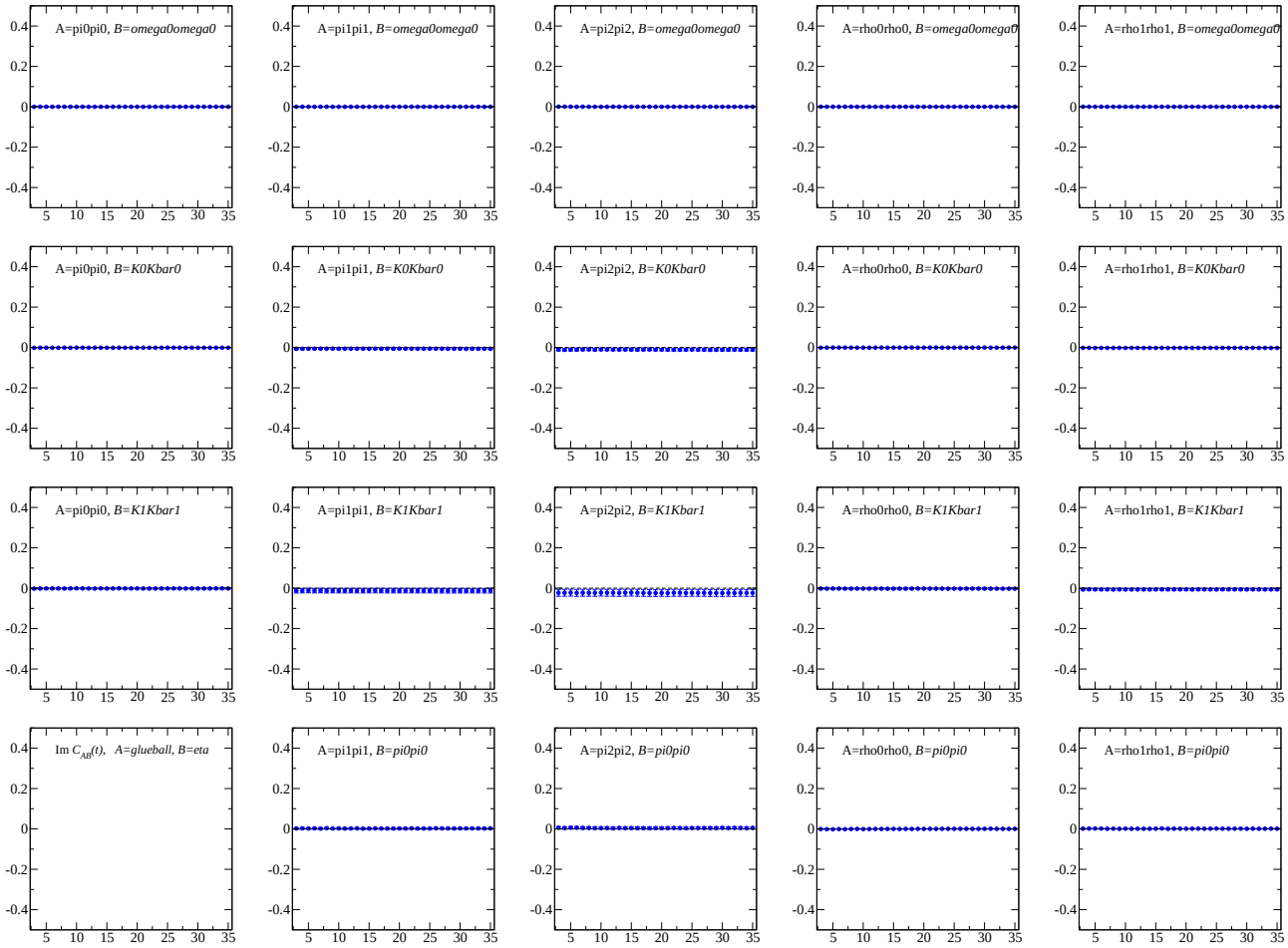

(e) $\mathrm{Im}\, C_{AB}(t)$ for block (e) of the A_{1g}^{+} correlation matrix.

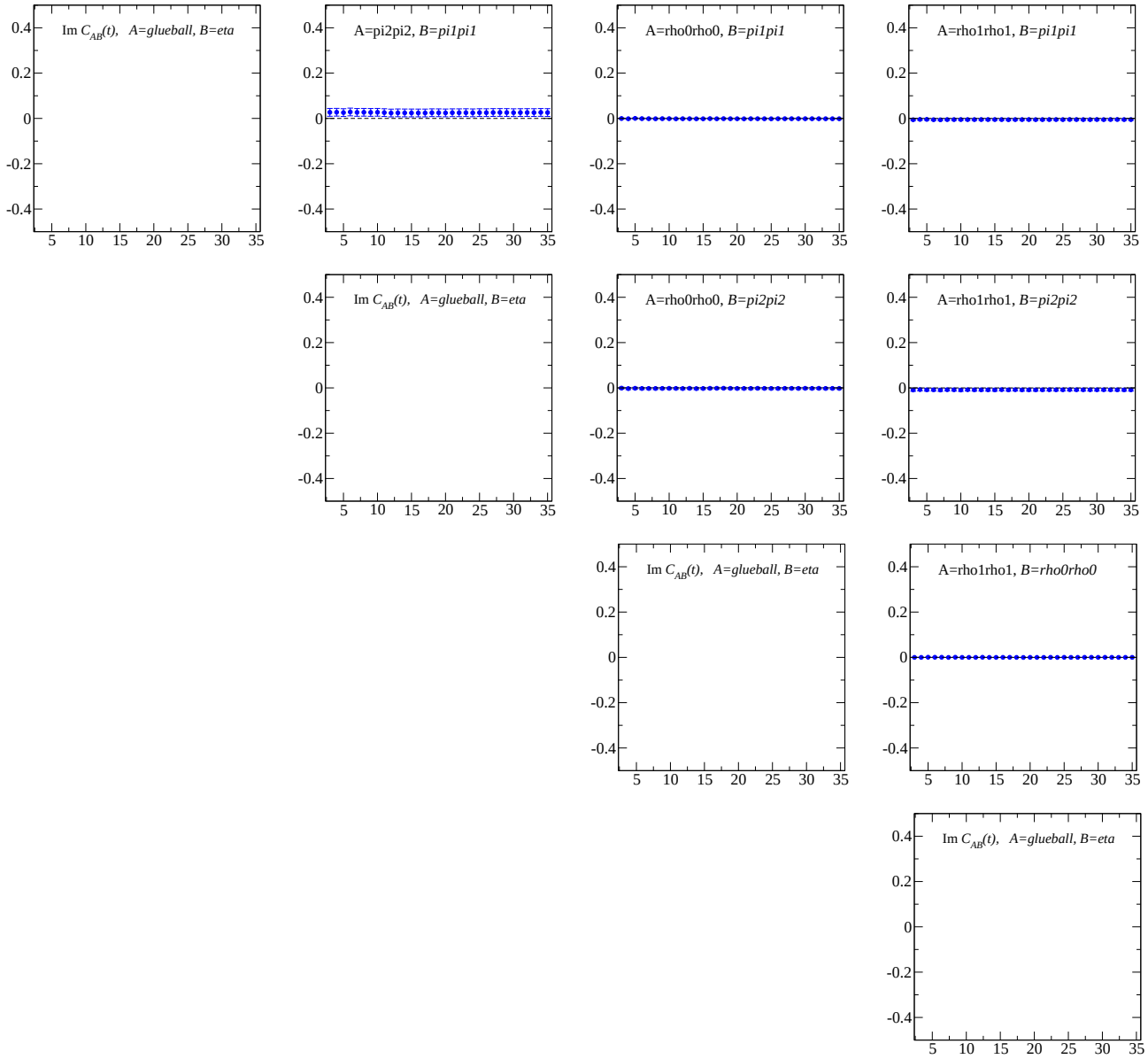

(f) $\mathrm{Im}\, C_{AB}(t)$ for block (f) of the A_{1g}^{+} correlation matrix.

Figure B.3: Imaginary part of each matrix element of the 13×13 correlation matrix used in the analysis in chapter 7.

Appendix C

t_{min}-Plots

Shown here are t_{min}-plots for the $K\pi$ scattering analysis in chapter 8. Each plot shows the best-fit values for the energy for a given level for many t_{min} with a fixed t_{max}. The colouring of each point gives a qualitative indication of the best-fit χ^2 per degree of freedom for each t_{min}. Red points indicate $\chi^2/\mathrm{d.o.f.} > 1$, black points $\chi^2/\mathrm{d.o.f.} \approx 1$, and green points $\chi^2/\mathrm{d.o.f.} < 1$. A particular t_{min} is chosen based on reduced χ^2 and stability to variations in t_{min} and t_{max}. Chosen t_{min} is indicated by the solid (central value) and dotted (1σ errors) blue lines. Fit forms used are described in section 5.3.

C.1 $K\pi$ Scattering

$P^2 = 0$, A_{1g} **Irrep**

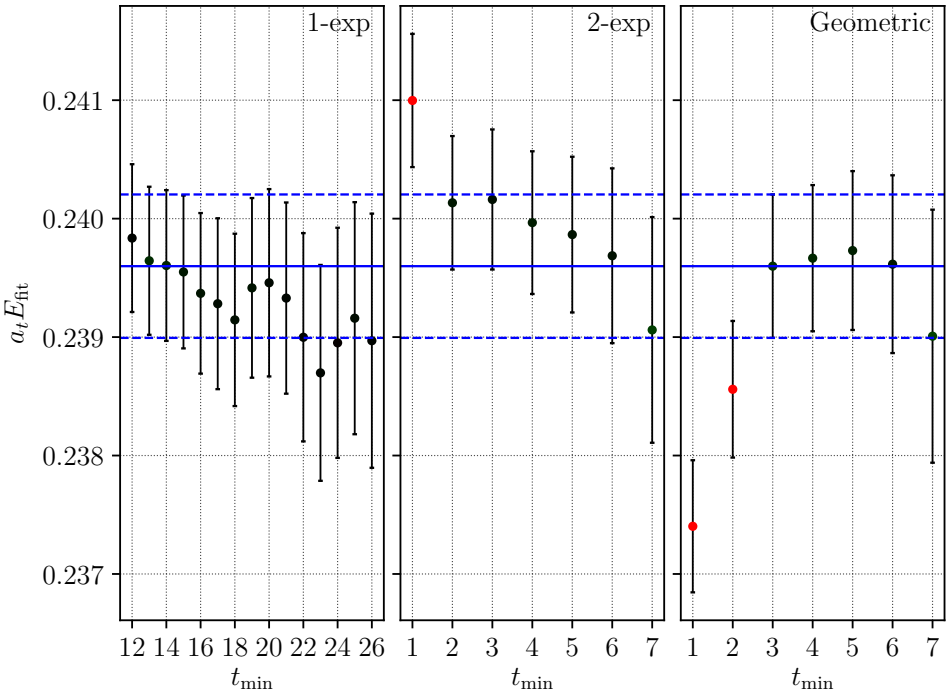

(a) Level 0

Figure C.1: t_{min}-plots for the $P^2 = 0$, A_{1g} irrep on the N200 ensemble.

$P^2 = 0$, T_{1u} **Irrep**

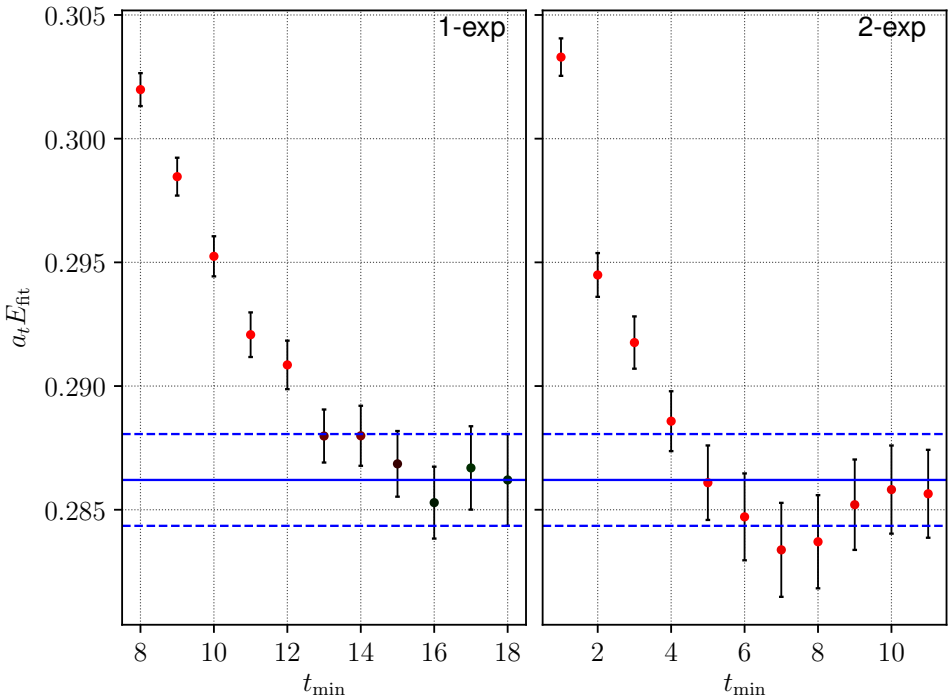

(a) Level 0

Figure C.2: t_{min}-plots for the $P^2 = 0$, T_{1u} irrep on the N200 ensemble.

$P^2 = 1$, A_1 **Irrep**

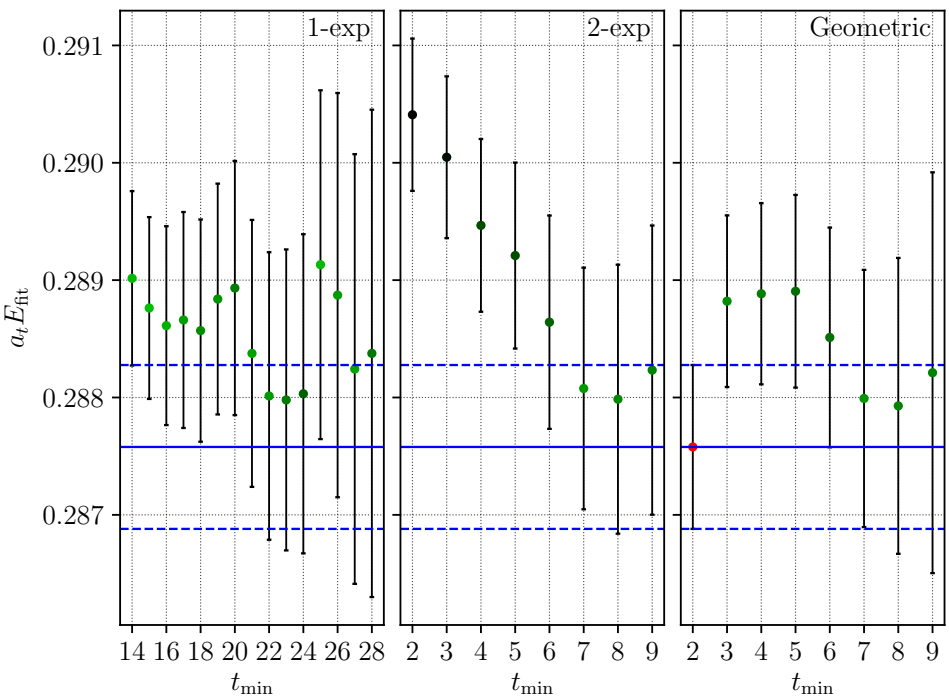

(a) Level 0

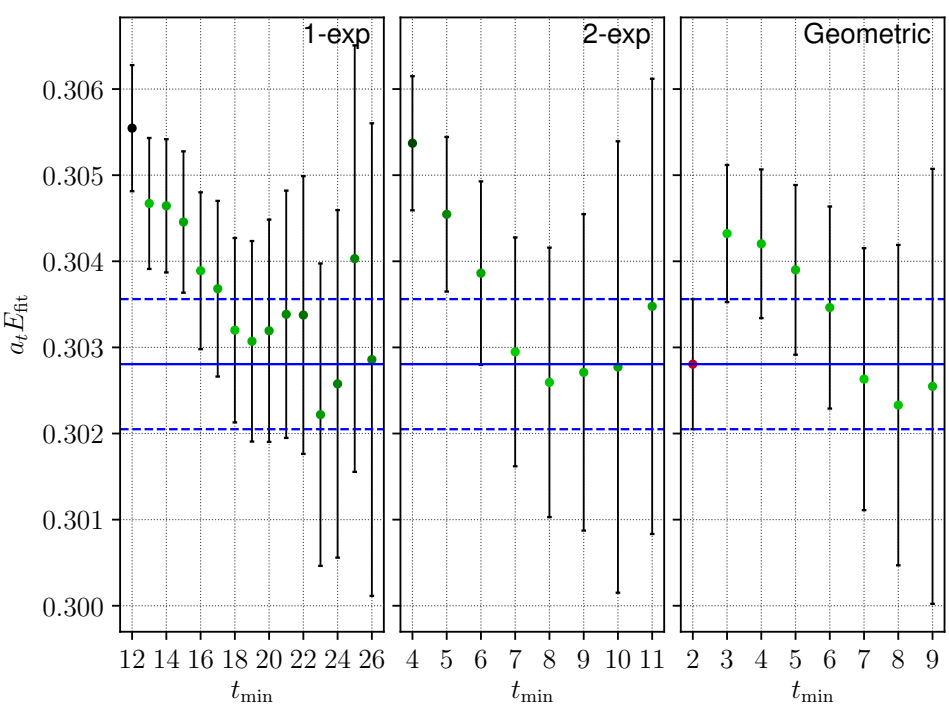

(b) Level 1

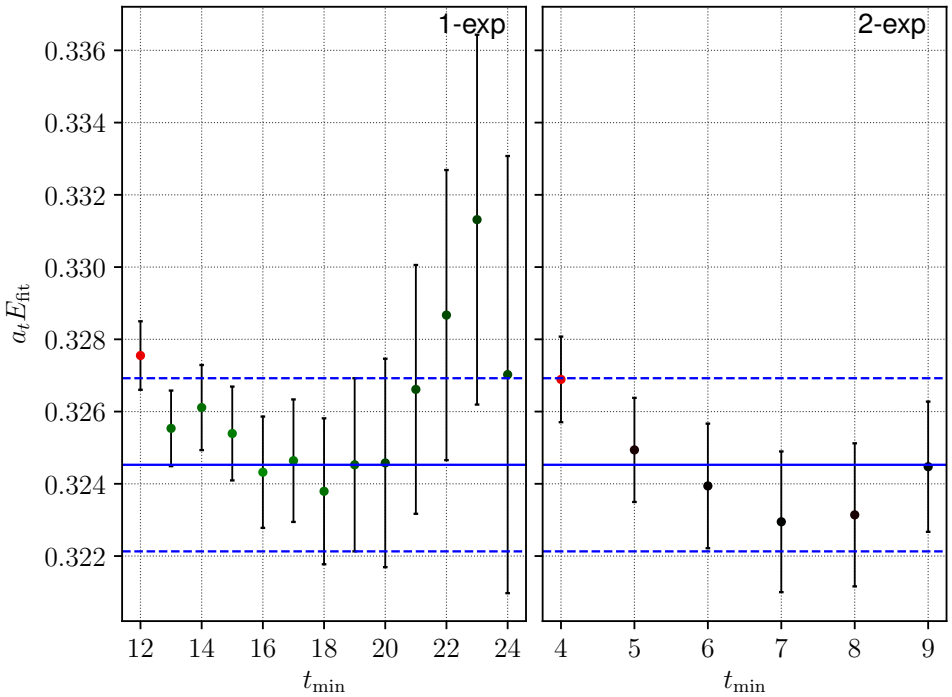

(c) Level 2

Figure C.3: t_{min}-plots for the $P^2 = 1$, A_1 irrep on the N200 ensemble.

$P^2 = 1$, E **Irrep**

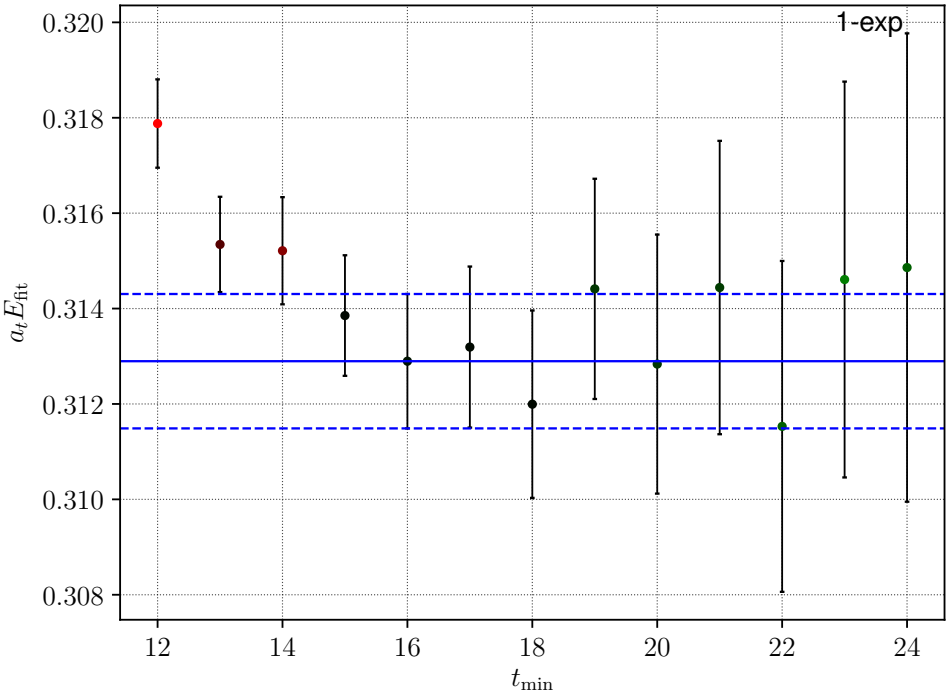

(a) Level 0

Figure C.4: t_{min}-plots for the $P^2 = 1$, E irrep on the N200 ensemble.

$P^2 = 2$, A_1 **Irrep**

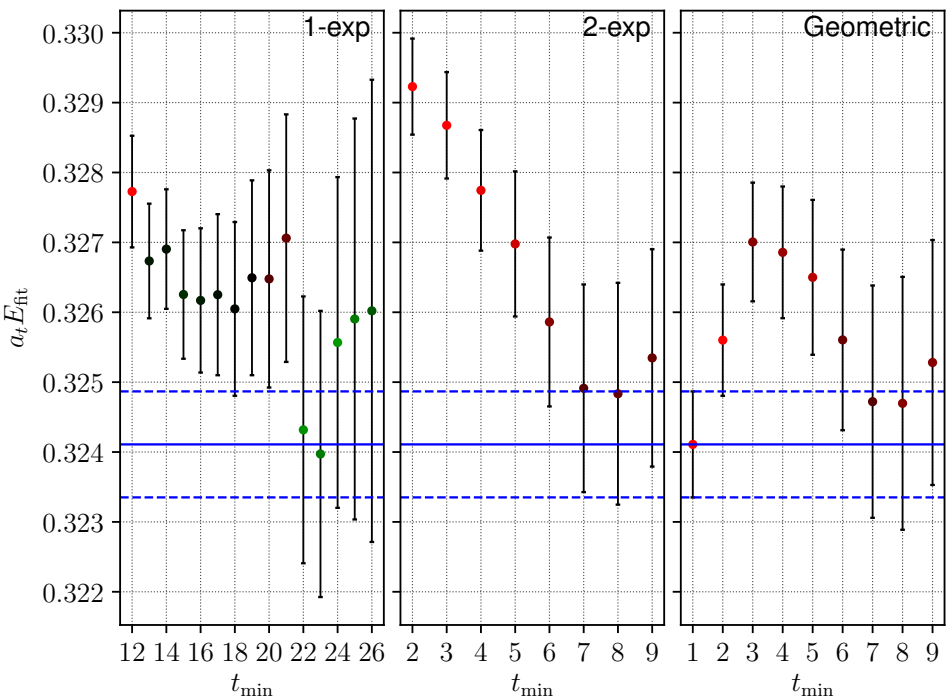

(a) Level 0

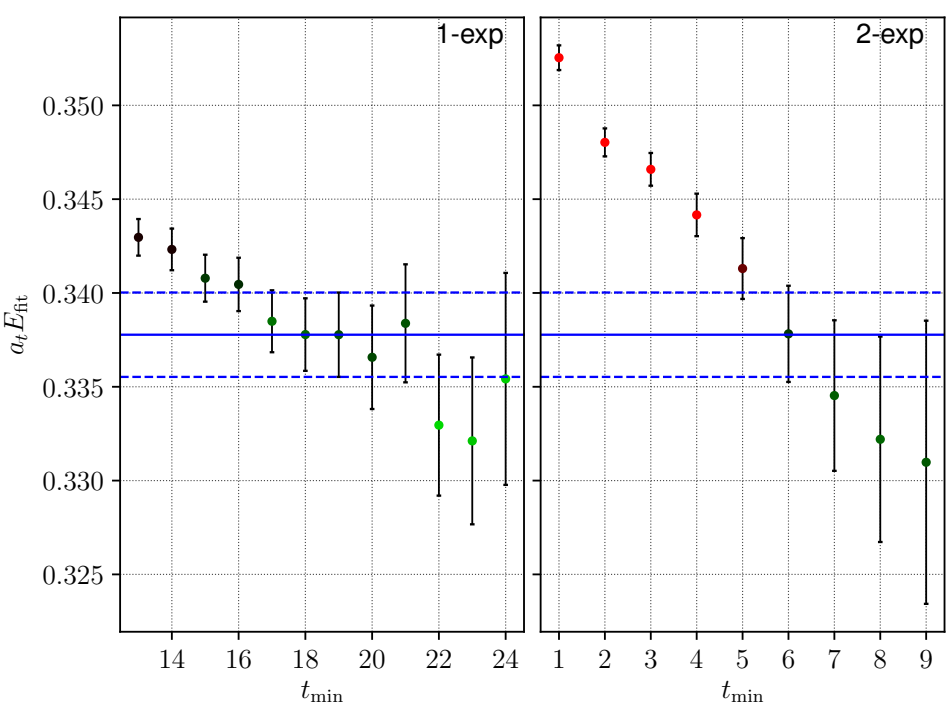

(b) Level 1

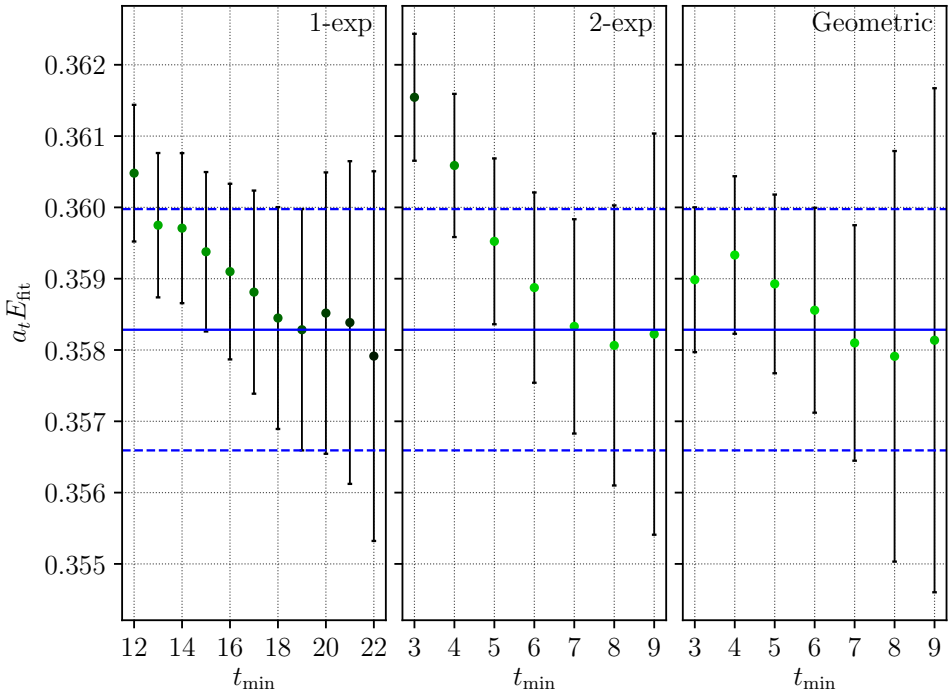

(c) Level 2

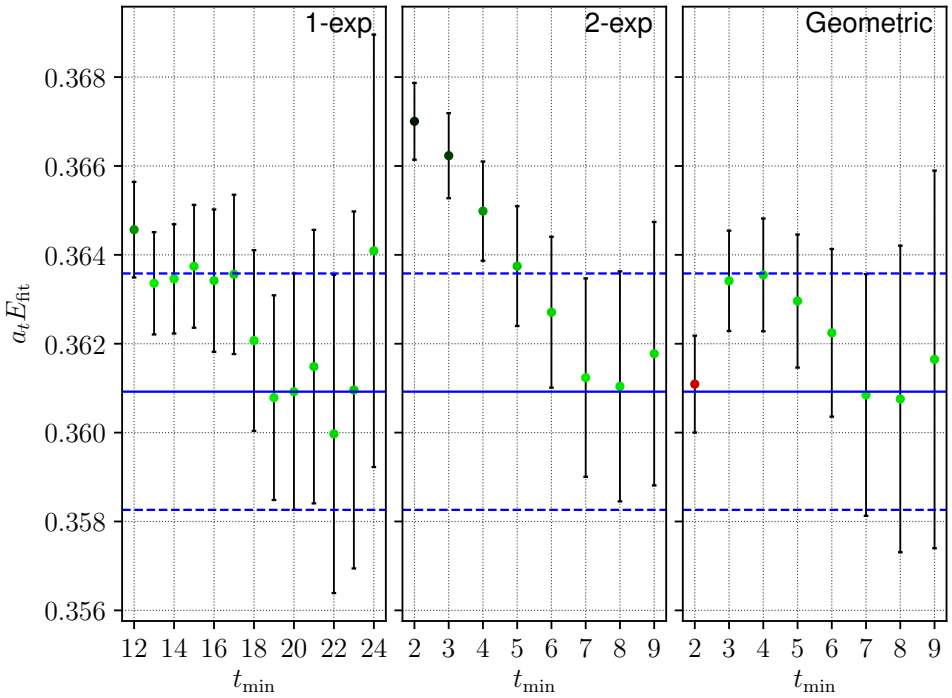

(d) Level 3

Figure C.5: t_{min}-plots for the $P^2 = 2$, A_1 irrep on the N200 ensemble.

$P^2 = 2$, B_1 **Irrep**

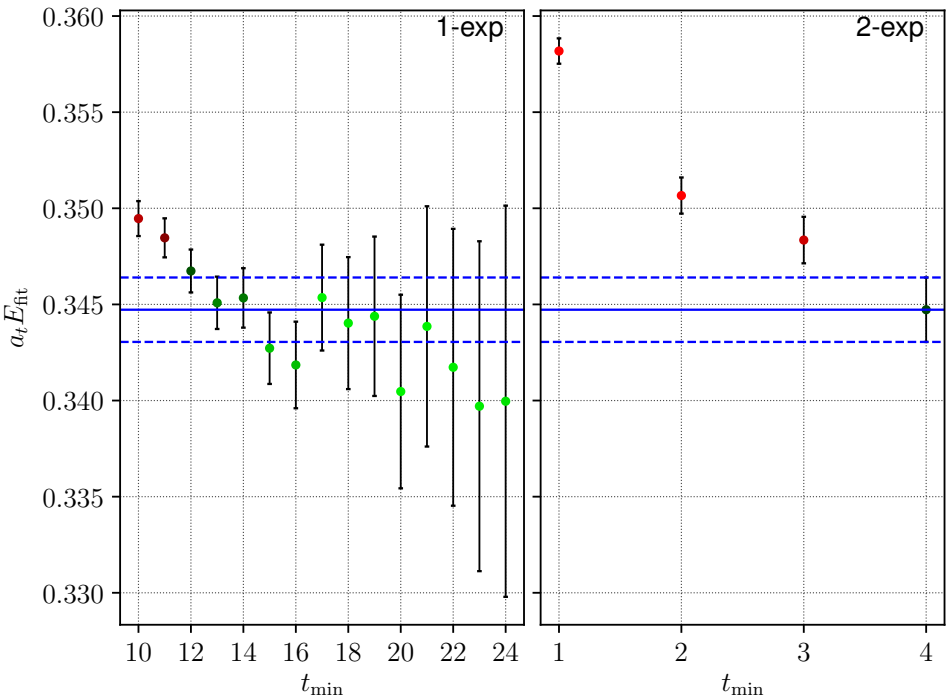

(a) Level 0

Figure C.6: t_{min}-plots for the $P^2 = 2$, B_1 irrep on the N200 ensemble.

$P^2 = 2$, B_2 **Irrep**

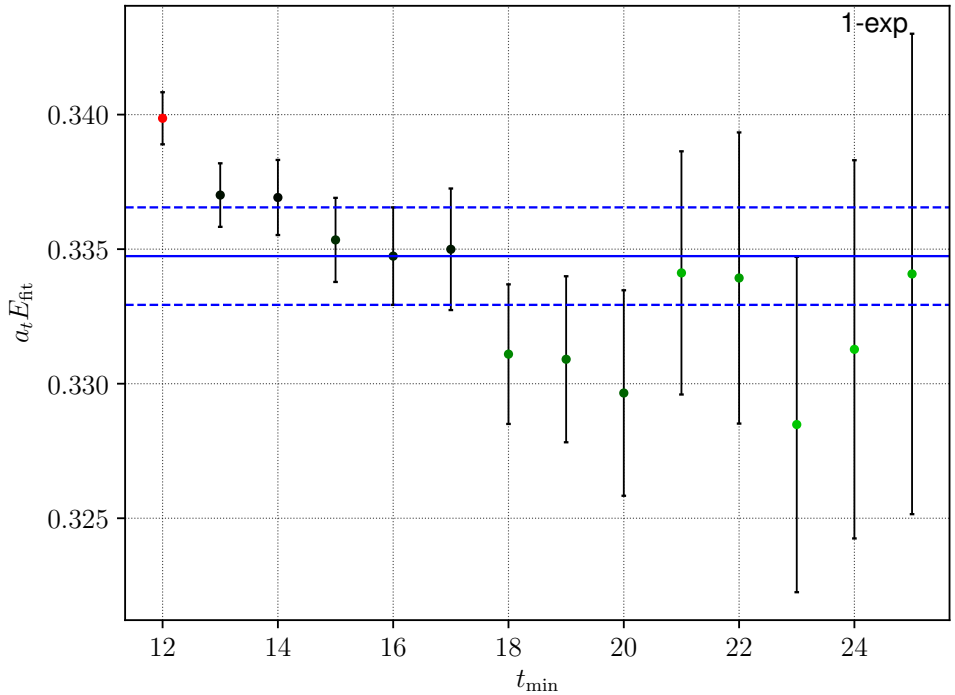

(a) Level 0

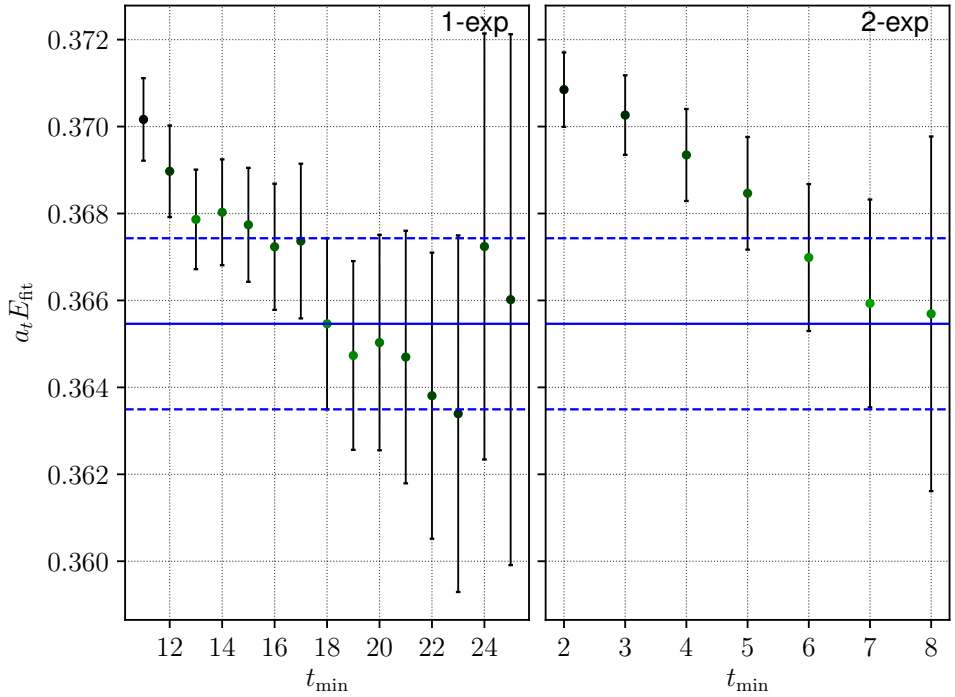

(b) Level 1

Figure C.7: t_{min}-plots for the $P^2 = 2$, B_2 irrep on the N200 ensemble.

$P^2 = 3,\ A_1$ **Irrep**

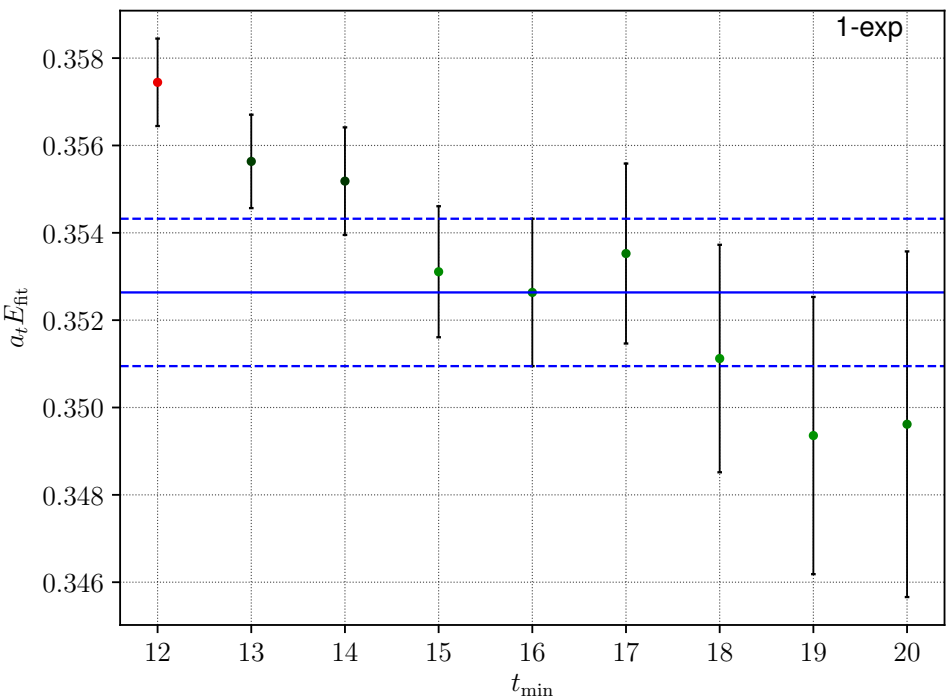

(a) Level 0

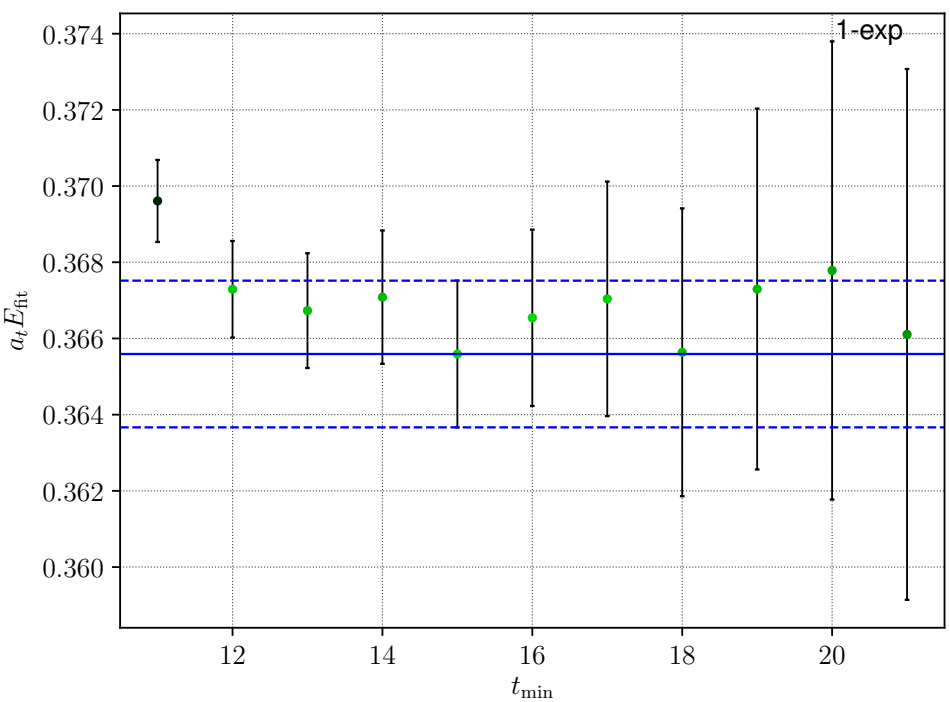

(b) Level 1

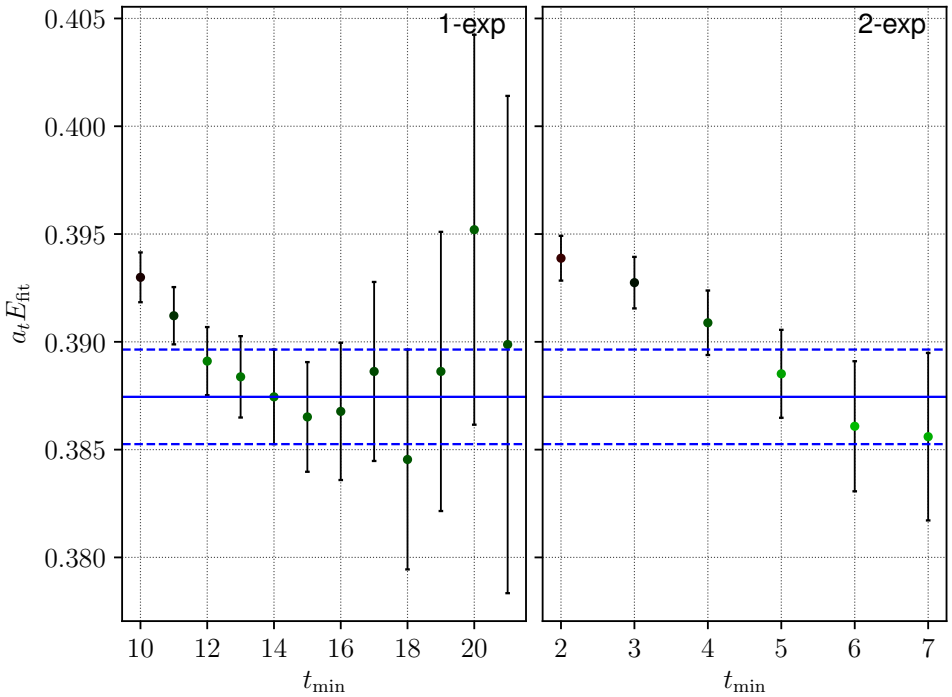

(c) Level 2

Figure C.8: t_{min}-plots for the $P^2 = 3$, A_1 irrep on the N200 ensemble.

$P^2 = 3$, E **Irrep**

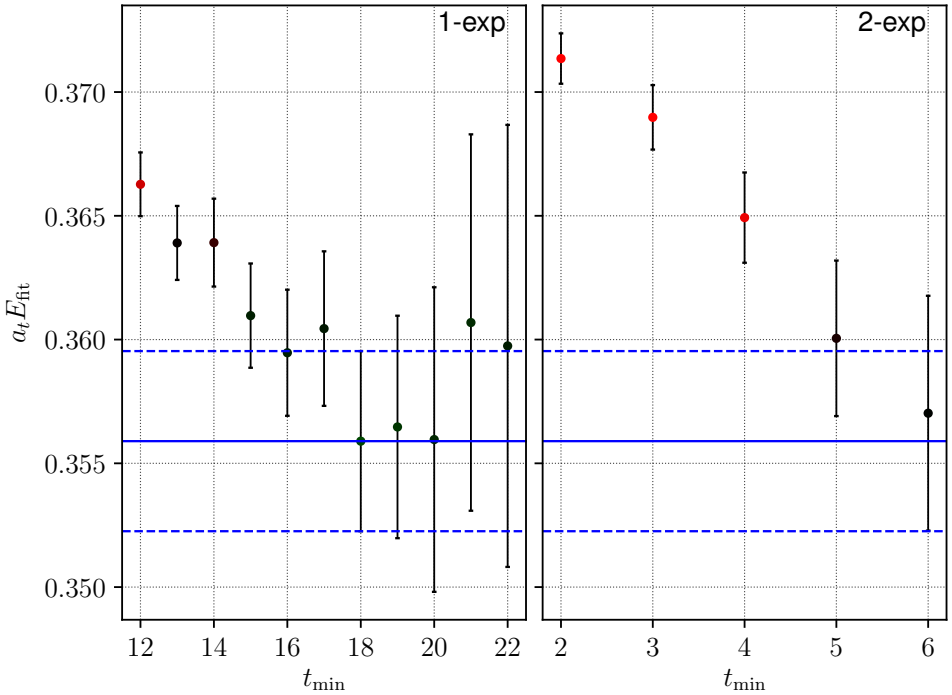

(a) Level 0

Figure C.9: t_{min}-plots for the $P^2 = 3$, E irrep on the N200 ensemble.

$P^2 = 4$, A_1 **Irrep**

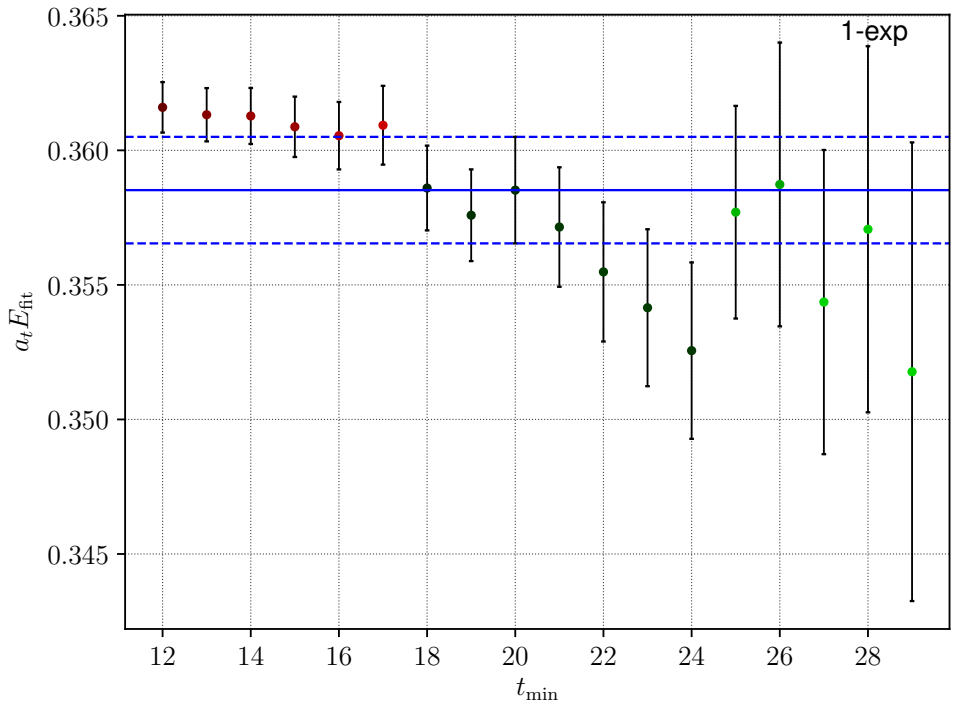

(a) Level 0

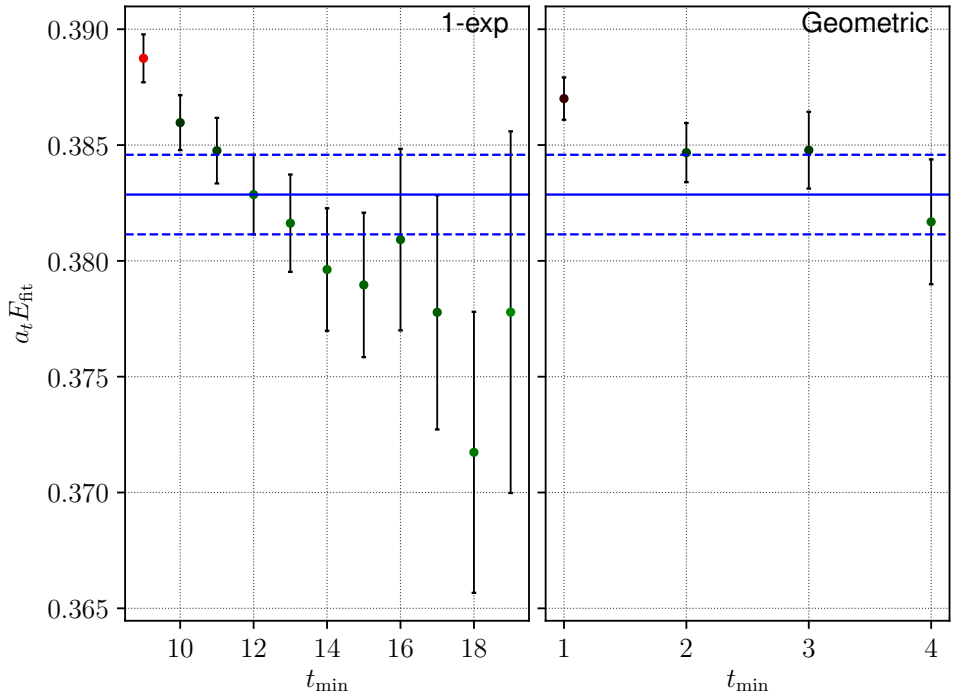

(b) Level 1

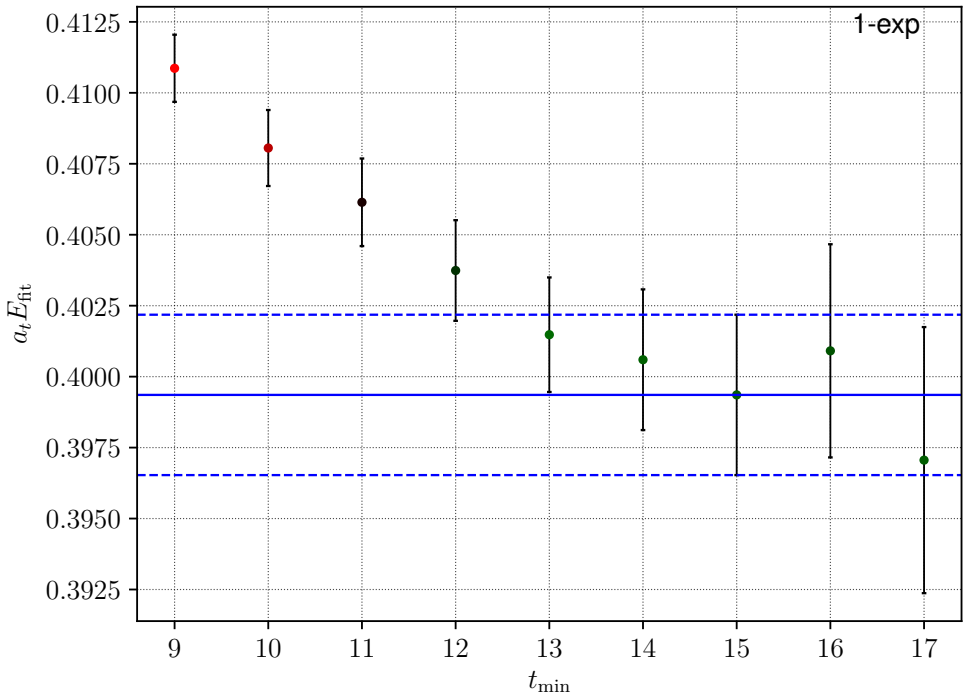

(c) Level 2

Figure C.10: t_{min}-plots for the $P^2 = 4$, A_1 irrep on the N200 ensemble.

$P^2 = 4$, E **Irrep**

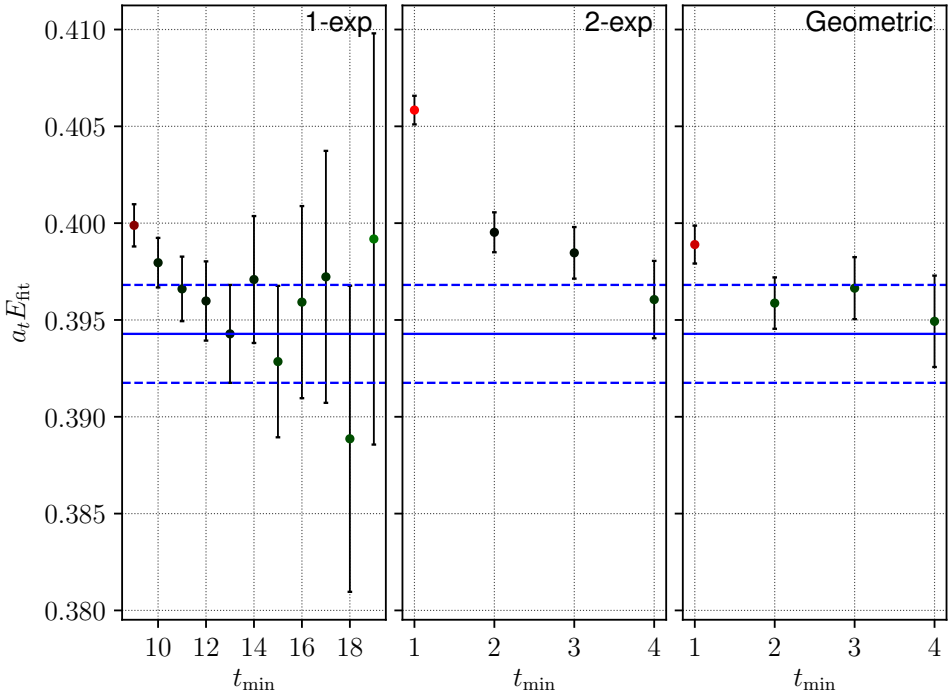

(a) Level 0

Figure C.11: t_{min}-plots for the $P^2 = 4$, E irrep on the N200 ensemble.

Appendix D

Computational Details and Approximations

In this appendix the computational resources used to perform the calculations in chapters 7 and 8 are described, followed by a synopsis of the various approximations that are made in this work.

D.1 Computational Details

The same set of computational steps are required to perform both of the calculations presented here. First, the gauge configurations are generated using the Hybrid Monte Carlo and Rational Hybrid Monte Carlo techniques described in section 2.5. The anisotropic configurations used in chapter 7 were generated using the `Chroma` software suite developed by the USQCD collaboration [164]. These calculations were performed on the Jaguar machine at Oak Ridge National Laboratory and Kraken at the University of Tennessee using approximately 50 million core-hours. The isotropic configurations used in chapter 8 were generated by the CLS consortium [82] using the openQCD code [165]. These calculations were performed on the SuperMUC machine at the Leibniz Supercomputing Centre using approximately 350,000 core-hours.

Next, utilising the `Chroma LapH` software written in C++ for applying the stochastic LapH method described in chapter 4, the quark source and sink functions (see section 4.3) are calculated and used to form the hadron source and sink functions described in section 4.4. The Dirac matrix inversions required here are very expensive, requiring approximately 25 million Kraken and 1.1 million Mogon II/HIMster II core-hours for the results in chapters 7 and 8, respectively. The final step is the calculation of temporal correlation functions using the hadron source and sink functions as described in section 4.4. For correlation functions involving meson and meson-meson operators, the computational cost for this step is comparatively minimal. These calculations were performed on the Ranger machine at the Texas Advanced Computing Center for the analysis in chapter 7, and using the Mogon II and HIMster II machines at the Johannes Gutenberg University Mainz, primarily to support the HVP determination of Ref. [166]. Note that the majority of the calculations

involved in the analysis in chapter 7 were performed as early as 2008, which accounts for the larger number of core hours.

D.2 Approximations

Here we list the various approximations and systematic uncertainties that are present in this thesis.

- **Finite lattice spacing:** Discretisation errors associated with the finite lattice spacing are assessed partially in our calculations by checking for deviations of hadron dispersion relations from the continuum expressions (see eq. (6.10)). We find these to be negligible compared to statistical errors. In future calculations, continuum extrapolations of the form $a \to 0$ can also be performed. This will require significant computational efforts as the computational costs increase dramatically as the lattice spacing decreases.

- **Finite volume effects:** Finite-volume effects of the form $e^{-m_\pi L}$ are neglected, where m_π is the correlation length of the system, for example when applying the quantisation condition derived in chapter 6. In order to mitigate these effects, we follow the general rule-of-thumb where we ensure that $m_\pi L \gtrsim 4$. See section 2.3.3.

- **Unphysical quark masses:** The use of unphysically heavy light quark masses results in the simulation of a theory that should not be compared directly with QCD at the physical point. Hence, in order to fully connect with experimental results, e.g. the $K^*(892)$ resonance parameters determined in chapter 8, extrapolations to the physical point using lattice calculations with various quark masses must be performed. In each of the analyses presented here such extrapolations must yet be performed, requiring significant computational resources.

- **3- and 4-particle states:** In this thesis the effects of three- and four-hadron states have been neglected throughout. As we restrict ourselves to energies below the $K\pi\pi$ threshold in chapter 8, this is only a relevant concern for the analysis performed in chapter 7. There we stress that we have extracted only the finite-volume spectrum of states which are created dominantly by single- and two-hadron interpolating operators. As we consider the spectrum above the 4π threshold, we cannot conclude that we have saturated the spectrum in this region. With the inclusion of such operators, we may see the appearance of additional finite-volume energies above the 4π threshold. This will be required in future studies of the scalar sector when determinations of infinite-volume scattering amplitudes are performed.

- **Exact zeros in $C(t)$:** In the analysis in chapter 7, certain matrix elements in the temporal correlation matrix are set exactly to zero in an effort to reduce some of the statistical noise in the calculation. We justify this decision by performing the analysis both with and without setting the matrix elements in question to zero. We observe little change to the final qualitative results, yet an increase in statistical precision when the matrix elements are set to zero. See section 7.1.3 for more details.

- **Correlator matrix analysis:** When we apply the correlation matrix analysis methods described in chapter 5, there are some systematic uncertainties to address. Systematic error in the choice of diagonalisation times (τ_0, τ_D) is assessed by performing the analysis for multiple choices of these parameters, where we observe no statistically significant deviation in our finite-volume energies. We must also ensure that we are not susceptible to errors arising from the finite operator bases used to construct the correlation matrices. To do this the operator basis is enlarged by adding additional operators until the spectrum in the region of interest does not change. This is discussed in section 5.1.1.

Bibliography

[1] M. Gell-Mann, *A Schematic Model of Baryons and Mesons*, *Phys. Lett.* **8** (1964) 214.

[2] G. Zweig, *An SU(3) model for strong interaction symmetry and its breaking. Version 1*, CERN-TH-401.

[3] G. Zweig, *An SU(3) model for strong interaction symmetry and its breaking. Version 2*, in *Developments in the Quark Theory of Hadrons. Vol. 1. 1964 - 1978*, D. Lichtenberg and S. P. Rosen, eds., pp. 22–101, (1964).

[4] V. E. Barnes et al., *Observation of a Hyperon with Strangeness -3*, *Phys. Rev. Lett.* **12** (1964) 204.

[5] H. Fritzsch, M. Gell-Mann and H. Leutwyler, *Advantages of the Color Octet Gluon Picture*, *Phys. Lett.* **47B** (1973) 365.

[6] D. J. Gross and F. Wilczek, *Ultraviolet Behavior of Nonabelian Gauge Theories*, *Phys. Rev. Lett.* **30** (1973) 1343.

[7] H. D. Politzer, *Reliable Perturbative Results for Strong Interactions?*, *Phys. Rev. Lett.* **30** (1973) 1346.

[8] J. C. Collins, D. E. Soper and G. F. Sterman, *Factorization of Hard Processes in QCD*, *Adv. Ser. Direct. High Energy Phys.* **5** (1989) 1 [hep-ph/0409313].

[9] Particle Data Group collaboration, *Review of Particle Physics*, *Phys. Rev.* **D98** (2018) 030001.

[10] S. Capstick and W. Roberts, *Quark models of baryon masses and decays*, *Prog. Part. Nucl. Phys.* **45** (2000) S241 [nucl-th/0008028].

[11] R. L. Jaffe, *Exotica*, in *Proceedings, 6th International Conference on Hyperons, charm and beauty hadrons (BEACH 2004): Chicago, USA, June 27-July 3, 2004*, vol. 409, pp. 1–45, 2005, hep-ph/0409065, DOI.

[12] C. Michael, *Adjoint Sources in Lattice Gauge Theory*, *Nucl. Phys.* **B259** (1985) 58.

[13] M. Luscher and U. Wolff, *How to Calculate the Elastic Scattering Matrix in Two-dimensional Quantum Field Theories by Numerical Simulation*, *Nucl. Phys.* **B339** (1990) 222.

[14] B. Blossier, M. Della Morte, G. von Hippel, T. Mendes and R. Sommer, *On the generalized eigenvalue method for energies and matrix elements in lattice field theory*, *JHEP* **04** (2009) 094 [0902.1265].

[15] C. Morningstar, J. Bulava, J. Foley, K. J. Juge, D. Lenkner, M. Peardon and C. H. Wong, *Improved stochastic estimation of quark propagation with Laplacian Heaviside smearing in lattice QCD*, *Phys. Rev.* **D83** (2011) 114505 [1104.3870].

[16] M. Luscher, *Two particle states on a torus and their relation to the scattering matrix*, *Nucl. Phys.* **B354** (1991) 531.

[17] L. Maiani and M. Testa, *Final state interactions from Euclidean correlation functions*, *Phys. Lett.* **B245** (1990) 585.

[18] J. Bulava, B. Fahy, B. Hörz, K. J. Juge, C. Morningstar and C. H. Wong, *$I = 1$ and $I = 2$ $\pi - \pi$ scattering phase shifts from $N_{\rm f} = 2 + 1$ lattice QCD*, *Nucl. Phys.* **B910** (2016) 842 [1604.05593].

[19] R. Brett, J. Bulava, J. Fallica, A. Hanlon, B. Hörz and C. Morningstar, *Determination of s- and p-wave $I = 1/2$ $K\pi$ scattering amplitudes in $N_{\rm f} = 2 + 1$ lattice QCD*, *Nucl. Phys.* **B932** (2018) 29 [1802.03100].

[20] C. Andersen, J. Bulava, B. Hörz and C. Morningstar, *The $I = 1$ pion-pion scattering amplitude and timelike pion form factor from $N_{\rm f} = 2 + 1$ lattice QCD*, *Nucl. Phys.* **B939** (2019) 145 [1808.05007].

[21] C. W. Andersen, J. Bulava, B. Hörz and C. Morningstar, *Elastic $I = 3/2$p-wave nucleon-pion scattering amplitude and the Δ(1232) resonance from N_f=2+1 lattice QCD*, *Phys. Rev.* **D97** (2018) 014506 [1710.01557].

[22] USQCD collaboration, *Hot-dense Lattice QCD: USQCD whitepaper 2018*, 1904.09951.

[23] USQCD collaboration, *Lattice Gauge Theory for Physics Beyond the Standard Model*, 1904.09964.

[24] USQCD collaboration, *The Role of Lattice QCD in Searches for Violations of Fundamental Symmetries and Signals for New Physics*, 1904.09704.

[25] USQCD collaboration, *Hadrons and Nuclei*, 1904.09512.

[26] USQCD collaboration, *Status and Future Perspectives for Lattice Gauge Theory Calculations to the Exascale and Beyond*, 1904.09725.

[27] USQCD collaboration, *Lattice QCD and Neutrino-Nucleus Scattering*, 1904.09931.

[28] USQCD collaboration, *Opportunities for lattice QCD in quark and lepton flavor physics*, 1904.09479.

[29] C. Morningstar, J. Bulava, B. Singha, R. Brett, J. Fallica, A. Hanlon and B. Hörz, *Estimating the two-particle K-matrix for multiple partial waves and decay channels from finite-volume energies*, *Nucl. Phys.* **B924** (2017) 477 [1707.05817].

[30] V. Crede and C. A. Meyer, *The Experimental Status of Glueballs*, *Prog. Part. Nucl. Phys.* **63** (2009) 74 [0812.0600].

[31] H.-Y. Cheng, C.-K. Chua and K.-F. Liu, *Revisiting Scalar Glueballs*, *Phys. Rev.* **D92** (2015) 094006 [1503.06827].

[32] UKQCD collaboration, *A Comprehensive lattice study of SU(3) glueballs*, *Phys. Lett.* **B309** (1993) 378 [hep-lat/9304012].

[33] C. J. Morningstar and M. J. Peardon, *The Glueball spectrum from an anisotropic lattice study*, *Phys. Rev.* **D60** (1999) 034509 [hep-lat/9901004].

[34] Y. Chen et al., *Glueball spectrum and matrix elements on anisotropic lattices*, *Phys. Rev.* **D73** (2006) 014516 [hep-lat/0510074].

[35] TXL, T(X)L collaboration, *Static potentials and glueball masses from QCD simulations with Wilson sea quarks*, *Phys. Rev.* **D62** (2000) 054503 [hep-lat/0003012].

[36] A. Hart and M. Teper, *On the glueball spectrum in O(a) improved lattice QCD*, *Phys. Rev.* **D65** (2002) 034502 [hep-lat/0108022].

[37] A. Hart, C. McNeile, C. Michael and J. Pickavance, *A Lattice study of the masses of singlet 0^{++} mesons*, *Phys. Rev.* **D74** (2006) 114504 [hep-lat/0608026].

[38] C. M. Richards, A. C. Irving, E. B. Gregory and C. McNeile, *Glueball mass measurements from improved staggered fermion simulations*, *Phys. Rev.* **D82** (2010) 034501 [1005.2473].

[39] E. Gregory, A. Irving, B. Lucini, C. McNeile, A. Rago, C. Richards and E. Rinaldi, *Towards the glueball spectrum from unquenched lattice QCD*, *JHEP* **10** (2012) 170 [1208.1858].

[40] W. Sun, L.-C. Gui, Y. Chen, M. Gong, C. Liu, Y.-B. Liu, Z. Liu, J.-P. Ma and J.-B. Zhang, *Glueball spectrum from $N_f = 2$ lattice QCD study on anisotropic lattices*, *Chin. Phys.* **C42** (2018) 093103 [1702.08174].

[41] S. Prelovsek, L. Leskovec, C. B. Lang and D. Mohler, *$K\pi$ Scattering and the K^* Decay width from Lattice QCD*, *Phys. Rev.* **D88** (2013) 054508 [1307.0736].

[42] D. J. Wilson, J. J. Dudek, R. G. Edwards and C. E. Thomas, *Resonances in coupled $\pi K, \eta K$ scattering from lattice QCD*, *Phys. Rev.* **D91** (2015) 054008 [1411.2004].

[43] RQCD collaboration, *ρ and K^* resonances on the lattice at nearly physical quark masses and $N_f = 2$*, *Phys. Rev.* **D93** (2016) 054509 [1512.08678].

[44] G. Rendon, L. Leskovec, S. Meinel, J. Negele, S. Paul, M. Petschlies, A. Pochinsky, G. Silvi and S. Syritsyn, *$K\pi$ scattering and the $K^*(892)$ resonance in 2+1 flavor QCD*, *PoS* **LATTICE2018** (2019) 073 [1811.10750].

[45] D. J. Wilson, R. A. Briceno, J. J. Dudek, R. G. Edwards and C. E. Thomas, *The quark-mass dependence of elastic πK scattering from QCD*, 1904.03188.

[46] K. G. Wilson, *Confinement of Quarks*, *Phys. Rev.* **D10** (1974) 2445.

[47] H. J. Rothe, *Lattice Gauge Theories: An Introduction*, *World Sci. Lect. Notes Phys.* **82** (2012) 1.

[48] C. Gattringer and C. B. Lang, *Quantum chromodynamics on the lattice*, *Lect. Notes Phys.* **788** (2010) 1.

[49] H. B. Nielsen and M. Ninomiya, *No Go Theorem for Regularizing Chiral Fermions*, *Phys. Lett.* **105B** (1981) 219.

[50] J. M. Pendlebury et al., *Revised experimental upper limit on the electric dipole moment of the neutron*, *Phys. Rev.* **D92** (2015) 092003 [1509.04411].

[51] K. Osterwalder and R. Schrader, *Euclidean fermi fields and a feynman-kac formula for boson-fermion models*, *Helv. Phys. Acta* **46** (1973) 277.

[52] K. Osterwalder and R. Schrader, *Axioms for Euclidean Green's Functions*, *Commun. Math. Phys.* **31** (1973) 83.

[53] M. E. Peskin and D. V. Schroeder, *An Introduction to quantum field theory.* Addison-Wesley, Reading, USA, 1995.

[54] K. G. Wilson, *Quarks and Strings on a Lattice*, in *New Phenomena in Subnuclear Physics: Proceedings, International School of Subnuclear Physics, Erice, Sicily, Jul 11-Aug 1 1975. Part A*, p. 99, 1975.

[55] J. B. Kogut and L. Susskind, *Hamiltonian Formulation of Wilson's Lattice Gauge Theories*, *Phys. Rev.* **D11** (1975) 395.

[56] L. Susskind, *Lattice Fermions*, *Phys. Rev.* **D16** (1977) 3031.

[57] H. S. Sharatchandra, H. J. Thun and P. Weisz, *Susskind Fermions on a Euclidean Lattice*, *Nucl. Phys.* **B192** (1981) 205.

[58] H. Neuberger, *Exactly massless quarks on the lattice*, *Phys. Lett.* **B417** (1998) 141 [hep-lat/9707022].

[59] H. Neuberger, *More about exactly massless quarks on the lattice*, *Phys. Lett.* **B427** (1998) 353 [hep-lat/9801031].

[60] D. B. Kaplan, *A Method for simulating chiral fermions on the lattice*, *Phys. Lett.* **B288** (1992) 342 [hep-lat/9206013].

[61] Y. Shamir, *Chiral fermions from lattice boundaries*, *Nucl. Phys.* **B406** (1993) 90 [hep-lat/9303005].

[62] Alpha collaboration, *Lattice QCD with a chirally twisted mass term*, *JHEP* **08** (2001) 058 [hep-lat/0101001].

[63] R. Frezzotti and G. C. Rossi, *Chirally improving Wilson fermions. 1. O(a) improvement*, *JHEP* **08** (2004) 007 [hep-lat/0306014].

[64] R. Frezzotti and G. C. Rossi, *Chirally improving Wilson fermions. II. Four-quark operators*, *JHEP* **10** (2004) 070 [hep-lat/0407002].

[65] K. Symanzik, *Continuum Limit and Improved Action in Lattice Theories. 1. Principles and ϕ^4 Theory*, *Nucl. Phys.* **B226** (1983) 187.

[66] K. Symanzik, *Continuum Limit and Improved Action in Lattice Theories. 2. O(N) Nonlinear Sigma Model in Perturbation Theory*, *Nucl. Phys.* **B226** (1983) 205.

[67] M. Luscher and P. Weisz, *On-Shell Improved Lattice Gauge Theories*, *Commun. Math. Phys.* **97** (1985) 59.

[68] D. Darvish, R. Brett, J. Bulava, J. Fallica, A. Hanlon and C. Morningstar, *Scattering phase shift determinations from a two-scalar field theory*, *PoS* **LATTICE2018** (2018) 070 [1810.11433].

[69] M. Luscher and P. Weisz, *O(a) improvement of the axial current in lattice QCD to one loop order of perturbation theory*, *Nucl. Phys.* **B479** (1996) 429 [hep-lat/9606016].

[70] J. Bulava and S. Schaefer, *Improvement of $N_f = 3$ lattice QCD with Wilson fermions and tree-level improved gauge action*, *Nucl. Phys.* **B874** (2013) 188 [1304.7093].

[71] R. G. Edwards, B. Joo and H.-W. Lin, *Tuning for Three-flavors of Anisotropic Clover Fermions with Stout-link Smearing*, *Phys. Rev.* **D78** (2008) 054501 [0803.3960].

[72] Hadron Spectrum collaboration, *First results from 2+1 dynamical quark flavors on an anisotropic lattice: Light-hadron spectroscopy and setting the strange-quark mass*, *Phys. Rev.* **D79** (2009) 034502 [0810.3588].

[73] B. Sheikholeslami and R. Wohlert, *Improved Continuum Limit Lattice Action for QCD with Wilson Fermions*, *Nucl. Phys.* **B259** (1985) 572.

[74] P. Chen, *Heavy quarks on anisotropic lattices: The Charmonium spectrum*, *Phys. Rev.* **D64** (2001) 034509 [hep-lat/0006019].

[75] M. Luscher, S. Sint, R. Sommer and P. Weisz, *Chiral symmetry and O(a) improvement in lattice QCD*, *Nucl. Phys.* **B478** (1996) 365 [hep-lat/9605038].

[76] T. A. DeGrand, A. Hasenfratz and T. G. Kovacs, *Improving the chiral properties of lattice fermions*, *Phys. Rev.* **D67** (2003) 054501 [hep-lat/0211006].

[77] G. P. Lepage and P. B. Mackenzie, *On the viability of lattice perturbation theory*, *Phys. Rev.* **D48** (1993) 2250 [hep-lat/9209022].

[78] M. Luscher, *Construction of a Selfadjoint, Strictly Positive Transfer Matrix for Euclidean Lattice Gauge Theories*, *Commun. Math. Phys.* **54** (1977) 283.

[79] M. Luscher and P. Weisz, *Definition and General Properties of the Transfer Matrix in Continuum Limit Improved Lattice Gauge Theories*, *Nucl. Phys.* **B240** (1984) 349.

[80] C. J. Morningstar and M. J. Peardon, *Efficient glueball simulations on anisotropic lattices*, *Phys. Rev.* **D56** (1997) 4043 [hep-lat/9704011].

[81] M. Luscher and P. Weisz, *Computation of the Action for On-Shell Improved Lattice Gauge Theories at Weak Coupling*, *Phys. Lett.* **158B** (1985) 250.

[82] M. Bruno et al., *Simulation of QCD with $N_f = 2 + 1$ flavors of non-perturbatively improved Wilson fermions*, *JHEP* **02** (2015) 043 [1411.3982].

[83] RQCD collaboration, *Lattice simulations with $N_f = 2 + 1$ improved Wilson fermions at a fixed strange quark mass*, *Phys. Rev.* **D94** (2016) 074501 [1606.09039].

[84] M. Luscher and F. Palombi, *Fluctuations and reweighting of the quark determinant on large lattices*, *PoS* **LATTICE2008** (2008) 049 [0810.0946].

[85] M. Luscher and S. Schaefer, *Lattice QCD with open boundary conditions and twisted-mass reweighting*, *Comput. Phys. Commun.* **184** (2013) 519 [1206.2809].

[86] A. Di Giacomo, *Topology in lattice QCD*, in *Theory of elementary particles. Proceedings, 31st International Symposium Ahrenshoop, Buckow, Germany, September 2-6, 1997*, pp. 213–220, 1997, hep-lat/9711034.

[87] A. Dromard and M. Wagner, *Extracting hadron masses from fixed topology simulations*, *Phys. Rev.* **D90** (2014) 074505 [1404.0247].

[88] M. Luscher, *Topology, the Wilson flow and the HMC algorithm*, *PoS* **LATTICE2010** (2010) 015 [1009.5877].

[89] M. Luscher and S. Schaefer, *Lattice QCD without topology barriers*, *JHEP* **07** (2011) 036 [1105.4749].

[90] M. Bruno, T. Korzec and S. Schaefer, *Setting the scale for the CLS* $2+1$ *flavor ensembles*, *Phys. Rev.* **D95** (2017) 074504 [1608.08900].

[91] M. Luscher, R. Narayanan, P. Weisz and U. Wolff, *The Schrodinger functional: A Renormalizable probe for nonAbelian gauge theories*, *Nucl. Phys.* **B384** (1992) 168 [hep-lat/9207009].

[92] M. Lüscher, *Properties and uses of the Wilson flow in lattice QCD*, *JHEP* **08** (2010) 071 [1006.4518].

[93] ALPHA collaboration, *On the* N_f*-dependence of gluonic observables*, *PoS* **LATTICE2013** (2014) 321 [1311.5585].

[94] S. Borsanyi et al., *High-precision scale setting in lattice QCD*, *JHEP* **09** (2012) 010 [1203.4469].

[95] W. Bietenholz et al., *Tuning the strange quark mass in lattice simulations*, *Phys. Lett.* **B690** (2010) 436 [1003.1114].

[96] T. Tilma and E. C. G. Sudarshan, *Generalized Euler angle parametrization for SU(N)*, *Journal of Physics A: Mathematical and General* **35** (2002) 10467.

[97] C. Morningstar, *The Monte Carlo method in quantum field theory*, in *21st Annual Hampton University Graduate Studies Program (HUGS 2006) Newport News, Virginia, June 5-23, 2006*, 2007, hep-lat/0702020.

[98] N. Metropolis, A. W. Rosenbluth, M. N. Rosenbluth, A. H. Teller and E. Teller, *Equation of state calculations by fast computing machines*, *J. Chem. Phys.* **21** (1953) 1087.

[99] W. K. Hastings, *Monte carlo sampling methods using markov chains and their applications*, *Biometrika* **57** (1970) 97.

[100] S. Duane, A. D. Kennedy, B. J. Pendleton and D. Roweth, *Hybrid Monte Carlo*, *Phys. Lett.* **B195** (1987) 216.

[101] M. A. Clark, A. D. Kennedy and Z. Sroczynski, *Exact 2+1 flavour RHMC simulations*, *Nucl. Phys. Proc. Suppl.* **140** (2005) 835 [hep-lat/0409133].

[102] M. A. Clark, *The Rational Hybrid Monte Carlo Algorithm*, *PoS* **LAT2006** (2006) 004 [hep-lat/0610048].

[103] J. M. Bulava et al., *Excited State Nucleon Spectrum with Two Flavors of Dynamical Fermions*, *Phys. Rev.* **D79** (2009) 034505 [0901.0027].

[104] C. Morningstar, *Hadron spectroscopy in Lattice QCD*, *Private Notes* .

[105] C. Morningstar and M. J. Peardon, *Analytic smearing of SU(3) link variables in lattice QCD*, *Phys. Rev.* **D69** (2004) 054501 [hep-lat/0311018].

[106] M. G. Alford, T. Klassen and P. Lepage, *The D234 action for light quarks*, *Nucl. Phys. Proc. Suppl.* **47** (1996) 370 [hep-lat/9509087].

[107] Hadron Spectrum collaboration, *A Novel quark-field creation operator construction for hadronic physics in lattice QCD*, *Phys. Rev.* **D80** (2009) 054506 [0905.2160].

[108] S. Basak, R. G. Edwards, G. T. Fleming, U. M. Heller, C. Morningstar, D. Richards, I. Sato and S. Wallace, *Group-theoretical construction of extended baryon operators in lattice QCD*, *Phys. Rev.* **D72** (2005) 094506 [hep-lat/0506029].

[109] C. Morningstar, J. Bulava, B. Fahy, J. Foley, Y. C. Jhang, K. J. Juge, D. Lenkner and C. H. Wong, *Extended hadron and two-hadron operators of definite momentum for spectrum calculations in lattice QCD*, *Phys. Rev.* **D88** (2013) 014511 [1303.6816].

[110] R. S. Mulliken, *Report on notation for the spectra of polyatomic molecules*, *The Journal of Chemical Physics* **23** (1955) 1997.

[111] R. S. Mulliken, *Erratum : Report on notation for the spectra of polyatomic molecules*, *The Journal of Chemical Physics* **24** (1956) 1118.

[112] R. C. Johnson, *Angular Momentum on a Lattice*, *Phys. Lett.* **114B** (1982) 147.

[113] J. Cornwell, *Group Theory in Physics: An Introduction*, Techniques of Physics. Elsevier Science, 1997.

[114] R. Brett, J. Bulava, D. Darvish, J. Fallica, A. Hanlon and C. Morningstar, *Tetraquark operators in the scalar meson sectors in lattice QCD*, To appear.

[115] J. Foley, K. Jimmy Juge, A. O'Cais, M. Peardon, S. M. Ryan and J.-I. Skullerud, *Practical all-to-all propagators for lattice QCD*, *Comput. Phys. Commun.* **172** (2005) 145 [hep-lat/0505023].

[116] S. Bernardson, P. McCarty and C. Thron, *Monte carlo methods for estimating linear combinations of inverse matrix entries in lattice qcd*, *Computer Physics Communications* **78** (1994) 256 .

[117] W. Wilcox, *Noise methods for flavor singlet quantities*, in *Numerical challenges in lattice quantum chromodynamics. Proceedings, Joint Interdisciplinary Workshop, Wuppertal, Germany, August 22-24, 1999*, pp. 127–141, 1999, hep-lat/9911013.

[118] H. C. Andrews and C. L. Patterson, *Outer product expansions and their uses in digital image processing*, *The American Mathematical Monthly* **82** (1975) 1.

[119] D. O'Leary and S. Peleg, *Digital image compression by outer product expansion*, *IEEE Transactions on Communications* **31** (1983) 441.

[120] K. G. Wilson, *Lecture presented at the Abingdon Meeting on Lattice Gauge Theories*, 1981.

[121] B. S. DeWitt, *Transition from discrete to continuous spectra*, *Phys. Rev.* **103** (1956) 1565.

[122] A. Reifman, B. S. DeWitt and R. G. Newton, *Relations between bound-state problems and scattering theory*, *Phys. Rev.* **101** (1956) 877.

[123] M. Luscher, *On a Relation Between Finite Size Effects and Elastic Scattering Processes*, in *Progress in Gauge Field Theory. Proceedings, NATO Advanced Study Institute, Cargese, France, September 1-15, 1983*, vol. 115, 1984.

[124] M. Luscher, *Volume Dependence of the Energy Spectrum in Massive Quantum Field Theories. 1. Stable Particle States*, *Commun. Math. Phys.* **104** (1986) 177.

[125] M. Luscher, *Volume Dependence of the Energy Spectrum in Massive Quantum Field Theories. 2. Scattering States*, *Commun. Math. Phys.* **105** (1986) 153.

[126] K. Rummukainen and S. A. Gottlieb, *Resonance scattering phase shifts on a nonrest frame lattice*, *Nucl. Phys.* **B450** (1995) 397 [hep-lat/9503028].

[127] C. h. Kim, C. T. Sachrajda and S. R. Sharpe, *Finite-volume effects for two-hadron states in moving frames*, *Nucl. Phys.* **B727** (2005) 218 [hep-lat/0507006].

[128] T. Luu and M. J. Savage, *Extracting Scattering Phase-Shifts in Higher Partial-Waves from Lattice QCD Calculations*, *Phys. Rev.* **D83** (2011) 114508 [1101.3347].

[129] Z. Fu, *Rummukainen-Gottlieb's formula on two-particle system with different mass*, *Phys. Rev.* **D85** (2012) 014506 [1110.0319].

[130] L. Leskovec and S. Prelovsek, *Scattering phase shifts for two particles of different mass and non-zero total momentum in lattice QCD*, *Phys. Rev.* **D85** (2012) 114507 [1202.2145].

[131] M. T. Hansen and S. R. Sharpe, *Multiple-channel generalization of Lellouch-Luscher formula*, *Phys. Rev.* **D86** (2012) 016007 [1204.0826].

[132] M. Gockeler, R. Horsley, M. Lage, U. G. Meissner, P. E. L. Rakow, A. Rusetsky, G. Schierholz and J. M. Zanotti, *Scattering phases for meson and baryon resonances on general moving-frame lattices*, *Phys. Rev.* **D86** (2012) 094513 [1206.4141].

[133] R. A. Briceno and Z. Davoudi, *Moving multichannel systems in a finite volume with application to proton-proton fusion*, *Phys. Rev.* **D88** (2013) 094507 [1204.1110].

[134] R. A. Briceño, *Two-particle multichannel systems in a finite volume with arbitrary spin*, arXiv:1401.3312v4.

[135] K. Polejaeva and A. Rusetsky, *Three particles in a finite volume*, *Eur. Phys. J.* **A48** (2012) 67 [1203.1241].

[136] R. A. Briceno and Z. Davoudi, *Three-particle scattering amplitudes from a finite volume formalism*, *Phys. Rev.* **D87** (2013) 094507 [1212.3398].

[137] M. T. Hansen and S. R. Sharpe, *Relativistic, model-independent, three-particle quantization condition*, *Phys. Rev.* **D90** (2014) 116003 [1408.5933].

[138] M. T. Hansen and S. R. Sharpe, *Expressing the three-particle finite-volume spectrum in terms of the three-to-three scattering amplitude*, *Phys. Rev.* **D92** (2015) 114509 [1504.04248].

[139] R. A. Briceño, M. T. Hansen and S. R. Sharpe, *Relating the finite-volume spectrum and the two-and-three-particle S matrix for relativistic systems of identical scalar particles*, *Phys. Rev.* **D95** (2017) 074510 [1701.07465].

[140] H. W. Hammer, J. Y. Pang and A. Rusetsky, *Three particle quantization condition in a finite volume: 2. general formalism and the analysis of data*, *JHEP* **10** (2017) 115 [1707.02176].

[141] M. Mai and M. Döring, *Three-body Unitarity in the Finite Volume*, *Eur. Phys. J.* **A53** (2017) 240 [1709.08222].

[142] R. A. Briceño, M. T. Hansen and S. R. Sharpe, *Numerical study of the relativistic three-body quantization condition in the isotropic approximation*, *Phys. Rev.* **D98** (2018) 014506 [1803.04169].

[143] M. Döring, H. W. Hammer, M. Mai, J. Y. Pang, A. Rusetsky and J. Wu, *Three-body spectrum in a finite volume: the role of cubic symmetry*, *Phys. Rev.* **D97** (2018) 114508 [1802.03362].

[144] M. T. Hansen and S. R. Sharpe, *Lattice QCD and Three-particle Decays of Resonances*, 1901.00483.

[145] R. A. Briceño, M. T. Hansen and S. R. Sharpe, *Three-particle systems with resonant subprocesses in a finite volume*, *arXiv e-prints* (2018) [1810.01429].

[146] T. D. Blanton, F. Romero-López and S. R. Sharpe, *Implementing the three-particle quantization condition including higher partial waves*, *JHEP* **03** (2019) 106 [1901.07095].

[147] M. Mai and M. Doring, *Finite-Volume Spectrum of $\pi^+\pi^+$ and $\pi^+\pi^+\pi^+$ Systems*, *Phys. Rev. Lett.* **122** (2019) 062503 [1807.04746].

[148] J. Bulava and M. T. Hansen, *Scattering amplitudes from finite-volume spectral functions*, 1903.11735.

[149] E. P. Wigner, *Resonance Reactions and Anomalous Scattering*, *Phys. Rev.* **70** (1946) 15.

[150] E. P. Wigner and L. Eisenbud, *Higher Angular Momenta and Long Range Interaction in Resonance Reactions*, *Phys. Rev.* **72** (1947) 29.

[151] H. A. Bethe, *Theory of the effective range in nuclear scattering*, *Phys. Rev.* **76** (1949) 38.

[152] M. H. Ross and G. L. Shaw, *Multichannel effective range theory*, *Annals of Physics* **13** (1961) 147 .

[153] J. de Swart and C. Dullemond, *Effective range theory and the low energy hyperon-nucleon interactions*, *Annals of Physics* **19** (1962) 458 .

[154] C. Morningstar. https://github.com/cjmorningstar10/TwoHadronsInBox, 2017.

[155] R. A. Briceno, J. J. Dudek, R. G. Edwards and D. J. Wilson, *Isoscalar $\pi\pi$ scattering and the σ meson resonance from QCD*, *Phys. Rev. Lett.* **118** (2017) 022002 [1607.05900].

[156] B. Hörz and A. Hanlon, *Two- and three-pion finite-volume spectra at maximal isospin from lattice QCD*, 1905.04277.

[157] S. R. Beane, P. F. Bedaque, T. C. Luu, K. Orginos, E. Pallante, A. Parreno and M. J. Savage, *πK scattering in full QCD with domain-wall valence quarks*, *Phys. Rev.* **D74** (2006) 114503 [hep-lat/0607036].

[158] Z. Fu, *Lattice study on πK scattering with moving wall source*, *Phys. Rev.* **D85** (2012) 074501 [1110.1422].

[159] C. B. Lang, L. Leskovec, D. Mohler and S. Prelovsek, *K pi scattering for isospin 1/2 and 3/2 in lattice QCD*, *Phys. Rev.* **D86** (2012) 054508 [1207.3204].

[160] PACS-CS collaboration, *Scattering lengths for two pseudoscalar meson systems*, *Phys. Rev.* **D89** (2014) 054502 [1311.7226].

[161] E. Berkowitz et al., *Progress in Multibaryon Spectroscopy*, *PoS* **LATTICE2018** (2018) 003 [1902.09416].

[162] B. Efron, *The jackknife, the bootstrap, and other resampling plans*, vol. 38. Siam, 1982.

[163] S. Piemonte, S. Collins, D. Mohler, M. Padmanath and S. Prelovsek, *Charmonium resonances with $J^{PC} = 1^{--}$ and 3^{--} from $\bar{D}D$ scattering on the lattice*, 1905.03506.

[164] SciDAC, LHPC, UKQCD collaboration, *The Chroma software system for lattice QCD*, *Nucl. Phys. Proc. Suppl.* **140** (2005) 832 [hep-lat/0409003].

[165] http://luscher.web.cern.ch/luscher/openQCD/.

[166] A. Gérardin, M. Cè, G. von Hippel, B. Hörz, H. B. Meyer, D. Mohler, K. Ottnad, J. Wilhelm and H. Wittig, *The leading hadronic contribution to $(g-2)_\mu$ from lattice QCD with $N_\mathrm{f} = 2+1$ flavours of O(a) improved Wilson quarks*, 1904.03120.